IPP-Report

Max-Planck-Institut für Plasmaphysik

Sofia Cristofaro

**Work function of caesiated surfaces in $H_2$/$D_2$ low temperature plasmas correlated with negative ion formation**

**IPP 2019-05**
**März 2019**

# Work function of caesiated surfaces in $H_2/D_2$ low temperature plasmas correlated with negative ion formation

## Dissertation

zur Erlangung des akademischen Grades

Dr. rer. nat

eingereicht an der

Mathematisch-Naturwissenschaftlich-Technischen Fakultät

der Universität Augsburg

von

**Sofia Cristofaro**

Augsburg, September 2018

Tag der mündlichen Prüfung: 15.01.2019

Erster Gutachter: apl. Prof. Dr.-Ing. U. Fantz

Zweiter Gutachter: Prof. Dr. H. Höppe

# Abstract

An important component of future fusion machines like ITER and DEMO is the neutral beam injection system based on negative hydrogen or deuterium ions (NNBI). The NNBI system for ITER will deliver 16.5 MW of power by means of a 1 MeV accelerated and homogeneous beam with pulses of up to one hour. A key element of the NNBI is the ion source, which will deliver an accelerated $D^-$ current density of 200 A/m$^2$ with a co-extracted electron to extracted negative ion current density ratio below unity. The ion source relies on the surface production of negative hydrogen ions via conversion of atomic hydrogen and positive hydrogen ions impinging on a caesiated low work function surface. At the ion sources a main issue is the temporal instability of the co-extracted electron current, which constantly increases during long pulses. Such instability is expected to be connected to a degradation or vanishing of the Cs layer at the converter surface, causing a variation of the work function. This issue is more evident in deuterium operation, where stronger dynamics of the electron current with respect to hydrogen operation is observed. Fundamental investigations of the negative ion formation and of the work function of caesiated surfaces are thus performed in the flexible laboratory experiment ACCesS, operating at ion source relevant vacuum (background pressure: $10^{-6}$ mbar) and plasma conditions. The setup consists of an inductively coupled plasma, of a Cs oven for the Cs evaporation, and of several diagnostic systems, in order to investigate the work function of a surface, the Cs dynamics, the $H^-$ density in front of the surface, and the plasma parameters.

It is known that during vacuum phases the moderate vacuum leads to the formation of non-metallic Cs compounds at the surface, leading to work functions of 2.7 eV in minimum. The current investigations have shown the impact of plasma exposure on the work function of a caesiated surface due to the impinging plasma particles and the UV/VUV radiation. On the one hand, the plasma cleans the Cs layer within 5–10 seconds leading to a decrease of the work function from 2.7 to 2.1 eV (corresponding to pure Cs). On the other hand, the plasma surface interaction also removes the Cs layer if not enough Cs flux towards the surface is sustained. Thus, the removal of the Cs layer must be counteracted by a Cs flux of at least $1.5 \times 10^{16}$ m$^{-2}$s$^{-1}$. Furthermore, a similar temporal variation of the work function in hydrogen and deuterium plasmas is observed.

Moreover, controlled and reproducible investigations allowed to correlate for the first time the negative ion density in front of the surface to the work function, showing a steep increase of the negative ion density for work functions below 2.7 eV both in $H_2$ and in $D_2$ operation.

Finally, due to the high Cs reactivity and complex redistribution dynamics, alternative materials were considered in view of the demonstration fusion reactor DEMO: $LaB_6$, lanthanated materials (W and Mo), a tungsten dispenser cathode, and europium were tested. However, none of the considered materials is a valid alternative to Cs evaporation due to either too high work function under ion source conditions or even higher dynamics compared to Cs.

# Contents


**1 Introduction** **9**

**2 Ion sources for negative hydrogen ions** **11**

**3 Low temperature low pressure hydrogen plasmas** **25**

3.1 Plasma properties . . . . . 25

3.2 Low temperature low pressure plasmas . . . . . 26

3.2.1 Electron energy distribution . . . . . 27

3.2.2 Plasma processes . . . . . 28

3.3 Plasma sheath . . . . . 32

3.4 Hydrogen plasmas . . . . . 34

3.4.1 Atomic hydrogen . . . . . 34

3.4.2 Hydrogen molecule . . . . . 35

3.4.3 Hydrogen plasma processes . . . . . 37

**4 Negative hydrogen ions and the converter surface** **41**

4.1 Volume formation . . . . . 41

4.2 Surface formation . . . . . 42

4.3 Destruction mechanisms . . . . . 46

4.4 Converter surfaces for negative ion sources . . . . . 49

**5 Caesium properties** **53**

5.1 Atomic properties . . . . . 53

5.2 Work function of caesiated surfaces . . . . . 54

5.3 Cs desorption and adsorption . . . . . 55

5.4 Cs compounds and ion source relevant conditions . . . . . 58

**6 Experimental setup and applied diagnostics** **61**

6.1 Experimental setup . . . . . 61

6.2 Sample holder . . . . . 64

6.3 Caesium source . . . . . 66

6.4 Monitoring systems . . . . . 68
6.4.1 Cs diagnostics . . . . . 68
6.4.2 Optical emission spectroscopy (OES) for hydrogen species 74
6.4.3 Langmuir probe . . . . . 78
6.4.4 Residual gas analyzer (RGA) . . . . . 82

**7 Determination of WF and $n_{H^-}$ & experimental procedure 83**
7.1 Work function diagnostic . . . . . 83
7.1.1 Fowler method . . . . . 83
7.1.2 Setup for work function measurements at ACCesS . . . . . 86
7.1.3 Benchmark and typical procedure for the work function measurements . . . . . 89
7.2 $H^-$ density diagnostic . . . . . 92
7.2.1 Cavity ring-down spectroscopy (CRDS) . . . . . 92
7.2.2 CRDS setup at ACCesS . . . . . 94
7.3 Typical plasma operation . . . . . 97
7.3.1 $H^-$ volume production at ACCesS . . . . . 99
7.3.2 $H^-$ surface production at ACCesS . . . . . 101

**8 Low work function materials 103**
8.1 Lanthanum hexaboride . . . . . 103
8.2 Lanthanated materials . . . . . 106
8.3 Tungsten dispenser cathode . . . . . 107
8.4 Europium . . . . . 112
8.5 Summary . . . . . 116

**9 Work function of caesiated surfaces 119**
9.1 Cs evaporation at ACCesS . . . . . 119
9.1.1 Evaporation under vacuum conditions . . . . . 121
9.1.2 Evaporation during plasma operation . . . . . 124
9.2 Surface caesiation in vacuum . . . . . 126
9.3 Plasma exposure on caesiated surfaces . . . . . 128
9.4 Caesiation during plasma . . . . . 134

**10 Correlation between $H^-/D^-$ density and work function 137**
10.1 Caesiation in $H_2$ plasma at 2 Pa/450 W . . . . . 138
10.2 Correlation between $H^-$ density and work function . . . . . 142
10.3 Comp. between $H_2$ and $D_2$ plasmas regarding surf. prod. of neg. ions 145

**11 Application to negative ion sources for fusion** **151**

**12 Conclusions** **159**

**Bibliography** **163**

**Acknowledgements** **177**

# 1 Introduction

Thermonuclear fusion is one of the promising candidates for a sustainable energy production, and the first reactor-scale nuclear fusion experiment ITER[1] is currently under construction in France (Cadarache). ITER represents an intermediate step towards a commercial fusion power plant, whose feasibility will be proved by the demonstration power plant DEMO.

An important component of such fusion machines is the neutral beam injection system based on negative hydrogen[2] ions (NNBI). The NNBI consists of a negative hydrogen ion source, where negative hydrogen ions are created in a low pressure low temperature hydrogen plasma by plasma surface interaction. The negative hydrogen ions are then extracted and accelerated, producing a high energetic ion beam. This beam is afterwards neutralized and injected into the fusion plasma.

ITER will include two high energetic neutral beam injection systems delivering 16.5 MW each. A 1 MeV accelerated and homogeneous $D^-$ beam of 40 A is required with an accelerated negative ion current density of 200 $A/m^2$ and for pulses of up to 1 hour. In particular, since electrons are inevitably co-extracted together with the negative ions, it is required that the ratio between the co-extracted electron current and the extracted negative ion current must not exceed unity. At present, no NNBI system fulfills simultaneously all the ITER requirements, hence research and extensive investigations are carried on to further develop the ion sources and the other NNBI components.

The NNBI source for ITER relies on the surface production mechanism of negative hydrogen ions via conversion of atomic hydrogen and positive hydrogen ions impinging on a low work function converter surface. To achieve the low work function, the converter surface is coated with caesium (i.e. the element with the lowest work function) by evaporation within the source. Cs easily reacts with the residual gases during vacuum phases, affecting the work function of the Cs layer, and the interactions of the plasma particles, together with the UV/VUV plasma

[1] ITER: latin word meaning 'the way'.
[2] Summarizing the hydrogen isotopes $^1H$ and $^2D$.

emission, lead to a cleaning and a removal of the Cs layer. Hence, a continuous evaporation of fresh Cs during plasma operation is mandatory for a stable bulk Cs layer. Nevertheless, particular attention has to be paid to minimize the Cs consumption in view of DEMO.

The prototype source for the ITER NNBI is the RF-driven ion source developed at the Max-Planck-Institut für Plasmaphysik (IPP) in Garching, Germany. Experiments carried out at the IPP test facilities demonstrated that the ITER requirements can be achieved for short plasma pulses, while the performance decreases during long plasma operation. A big issue is the co-extracted electron current, which constantly increases during long pulses. This problem is particularly relevant during deuterium operation, since the co-extracted electron current is much higher than during hydrogen operation.

In order to gain insight into the behavior of the negative ion current and the co-extracted electron current in correlation with the work function of a caesiated surface (diagnostically not easily accessible at the ion sources), fundamental investigations are performed at the flexible laboratory experiment ACCesS[3], which can reproduce ion source relevant vacuum and plasma parameters at controlled conditions. The setup consists of an inductively coupled plasma (ICP), a Cs oven for the Cs evaporation, and several diagnostic systems, in order to investigate the work function of a surface, the Cs dynamics, the $H^-$ density in front of the surface, and the plasma parameters.

ACCesS allows studying the impact on the Cs layer (namely on the work function) of a plasma equivalent to the one in front of the converter surface in the ion sources. The removal of Cs must be balanced by a sufficient Cs flux towards the surface, and extensive investigations require reproducible conditions, which are assured at ACCesS. Moreover, ACCesS allows studying the correlation between the negative ion density in front of the caesiated surface and the work function in a hydrogen plasma where the plasma parameters are known and the surface work function can be controlled. In particular, it is still unknown if an isotopic difference occurs in the negative ion formation of $H^-$ and $D^-$, and ACCesS assures reproducible conditions for the investigations with the two separate isotopes. Finally, due to the high Cs reactivity, alternative materials are considered in view of DEMO. Such materials must be compared to Cs in terms of reliability and work function at reproducible and ion source relevant conditions. ACCesS is thus perfectly suitable for such investigations.

[3] Augsburg Comprehensive Cesium Setup.

# 2 Ion sources for negative hydrogen ions

ITER is a thermonuclear fusion experiment currently under construction in Cadarache (south of France). It is based on the thermonuclear fusion of deuterium and tritium in a magnetically confined plasma [KLT12]:

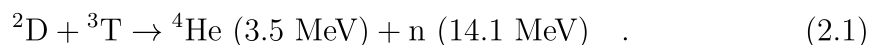

$$^{2}\mathrm{D} + {}^{3}\mathrm{T} \rightarrow {}^{4}\mathrm{He}\ (3.5\ \mathrm{MeV}) + \mathrm{n}\ (14.1\ \mathrm{MeV}) \quad . \tag{2.1}$$

The plasma, that is heated up to $10^8$ K in order to have sufficient fusion reactions, is confined in the shape of a torus by a toroidal and a poloidal magnetic field in order to avoid contacts between the hot plasma and the walls. The magnetic configuration chosen for ITER is the Tokamak: a set of coils surrounding the torus creates the toroidal magnetic field, while the poloidal component is created by inducing a toroidal electric current inside the plasma. To this purpose, a solenoid is located on the axis of symmetry at the center of the torus and the variation of the current flowing in this solenoid drives the induced current in the plasma. For this reason the tokamak can only be operated in pulsed mode and for continuous operation additional mechanisms to drive a current in the plasma are needed to sustain the poloidal magnetic field.

At present, the first plasma operation in the ITER experiment is planned for 2025 [ITE17]. ITER will be the first fusion reactor-scale experiment and its purpose is to prove the feasibility of thermonuclear fusion in a reactor-scale device for plasma pulses of up to one hour and a power gain factor (the so-called *Q value*) equal or greater than ten[1] [SCM+07]. In order to reach the required temperature of tens of keV[2] in the toroidal plasma, different heating mechanisms will be used like the electron (ECRH) and ion (ICRH) cyclotron resonance heating, which will deliver a power of 20 MW each, and the neutral beam injection (NBI), which will

[1] Aim of ITER is to obtain 500 MW of fusion power by using 50 MW of injected heating power.

[2] In plasma physics it is common practice to give the temperature $T$ as the energy equivalent $k_\mathrm{B}T$, with $k_\mathrm{B}$ the Boltzmann constant.

provide 33 MW to the fusion plasma by means of two beamlines at a beam energy of 1 MeV [IAE02, SCM+07]. The latter heating system has a crucial role in the plasma stability, since it may efficiently drive a non-inductive toroidal current which sustains the poloidal magnetic field and enhances the plasma confinement, allowing for long pulse operation.

Beyond ITER, the next step before the commercial exploitation of fusion energy is represented by the DEMO demonstration reactor, whose aim is to prove the feasibility of the technologies needed for the construction of a commercial fusion power plant, supplying eventually net electricity to the grid by 2050 [RBB+12]. DEMO construction is foreseen to start around 2040 [FBG+17], after the lessons learned from the ITER experiment. At present, the final design of DEMO has not yet been selected and two options are considered in case of a Tokamak (i.e. a pulsed and a steady-state scenarios) [FBB+16], which may lead to different developments for the heating and current drive systems [GAB+15, SAB+17, FHF+18]. Modelling codes in [GAB+15] show that in the case of pulsed operations the NBI system will deliver a total injected power of up to 50 MW for plasma pulses of up to 2 hours, while for the steady-state case the total injected power increases up to 135–210 MW in continuous mode. In both scenarios the beam energy is assumed to be higher than 0.8 MeV [GAB+15]. Furthermore, the DEMO NBI requires high standards of reliability, availability, maintainability and inspectability (known as RAMI requirements) as each component of the future fusion power plant [FAA+17].

### Neutral Beam Injection (NBI)

As the name suggests, the NBI system is based on injection of fast neutral particles into the fusion plasma, since they are not deflected by the strong magnetic confinement fields. The neutral beam for ITER will consist of hydrogen or deuterium[3] atoms, and it will then release its energy to the fusion plasma by charge exchange and ionization reactions. Furthermore, if the beam is injected tangentially to the torus, the NBI can be also used for an efficient current drive.

The main components of a neutral beam injection system are displayed in figure 2.1: positive or negative hydrogen ions are produced in a low temperature low pressure hydrogen plasma as ion source; these ions are then extracted and accelerated electrostatically through a multi-aperture multi-grid system operating at high voltages; the so-created fast ion beam is neutralized by charge exchange

[3]NBI systems for ITER should work with both isotopes, $^1$H and $^2$D. In the present work, the term hydrogen will generally refer to both isotopes, unless otherwise stated.

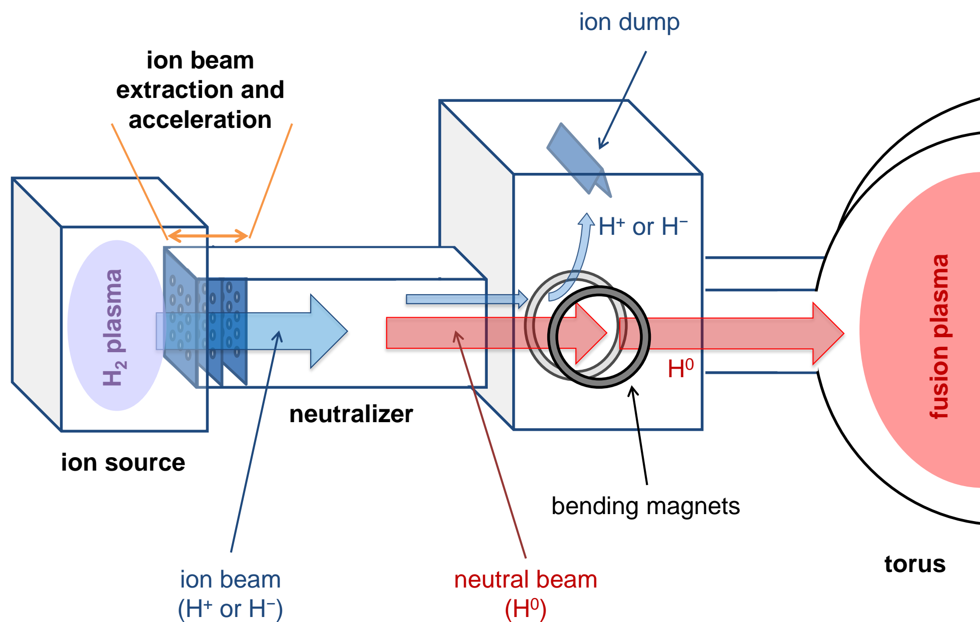


**Figure 2.1:** *Schematic drawing of a neutral beam injection system.*

collisions in a hydrogen gas target[4]. Residual ions are removed from the beam via a magnetic field and collected onto an ion dump, and the high energetic neutral beam is finally injected into the fusion plasma. Large scale vacuum pumps are applied to reduce the pressure downstream of the accelerator and downstream of the neutralizer in order to minimize the possible losses of fast particles due to collisions with background gases and re-ionization in the duct.

Currently, most of the NBI systems operating in fusion devices are based on positive ions and the beam energy is quite moderate: at present, the largest operating Tokamak device JET (Joint European Torus, located in Culham, U.K.) is equipped with two beamlines, delivering a total injected power of up to 34 MW with a beam energy of up to 125 keV and a pulse length at full power of up to 20 s [CCD+11]. Instead, for the NBI systems of ITER beam energies of 1 MeV are required in deuterium for pulses of up to 1 hour [IAE02]. The neutralization efficiency of positive ions in a gas neutralizer decreases significantly at such high energies [BPS75], as shown in figure 2.2, while for negative hydrogen ions it stabilizes around 60 % because of the low binding energy of the second electron (0.75 eV [Lid05]). Hence, the neutral beam injection systems for ITER and DEMO will be based on negative hydrogen ions (NNBI) due to their higher neutralization efficiency with respect to positive ions at the required beam energy of 1 MeV.

[4]For DEMO different and more efficient neutralization systems are currently under investigation [McA14].

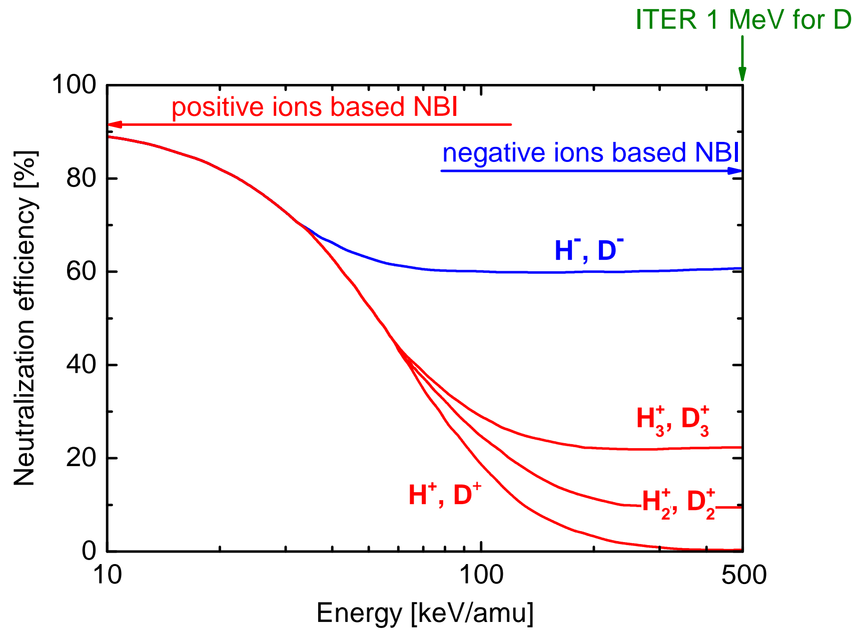


**Figure 2.2:** *Neutralization efficiency of positive and negative hydrogen and deuterium ions in a gas neutralizer of optimal thickness as a function of the ion energy [BPS75].*

### Requirements for ITER NNBI

The neutral beam energy for the NBI system at ITER is required to be about 1 MeV for deuterium in order to ensure a high efficiency non-inductive current drive and to supply 16.5 MW of heating power to the core of the fusion plasma for each beamline [IAE02]. To achieve the requested heating power, the ion source must deliver an accelerated $D^-$ current of 40 A, corresponding to a power of 40 MW (more than 50 % of the power is lost along the beamline before reaching the plasma core), with a current density of 200 A/m$^2$ [IAE02, HDG+09]. Hence, the extraction area is of 0.2 m$^2$ and it consists of 1280 extraction apertures of 14 mm diameter each. The resulting size of the beam is $1 \times 2$ m$^2$.

In order to achieve the requested accelerated current, the source has to deliver an extracted negative ion current of 57 A for $D^-$ (286 A/m$^2$ of extracted current density) considering 30 % of stripping losses in the accelerator [KH06]: in fact, interactions between the negative ion beam and the background gases in the accelerator may neutralize a fraction of the ions before reaching their full acceleration energy. The ion source must thus operate at a pressure of maximum 0.3 Pa [IAE02] in order to limit the stripping losses to 30 % in the acceleration stages.

Together with negative ions, also electrons are inevitably co-extracted and they must be dumped away from the beam at the first stage of the acceleration (hence, before reaching the full acceleration) in order to limit the heat load on the electron dump. This is performed by including deflection magnets in the second grid after the extraction, dumping the electrons onto one of the grids. In order to limit the heat load on the grid, the ratio between the co-extracted electron current density $j_\mathrm{e}$ and the extracted negative deuterium current density $j_{\mathrm{D}^-}$ must not exceed unity ($j_\mathrm{e}/j_{\mathrm{D}^-} < 1$). This constitutes the real limit for operation and ion extraction at full power.

Furthermore, the beam inhomogeneity must not exceed 10 % in order to minimize the transmission losses in the beamline, and the requirements of the whole NBI system must be stable for 1 hour for long pulse operation.

Negative ion NBI systems are currently in operation at two fusion experiments in Japan: at LHD (Large Helical Device, in Toki) with a nominal beam energy of 180 keV and an achieved maximum deposited power of 5.7 MW per beamline [TKT+06], and at JT-60U (Japan Torus-60 Upgrade, in Naka) with an achieved beam energy of 416 keV and an injected power of 5.8 MW [KHT+10]. Furthermore, the MeV accelerator located in Naka has shown the feasibility to reach a negative ion acceleration energy of 1 MeV for pulse lengths of up to 60 s and with extracted current densities below the value required for ITER [UHK+17].

The experience gained with the neutral beam injection system at ITER will be extremely important in view of the NNBI system for the demonstration reactor DEMO, whose requirements might even be more demanding with respect to ITER [FAA+17]. The final design of the NNBI for DEMO is not yet defined: research and development are aiming to fulfill the ITER NNBI requirements since at present no NNBI system has yet achieved all the ITER requirements simultaneously. At the same time, research and development for the NNBI for DEMO are already started, considering in particular the RAMI requirements.

### Negative hydrogen ion sources

One of the challenging components of the NNBI is the negative ion source, which has to provide a stable and homogeneous negative ion current density. In general, negative hydrogen ions can be created either by reactions in the bulk plasma volume or by particle conversion in vicinity of a surface (see chapter 4). In the case of negative ion sources for fusion, an ITER-relevant high extracted negative ion current density (286 A/m$^2$ for $\mathrm{D}^-$) and a low co-extracted electron current density

($j_e/j_{D^-} < 1$) are required. These requirements cannot be achieved if the source is based on volume production of negative ions, since this mechanism would lead to high co-extracted electron currents (see section 4.1). As a consequence, negative ion sources for fusion must rely on the surface conversion of positive hydrogen ions and atomic hydrogen at the plasma grid (PG, the first grid of the multi-grid extraction and acceleration system). Furthermore, the surface created negative ions repel the electrons from the plasma grid, lowering the co-extracted electron current. In order to efficiently create negative ions at the surface, the plasma grid must have a low work function (see section 4.2) and this is obtained by evaporating caesium continuously into the source (see chapter 5). The work function of a caesiated surface depends on the Cs coverage and it reaches the bulk Cs value (2.1 eV [Mic77]) for coverages over 1 monolayer, as it is described in section 5.2. Hence, the ion sources should operate with more than a monolayer of Cs on the PG to achieve and maintain the work function of bulk Cs. Moreover, ion sources operate at a moderate vacuum ($10^{-7}$–$10^{-6}$ mbar) and the background impurities (e.g. water vapor) lead to the formation of a non-pure Cs layer, affecting the work function consequently. Moreover, also the plasma has a relevant influence on the Cs layer. A schematic of the involved interactions is given in the next section. The different influences in vacuum and in plasma phases are both important, since ion sources for fusion must operate in pulsed mode (with pulses of up to 1 hour).

The reference design for the ITER NNBI ion source is the RF-driven negative ion source developed and optimized at Max-Planck-Institut für Plasmaphysik (IPP) in Garching, Germany [SFF+06, HDG+09]. Figure 2.3 shows a CAD drawing of the IPP prototype source (a) and a schematic of the extraction of the negative ions for such a source (b). The prototype source has a size of 1/8 the ITER source size and it consists mainly of three parts [SFF+06]. The *driver* is mounted on the back of the source body and here the hydrogen plasma is generated via inductive coupling by a coil connected to an RF generator with frequency of 1 MHz and power of up to 150 kW. In this region the plasma is characterized by an electron density of $10^{18}$ m$^{-3}$ and an electron temperature of 10 eV, providing consequently high fluxes of positive ions and atomic hydrogen required for the surface conversion into negative ions. In order to reduce the probability of destruction of negative ions by electron impact (see chapter 4.3) and to limit the amount of electrons close to the plasma grid, the plasma expands in the *expansion region* and is cooled down with the help of a magnetic filter field of several mT: in this way, the electron temperature and density decrease to around 1 eV and $10^{17}$ m$^{-3}$,

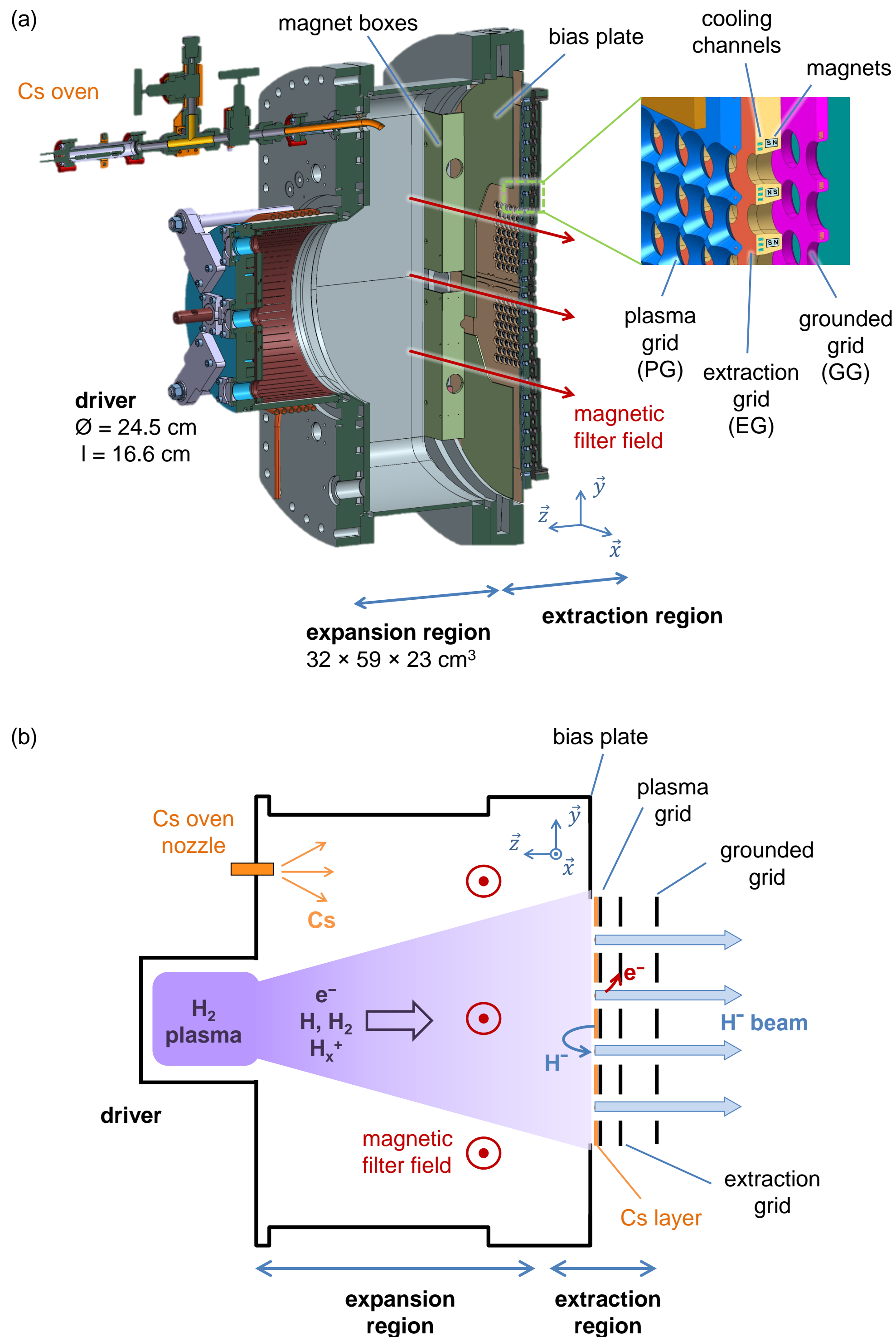


**Figure 2.3:** *(a) CAD drawing of the IPP prototype source [HFK+17] and (b) schematic of the extraction of negative ions from the hydrogen plasma. The three main parts of the source are highlighted: the driver, the expansion region and the extraction region.*

respectively. Finally, in the *extraction region* the negative ions are created by surface conversion at the multi-aperture plasma grid. The plasma grid is made of molybdenum-coated copper and caesium is evaporated into the source by means of a Cs oven located at the backplate of the expansion region. The Cs oven contains a Cs reservoir which is heated up during operation, and the Cs vapor is introduced into the source through a nozzle. The Cs evaporation rate is typically around 10 mg/h, with a typical neutral Cs density in front of the PG of the order of $10^{15}$ m$^{-3}$ [FW11].

Extraction and acceleration of negative ions are performed at the IPP prototype source by applying high voltage on a system of three grids, where the source is at negative potential (typically around −20 kV) and the last grid is grounded. The first grid is the plasma grid and it faces the plasma in the source. Here the negative ions created by surface conversion are extracted through multiple apertures. In order to reduce the amount of electrons that are inevitably co-extracted together with the negative ions, the PG is positively biased with voltages of around 10 V against the source body and the so-called *bias plate*, which is located in front of the plasma grid and is at the same high potential as the source walls. The second grid is the extraction grid (EG), whose relative potential with respect to the PG is typically around +9 kV, as for the ITER source. The EG is equipped with embedded magnets in order to deflect the co-extracted electrons out of the negative ion beam and collect them onto the extraction grid itself. The main technical limitation to the source operation is the heat load on this grid, in fact the deposited power density can reach values of the order of kW/cm$^2$ [NGH$^+$11]. The negative ions instead are only slightly affected by the deflection field created at the EG and they are further accelerated towards the grounded grid (GG, last grid of the acceleration system), whose relative potential with respect to the EG is typically around +11 kV at the IPP prototype source. A more detailed description of the IPP prototype source can be found in [SFF$^+$06].

Currently, two test facilities are in operation at IPP, both based on the RF-driven prototype source: BATMAN (BAvarian Test MAchine for Negative ions) [SFF$^+$06] and ELISE (Extraction from a Large Ion Source Experiment) [FHF$^+$13, FHW$^+$17]. The former is equipped with a source of size of 1/8 the ITER source size, with an extraction area of 63 cm$^2$, and it can perform plasma pulses with a limited length (4 s). BATMAN has already demonstrated the feasibility to achieve the ITER required current densities and the electron-to-ion current density ratio at the desired low pressure of 0.3 Pa [FFK$^+$07]. The second test facility ELISE (in

operation since 2013) is equipped with a source half of the size of the ITER ion source, with 4 drivers (for a maximal total RF power of 360 kW) and an extraction area of 0.1 $m^2$. The negative ion beam can be extracted and accelerated with a total voltage of up to 60 kV. Long pulse operation is possible at ELISE with plasma pulses of up to 1 hour, though the extraction of negative ions is only pulsed (10 s of beam extraction every 3 minutes). The aim of this test facility is to demonstrate the size scaling towards ITER ion source and the feasibility to fulfill the ITER requirements for long pulses[5]. At present, the ITER requirements have not yet been fulfilled at ELISE for the entire length of the plasma pulse (1 hour): while for short pulses the required $D^-$ current density has almost been achieved (250 $A/m^2$ for 20 s [KWF+18]), the source performance during long pulse operation depends on the unstable co-extracted electron current density, which strongly increases during the 1 hour pulse, limiting the total RF power that can be applied to the source to values below 230 kW. The highest extracted $D^-$ current density achieved during a long pulse is of 190 $A/m^2$ (corresponding to 66 % of the current density required for ITER) for 45 minutes [KWF+18]. For hydrogen, an extracted current density of 304 $A/m^2$ and of 220 $A/m^2$ has been achieved during short and long (1160 s) pulses, respectively (ITER requirements for hydrogen: 329 $A/m^2$ for 1000 s) [KWF+18].

ELISE constitutes an important step between the small-scale experiment BATMAN and the full ITER size NNBI. The latter will be tested at the ITER Neutral Beam Test Facility (NBTF), also called PRIMA (Padova Research on ITER Megavolt Accelerator), hosted at Consorzio RFX in Padova (Italy) and consisting of two experiments [TPB+17]. SPIDER (Source for Production of Ion of Deuterium Extracted from RF plasma) is an experiment equipped with a full ITER-size ion source and has started first operation in the current year (2018). SPIDER will take advantage of the experience gained at ELISE and it has the aim to demonstrate the feasibility to achieve the ITER requirements for long pulse operation (pulse length of up to 1 hour) with a source of the same size scale of the ITER ion source and a total acceleration voltage of up to 100 kV for the extracted negative ions. The second testbed is currently under construction at Consorzio RFX (first operation foreseen for 2021 [TPB+17]): MITICA (Megavolt ITER Injector & Concept Advancement) will consist of a full ITER-like NBI system, where the negative ions will be accelerated up to 1 MeV and neutralized afterwards.

[5] At MANITU (Multi Ampere Negative Ion Test Unit), in operation at IPP until 2011, the stability of the extracted current density for pulses of up to 1 hour was demonstrated, with $j_e/j_{D^-} \approx 1$, but at lower $j_{D^-}$ with respect to ITER requirements [KFF+12].

### Issues at the big test facilities

In order to fulfill ITER requirements, one of the main issues to deal with during ion source long pulse operation is the increase of the co-extracted electron current density up to values harmful for the extraction grid. This issue seems to be dependent on the conditions of the Cs layer on the plasma grid, which determines the surface work function, and to be correlated with a decrease of the Cs content in front of the PG [HFK+17, FHW+17, Mim18]. The extracted negative ion current is instead not so strongly affected because in front of the caesiated plasma grid the electrons are the minority species with respect to the negative ions [HFK+17], hence the co-extracted electron current reacts easily to variations of the Cs layer on the PG and consequent changes of the work function. Figure 2.4 shows the typical behavior of the extracted negative ion current and the co-extracted electron current for a long pulse operation of 1175 s in hydrogen at the ELISE test facility [Wün17], where the extraction phase is performed for 10 s every 150 s. The negative hydrogen ion current slightly decreases with the time, however the co-extracted electron current shows a high instability: it strongly increases with the time, while within an extraction phase the electron current decreases, probably due to the contribution of the Cs released from the backplate by the backstreaming positive ions [KWF+18, Mim18]. In deuterium, the operation is

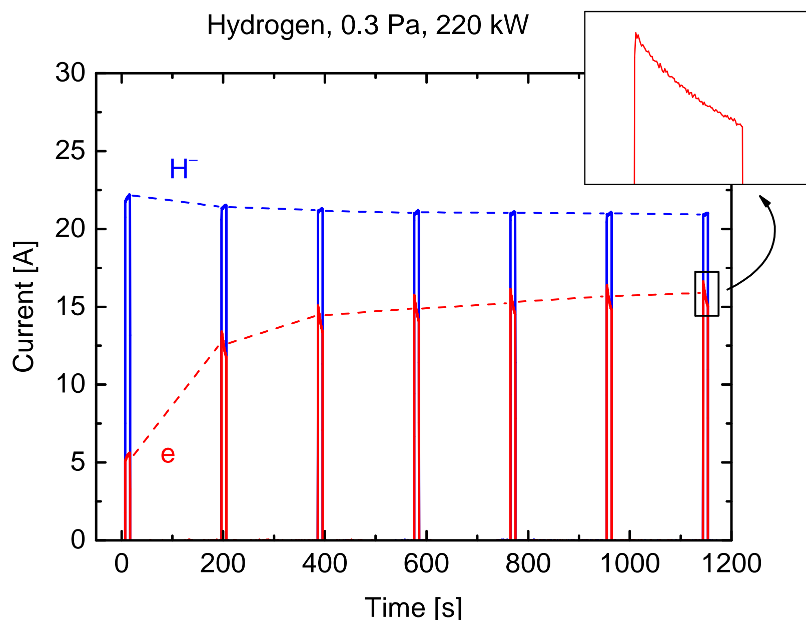


**Figure 2.4:** *Time traces of the extracted $H^-$ current and co-extracted electron current for a long pulse (1175 s) at the ELISE test facility [Wün17].*

even more difficult, showing a stronger dynamics of the electron current, and a higher Cs content is needed [KWF+18]. The strong increase of the co-extracted electron current suggests that a deterioration or vanishing of the Cs layer takes place during long pulse operation, hence the maintainability of a constant low work function at the caesiated PG is thus the key parameter to assure good performance of the negative ion source.

At present, the work function of bulk Cs (2.1 eV [Mic77]) can be reached at the ion sources, however several factors contribute to the formation and maintenance of the Cs layer, affecting the resulting surface work function as well. A schematic of these contributions is represented in figure 2.5. During vacuum phases, the Cs high chemical reactivity together with the presence of residual gases in the source (due to the limited vacuum of $10^{-7}$–$10^{-6}$ mbar) leads to the contamination and degradation of the Cs layer, and hence to work functions higher than for bulk Cs (> 2.7 eV [FF17]). When a plasma is applied in front of the caesiated surface, the plasma exposure leads to a redistribution of Cs all over the source surfaces [GWF+11, Mim18] and to a cleaning of the Cs layer (thanks to the impinging plasma particles and/or to the UV and VUV plasma radiation), establishing the low work function of 2.1 eV [FF17] and having positive effects on the ion source performance. However, the plasma also leads to a deterioration or removal of the caesium layer on the PG during long plasma pulses, modifying the work function

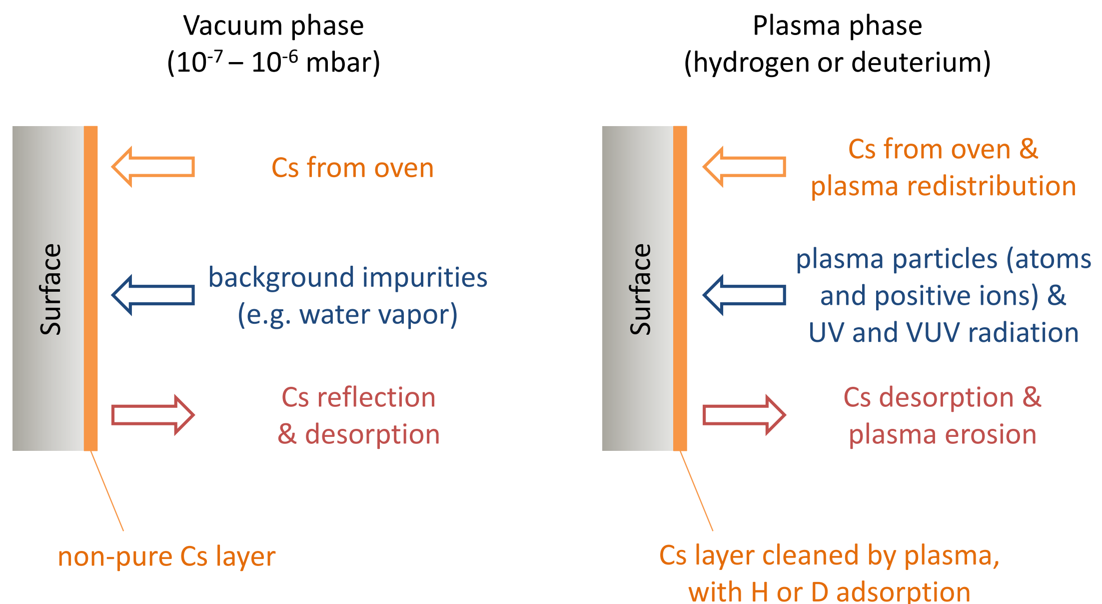


**Figure 2.5:** *Schematic of the contributions to the Cs dynamics during vacuum and plasma phases.*

of the plasma grid and decreasing the source performance [FHW⁺17, KWF⁺18]. In order to maintain the Cs layer on the PG and assure in this way high source performance, fresh Cs must be continuously evaporated into the source. Typical neutral Cs densities are of the order of $10^{14}$–$10^{15}$ m$^{-3}$, but experiments at ELISE have shown that higher Cs densities are needed during long pulses in deuterium to counteract the increase of the co-extracted electron current [KWF⁺18]. However, a high Cs content in the source is not recommended, since it significantly changes the plasma parameters and it also causes breakdowns between the grids due to the outflow [FHW⁺17]. In particular in view of the DEMO reactor, the ion source requires high standards of reliability, availability, maintainability and inspectability (RAMI requirements), hence a better Cs management in order to maintain a sufficient Cs flux towards the surface minimizing the Cs consumption –or otherwise a valid alternative to Cs evaporation– is highly needed.

**Aim for the current investigations**

Three main topics related to as many open issues are considered in the current work:

- The influence of the plasma on the work function of a caesiated surface, which results in a cleaning of the Cs layer but also in a gradual removal of the deposited Cs. The Cs removal and the minimally required fresh Cs flux towards the surface to maintain a low work function during long plasma operation are thus investigated.
- Fundamental investigations on the negative ion density close to a surface in correlation with its work function, comparing hydrogen and deuterium plasmas. The stronger dynamics of the co-extracted electron current for deuterium operation with respect to hydrogen suggests a possible isotopic difference in the negative ion formation by surface mechanisms, which has to be studied.
- Possible alternatives to the evaporation of caesium. The strong electron dynamics might be correlated to a temporal instability of the work function during long pulses due to a not stable Cs layer, hence possible alternative materials characterized by a low surface work function have to be considered and compared to the Cs performance at ion source relevant vacuum and plasma conditions in view of DEMO (while the application of Cs is already established for the ITER ion sources, it is still under discussion for DEMO).

Information about the status of the Cs layer at the ion sources is hardly achievable: the work function (key parameter for the performance of the source and for all the three topics previously announced) is not easily accessible at ion sources (e.g. several laser wavelengths would be needed for absolute measurements of the work function by Fowler method, described in section 7.1.1) and it was never absolutely quantified (e.g. in [SOA+96] the work function of the caesiated surface in an ion source is obtained by means of a comparison with measurements performed in a separate experiment and not absolutely measured). Moreover, ion sources are a complex system, where a limited diagnostic access is provided and many influences contribute to the resulting performance. The flexibility is thus not always guaranteed: systematic and reproducible investigations might require time to be performed.

Absolute work function measurements of caesiated surfaces can be found in literature, e.g. in [SS68], however these measurements refer to ultra-high vacuum systems where a pure Cs layer is created on the metallic surface. The moderate vacuum of the ion sources and the presence of a pulsed plasma strongly influence the work function, and the literature measurements cannot be applied.

Hence, the current investigations are performed at the flexible laboratory experiment ACCesS (Augsburg Comprehensive Cesium Setup), where vacuum and plasma conditions comparable to the ones in front of the plasma grid in the ion sources can be achieved. However, while for ion sources a hydrogen pressure of 0.3 Pa and a total RF power of the order of hundreds of kW are applied in the plasma volume, at ACCesS a pressure of 10 Pa and an RF power of 250 W are needed to achieve similar densities, temperatures, and particle fluxes as in front of the plasma grid at the ion sources, as summarized in table 2.1.

ACCesS allows operation in a controlled environment: investigations of the complex Cs dynamics and the several influences of the limited vacuum and of the plasma on the Cs layer require controlled conditions, where a high reproducibility must be assured (this requirement is difficult to achieve at the ion sources). Within this work, careful preparation of the experiment and reproducibility of the experimental conditions are always accomplished. Furthermore, ACCesS is equipped with several diagnostic systems, which make this experiment unique and extremely useful for investigations on the work function, on the Cs dynamics, and on the negative ion density close to the converter surface.

The current work is a continuation of the work started by Dr. Friedl during his PhD [Fri13]: in his work, the work function of a caesiated surface was investigated

**Table 2.1:** *Typical plasma parameters at ACCesS and in front of the PG at the BATMAN test facility [HFK+17, Wim14].*

| | ACCesS | BATMAN |
|---|---|---|
| Pressure [Pa] | 10 ($H_2$, $D_2$) | $\geq 0.3$ ($H_2$, $D_2$) |
| RF power [kW] | 0.250 | $\leq 150$ |
| Electron density [$m^{-3}$] | $10^{16}$ | $< 10^{17}$ |
| Positive ion density [$m^{-3}$] | $10^{16}$ | $10^{17}$ |
| Negative ion density [$m^{-3}$] | $10^{15}$ | $10^{16}$–$10^{17}$ |
| Atomic hydrogen density [$m^{-3}$] | $10^{19}$ | $10^{18}$–$10^{19}$ |
| Neutral Cs density [$m^{-3}$] | $10^{14}$–$10^{15}$ | $10^{14}$–$10^{15}$ |
| Electron temperature [eV] | 2 | 1 |
| Gas temperature [K] | 550 | 1000 |
| Atomic hydrogen temperature [eV] | 0.05 | 0.8 |
| Negative ion temperature (in volume) [eV] | 0.2 | 0.8 |
| Potential difference at the surface [V] | 8 | $\sim 0$ |
| Atomic hydrogen flux [$m^{-2}s^{-1}$] | $10^{22}$ | $10^{22}$ |
| Positive ion flux [$m^{-2}s^{-1}$] | $10^{20}$ | $10^{20}$–$10^{21}$ |

in vacuum, including the study on the degradation effect of the Cs layer due to the background gases, and investigations of the Cs evaporation on the plasma parameters were performed. Additionally, the beneficial cleaning effect of the plasma exposure on the caesiated surfaces was also investigated shortly after his PhD in [FF17]. With the current work, the Cs investigations continue after improving the setup with new diagnostics for the detection of negative hydrogen ions and for faster and more sensitive measurements of the Cs density in vacuum and plasma operation. Additionally, different alternative materials are also considered.

# 3 Low temperature low pressure hydrogen plasmas

## 3.1 Plasma properties

A *plasma* is defined as a partially or fully ionized gas showing collective behavior. In case of low temperature low pressure plasmas as in the ion sources the gas is partly ionized, this means that it consists of neutral particles (in case of hydrogen plasmas these are $H_2$ molecules and H atoms) and charged particles (positive ions $H^+$, $H_2^+$ and $H_3^+$, negative ions $H^-$ and electrons).

A plasma is globally quasi-neutral, i.e. no macroscopic concentration of charges occurs and the density of positively and negatively charged particles is the same. In case of a hydrogen plasma, this means

$$n_{\mathrm{H}^+} + n_{\mathrm{H}_2^+} + n_{\mathrm{H}_3^+} = n_{\mathrm{H}^-} + n_{\mathrm{e}} \quad , \tag{3.1}$$

where $n_{\mathrm{H}^+}$, $n_{\mathrm{H}_2^+}$, $n_{\mathrm{H}_3^+}$ and $n_{\mathrm{H}^-}$ are the densities of the corresponding ions $H^+$, $H_2^+$, $H_3^+$, and $H^-$, and $n_{\mathrm{e}}$ is the electron density.

In order to maintain the quasi-neutrality, the plasma is able to shield electric potentials applied to it. The *Debye length* $\lambda_{\mathrm{D}}$ is the natural scale length beyond which this shield effect takes place, and for the electrons it corresponds to:

$$\lambda_{\mathrm{D,e}} = \sqrt{\frac{\epsilon_0 k_{\mathrm{B}} T_{\mathrm{e}}}{e^2 n_{\mathrm{e}}}} \quad , \tag{3.2}$$

where $\epsilon_0$ is the permittivity of free space, $k_{\mathrm{B}}$ the Boltzmann constant, $T_{\mathrm{e}}$ and $e$ the electron temperature and charge, respectively. Violations of the quasi-neutrality are only possible within the length of $\lambda_{\mathrm{D}}$, which is typically of the order of 10 µm for hydrogen plasmas in ion sources.

## 3.2 Low temperature low pressure plasmas

For a species of mass $m$ and particle density $n$ in thermodynamic equilibrium, the energy distribution function $f_{\mathrm{M}}(E)$ is the *Maxwell-Boltzmann distribution* (or shortly Maxwell distribution), which depends on the particles energy $E$:

$$f_{\mathrm{M}}(E) = \frac{2}{\sqrt{\pi}} n \left(k_{\mathrm{B}}T\right)^{-3/2} \sqrt{E} \exp\left(-\frac{E}{k_{\mathrm{B}}T}\right) \quad , \tag{3.3}$$

where $T$ is the thermodynamic temperature.
The resulting mean energy $\langle E \rangle$ is

$$\langle E \rangle = \frac{1}{n} \int E\, f_{\mathrm{M}}(E)\, \mathrm{d}E = \frac{3}{2} k_{\mathrm{B}} T \quad . \tag{3.4}$$

Since the temperature and the mean energy are so closely related, it is common rule in plasma physics to give temperatures in units of energy. It means that the energy equivalent $k_{\mathrm{B}}T$ is usually referred to as a temperature, typically in units of [eV] (hence, 1 eV corresponds to a thermodynamic temperature of ca. 11600 K). The mean velocity $\langle v \rangle$ of this system of particles is thus given by

$$\langle v \rangle = \sqrt{\frac{8 k_{\mathrm{B}} T}{\pi m}} \quad . \tag{3.5}$$

Low pressure plasmas (typically in the pressure range between 0.1 and 100 Pa) are usually generated via electric or electromagnetic fields. The hydrogen plasma generated at the IPP ion sources is an inductively coupled plasma (ICP): the discharge is sustained via inductive RF coupling to the plasma from an antenna external to the vacuum chamber (more details about ICP discharges can be found in [LL05]). In such sources, the plasma heating mostly affects electrons, while heavy particles like neutrals and ions are mainly heated via elastic collisions with the electrons. However, this energy transfer from the electrons to heavier particles is not efficient due to the difference in mass and to the low collision frequency in such low pressure systems. Hence, electrons and heavy particles do not thermalize among each other, and as a consequence the electron temperature $T_{\mathrm{e}}$ is higher than the temperature of the heavy particles species, i.e. of neutrals (e.g. the gas temperature $T_{\mathrm{gas}}$) and ions ($T_{\mathrm{i}}$). Typical temperatures in low temperature low pressure plasmas are of the order of few eV for the electrons and below 1 eV for the heavy particles.

### 3.2.1 Electron energy distribution

If the electrons are in thermal equilibrium among each other, their energy distribution function corresponds to a Maxwell-Boltzmann distribution. However, in low pressure plasmas additional heating or loss mechanisms may occur, leading to significant deviations from a Maxwellian distribution [LL05]. A possible electron energy distribution function (EEDF) is the so-called *Bi-Maxwellian distribution* $f_{\mathrm{BiM}}(E_\mathrm{e})$, consisting of two different electron ensembles which are thermalized within themselves but not between each other. Hence, the two groups are characterized by two different electron temperatures[1], $T_{\mathrm{e,low}}$ and $T_{\mathrm{e,high}}$. In this case the total EEDF depending on the electron energy $E_\mathrm{e}$ is the following [GMS95]:

$$\begin{aligned} f_{\mathrm{Bi-M}}(E_\mathrm{e}) =& \frac{2}{\sqrt{\pi}}\,(1-\beta)\,n_\mathrm{e}\,(k_\mathrm{B}T_{\mathrm{e,low}})^{-3/2}\,\sqrt{E_\mathrm{e}}\,\exp\left(-\frac{E_\mathrm{e}}{k_\mathrm{B}T_{\mathrm{e,low}}}\right) \\ &+ \frac{2}{\sqrt{\pi}}\,\beta\,n_\mathrm{e}\,(k_\mathrm{B}T_{\mathrm{e,high}})^{-3/2}\,\sqrt{E_\mathrm{e}}\,\exp\left(-\frac{E_\mathrm{e}}{k_\mathrm{B}T_{\mathrm{e,high}}}\right) \quad , \end{aligned} \tag{3.6}$$

where $\beta$ is the weighting factor of the ensemble with the higher electron temperature ($T_{\mathrm{e,high}}$). Usually the EEDF is normalized to the electron density $n_\mathrm{e}$ and given in units of $[\mathrm{eV}^{-1}\mathrm{m}^{-3}]$. In the case of the Bi-Maxwellian distribution, an effective electron temperature $T_\mathrm{e}^{\mathrm{eff}}$ is defined as

$$T_\mathrm{e}^{\mathrm{eff}} \overset{(3.4)}{=} \frac{2}{3}\frac{\langle E_\mathrm{e}\rangle}{k_\mathrm{B}} = (1-\beta)\,T_{\mathrm{e,low}} + \beta\,T_{\mathrm{e,high}} \quad . \tag{3.7}$$

It is useful to introduce also the electron energy probability function (EEPF) $g(E_\mathrm{e})$, given in units of $[\mathrm{eV}^{-3/2}\ \mathrm{m}^{-3}]$ and defined as

$$g(E_\mathrm{e}) = \frac{f(E_\mathrm{e})}{\sqrt{E_\mathrm{e}}} \quad . \tag{3.8}$$

The EEPF helps to discriminate the different types of distribution function: in the Maxwellian case, the logarithm $\ln g(E_\mathrm{e})$ decreases linearly by increasing $E_\mathrm{e}$ and the slope is given by $(-k_\mathrm{B}T_\mathrm{e})^{-1}$. Instead, in the case of a Bi-Maxwellian distribution, the plot has a concave shape and two different linear regressions with different slopes, correlating to two different temperatures, can be identified to the low energy and to the high energy region. Furthermore, other types of EEPF can occur, such as the so-called *Druyvesteyn distribution* or the *$\nu$-distributions* [DP40, BF94].

[1] Here, the term 'temperature' is misleading: $T_\mathrm{e}$ is a thermodynamic temperature only in the Maxwellian case.

### 3.2.2 Plasma processes

Several plasma processes may occur within the plasma, e.g. excitation, ionization, and dissociation [SVY81]. In order to describe a plasma process the *reaction rate* is introduced, that is the number of reactions taking place per unit volume and unit time given in units of [$\mathrm{m}^{-3}\ \mathrm{s}^{-1}$]. Hence, the density of particles or states $n_x$ of a particular species $x$ can be found by balancing the different reaction rates $R_i$ for the processes that might act as a source or a sink for the particles or states of the considered species:

$$\frac{\mathrm{d}n_x}{\mathrm{d}t} = \sum_{\text{sources}} R_j - \sum_{\text{sinks}} R_k \quad . \tag{3.9}$$

In the case of collisions between two species 1 and 2, the reaction rate is given by the product of the densities $n_1$ and $n_2$ of the two species and the rate coefficient $X_{\text{react.}}(E_1, E_2, ...)$ depending on the specific reaction and on the energies $E_i$ of the involved particles. This rate coefficient can be calculated from the reaction cross section $\sigma_{\text{react.}}(E_{\text{rel}})$ [$\mathrm{m}^2$], which depends on the relative kinetic energy $E_{\text{rel}}$ of the two particles, and from the energy distribution functions of the two species involved. In case of collisions between electrons and heavy particles, the relative kinetic energy can be considered as the electron energy $E_{\text{e}}$ and the rate coefficient depends on the EEDF [SVY81]:

$$X_{\text{react.}}(\text{EEDF}) = \langle \sigma v \rangle = \int_0^\infty \sigma_{\text{react.}}(E_{\text{e}}) \sqrt{\frac{2eE_{\text{e}}}{m_{\text{e}}}} \frac{f(E_{\text{e}})}{n_{\text{e}}} \, \mathrm{d}E_{\text{e}} \quad \left[\frac{\mathrm{m}^3}{\mathrm{s}}\right] , \tag{3.10}$$

where the energy $E_{\text{e}}$ is given in units of [eV] and $m_{\text{e}}$ is the electron mass.

A threshold energy $E_{\text{thr}}$ might occur for particular processes, e.g. for ionization reactions. In this case, the cross section for energies below $E_{\text{thr}}$ is equal to zero and only particles with higher energies can contribute to the corresponding rate coefficient.

The rate coefficient determines also the *mean free paths* $\lambda_{\text{mfp}}^{\text{react}}$ of the parent particles 1 and 2 for the specific reaction. In general, $\lambda_{\text{mfp},1}^{\text{react}}$ is defined as the average distance traveled by particles of species 1 with an average speed $\langle v_1 \rangle$ between two subsequent collisions with the particles of species 2 with a particle

density $n_2$. The mean free path is thus defined as [CB11]

$$\lambda_{\text{mfp},1}^{\text{react}} = \frac{1}{n_2 \sigma_{\text{react}}(E_{\text{rel}})} = \frac{\langle v_1 \rangle}{n_2 X_{\text{react}}(E_{\text{rel}})} \quad . \tag{3.11}$$

A particular species is usually involved in more than one reaction. Hence, the total mean free path $\lambda_{\text{mfp}}^{\text{tot}}$ should take into account all the possible interactions and it is defined as

$$\frac{1}{\lambda_{\text{mfp}}^{\text{tot}}} = \sum_{\text{reactions}} \frac{1}{\lambda_{\text{mfp}}^{\text{react}}} \quad . \tag{3.12}$$

A set of equations of the form of (3.9) for different species leads to the set-up of population density models, such as collisional radiative or ionization and dissociation models, where these equations are to be solved simultaneously.

### Plasma emission

Spontaneous emission occurs when a particle in an electronically excited states $i$ with energy $E_i$ relaxes to a lower energy state $k$ with energy $E_k$, releasing a photon at the wavelength [TLJ99]

$$\lambda = \frac{hc}{E_i - E_k} \quad , \tag{3.13}$$

where $h$ is the Planck constant and $c$ the speed of light.

In this case the rate of the optical transition is given by the emissivity $\epsilon_{ik}$, which depends on the density of the higher energy state $n_i$ and the transition probability identified by the so-called *Einstein coefficient* $A_{ik}$, specific for each single transition and given in units of [$\text{s}^{-1}$] [TLJ99]:

$$\epsilon_{ik} = n_i \, A_{ik} \quad \left[ \frac{1}{\text{m}^3 \ \text{s}} \right] . \tag{3.14}$$

As a consequence, information about the population density of the excited states can be gained by monitoring the plasma emission.

### Ionization balance

In low temperature low pressure plasmas, ions are mainly created by electron impact ionization, while the main destruction mechanism is the diffusion to the vessel walls [Beh91]. For simplicity reasons in the current section the plasma is

considered to be constituted by only one species of neutrals with density $n_0$, one species of positive ions with density $n_{\mathrm{i}^+}$ and only by electrons with density $n_\mathrm{e}$ as negatively charged particles, assuming a Maxwellian EEDF.

The diffusion of charged particles can be driven by electric fields or density gradients. The electrons are faster than the positive ions due to their lighter mass, leading to higher fluxes. The slow positive ions create thus an electric field (called *ambipolar*) in order to maintain the local flux balance and fulfill the quasi-neutrality principle. This *ambipolar diffusion* is characterized by the diffusion rate $R_\mathrm{diff}$, given by [Möl93]

$$R_\mathrm{diff} = \frac{n_{\mathrm{i}^+}}{\tau_\mathrm{conf}} \quad , \tag{3.15}$$

where $\tau_\mathrm{conf}$ is the confinement time.

In case the mean free path $\lambda_{\mathrm{mfp,i}^+}$ of the positive ions colliding with neutrals is smaller than the characteristic length $d$ of the plasma (defined as the ratio of the plasma volume to the plasma surface area), the diffusion is called *laminar* and it is dominated by particle collisions within the plasma volume. In this case the confinement time depends on the ambipolar diffusion coefficient $D_\mathrm{a}$ by the relation

$$\tau_\mathrm{conf} \propto D_\mathrm{a}^{-1} \propto \frac{T_\mathrm{gas}}{T_\mathrm{e}} \, \lambda_{\mathrm{mfp,i}^+}^{-1} \sqrt{\frac{m_\mathrm{i}}{k_\mathrm{B} T_\mathrm{gas}}} \quad , \tag{3.16}$$

with $m_\mathrm{i}$ the ion mass.

After the balance equation (3.9) for a steady state plasma, the following relation is valid:

$$0 = n_\mathrm{e} n_0 X_\mathrm{ion}(T_\mathrm{e}) - \frac{n_{\mathrm{i}^+}}{\tau_\mathrm{conf}} \quad , \tag{3.17}$$

where $X_\mathrm{ion}(T_\mathrm{e})$ is the ionization rate coefficient assuming a Maxwellian EEDF, and $n_\mathrm{e}$ is equal to $n_{\mathrm{i}^+}$ because of the plasma quasi-neutrality. The ionization rate has a steep dependence on the electron temperature, hence small variations of $T_\mathrm{e}$ have a big impact on $X_\mathrm{ion}(T_\mathrm{e})$. Consequently, to a first approximation it is possible to neglect the influence of $T_\mathrm{e}$ on the confinement time in equation (3.16). As a result, the equations (3.16) and (3.17) yield

$$X_\mathrm{ion}(T_\mathrm{e}) \propto \frac{\lambda_{\mathrm{mfp,i}^+}}{n_0 \sqrt{m_\mathrm{i}}} \quad . \tag{3.18}$$

This correlation allows to predict the behavior of the electron temperature, e.g. by decreasing pressure the mean free path of the positive ions increases and

$n_0$ decreases and, as a consequence, the electron temperature must increase in order to balance the loss of positive ions at the vessel walls by increasing the ionization rate. On the other hand, the dependence from the ion mass leads to a decreasing diffusion rate for ion species with a higher mass, hence a lower electron temperature is sufficient to compensate the diffusion.

**Power balance**

The external power $P_{\mathrm{ext}}$ given as input into the bulk plasma of volume $V$ is mainly delivered to the electrons, which lose it mostly by means of inelastic collisions (e.g. excitation, ionization and dissociation) with the neutral species $j$ with densities $n_{j,0}$. The power balance is then given by [Beh91]

$$P_{\mathrm{ext}} = P_{\mathrm{exc}} + P_{\mathrm{ion}} + P_{\mathrm{diss}} \tag{3.19}$$

with $P_{\mathrm{exc}} = n_{\mathrm{e}}\, V\, \sum_{j,i} n_{j,0}\, E_{\mathrm{exc},j,i}\, X_{\mathrm{exc},j,i}(T_{\mathrm{e}})$ , the excitation term,
$P_{\mathrm{ion}} = n_{\mathrm{e}}\, V\, \sum_{j,s} n_{j,0}\, E_{\mathrm{ion},j,s}\, X_{\mathrm{ion},j,s}(T_{\mathrm{e}})$ , the ionization term, and
$P_{\mathrm{diss}} = n_{\mathrm{e}}\, V\, \sum_{j,m} n_{j,0}\, E_{\mathrm{diss},j,m}\, X_{\mathrm{diss},j,m}(T_{\mathrm{e}})$ , the dissociation term,

where $E_{\mathrm{exc},j,i}$ and $X_{\mathrm{exc},j,i}$ are the excitation energy and the electron impact excitation rate coefficient for the state $i$ of species $j$, respectively, $E_{\mathrm{ion},j,s}$ and $X_{\mathrm{ion},j,s}$ are the ionization energy and the electron impact ionization rate coefficient into the ionization state $s$ of species $j$, and $E_{\mathrm{diss},j,m}$ and $X_{\mathrm{diss},j,m}$ are the dissociation energy and the electron impact dissociation rate coefficient for the dissociation reaction $m$ of species $j$ in case the latter is a molecular species.

For a certain volume and pressure, hence for constant particle densities $n_{j,0}$, an increase of the input power leads to an increasing electron density, since the energies are fixed parameters and the rate coefficients have a steep dependence on the electron temperature. Furthermore, in a molecular plasma vibrational excitation processes of molecules have large excitation rate coefficients, since the threshold energy is low, enhancing the energy loss via vibrational excitation of the molecules. As a consequence, a lessened share of the input power is given to ionization processes with respect to excitation and dissociation processes of molecules in molecular plasmas compared to atomic discharges.

## 3.3 Plasma sheath

When a plasma is facing an insulated surface, a thin layer called *sheath* is created in front of the surface. The reason why this sheath is produced derives directly from quasi-neutrality. In the following, the case of a low temperature low pressure plasma where the electrons are the dominant negatively charged particles is considered. Since the electrons move faster than the positive ions, they tend to leave the plasma first. The flux of electrons $\Gamma_{\mathrm{e}}$ towards the surface, and consequently the loss of electrons, would be in this case much higher with respect to the positive ion flux $\Gamma_{\mathrm{i+}}$, contradicting the quasi-neutrality principle. Hence, a potential difference is created in the sheath region between the bulk plasma and the surface: the potential of the surface decreases with respect to the bulk plasma potential $U_{\mathrm{pl}}$ in order to balance the fluxes of oppositely charged particles ($\Gamma_{\mathrm{e}} = \Gamma_{\mathrm{i+}}$). In this way the loss of electrons is retarded, while the ions are accelerated towards the surface. As a consequence, the sheath region shows a higher density of positive ions with respect to the electron density, and the quasi-neutrality principle here is not fulfilled. In a steady state situation, the potential difference is adjusted in such a way that the fluxes of the positive ions and of the electrons towards an insulated and isolated surface are equal, and the corresponding surface potential is called *floating potential* $U_{\mathrm{fl}}$.

Figure 3.1 shows schematically the behavior of the electron and the positive ion densities, as well as the potential curve, as a function of the distance from a surface at floating potential. The velocity of the positive ions entering the sheath region must exceed a lower limit, called *Bohm velocity*, in order to ensure the flux equality within the sheath region. The Bohm velocity $v_{\mathrm{B}}$ is given by [LL05]

$$v_{\mathrm{B}} = \sqrt{\frac{k_{\mathrm{B}} T_{\mathrm{e}}}{m_{\mathrm{i}}}} \quad . \tag{3.20}$$

In order to acquire this velocity, the positive ions are already slightly accelerated in the region before the sheath by a small potential drop (ca. 0.5 V for an electron temperature of 1 eV, much smaller than the potential drop in the sheath region, which is typically of several V). This region is thus called *pre-sheath*, and here the quasi-neutrality principle is still valid.

The flux $\Gamma_{\mathrm{B}}$ of positive ions entering the sheath region with density $n_{\mathrm{i+}}$ and Bohm velocity is thus

$$\Gamma_{\mathrm{B}} = n_{\mathrm{i+}}\, v_{\mathrm{B}} \quad . \tag{3.21}$$

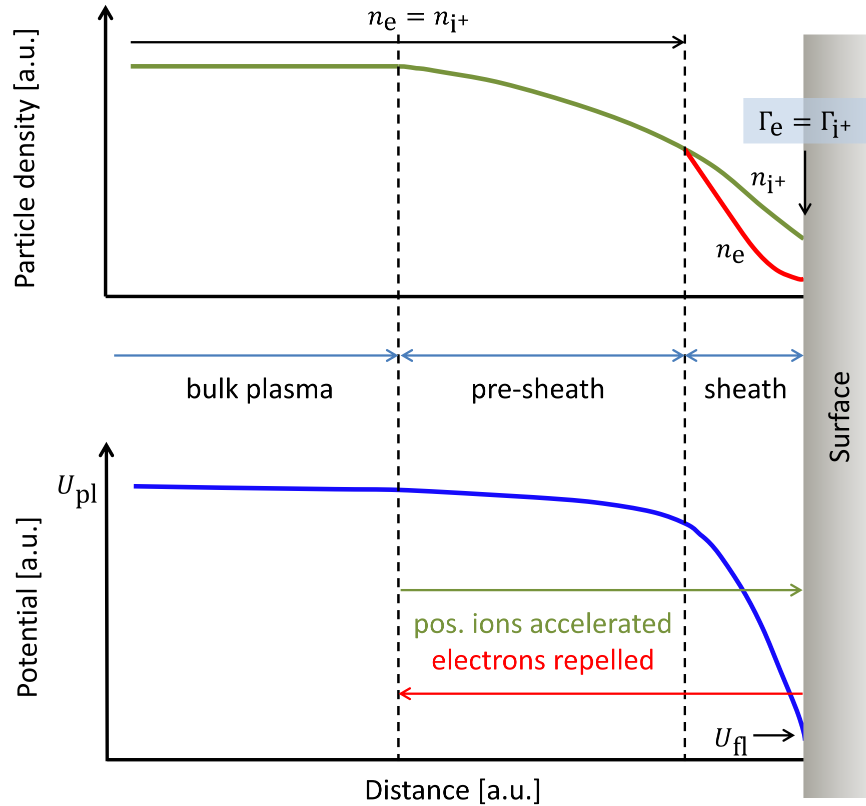


**Figure 3.1:** *Electron and positive ion densities and potential profile as functions of distance to a floating surface [LL05].*

The pre-sheath thickness depends on the ion mean free path, and for low pressure plasmas it is of the order of few mm, while the thickness of the sheath region is typically of the order of few Debye lengths due to violation of quasi-neutrality (hence far below the mm).

Generally, in laboratory experiments metallic vessel walls are purposely at ground potential (0 V), and the plasma and floating potentials are usually measured relatively to the ground. In the case of large surfaces, like the metallic vessel walls, the balance of the fluxes can consider also possible compensating currents within the walls themselves. In that event, only the global fluxes are in balance, while local fluxes may not be compensated.

### Influence of negative ions

The presence of negative ions in the plasma volume may affect the plasma sheath due to their higher mass with respect to the electrons. However, if the electron temperature $T_e$ is higher compared to the negative ion temperature $T_{i-}$ (as it is

usually the case due to the high ion mass), the negative ions barely penetrate the pre-sheath and are instead confined in the plasma volume, and the effect on the Bohm velocity is negligible [CB11]. Nevertheless, the Debye length $\lambda_D^*$ might be affected by the presence of negative ions in the plasma volume as following [CB11]:

$$\lambda_D^* = \lambda_{D,e} \sqrt{\frac{1}{1 + \frac{T_e}{T_{i^-}} \frac{n_{i^-}}{n_e}}} \quad , \tag{3.22}$$

where $n_{i^-}$ is the negative ion density. Hence, the Debye length is affected by the presence of negative ions only if $n_{i^-} \gg n_e$.

In presence of negative ions created at the surface, e.g. at the caesiated plasma grid in negative ion sources, the situation in the sheath is instead more complex, since the flux of negative ions from the surface into the plasma must be taken into account. For this purpose, a particle-in-cell (PIC) model has been developed at IPP in order to investigate self consistently the different particles' behavior in the sheath region close to the plasma grid at the IPP prototype source [WGF09]. Approaching the surface from the bulk plasma, the density of the negative ions increases, while the positive ion and electron density profiles closely follow the ones shown in figure 3.1. However, a significant amount of surface produced negative ions may create a local potential minimum in the vicinity of the surface. The depth of this potential well increases with increasing negative ion production rate and consequently the emission of negative ions from the surface into the bulk plasma may be space charge limited.

## 3.4 Hydrogen plasmas

### 3.4.1 Atomic hydrogen

The hydrogen atom is constituted by a proton and an electron. The electronic energy level structure is well described by

$$E_n = 13.60 \times \left(1 - \frac{1}{n^2}\right) \quad [\text{eV}] \ , \tag{3.23}$$

where $n$ is the principal quantum number and 13.60 eV is the ionization energy of the hydrogen atom. At the ground state $n = 1$ the electron affinity $E_a$ is of 0.75 eV, leading to the formation of the negative ion $H^-$.

**Table 3.1:** *Transition lines $i \rightarrow k$ from the Balmer series of atomic hydrogen and deuterium with the principal quantum numbers $n_i$ and $n_k$ for the upper and the lower state, respectively, and the corresponding wavelengths $\lambda$.*

| | | Hydrogen | | Deuterium | |
|---|---|---|---|---|---|
| $n_i$ | $n_k$ | designation | $\lambda$ [nm] | designation | $\lambda$ [nm] |
| 3 | 2 | $H_\alpha$ | 656.3 | $D_\alpha$ | 656.1 |
| 4 | 2 | $H_\beta$ | 486.1 | $D_\beta$ | 486.0 |
| 5 | 2 | $H_\gamma$ | 434.0 | $D_\gamma$ | 433.9 |
| 6 | 2 | $H_\delta$ | 410.2 | $D_\delta$ | 410.1 |

Excitation of atomic hydrogen may occur in the plasma via several processes, e.g. electron impact excitation, dissociative excitation, heavy particles collisions, or absorption of photons. Spontaneous emission is allowed between each energy level, in particular the optical transitions terminating on the level with principal quantum number $n = 2$ are specially relevant: they are called *Balmer series* and emit in the visible range. Hence, these transitions are easily accessible by diagnostics, e.g. optical emission spectroscopy, providing information about the population density of the excited states. In table 3.1 the wavelengths of the first 4 transition lines for the Balmer series are summarized for the hydrogen and the deuterium atom. Slight isotopic variations can be observed due to the bigger mass of deuterium.

### 3.4.2 Hydrogen molecule

The energy structure of molecular hydrogen $H_2$ is instead much more complex, since not only electronic states are involved, but also vibrational and rotational levels, which are associated to the relative motion of the two hydrogen nuclei and to the rotational movement of the molecule, respectively. Further internal energy levels are thus existing. The structure of the hydrogen molecule is shortly described in the following, while a detailed overview on molecular structures can be found for example in [Her50].

The electronic energy levels discriminate between singlet systems (total electron spin $S = 0$) and triplet systems ($S = 1$), and optical transitions between the two systems are not allowed. The ground state of the hydrogen molecule is denoted by $\mathrm{X}^1\Sigma_\mathrm{g}^+$, which is a singlet and binding state, hence the potential curve over the internuclear distance has a minimum and the molecule is stable. On the other hand, the lowest energy state in the triplet system is denoted by $\mathrm{b}^3\Sigma_\mathrm{u}^+$, which

is an anti-binding state. It means that no minimum is present on the potential curve, but the curve monotonically decreases with increasing internuclear distance. As a consequence, in this configuration the molecule dissociates immediately, releasing two hydrogen atoms in the ground state. However, dissociation can also occur from the ground state X via highly vibrational and rotational excitation (dissociation energy of 4.5 eV). More detailed information about the potential energy curves for molecular hydrogen can be found in [Sha70, Sha71].

Each electronic energy level presents different vibrational states due to the vibrational movement of the two nuclei against each other, and the vibrational states are characterized by the vibrational quantum number $\nu = \{0, 1, ...\}$. Each vibrational state presents in turn different rotational levels, attributed to the rotational movement of the molecule about the axis perpendicular to the internuclear axis and passing through the center of gravity of the molecule. The rotational states are characterized by the rotational quantum number $N = \{0, 1, ...\}$.

Typical energy differences between two electronic states are usually of the order of several eV, while between two vibrational levels and two rotational levels they are of the order of 0.1 and 0.01 eV, respectively.

The optical transitions between the electronically excited triplet states $d^3\Pi_u$ and $a^3\Sigma_g^+$ are relevant for diagnostic purposes, since spontaneous emission between the ro-vibronic states denotes the so-called *Fulcher system*, consisting of several spectral lines emitted in the visible range between 590 and 650 nm.

Furthermore, the ionization energy of the hydrogen molecule at the ground state into $H_2^+$ is 15.4 eV. The ground state of this molecular ion is stable, and the energy required for the dissociation is 2.65 eV, resulting into the generation of a ground state atom and a proton.

In case of molecular deuterium, the electronic structure is not affected by the different mass in first approximation, while the energy differences between the ro-vibronic states are smaller than in the case of hydrogen due to its bigger mass, leading for example to a narrower spectral range for the Fulcher emission (between 595 and 635 nm).

**Triatomic hydrogen**

The $H_3$ molecule is not stable at the ground state and dissociates immediately into H and $H_2$. However, the excited states of the molecule are stable, as well as the positive ion $H_3^+$. The latter can have a significant role in the plasma, since

its dissociation energy is 4.5 eV, so it is more stable than $H_2^+$ and as stable as the hydrogen molecule. Furthermore, the positive ion $H_3^+$ is easily produced by collisions between $H_2$ and $H_2^+$.

### 3.4.3 Hydrogen plasma processes

The constituents of a hydrogen plasma –i.e. the neutral particles H and $H_2$, the positive ions $H^+$, $H_2^+$ and $H_3^+$, the negative ions $H^-$ and the electrons– are involved in several inelastic processes, such as excitation, ionization, dissociation, attachment, and other formation and destruction mechanisms for each different species. A detailed review about these processes and their cross sections can be found in [JRS03], while in the present section the most relevant processes occurring in the plasma volume of ion sources and ACCesS are reported.

Excitation of neutral particles mainly occurs by electron impact collisions, in which the electron loses part of its energy and an electronically excited state of the neutral particle is thus populated. Depopulation of these excited states may instead occur by spontaneous emission of photons (if optical transitions are allowed): in this case the optical transition can be studied for diagnostic purposes.

A particular excitation process involving the $H_2$ molecule may lead to the final formation of atomic hydrogen. In fact, the *dissociative excitation* of $H_2$ via the repulsive state $b^3\Sigma_u^+$ is the main production channel of H in the ground state:

$$\mathrm{H_2(X^1\Sigma_g^+) + e \;\rightarrow\; H_2(b^3\Sigma_u^+) + e \;\rightarrow\; H}(n=1) + \mathrm{H}(n=1) + \mathrm{e} \quad . \qquad (3.24)$$

Further dissociative excitation processes involving excited hydrogen molecules may result in an excited hydrogen atom:

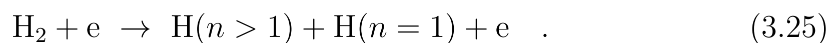

$$\mathrm{H_2 + e \;\rightarrow\; H}(n>1) + \mathrm{H}(n=1) + \mathrm{e} \quad . \qquad (3.25)$$

However, the corresponding cross sections are about an order of magnitude smaller than the one for the process (3.24) [CJL+01].

The formation of the positive ions $H^+$ and $H_2^+$ is mainly due to electron impact collisions with atomic and molecular hydrogen, respectively.

The positive ion $H_2^+$ in collision with a low energetic electron may lead to *dissociative recombination*, where two atomic hydrogen particles are formed, one

in the ground state and the other in an excited state:

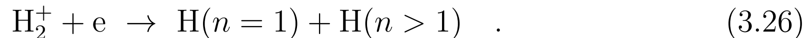

$$H_2^+ + e \;\rightarrow\; H(n=1) + H(n>1) \quad . \tag{3.26}$$

The positive ion $H_3^+$ is formed via collisions between the heavy particles $H_2$ and $H_2^+$:

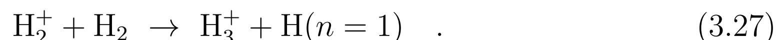

$$H_2^+ + H_2 \;\rightarrow\; H_3^+ + H(n=1) \quad . \tag{3.27}$$

This process is exothermic with an energy of 1.7 eV and is particularly significant in view of the results shown in the present work. In fact, the current investigations have been performed with a $H_2$ pressure varying between 2 and 10 Pa: at 10 Pa $H_3^+$ is the dominant ion, as also confirmed in a different experimental setup at similar plasma conditions [NK07]. However, the relative contribution of $H_2^+$ increases by decreasing the pressure, and $H_2^+$ is the dominant ion at 2 Pa as observed in an ICP setup equivalent to the present experiment [Ert10, Bri17].

The production of the negative ion $H^-$ in the plasma volume occurs by *dissociative attachment* of a vibrationally excited hydrogen molecule in the ground state $H_2(X^1\Sigma_g^+, \nu)$ colliding with a slow electron ($T_e \leq 1$ eV) via an unstable negative hydrogen molecular ion:

$$H_2(X^1\Sigma_g^+, \nu) + e \;\rightarrow\; H_2^- \;\rightarrow\; H^- + H(n=1) \quad . \tag{3.28}$$

The processes involving the negative ion $H^-$ will be presented and further discussed in chapter 4.

### Processes in $D_2$ plasmas

Since the atomic energy levels show just slight variations between hydrogen and deuterium atoms, the collisions involving only atomic species as heavy particles should not exhibit a relevant difference between the two isotopes, hence the processes can be directly transferred from hydrogen to deuterium.

This is also valid for the electronically excited states of the deuterium molecule, however molecular deuterium shows different vibrational and rotational levels with respect to the hydrogen molecule, since these energy levels depend on the nuclear mass. Hence, possible variations in the rate coefficients for processes where a molecular species is involved might occur among isotopes. However, not much

data are available in the literature for the deuterium case, hence it is not possible to have a full overview on all the processes involving molecular deuterium. In the following, a brief discussion about the differences is given.

- *Dissociative excitation of $D_2$.* In case of deuterium, the cross sections for the particular process in equation (3.24) are given in the literature vibrationally resolved, and they are larger than for the hydrogen molecule [CJL$^+$01] leading to a higher dissociation rate for $D_2$ with respect to $H_2$ at similar plasma conditions, i.e. for similar electron density and temperature. Regarding instead dissociative excitation processes of the form of equation (3.25) and resulting in an excited atom, the cross sections are lower in the case of the deuterium molecule with respect to hydrogen, as observed for the excitation of the Balmer series in [MDL77].

- *Dissociative recombination from $D_2^+$.* A comparison between the cross sections for different initial vibrational levels for the $H_2^+$ and $D_2^+$ recombination process of equation (3.26) can be found in [NTN87, Tak02]. Slight variations between the cross sections are present, however the effective cross sections given by the weighted sum of the vibrationally resolved cross sections are similar for $H_2^+$ and $D_2^+$, hence no effective difference can be assumed for this process between the two isotopes.

- *Formation of $D_3^+$.* The cross sections for the corresponding $D_3^+$ ion formation of equation (3.27) are similar to the cross sections for the hydrogen case [CF72]. Hence, $D_3^+$ is expected to be the dominant ion at 10 Pa also for the current investigations with deuterium plasmas, while at 2 Pa $D_2^+$ can be assumed as the most relevant ion.

- *Formation of $D^-$ by dissociative attachment.* The rate coefficients depend on the vibrational levels (i.e. on the energy associated to each level), as shown in the next chapter. For the same vibrational level, the rate coefficients of the corresponding deuterium process of equation (3.28) are lower with respect to the ones for hydrogen for similar electron density and temperature, due to the different energy of the ro-vibronic states, as shown in [BW79]. This process will be discussed in detail in the next chapter.

# 4 Negative hydrogen ions and the converter surface

## 4.1 Volume formation

As already shortly described in the previous chapter, negative hydrogen ions are formed in the plasma volume via *dissociative attachment* (DA), where the collision involves an electron and a vibrationally excited hydrogen molecule in the ground state, characterized by the vibrational quantum number $\nu$:

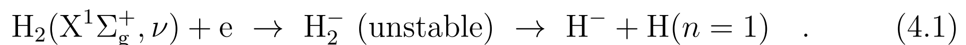

$$\mathrm{H_2(X^1\Sigma_g^+}, \nu) + \mathrm{e} \;\rightarrow\; \mathrm{H_2^-}\ \text{(unstable)} \;\rightarrow\; \mathrm{H^-} + \mathrm{H}(n=1) \quad . \tag{4.1}$$

The cross sections for this process depend on the quantum number $\nu$ and can be found in [JRS03]. By considering a Maxwellian EEDF, the rate coefficients $X^{\nu}_{\mathrm{DA}}$ for the different vibrational levels of the hydrogen molecule can be calculated after equation (3.10) and are shown in figure 4.1. It can be observed that the rate coefficient strongly increases with increasing $\nu$, i.e. with increasing energy. In particular, an increase of more than 4 orders of magnitude takes place between the levels $\nu = 0$ and $\nu = 5$. In case of deuterium, the cross sections for the dissociative electron attachment are lower with respect to the hydrogen case for the same vibrational level [BW79], and the rate coefficients become significant for vibrational levels with quantum number $\nu \geq 8$.

Figure 4.1 shows also the dependence of the rate coefficient on the electron temperature. In particular, for highly vibrationally excited states ($\nu \geq 8$) the rate coefficients decrease with increasing electron temperature. As a consequence, beneficial conditions for the production of negative hydrogen ions in the plasma volume are a low electron temperature ($T_{\mathrm{e}} \leq 1$ eV) and a high vibrational excitation of the hydrogen molecule ($\nu \geq 5$ for $H_2$, $\nu \geq 8$ for $D_2$). These conditions can be typically met at pressures of around several Pa [BW15], which are not compatible with the ITER requirements ($\leq 0.3$ Pa). Moreover, the volume production rate

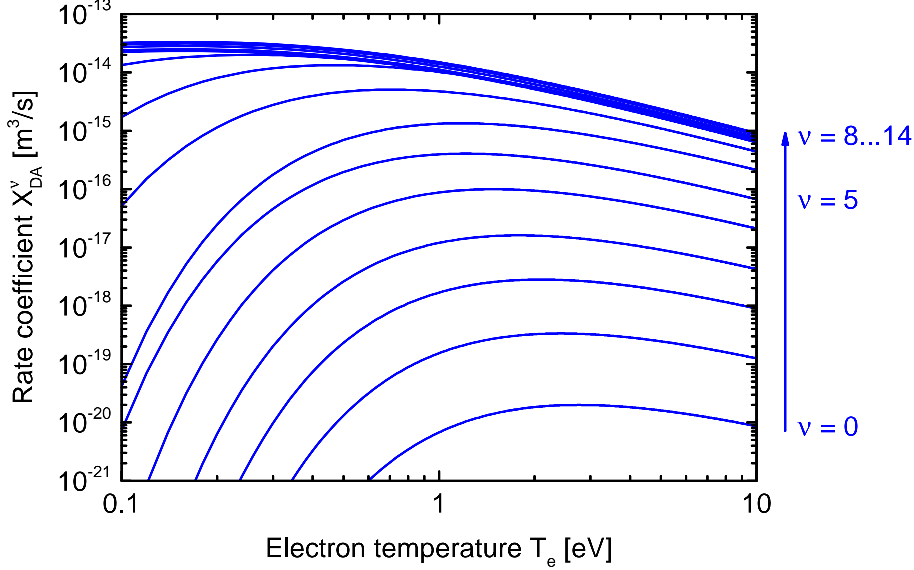


**Figure 4.1:** *Rate coefficients for the dissociative electron attachment for different vibrational levels of the hydrogen molecule, considering the cross sections from [JRS03] and a Maxwellian EEDF with electron temperature* $T_e$.

depends on the electron density and on the vibrational population density of the hydrogen molecules as described in section 3.2.2, hence high densities enhance the volume production of negative ions. The limited pressure required for the ITER ion source ($\leq$ 0.3 Pa) is directly connected to a limited molecular hydrogen density and thus to the necessity of increasing the electron density. Such event would not satisfy the ITER requirements in terms of co-extracted electron current [BW15]. Hence, the volume production of negative hydrogen ions at 0.3 Pa is insufficient to fulfill the ITER requests [SFF$^+$06], instead negative ion sources based on the surface formation of negative hydrogen ions show much better performance at the ITER NBI relevant parameters [SFF$^+$06].

## 4.2 Surface formation

In order to fulfill the ITER requirements, the most efficient and promising process is the conversion of atomic hydrogen and positive hydrogen ions into negative hydrogen ions by electron transfer from a low work function metallic surface. The probability for this process to happen depends on several factors, such as the work function of the converter surface and the energy and type of the impinging

particle (H or $H_x^+$, with $x = 1, 2$, or 3).

For impinging atomic hydrogen, the conversion process is the following:

$$H + e_{\text{surface}} \rightarrow H^- \quad . \tag{4.2}$$

Impinging positive ions are neutralized first when approaching the converter surface either by Auger neutralization and/or by resonant charge transfer, and the resulting neutral particles are converted into negative ions [IKS92, SCI+96]:

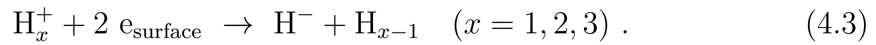

$$H_x^+ + 2\, e_{\text{surface}} \rightarrow H^- + H_{x-1} \quad (x = 1, 2, 3) \ . \tag{4.3}$$

The conversion process of a hydrogen atom impinging on a metallic surface is shown schematically in figure 4.2: the electron affinity $E_A$ of H at infinite distance is 0.75 eV below the vacuum level. When the atom approaches the surface an image charge is induced within the metal, and the electron affinity level of the atom lowers. When the affinity level is close to or below the Fermi energy $E_F$ of the metal, the electron can be transferred to the hydrogen atom by tunnel

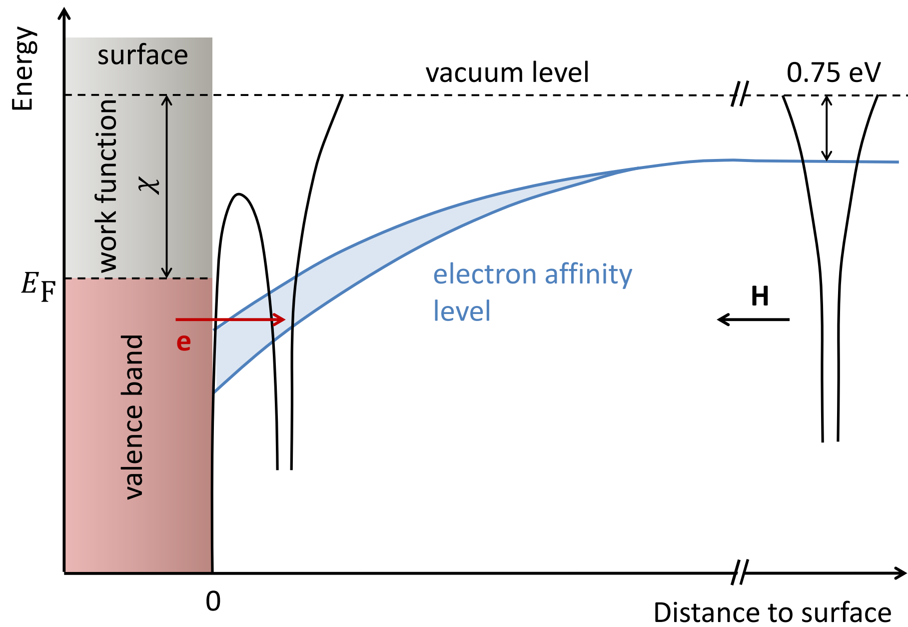


**Figure 4.2:** *Schematic of the variation of the electron affinity level of a hydrogen atom with the distance to a metal surface. In the vicinity of the solid, the electron affinity level is shifted and broadened, allowing the electron tunneling from the valence band to the hydrogen atom.*

effect. Moreover, the finite lifetime of the electron within the atom leads to a broadening of the affinity level in the vicinity of the surface, increasing the tunneling probability. Hence, the formation of negative hydrogen ions by surface conversion depends on the surface work function $\chi$ (defined as the difference between the vacuum level and the Fermi energy) and on the probability that the ion survives while escaping from the surface (the electron, in fact, might be transferred back to the metallic surface).

The probability to create negative hydrogen ions is thus given by [RWL82, NL79, LN83]

$$P^- \propto \exp\left(-\frac{\chi - E_\mathrm{A}}{C\, v_{\mathrm{H}^-}}\right) \quad , \tag{4.4}$$

where $C$ is a constant proportional to the exponential decay constant of the transition rate for the tunneling process, and $v_{\mathrm{H}^-}$ is the velocity of the escaping negative hydrogen ion perpendicular to the surface, which depends on the energy of the particle impinging onto the surface. For high velocities, the time spent by the newly formed $\mathrm{H}^-$ in the vicinity of the surface decreases and with that the probability to lose the additional electron.

For the deuterium case, the conversion processes are the same as in hydrogen, as well as the electron affinity (0.75 eV). Due to the high mass of $\mathrm{D}^-$, the velocity of the $\mathrm{D}^-$ ions leaving the surface is lower with respect to the $\mathrm{H}^-$ ions, leading presumably to a lower formation probability $P^-$ for the deuterium case with respect to hydrogen.

As equation (4.4) suggests, the probability to create negative hydrogen ions is highly enhanced by lowering the work function of the converter surface. Since the work function of most of the metals is above 4 eV [Mic77], in negative hydrogen ion sources based on surface conversion the $\mathrm{H}^-$ production is enhanced by evaporation and adsorption of caesium –the alkali metal with the lowest work function (2.1 eV [Mic77])– at the converter surface as observed for example by [BDD74].

However, it is difficult to measure experimentally the probability $P^-$, due to the angular distribution of the escaping negative ions created by surface conversion. Hence, the conversion yield $Y$ is introduced to describe the surface formation of negative ions: the flux $\Gamma_{\mathrm{H}\rightarrow\mathrm{H}^-}$ (or $\Gamma_{\mathrm{H}_x^+\rightarrow\mathrm{H}^-}$) of the negative ions leaving the surface and created by surface conversion is, in fact, related to the flux $\Gamma_\mathrm{H}$ (or $\Gamma_{\mathrm{H}_x^+}$) of impinging atoms (or positive ions) onto the surface by the conversion

yield $Y_{\mathrm{H}\to\mathrm{H}^-}$ (or $Y_{\mathrm{H}_x^+\to\mathrm{H}^-}$):

$$\Gamma_{\mathrm{H}\to\mathrm{H}^-} = Y_{\mathrm{H}\to\mathrm{H}^-}\,\Gamma_{\mathrm{H}} \quad \text{and} \tag{4.5}$$

$$\Gamma_{\mathrm{H}_x^+\to\mathrm{H}^-} = Y_{\mathrm{H}_x^+\to\mathrm{H}^-}\,\Gamma_{\mathrm{H}_x^+} \quad . \tag{4.6}$$

Conversion yields at partially caesiated molybdenum surfaces (work function of 1.4–1.5 eV, below the value for bulk Cs as it will be described in section 5.2) have been experimentally measured in ultra-high vacuum systems in [Cui91, MS91, LS92, SCI+96] for conversion of atomic hydrogen and in [IKS92, SCI+96] for conversion of positive ions. Such conversion yields are only indicative for the ion sources since the work function of the plasma grid in a moderate vacuum environment ($10^{-6}$ mbar) is different from the one measured for partially caesiated surfaces in ultra-high vacuum experiments (see chapter 5). No data are currently available in the literature for the conversion yields in case of bulk Cs (2.1 eV).

The conversion yields are strongly dependent on the impinging particle energy since the latter has an influence on the escaping velocity of the newly formed $\mathrm{H}^-$ particles. Moreover, the energy of the impinging particles must overcome a cutoff energy (around 1 eV) below which the $\mathrm{H}^-$ creation probability $P^-$ and the conversion yields rapidly drop to zero [Cui91].

Figure 4.3 shows on the left the negative hydrogen ion conversion yield $Y_{\mathrm{H}\to\mathrm{H}^-}$ for the process involving thermal hydrogen atoms of varying temperature $T_{\mathrm{H}}$ impinging on a partially caesiated Mo surface from the experimental observations of [MS91] and [LS92]. The conversion yield for atomic hydrogen shows a maximum at 25 % for temperatures above 2 eV and it decreases drastically with decreasing temperature. The conversion yield is negligible for temperatures of the atomic hydrogen below 0.1 eV.

On the right of figure 4.3, the conversion yields $Y_{\mathrm{H}_x^+\to\mathrm{H}^-}$ for the processes involving the proton $\mathrm{H}^+$ and the molecular ion $\mathrm{H}_2^+$ are shown for different positive ion energies $E_{\mathrm{in}}$. Both the conversion yields and the positive ion energy are indicated per nucleus. The data are taken from the experimental observations of [IKS92]. The conversion yields increase for increasing positive ion energy until a saturation value of around 22 % per nucleus is reached for energies per nucleus above 15 eV. Unfortunately, at present no information is available for the conversion process involving the positive ion $\mathrm{H}_3^+$. However, it is assumed that the conversion yield per nucleus is comparable to the case with $\mathrm{H}^+$ and $\mathrm{H}_2^+$.

For the deuterium case, no information about the conversion yields is available

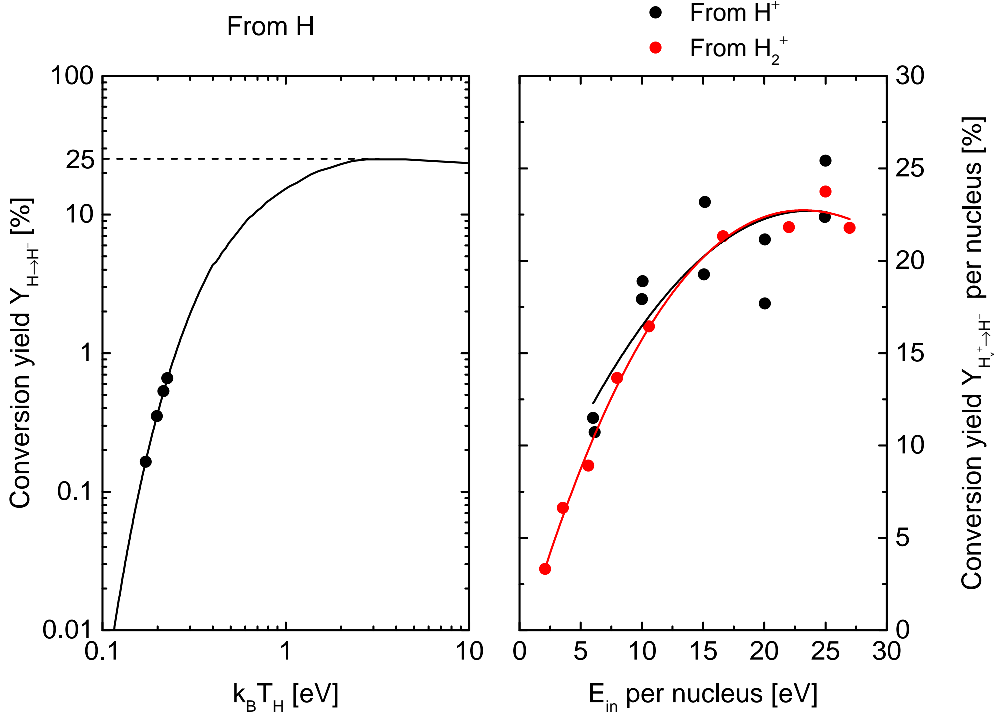


**Figure 4.3:** *Negative hydrogen ion conversion yields at a partially caesiated Mo surface (work function of 1.4–1.5 eV) as function of the energy of the impinging particles for conversion of atomic hydrogen (on the left) from [MS91, LS92] and for positive ions (on the right) from [IKS92]. For the latter, both the energy and the conversion yield refer to the single nucleus in case of molecular ions and the lines are obtained by a 3rd degree polynomial fit, as performed in [IKS92].*

in the literature at present. However, lower conversion yields can be expected due to the lower velocity of the escaping $D^-$ ions with respect to $H^-$.

## 4.3 Destruction mechanisms

The low binding energy of the $H^-$ additional electron (0.75 eV) may lead to several destruction processes that can occur in the plasma volume:

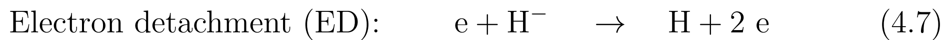

$$\text{Electron detachment (ED):} \quad e + H^- \rightarrow H + 2\,e \tag{4.7}$$

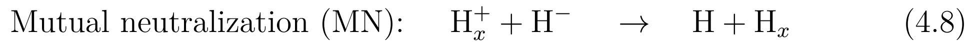

$$\text{Mutual neutralization (MN):} \quad H_x^+ + H^- \rightarrow H + H_x \tag{4.8}$$

$$\text{Associative detachment (AD):} \quad H + H^- \rightarrow H_2 + e \tag{4.9}$$

$$\text{Non-associative detachment (nAD):} \quad H + H^- \rightarrow 2\,H + e \tag{4.10}$$

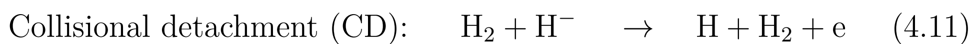

$$\text{Collisional detachment (CD):} \quad H_2 + H^- \rightarrow H + H_2 + e \tag{4.11}$$

Cross sections for the different processes can be found in [JRS03]. The rate coefficients can thus be calculated from the cross sections, applying equation (3.10) for the electron detachment process (neglecting the $H^-$ motion), while for the other processes the rate coefficients have been determined after [SS74] considering the effective temperature of both the species involved in each collisional process.

The rate coefficients for the different processes are shown in figure 4.4, where the electron detachment rate coefficient is a function of the electron temperature $T_e$ while for the other collisions the rate coefficient is a function of the negative ion temperature $T_{H^-}$. The temperature of the other species has been set to 500 K (typical gas temperature at low temperature hydrogen plasmas) for the solid lines, while for processes where the involved particles have a similar mass (mutual neutralization with $H^+$ and non-associative/associative detachment with H) the case with $T_H = T_{H^+} = T_{H^-}$ is also shown with dashed lines. Since the associative and non-associative detachment processes originate from the same particle species, the sum of the respective rate coefficients is given in figure 4.4. The two single processes are not shown in the graph, however the AD process is the dominant process in the low temperature region ($T_{H^-} \lesssim 5$ eV), while in the high temperature

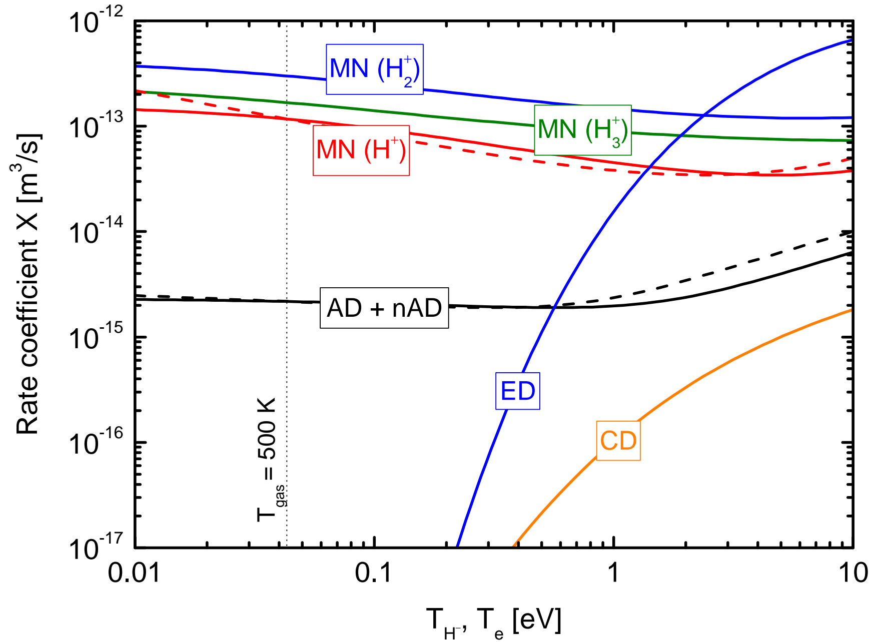


**Figure 4.4:** *Rate coefficients of the different $H^-$ destruction processes, calculated from the cross sections in [JRS03] as function of the electron temperature for the electron detachment process and of the $H^-$ temperature for the other processes. Solid lines correspond to fixed temperatures for neutral particles and positive ions of 500 K, while the dashed lines correspond to* $T_H = T_{H^+} = T_{H^-}$.

region ($T_{H^-} \gtrsim 5$ eV) the nAD process predominates.

The electron detachment is strongly dependent on $T_e$, showing a steep increase by increasing electron temperature. Therefore, an electron temperature below 2 eV is recommended at ion sources in front of the plasma grid in order to reduce the destruction rate by electron detachment. For the heavy particle collisions, the collisional detachment shows a strong influence of the $H^-$ temperature on its rate coefficient since this process occurs only for energies higher than a certain threshold energy (around 1 eV). For the processes involving positive ions and atomic hydrogen, no threshold energy occurs and the dependence on $T_{H^-}$ is weaker.

The negative ion density depends on the destruction rate $R_k$ for each destruction process $k$:

$$R_k = n_{H^-} n_k X_k \quad , \tag{4.12}$$

where $n_k$ and $X_k$ are the density of the particle species involved in the $k$ destruction process and its rate coefficient, respectively.

In the current work, a temperature of 0.2 eV is assumed for the $H^-$ created by volume processes since this value was measured in different experimental setups at similar plasma conditions [DAB+89, BBB+91, CBB95, NSB98], while at ion sources the volume produced $H^-$ temperature is expected to be similar to hydrogen atoms and protons (0.8 eV [FFK+09, WMF+14]). At these temperatures, the collisional detachment rate is negligible, while the main destruction process is the associative and non-associative detachment with atomic hydrogen. However, H atoms are relevant also for the formation of negative ions by surface conversion, hence a reduction of the atomic hydrogen density is not recommended. Furthermore, the maximal energy that the surface produced $H^-$ can achieve is determined by the sheath potential difference and is typically around several eV. In the current work, the dominant destruction process for surface produced $H^-$ is the collisional detachment with the hydrogen molecules.

For the case of deuterium, the same destruction processes are present. The cross sections for the associative detachment and collisional detachment are available in the literature in [MBC+12] and in [HDC83], respectively: for the first process, the cross sections for deuterium are comparable with respect to the hydrogen case, while for the collisional detachment the threshold energy is ca. 0.2 eV lower in deuterium with respect to hydrogen, leading to higher cross sections in deuterium for energies close to the threshold. For higher energies instead, the cross sections are comparable. Unfortunately, no cross sections are available at present in the literature for the other destruction processes.

## 4.4 Converter surfaces for negative ion sources

As explained in section 4.2, the work function of the converter surface has to be as low as possible in order to enhance the formation of negative ions by surface processes, but this is not the only requirement for a plasma grid. The material should be able to stand the plasma in front of it, e.g. without being eroded and without releasing impurities. The impurities, in fact, might change the plasma parameters or deposit again on the PG, resulting in a strong dynamics. The material should thus assure a mechanical and physical stability for the entire life of the fusion reactor. Furthermore, the plasma grid has a complex geometry due to the required apertures for the extraction of negative ions, hence a good machinability of the selected material is required.

As already mentioned, at present negative ion sources, a molybdenum-coated copper surface is used as converter surface due to its stability and machinability. The Mo coating is applied to avoid sputtering of copper, which would otherwise be released in the plasma, and to avoid reactions between copper and caesium. Cs is in fact evaporated and adsorbed at the surface in order to achieve a low surface work function and to give the possibility to be replenished at the surface (the property of Cs will be described in chapter 5). This method assures high performance, but the complex Cs dynamics together with the interaction between plasma and Cs layer leads to instabilities during long plasma pulses, as explained in chapter 2. Alternative materials might be thus considered.

However, the interactions of the background gases and of the plasma with the converter surface have an impact on the work function, both in the case of a caesiated surface and in case of an alternative material. Such interactions are shortly analyzed in the following section.

### Interactions with the surface

As previously stated, negative ion sources for ITER and DEMO, as well as the experiment ACCesS, have a limited vacuum level (ca. $10^{-6}$ mbar), hence the flux of impurities towards the surface from the background gas (composed mostly by water vapor) is not negligible ($\sim 10^{18}$ m$^{-2}$s$^{-1}$). Such impurities produce at the converter surface oxides and hydroxyl species which have a strong impact on the work function (see for example [Tre12]).

Heating the surfaces might help to clean the material due to the desorption and the thermal decomposition of the impurities compounds. Furthermore, the

interaction of the hydrogen plasma with the surface also have significant effects: the adsorption of hydrogen at the surface influences the impurity content and the surface work function. The plasma particles such as atomic hydrogen and positive hydrogen ions impinging on the surface may lead to physical and/or chemical sputtering and the UV and VUV light emitted by de-excitation of plasma particles may contribute to particles' desorption. Moreover, the plasma heats the surface, hence thermal desorption occurs simultaneously.

Physical sputtering occurs when the impinging particles have an energy greater than a certain threshold energy $E_{\mathrm{thr}}$, which depends on the binding energy $E_{\mathrm{b}}$ of the target atom and the mass of the involved atoms $m_1$ and $m_2$ [Hot75]:

$$E_{\mathrm{thr}} = E_{\mathrm{b}} \, \frac{(m_1 + m_2)^2}{4\, m_1 m_2} \quad . \tag{4.13}$$

In case of hydrogen plasmas at ACCesS, the most energetic particles impinging on the target surface are the positive hydrogen ions, which hit the surface with an energy determined in maximum by the difference between plasma and surface potentials, typically around 8 eV. The binding energy depends on which particle is hit by the positive ions: in case of metallic substrates, e.g. molybdenum, the binding energy corresponds to the sublimation energy of the metal and for refractory metals it is usually higher than 7 eV [Cha98]. Due to the big difference between the hydrogen and the refractory metal atomic mass, a threshold energy of the order of 100 eV can be assumed, which is much greater than the energy of the impinging ions from the plasma volume, hence in this case physical sputtering does not occur. In the case of adsorbed particles at the metallic surface, physical sputtering might occur depending on the particular adsorbed species and on the actual coverage of the surface. In the case of adsorbed water or hydrogen, the threshold energy is comparable to the energy of the impinging particles from the plasma volume and the physical sputtering can occur (the binding energies can be found in [TM87] and in [TS79], respectively). In the case of adsorbed Cs, the binding energy varies between 0.8 eV [Cha98] and 3.3 eV [KVG$^{+}$05], depending on the Cs coverage and on the substrate material, leading to threshold energies higher than 27 eV, much higher than the energy of the impinging particles from the plasma volume.

Finally, chemical bondings of the oxides and hydroxyl species can be broken by the impinging positive ions if the energy of the ions is higher than the strength of the bond. At ACCesS, the typical positive ion energy is in maximum 8 eV, with

fluxes of the order of $10^{20}$ m$^{-2}$s$^{-1}$. Also radiation in the VUV/UV spectral range (corresponding to energies between 3 and 15 eV) can have a relevant impact in cleaning the surface: calculations performed in [FBR+16] has shown that VUV photon fluxes of the same order of magnitude as the ion fluxes are achieved in hydrogen and deuterium plasmas at comparable conditions as in ACCesS.

The relevant fluxes towards the surface during vacuum and plasma phases at ACCesS are summarized in the following table.

| Typical fluxes [m$^{-2}$s$^{-1}$] in | | | |
|---|---|---|---|
| vacuum phase | | plasma phase | |
| | | Atomic hydrogen: | $10^{22}$ |
| Residual gases (water vapor): | $10^{18}$ | Positive ions (energy 8 eV): | $10^{20}$ |
| | | VUV photons: | $10^{20}$ |
| (Typical Cs flux: $10^{16}$–$10^{17}$) | | | |

**Options for a low work function converter surface**

Due to the several interactions contributing to the work function of the converter surface, specific tests at ion source relevant vacuum and plasma conditions must be performed. Moreover, ACCesS allows investigations at reproducible conditions, in order to have a reliable comparison among the tested materials. Apart from alkali adsorption, e.g. Cs, low work function surfaces are achieved by diffusion to the surface of a low work function element from the inner bulk (e.g. lanthanated and bariated materials) or using materials with an inherent low work function (e.g. lanthanum hexaboride and europium). However, many materials require high temperatures to be activated (above 1000 °C), which are not recommended at ion sources for fusion since the heat load might twist and deform the large plasma grid and misalign in this way the precisely arranged apertures. Nevertheless, an activation of these materials might be possible by means of the plasma, without reaching such high temperatures. In the following, a short description of the materials considered in the current investigations is presented, while Cs and Cs layers are discussed in detail in chapter 5.

Lanthanum hexaboride

Among materials with an inherent low work function, one of the most promising regarding work function (2.7 eV) and stability is the lanthanum hexaboride ($LaB_6$) [Laf51], where the La atoms are trapped in B cages. This material is sensi-

tive to oxygen and air poisoning [Gal69], hence an activation procedure is usually recommended in order to achieve a low work function at the surface. The activation consists in heating the sample to high temperatures (ca. 1500 °C) for few minutes in order to desorb the impurities present on the surface. This material is commonly used in hot cathodes and is able to sustain hydrogen plasmas. However, there is no information available in the literature about its performance at temperatures below 800 °C and about a possible activation by low temperature plasma exposure.

Lanthanated materials

Good performance at hot cathode applications is obtained with lanthanated materials, where lanthanum oxide is added to a refractory metal such as molybdenum or tungsten. These materials are based on the diffusion of lanthanum to the surface in order to decrease its work function: 2.6 eV for lanthanated molybdenum (MoLa) [YNX+04] and 2.8 eV for lanthanated tungsten (WL) [HHB+15]. For this purpose, an activation procedure at high temperatures (above 1300 °C) is needed for an annealing time of at least one hour [BBG78, HHB+15]. These materials are usually in operation at temperatures higher than 1300 °C in order to assure a continuous replacement of lanthanum onto the surface, while their performance in a lower temperature range is unknown.

Tungsten dispenser cathode

This cathode is based on the same principle as the previous material: different oxides (BaO, CaO and $Al_2O_3$) are present in a porous tungsten matrix, and the barium diffusion towards the tungsten surface decreases its work function down to 2.1 eV [Cro81]. Besides the low work function, the required activation temperature (1000 °C) as well as the operation temperature (usually above 850 °C) are lower with respect to the lanthanated materials due to the presence of Ca and Al oxides, which also help to stabilize the cathode during long operation.

Europium

Among all the lanthanides, the element with the lowest work function is europium with 2.5 eV [Mic77]. This material is one of the most reactive elements, together with Cs: it shows a fast oxidation in air and a high reactivity with water. The effects of the exposure to a hydrogen plasma on the bulk Eu are at present unknown.

# 5 Caesium properties

## 5.1 Atomic properties

Caesium is an alkali metal with an atomic mass of 132.9 u and 55 electrons, with only one electron in the outermost shell $6s^1$ [Lid05]. This configuration leads to a low ionization energy (3.89 eV) and to a very high chemical reactivity. In fact, it ignites spontaneously in air and reacts easily with water. The caesium melting point is low (28.5 °C), hence it is one of the few metals that are liquid near room temperature.

Electronic excitation of the caesium atom may occur in the plasma by electron impact, absorption of photons or recombination of positive Cs ions with electrons. The optical transition between the excited level $6^2P_{3/2}$ and the ground state $6^2S_{1/2}$ is particularly relevant for diagnostic purposes, in fact it results in the resonant transition at 852.1 nm called *$D_2$ resonance line*, easily accessible by optical emission spectroscopy or laser absorption (see section 6.4.1). Due to the hyperfine structure, i.e. the splitting of the lines due to the interaction between the angular momenta of the nucleus and the electron, the excited state $6^2P_{3/2}$ splits into four levels, while the ground state splits into two levels [Ste10]. The selection rules for optical transitions generate 6 lines. The energy difference between the two levels of the ground state (38 µeV) is much larger than the energy difference among the levels at the excited state $6^2P_{3/2}$ (2.5 µeV), leading to the formation of two groups of three lines each. The Doppler broadening of the lines is already sufficient to not allow to resolve the single lines but only the two groups, which are distant 20–25 pm from each other. A simulation of the spectrum obtained for the $D_2$ optical transition at the temperature of 500 K is shown in figure 5.1. The distribution of the line around the central wavelength $\lambda_0$ due to broadening effects defines the line profile $P_{\mathrm{line}}$, which is important to determine the Cs density by absorption spectroscopy for example.

The Doppler broadening of a line with central wavelength $\lambda_0$ is due to the thermal motion of the emitting or absorbing particles of mass $m$ at the temperature $T$.

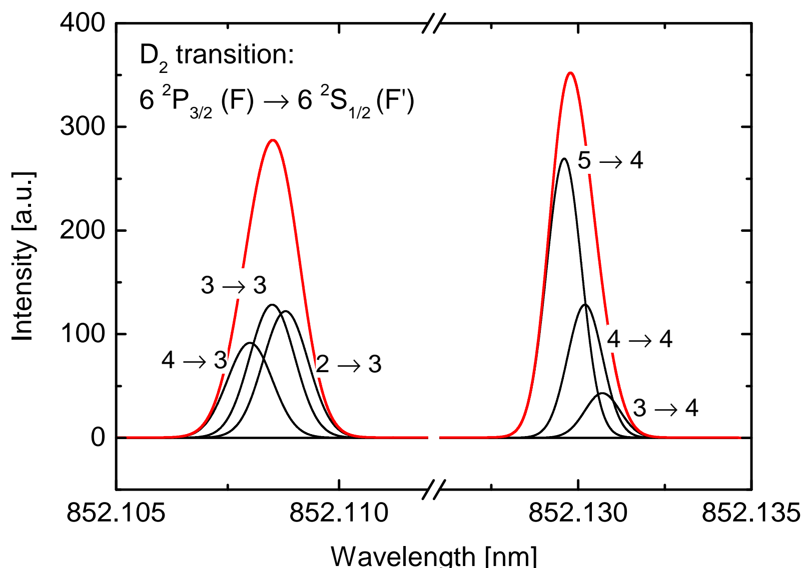


**Figure 5.1:** *Simulated emission spectrum for the $D_2$ transition of the Cs atom at a temperature of 500 K. F and F′ indicate the hyperfine structure levels. The considered lines broadening mechanisms are the Doppler effect, the natural line broadening and the pressure broadening at 10 Pa.*

This broadening creates a Gaussian profile of the transition line with a full width half maximum $\omega_{\mathrm{Doppler}}$ given by [TLJ99]

$$\omega_{\mathrm{Doppler}}(T,m) = 2\lambda_0 \sqrt{\frac{2k_{\mathrm{B}}T\ln 2}{mc^2}} \quad [\mathrm{m}] \ . \tag{5.1}$$

For the Cs $D_2$ line at 852.1 nm the Doppler broadening is between 0.9 and 1.7 pm for the temperature range between 300 and 1000 K. Other broadening mechanisms are the natural line broadening and the pressure broadening [TLJ99], which are for the Cs $D_2$ line of the order of magnitude of 0.01 and 0.001 pm, respectively.

## 5.2 Work function of caesiated surfaces

When caesium is evaporated onto a metallic surface (*caesiation process*), the caesium atoms create a dipole bond with the atoms of the substrate where the electron of the outermost shell of the Cs atom is transferred to the conduction band of the metal. The formation of this bond lowers the work function $\chi$ of the metal (typical values for the work function of the metallic substrate material

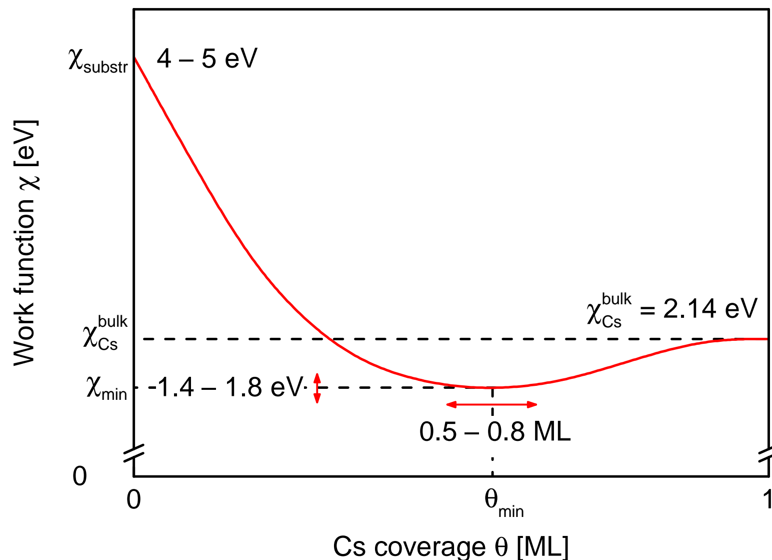


**Figure 5.2:** *Schematic of the work function of a metallic substrate as a function of the Cs coverage during the caesiation process.*

are between 4 and 5 eV, e.g. 4.6 eV for polycrystalline molybdenum [Mic77]). The work function hence decreases with increasing Cs coverage $\theta$ as shown in figure 5.2, until the work function reaches a minimum value $\chi_{\mathrm{min}}$ for a partial coverage $\theta_{\mathrm{min}}$ of pure Cs and then it increases again due to the repulsive forces among the dipoles, reaching the value for bulk caesium $\chi_{\mathrm{Cs}}^{\mathrm{bulk}} = 2.14$ eV [Mic77] once the substrate is covered by one monolayer (1 ML) of Cs atoms. Considering the radius of the Cs atom in a metallic bond (265 pm), 1 ML of pure Cs on the surface corresponds to a surface density of $4.5 \times 10^{18}$ Cs atoms/m$^2$. However, the actual Cs surface density depends on the crystallographic structure of the substrate and on the particular bond between Cs and the substrate atoms.

The exact evolution of the work function, i.e. the minimum work function value and its position, depends on the actual substrate and on its crystallographic structure at the surface. Different experiments in ultra-high vacuum systems have shown values of 1.4–1.8 eV at about 0.5–0.8 ML [Wil66a, Wil66b, SS68].

## 5.3 Cs desorption and adsorption

For coverages $\theta$ below 1 ML, the Cs desorption flux $\Gamma_{\mathrm{Cs}}^{\mathrm{desorp}}$ from a tungsten substrate has been described by [ATG85] and depends on the coverage itself and

on the temperature of the surface $T_{\text{surf}}$:

$$\Gamma_{\text{Cs}}^{\text{desorp}} = \left(7.5 \times 10^{30}\ [\text{m}^{-2}\text{s}^{-1}]\right) \theta \exp\left(-\frac{3.37\ [\text{eV}] - \theta\ 2.78\ [\text{eV}]}{k_{\text{B}} T_{\text{surf}}}\right) \left[\frac{1}{\text{m}^2\text{s}}\right] . \quad (5.2)$$

The desorption fluxes for different surface temperatures are plotted in figure 5.3: the desorption flux increases drastically with the coverage due to the increasing repulsive force among the dipoles formed by Cs and the substrate at the surface, which consequently leads to a decrease of the binding energy of the Cs atoms at the metallic substrate.

For coverages above 1 ML, the desorption flux is no more dependent on the coverage but on the temperature dependent vapor pressure $p_{\text{Cs}}(T_{\text{surf}})$ at saturated Cs vapor above the surface:

$$\Gamma_{\text{Cs}}^{\text{desorp}} = \frac{p_{\text{Cs}}(T_{\text{surf}})}{\sqrt{2\pi m_{\text{Cs}} k_{\text{B}} T_{\text{Cs}}}} \quad \left[\frac{1}{\text{m}^2\text{s}}\right] , \quad (5.3)$$

where $m_{\text{Cs}}$ and $T_{\text{Cs}}$ are the mass and the temperature of the Cs atoms, respectively. Values for the Cs vapor pressure can be found in [TL37] and are plotted in figure 5.4 together with the resulting Cs desorption flux considering $T_{\text{surf}} = T_{\text{Cs}}$. Typical

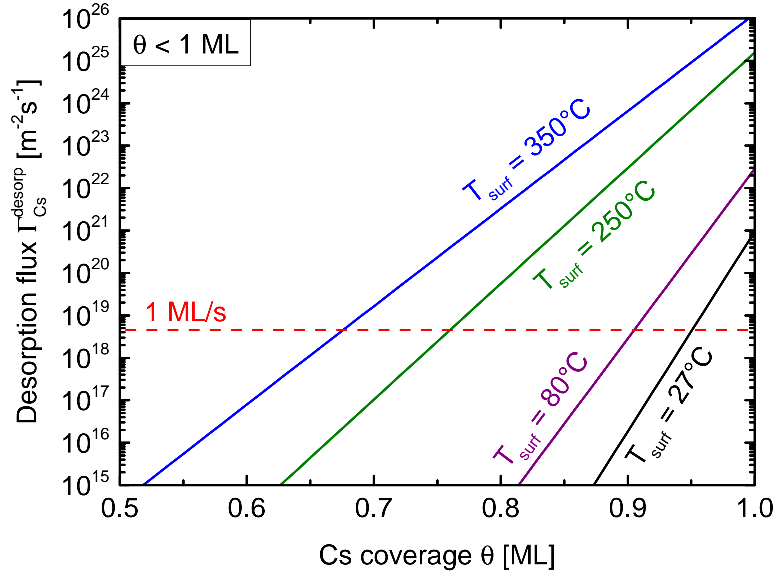


**Figure 5.3:** *Cs desorption flux from a tungsten surface for Cs coverages below 1 ML and for different surface temperatures [ATG85]. The value for a desorption flux corresponding to 1 ML/s is also illustrated.*

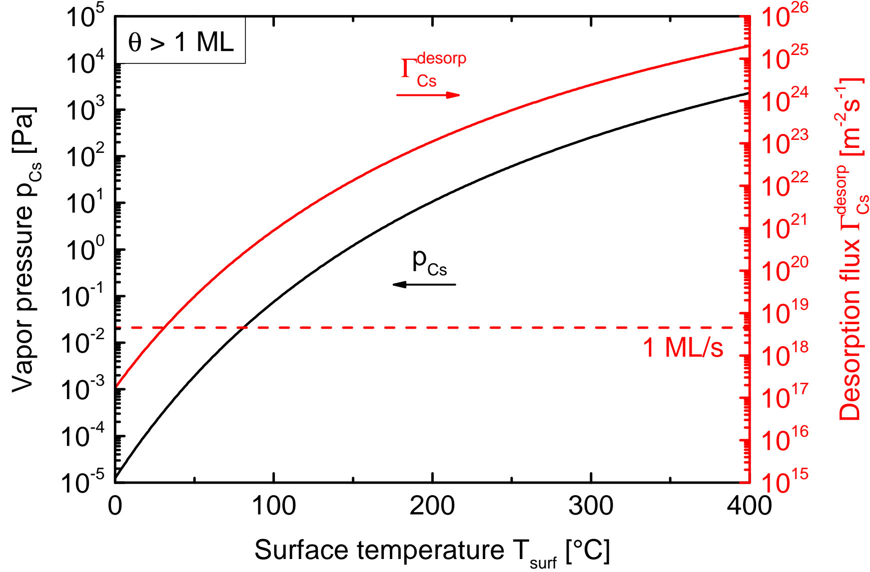


**Figure 5.4:** *Caesium vapor pressure from [TL37] and corresponding Cs desorption flux as function of the surface temperature for Cs coverages above 1 ML. The value for a desorption flux corresponding to 1 ML/s is also illustrated.*

surface temperatures are usually at or above room temperature, hence a desorption flux around or higher than 1 ML/s can be expected.

Hence, to counteract the desorption of Cs from the surface, a continuous flux of Cs towards the surface is mandatory. The flux of Cs towards the surface is given by

$$\Gamma_{\mathrm{Cs}} = \frac{1}{4} n_{\mathrm{Cs}} v_{\mathrm{Cs}} = \frac{1}{4} n_{\mathrm{Cs}} \sqrt{\frac{8 k_{\mathrm{B}} T_{\mathrm{Cs}}}{\pi m_{\mathrm{Cs}}}} \quad \left[\frac{1}{\mathrm{m}^2\ \mathrm{s}}\right] , \tag{5.4}$$

where $n_{\mathrm{Cs}}$ and $v_{\mathrm{Cs}}$ are the density and the thermal velocity of the Cs atoms, respectively. Typical values for the neutral Cs density in the laboratory experiment ACCesS are in the range of $10^{14}$–$10^{15}$ $\mathrm{m}^{-3}$ and the typical Cs temperature is around 500 K, resulting in a Cs flux towards the surface of the order of $10^{16}$–$10^{17}$ $\mathrm{m}^{-2}\mathrm{s}^{-1}$, corresponding to 0.001–0.01 ML/s. Hence, sub-monolayers are expected if only pure Cs is involved.

## 5.4 Cs compounds and ion source relevant conditions

Most of the information available in the literature about caesiated surfaces refers to ultra-high vacuum systems. As already mentioned, the background pressure in ACCesS and at the ion sources is of the order of $10^{-6}$ mbar, hence the flux of impurities (mainly water vapor) towards the surface is not negligible, but it is of the order of $10^{18}$ $m^{-2}s^{-1}$ (larger than the typical Cs flux). The low ionization potential of caesium and its high electropositivity lead to a high chemical reactivity and to the consequent possible formation of several Cs compounds with ionic bond. The Cs layer is thus constituted by Cs compounds, which may significantly reduce the Cs desorption flux depending on the binding energy and stability of the Cs compounds. However, cleaning of the Cs layer is possible by exposing the surface to the plasma.

In vacuum, the main component of the residual gases is the water vapor. The presence of Cs leads to the formation of the caesium hydroxide CsOH, which is very stable both in crystalline and in gaseous phases [Cha98]. As a consequence, Cs is gettered by the impurities and the resulting work function at the caesiated surface in vacuum is higher with respect to the bulk Cs due to the non-metallic nature of these bonds: a minimum work function of 2.75 eV was achieved in [FF17] for a thick Cs layer in vacuum at typical background pressures of $10^{-6}$ mbar. Moreover, due to the gettering effect and the degradation of the Cs layer because of the background impurities, continuous evaporation of Cs in the source is necessary, leading to an increase in the Cs consumption. The degradation of the Cs layer observed at ACCesS during vacuum phases occurs in fact if no fresh Cs is evaporated into the volume [FF17]: the work function increases with a rate of 0.1 eV/h if no plasma was previously applied and with a rate of 0.4 eV/h if the caesiated surface was previously exposed to plasma. The impurity control and reduction are thus key issues for negative ion sources, in particular for pulse mode operation where vacuum phases occur between subsequents pulses [FFW12].

In order to clean the Cs layer on the converter surface, the chemical bonds must be broken (e.g. the bond dissociation energy of CsOH is 3.9 eV [CJ69]). This can be achieved by thermal decomposition or by plasma treatment (as mentioned in section 4.4). Thermal decomposition can be difficult to achieve, since it requires high temperatures, while plasma reactions with the surface lead to the cleaning and redistribution of the Cs layer by thermal, physical and chemical interactions.

However, physical sputtering of Cs is difficult to occur in case of a non-pure Cs layer, due to the high binding energy of the Cs compounds (above 0.8 eV [Cha98]), leading to threshold energies much higher than the energy of the impinging plasma particles [Wad18].

Nevertheless, the positive ions impinging on the sample surface (with a flux of $10^{20}$ $m^{-2}s^{-1}$) have energies of 8 eV in maximum, determined by the potential drop at the surface. Hence, their energy is sufficient to break the bondings of Cs compounds such as CsOH. Also the UV and VUV light emitted by de-excitation of plasma particles might contribute to the cleaning of the Cs layer, since the energy of the photons reaches values of up to 15 eV (with photon fluxes in the VUV of the same order of magnitude as the positive ion flux). The cleaning effect of the plasma on the Cs layer was observed in [FF17], where the work function of a caesiated surface at ion source relevant conditions decreases down to 2.1 eV (corresponding to bulk Cs) due to the plasma treatment. At ion sources, good performance can be reached only after some days of operation, which constitute the so-called *Cs conditioning phase* [FFW12], where Cs is continuously evaporated into the source and the Cs layer at the converter surface is cleaned and redistributed by the plasma.

The plasma interaction with the surface leads not only to the dissociation of the Cs compounds and to a cleaning of the Cs layer, but also to the release and redistribution of Cs or Cs compounds into the volume. In fact, the plasma can remove the Cs from the converter surface, since the binding energy of Cs varies between 0.8 eV [Cha98] and 3.3 eV [KVG+05] (depending on the Cs coverage and on the substrate material) and is lower than the energy of the positive ions and UV and VUV photons impinging onto the surface. To counteract the Cs removal from the surface, a minimum flux of Cs towards the surface must be assured during the plasma phases.

In the case of hydrogen plasma, the presence of hydrogen adsorbed within the Cs layer also has an influence on the work function, as observed in ultra-high vacuum systems by [PC73] and [EKP87] for partially caesiated surfaces. In the first paper, Cs is evaporated onto a hydrogen covered W surface, while in the second paper molecular hydrogen is adsorbed on a partially caesiated Mo surface. In both cases, for low Cs coverages (before the work function minimum in figure 5.2) the hydrogen adsorption increases the work function, while for Cs coverages close or above the position of the minimum the absorbed hydrogen leads to a decrease of the work function. Unfortunately, the actual composition of the Cs layer at

the surface in vacuum and plasma operation is not easily accessible and it would require in-situ diagnostics.

The following table summarizes the effects contributing to the work function of the Cs layer in ACCesS and at the ion sources:

| Vacuum phase | Plasma phase |
|---|---|
| • non-pure Cs layer<br>• degradation of the layer | • cleaning of the Cs layer<br>• Cs removal<br>• H adsorption in the layer |

Thus, fundamental investigations with Cs evaporation require high standards of reproducibility due to the high and uncontrollable Cs dynamics. In order to maintain consistent conditions of the Cs layer in the different experimental investigations and to study in depth the mechanisms contributing to changes of the Cs layer, the experimental procedures must always be identical, e.g. with the same starting conditions and caesiation method.

# 6 Experimental setup and applied diagnostics

## 6.1 Experimental setup

The laboratory experiment ACCesS (Augsburg Comprehensive Cesium Setup) consists of a cylindrical stainless steel vessel with a diameter of 15 cm and a height of 10 cm. A sketch of the setup is shown in figure 6.1. Vacuum in the vessel is obtained by a turbomolecular pump and a rotary vane forepump, allowing to have a background pressure of the order of $10^{-6}$–$10^{-5}$ mbar. The gas inlet system is regulated through mass flow controllers and the absolute operating pressure is measured by a capacitive pressure gauge. The hydrogen plasma is generated by inductive RF coupling via an external planar coil located in atmosphere on

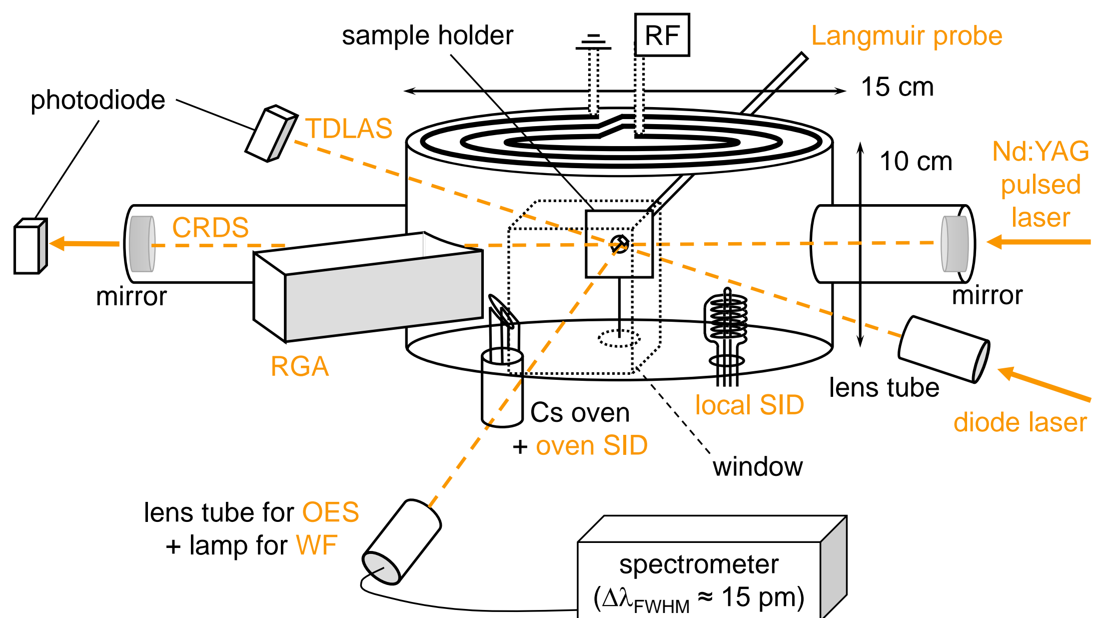


**Figure 6.1:** *Sketch of the experimental setup ACCesS with an overview of the different diagnostics applied during the current investigation (for the meaning of the acronyms, see table 6.1).*

top of the vessel. A grounded Faraday screen and a Borosilicate glass plate, functioning as a dielectric medium, are situated between the antenna and the vacuum chamber. The RF generator operates at a frequency of 27.12 MHz and it can deliver a maximal RF power of 600 W. In the present work, hydrogen and deuterium discharges (and occasionally also argon plasmas) are sustained by an RF power between 250 and 450 W at pressures between 2 and 10 Pa.

The temperature of the grounded vessel walls is controlled through a water cooling system whose circuit surrounds the vessel walls, and the water temperature can be adjusted thanks to a temperature control system. During the present investigations, the temperature of the walls is always kept between 20 and 60 °C, depending on the specific operation.

The setup counts several diagnostic systems thanks to the many ports at the vessel and to the exchangeable bottom plate. The latter includes the sample holder, Cs diagnostics, several feedthroughs and the caesium source. The diagnostic systems allow investigations in vacuum and in plasma environment, and a complete list of the diagnostics is given in table 6.1, together with the measured quantity, the spatial resolution, and the particular situation where they can be applied (during vacuum and/or plasma operation).

The vertical sample holder is located close to the middle of the vessel, and the sample under investigation can be clamped and actively heated. Furthermore, the sample can be biased, and a quartz window is located in front of the sample, allowing for measurements of the surface work function from the photoelectric effect by the Fowler method. The negative ion density is measured by cavity ring-down spectroscopy along the horizontal line of sight at 2 cm distance in front of the sample. Two high reflectivity mirrors are situated at the two ends of the cavity tubes located on the left-hand side and on the right-hand side of the sample holder. Several diagnostic systems for Cs detection surround the sample: two surface ionization detectors monitor the Cs flux, while the Cs density is obtained by tunable diode laser absorption spectroscopy, and the Cs emissivity is monitored additionally by optical emission spectroscopy during plasma operation. The line of sight for the absorption spectroscopy is slightly tilted, crossing diagonally the vessel, and the Cs emissivity is measured on a different line of sight, looking within the experiment from the quartz window in front of the sample. Quartz windows are also applied for the line of sight of the laser absorption spectroscopy. Optical emission spectroscopy can also be applied for monitoring the plasma parameters, e.g. densities and temperatures of the different species via the Balmer and Fulcher

**Table 6.1:** *List of the applied diagnostic systems at ACCesS. For each diagnostic system, the measured quantity and the spatial resolution are given, as well as its applicability (in vacuum and/or in plasma operation).*

| Diagnostic | | Measured quantity and spatial resolution | Vacuum or plasma operation |
|---|---|---|---|
| WF | work function diagnostic | work function (local) | vacuum |
| CRDS | cavity ring-down spectroscopy | $H^-$ density (LOS integr.) | vacuum & plasma |
| SID | surface ionization detector | caesium flux (local) | vacuum |
| TDLAS | tunable diode laser absorption spectroscopy | caesium density (LOS integr.) | vacuum & plasma |
| OES | optical emission spectroscopy | plasma parameters & Cs density (LOS integr.) | plasma |
| Langmuir probe | | plasma parameters (local) | plasma |
| RGA | residual gas analyzer | impurities content (volume integr.) | vacuum & plasma |

emission lines of the hydrogen plasma. Local measurements of electron density and electron temperature, as well as the electrostatic potentials, are obtained by a movable Langmuir probe in vicinity of the surface. The port for the probe is located on the backside of the sample holder. Finally, a residual gas analyzer is applied to monitor the background gases during operation, using the port on the half left-hand side.

All diagnostics can be operated simultaneously in order to relate the different parameters to the same experimental condition.

The bottom plate can be easily removed and re-installed, allowing an easy and fast exchange of the sample under investigation. Furthermore, the samples can be investigated also by ex-situ diagnostics, like Rutherford backscattering

spectroscopy (RBS)[1,2] and energy-dispersive X-ray spectrscopy (EDX)[3] performed at different setups, in order to verify the material composition at the sample surface and possible changes after plasma exposure.

Cs evaporation is typically performed by a Cs oven equipped with a Cs reservoir that can be heated up. Caesium is thus injected in ACCesS through a nozzle located at the bottom plate, equipped with a surface ionization detector. However, different Cs reservoirs were tested during the current work, using Cs dispensers or Cs ampules. The different Cs sources are described in section 6.3, and their characteristics are examined in section 9.1.

In the following, a brief description of the sample holder and of the monitoring diagnostic systems (applied to monitor the plasma parameters and the Cs density) is given. A more detailed description can be found in [Fri13] for most of the monitoring diagnostics applied in ACCesS. The methodology for the work function measurements and the cavity ring-down spectroscopy for $H^-$ detection (main diagnostic systems in the current work) will be instead described in detail in chapter 7.

## 6.2 Sample holder

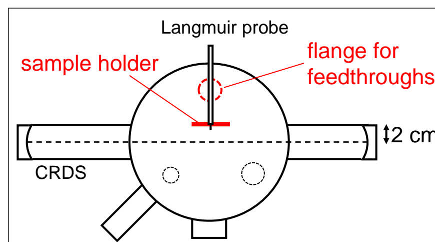


The sample holder (a top view schematic of the experiment is shown on the left) is mounted directly on the bottom plate and is electrically and thermally insulated from the vessel walls by a Teflon mount. The sample holder is located at 2 cm from the symmetry axis of the cylindrical vessel and is parallel to the line of sight of the cavity ring-down spectroscopy.

The sample holder is made of stainless steel and has a size of 30 × 30 mm$^2$, as indicated on the left-hand side of figure 6.2. When a sample is installed, the coaxial thermocouple measures the temperature of the sample surface on the top right corner, and the sample can be heated up to 400–450 °C by means of a coaxial heating wire within the sample holder. Both the thermocouple and the heating wire are connected to a temperature control unit via vacuum feedthroughs

[1] Department of Experimental Physics IV, University of Augsburg.
[2] Max-Planck-Institut für Plasmaphysik (IPP), Garching.
[3] Anwenderzentrum Material- und Umweltforschung (AMU), University of Augsburg.

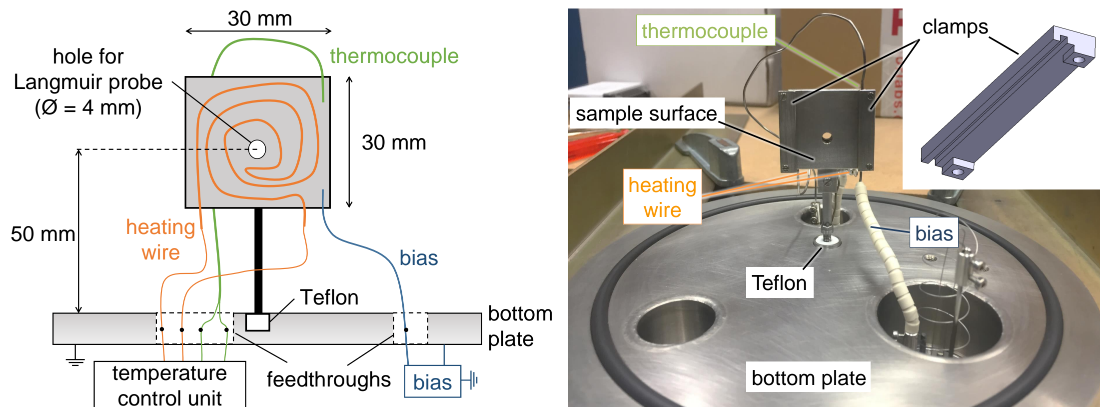


**Figure 6.2:** *On the left: front view schematic of the sample holder. On the right: picture of the bottom plate with the sample holder, the heating wire, the thermocouple, and the bias connection. A CAD drawing of the specially manufactured clamps is shown on the top right corner [Noc16].*

insulated from the vessel. The coaxial outer shields of the wires are insulated from the grounded vessel as well, assuring the electrical insulation of the sample holder. In turn, also the temperature control unit is insulated from ground, in order to avoid any capacitive coupling to it. Furthermore, the sample can be biased by means of a stainless steel wire attached at the bottom right corner of the sample holder, allowing for work function measurements (see section 7.1). The bias connection is shielded from the plasma by ceramics surrounding the wire. A picture of the bottom plate with the sample holder is shown on the right of figure 6.2. At the sides of the sample holder, two vertical stainless steel clamps hold the sample under investigation. These clamps are specially manufactured to assure a good thermal contact between the sample and the sample holder, and they present a slot for the thermocouple and the bias wire, as shown in the CAD drawing in the figure [Noc16].

A hole in the middle of the sample holder allows the access of the Langmuir probe from the backside (if the sample is punched as well). In this way, the plasma parameters can be monitored in the vicinity of the sample surface: the hole has the same diameter as the glass tube containing the Langmuir probe (4 mm) and the probe tip is axially centered, hence the minimal distance of the probe from the surface is of 2 mm.

## 6.3 Caesium source

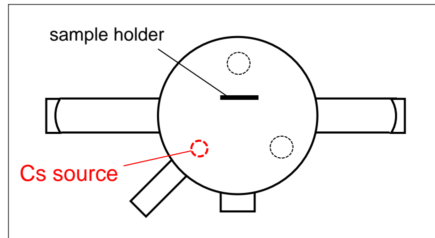


For the evaporation of caesium, different Cs sources were tested and applied at ACCesS. The position of the Cs source is shown in the top view schematic on the left. During the work of [Fri13] Cs dispensers were tested, and a Cs oven suitable to host the dispenser was applied (the Cs dispenser oven is described in [FFF12]). The dispensers showing good performance in terms of stability and evaporation rate (up to more than 10 mg/h [Fri13]) were the ones purchased in 2010 from Alvatec [Alv16], an Austrian company that ceased all operations in 2016. These dispensers consist of a stainless steel sleeve containing 100 mg of $BiCs_3$, an alloy stable at room temperature which decomposes when heated, allowing the evaporation of Cs from a narrow slit of 10 mm length on the side of the dispenser tube. A picture of the Alvatec dispenser is shown on the left of figure 6.3. During Cs operation the dispenser is ohmically heated with currents up to 10 A, allowing to adjust the Cs evaporation rate by varying the current. However, it is not recommended to apply currents higher than 8 A, which would cause evaporation not only of Cs, but also of heavy metallic impurities such as Bi and In (the latter is used as sealing of the slit).

The company AlfaVakuo e.U. [Alf16], formed in 2016 after the experience of Alvatec, offers similar Cs dispensers as Alvatec, containing 100 mg of $BiCs_3$ as

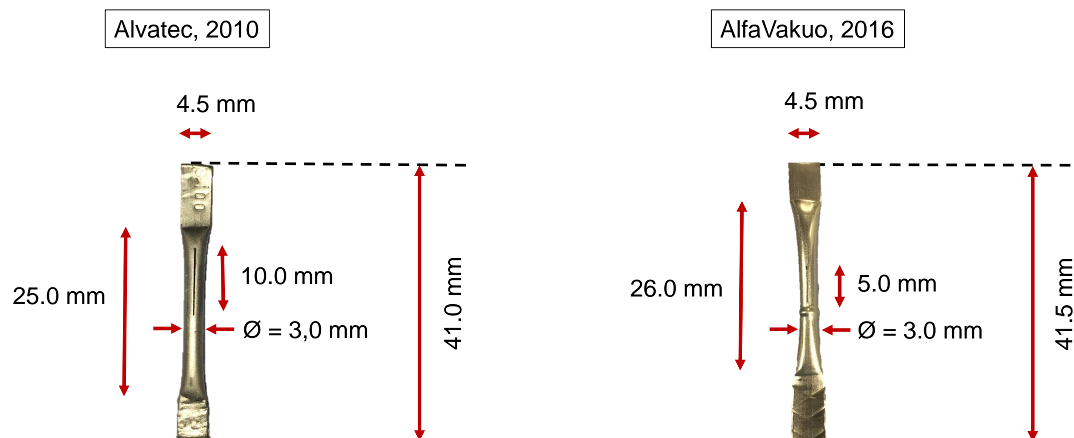


**Figure 6.3:** *Pictures and dimensions of the dispensers purchased from Alvatec in 2010 [Alv16] and from AlfaVakuo in 2016 [Alf16].*

well. A picture of the dispenser purchased from AlfaVakuo in 2016 is shown on the right of figure 6.3. However, the evaporation rate of these dispensers from the Cs dispenser oven is much lower with respect to the Alvatec dispensers ($<$ 0.1 mg/h), probably due to the shorter slit (5 mm long). As a consequence, these dispensers cannot be applied in the oven, but they have to be located directly in the experimental chamber in order to observe Cs evaporation.

In order to obtain higher Cs evaporation rates, Cs ampules are applied in this work instead of Cs dispensers: they contain 1 g of pure Cs as in use also at the IPP ion sources. A CAD drawing of the particular Cs ampule oven applied at ACCesS is shown in figure 6.4 [Frö18]: the sealed glass ampule containing Cs is located at the bottom part of the oven. When the oven is kept at a minimum temperature of 30 °C, the caesium contained in the ampule is liquid and the ampule can be easily cracked from the outside, without breaking the vacuum within the oven. Once the ampule is broken, the liquid Cs is collected in the reservoir at the cooling plate, which is the coldest spot of the oven. The Cs is evaporated by heating the cooling plate, and the evaporation rate is controlled by the temperature of the

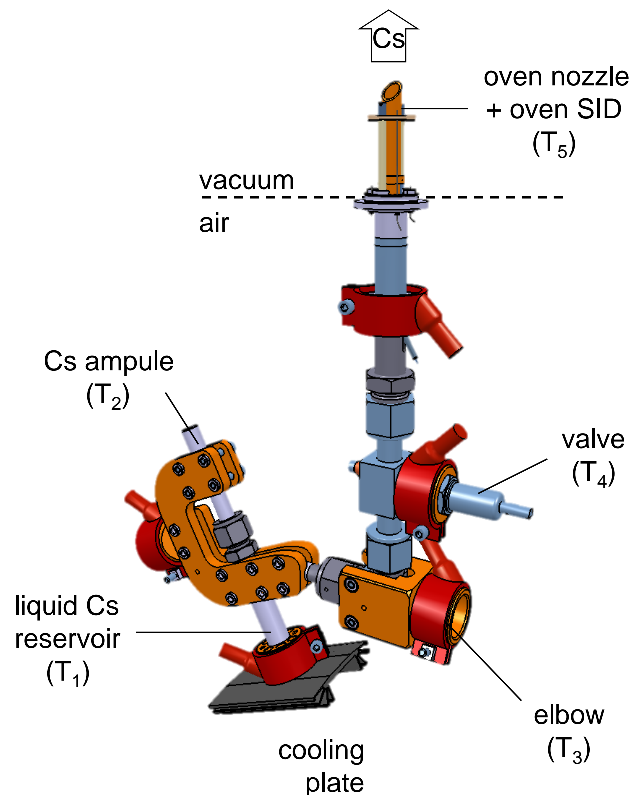


**Figure 6.4:** *CAD drawing of the Cs ampule oven applied at ACCesS [Frö18]. The positions of the five thermocouples are indicated by $T_i$, with i=1,...,5.*

reservoir, typically between 100 °C and 150 °C. The rest of the oven is kept at a higher temperature (around 280 °C) in order to avoid the presence of cold spots and to assure high Cs transport to the experiment vessel. The oven temperature is feedback controlled by five heating sleeves and thermocouples (indicated in the figure by $T_i$, with $i = 1, .., 5$), which monitor the temperature of the different parts of the oven. A valve at mid height is used to stop quickly the Cs evaporation when required and to separate the Cs reservoir from the experiment vessel: in this way, the experiment can be vented and opened while keeping the Cs reservoir still in vacuum, avoiding oxidation. Cs is evaporated into the experiment at a height of ca. 2.5 cm above the bottom plate through a nozzle, with an edge cut at 45° angle looking towards the sample holder. In order to monitor the Cs evaporation, the so-called *oven SID* is located above the nozzle and will be described in the next section. Typical evaporation rates for such a Cs liquid oven are of several mg/h [FHW+17].

## 6.4 Monitoring systems

### 6.4.1 Cs diagnostics

#### Surface ionization detector (SID)

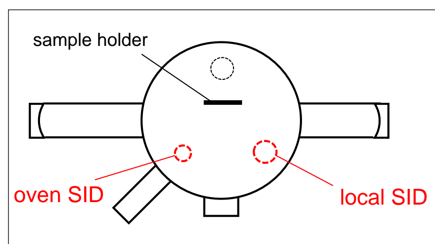


In order to monitor the Cs flux at two different positions (shown in the top view schematic on the left), two surface ionization detectors (SID) are applied at ACCesS: the so-called *oven SID* and *local SID*. As it can be observed in figure 6.5, each SID consists of two ohmically heated tungsten filaments (diameter of 300 µm), which are biased against each other by around 50–60 V. When Cs atoms approach the first tungsten filament (called *ionization filament*) they are ionized, since the Cs ionization energy (3.89 eV [Lid05]) is lower than the work function of tungsten (4.55 eV [Mic77]), and energy can be gained by electron transfer from the Cs atom to the conduction band of tungsten. The temperature of the filaments must be higher than 900 °C in order to avoid the Cs deposition onto the filament, which would decrease the tungsten work function (as shown in section 5.2) and change the sensitivity of the apparatus [TL33].

The $Cs^+$ ions are then accelerated and collected onto the second tungsten

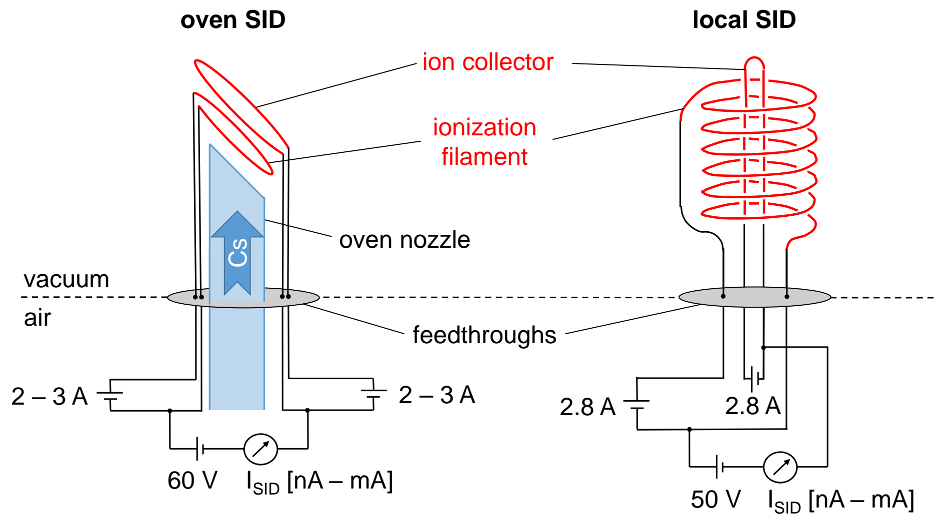


**Figure 6.5:** *Schematic of the oven SID (on the left) and the local SID (on the right).*

filament (called *ion collector*), which is also heated in order to avoid adsorption and desorption of Cs that would disturb the measurement. The resulting SID current $I_{\mathrm{SID}}$ flowing between the two filaments, named also *SID signal* in the current work, is typically in the range from nA to mA and is proportional to the flux of Cs atoms impinging on the ionization filament.

Since the SID is based on a current measurement, this diagnostic can be used only during vacuum operation, since in plasma operation it would not be possible to discriminate the contribution of Cs from the plasma current in the resulting measured current.

At ACCesS two SIDs are applied: the first SID (*oven SID*) is located directly above the nozzle of the Cs oven, as illustrated on the left of figure 6.5. Due to the strategic position and shape of this SID, the oven SID signal is directly proportional to the evaporation rate of the Cs oven, generally given in [mg/h]. A calibration of the SID current can be empirically obtained when the amount of caesium in the Cs source (dispenser or ampule) is known and it is completely evaporated: in that case, the integral of the entire SID current over the time in [A h] corresponds to the evaporated mass of caesium in [mg], and a maximal value of the calibration factor can be estimated (assuming that no Cs is trapped at the oven walls). However, it can take several months to deplete all the Cs inside the Cs source, hence an absolute calibration is at the moment not available and the SID can be used only for a relative estimation of the evaporation rate.

The second SID (*local SID*) is located on the bottom plate at around 8.5 cm distance from the Cs source nozzle. Its aim is to monitor the Cs redistribution within the vessel, and an absolute calibration is not easily achievable due to its complex geometry (see figure 6.5 on the right). However, the measured current is still directly proportional to the Cs flux and provides information on the relative redistribution of the Cs atoms.

### Optical emission spectroscopy (OES) for Cs

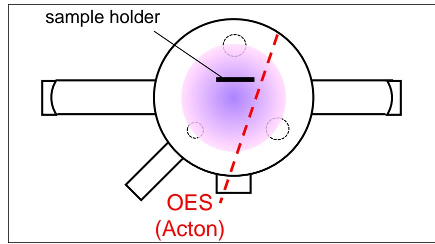


During plasma operation, the Cs atom can be excited by electron impact. The spontaneous emission of the Cs atom between the excited state $6^2P_{3/2}$ and the ground state $6^2S_{1/2}$ results in the $D_2$ resonance line at 852.1 nm and it is easily accessible by optical emission spectroscopy (OES). The line of sight crossing the vessel is shown in the top view schematic on the left (the LOS is usually at half height of the vessel, but for big samples the LOS is moved above the sample holder) and the emitted radiation is collected by a lens tube coupled to a spectrometer by means of an optical fiber. For Cs detection, a high-resolution spectrometer (Acton Spectra Pro) with a Gaussian apparatus profile of 15 pm of FWHM at 852 nm is applied.

The line of sight averaged emissivity $\epsilon_{ik}$ of a transition line $i \rightarrow k$ is obtained from the measured spectral intensity distribution $I(\lambda)$ (normalized by the applied integration time) by

$$\epsilon_{ik} = \frac{1}{l_{\mathrm{pl}}} \int_{\mathrm{line}} I(\lambda)\, C(\lambda)\, \mathrm{d}\lambda \quad \left[\frac{1}{\mathrm{m}^3\,\mathrm{s}}\right] \quad , \tag{6.1}$$

where $l_{\mathrm{pl}} = 14.5$ cm is the plasma length for the tilted line of sight at ACCesS and $C(\lambda)$ is the absolute intensity calibration factor depending on the wavelength $\lambda$.

The emissivity of the line is directly related to the density of the excited state $i$ by equation (3.14). In the case of the Cs $D_2$ line, the density of the excited state $6^2P_{3/2}$ can further be coupled to the ground state density $n_{\mathrm{Cs}}$ by [Fri13]

$$\epsilon_{ik} = n_{\mathrm{e}}\, n_{\mathrm{Cs}}\, X_{\mathrm{em,D_2}}(T_{\mathrm{e}}) \quad , \tag{6.2}$$

where $X_{\mathrm{em,D_2}}(T_{\mathrm{e}})$ is the *emission rate coefficient* for the specific $D_2$ transition depending on the electron temperature. As a consequence, the Cs density of the

ground state is accessible if the electron density and temperature are both known, which is not always the case.

At the current setup, OES for Cs detection is used to monitor the behavior of the Cs emissivity, while absolute measurements of the Cs density at the ground state can be directly obtained by Cs absorption spectroscopy (see the following section). The measured emissivity of the Cs $D_2$ line has a detection limit of $\epsilon_{Cs} \geq 1 \times 10^{17}$ $m^{-3}s^{-1}$, while the associated error is $\pm 10\,\%$.

### Tunable diode laser absorption spectroscopy (TDLAS) for Cs

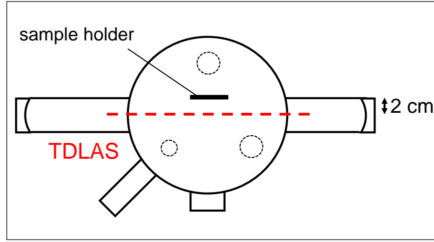


The tunable diode laser absorption spectroscopy (TDLAS) is a reliable diagnostic for absolute measurements of neutral Cs density, independent from the plasma parameters and available both in vacuum and in plasma operation [FW11]. This technique relies on the absorption of radiation of intensity $I(\lambda, 0)$ through an absorbing medium at the wavelength $\lambda$, exciting the absorbing particles from the lower state $k$ to the upper state $i$. The intensity of the radiation after traveling through a homogeneously absorbing medium of length $L$ is thus reduced to

$$I(\lambda, L) = I(\lambda, 0)\, e^{-k(\lambda)\, L} \quad , \tag{6.3}$$

where $k(\lambda)$ is the spectral absorption coefficient given by [TLJ99]

$$k(\lambda) = \frac{\lambda_0^4}{8\pi c} \frac{g_i}{g_k} A_{ik}\, n_k\, P_{\mathrm{line}}(\lambda) \quad , \tag{6.4}$$

with $\lambda_0$ the central wavelength of the absorption line, $g_i$ and $g_k$ the statistical weights of the upper and lower level, respectively, $A_{ik}$ the Einstein coefficient for spontaneous emission for the transition from $i$ to $k$, $n_k$ the absorbing particle density in the lower state, and $P_{\mathrm{line}}$ the line profile, which is normalized to 1 ($\int_{\mathrm{line}} P_{\mathrm{line}}(\lambda) \mathrm{d}\lambda = 1$).

The line of sight averaged density $n_k$ is then obtained by integrating equation (6.3) over the wavelength range of the absorption line:

$$n_k = \frac{8\pi c}{\lambda_0^4} \frac{g_k}{g_i} \frac{1}{A_{ik} L} \int_{\mathrm{line}} \ln\left(\frac{I(\lambda, 0)}{I(\lambda, L)}\right) \mathrm{d}\lambda \quad . \tag{6.5}$$

In the case of Cs, the $D_2$ resonance line from the ground state $6^2S_{1/2}$ ($g_k = 2$) to the excited state $6^2P_{3/2}$ ($g_i = 4$) has been chosen as absorption line ($\lambda_0 = 852.1$ nm and $A_{ik} = 3.3 \times 10^7$ s$^{-1}$).

Figure 6.6 shows on the left a schematic of the TDLAS setup installed at ACCesS and on the right a front view schematic of ACCesS with the TDLAS line of sight. The source of radiation is a laser beam generated by a single mode distributed feedback (DFB) diode laser with a maximum output power around 45 mW at 852 nm. By tuning the operating temperature of the diode and by modulating the current flowing through the diode, the wavelength of the laser is varied between 851 and 853 nm. The laser light is then coupled into an optical fiber. At its end an optical head equipped with a focal lens creates a laser beam of ca. 8 mm of diameter. A neutral density filter (transmission of 0.07 % at 852 nm) is installed in the optical head in order to avoid the depopulation of the ground state due to too intense laser light, which would lead to an underestimation of the Cs density [FW11, Lin17]. After crossing the absorbing medium, the laser light is collected on a photodiode equipped with an interference filter (central wavelength = 852 nm; FWHM = 10 nm) to decouple the signal from the plasma emission. A full description of the setup, including the data acquisition system, can be found in [Lin17] (the applied setup is similar to the one applied at the BATMAN test facility [FW11]). At ACCesS, the Cs density is continuously monitored during vacuum and plasma operation with a time resolution of 5 s.

The line of sight of the TDLAS is parallel to the sample holder, at 2 cm distance, and crosses diagonally the vacuum vessel, as it can be seen on the right of figure 6.6. The resulting length $L$ of the absorbing medium is 16 cm.

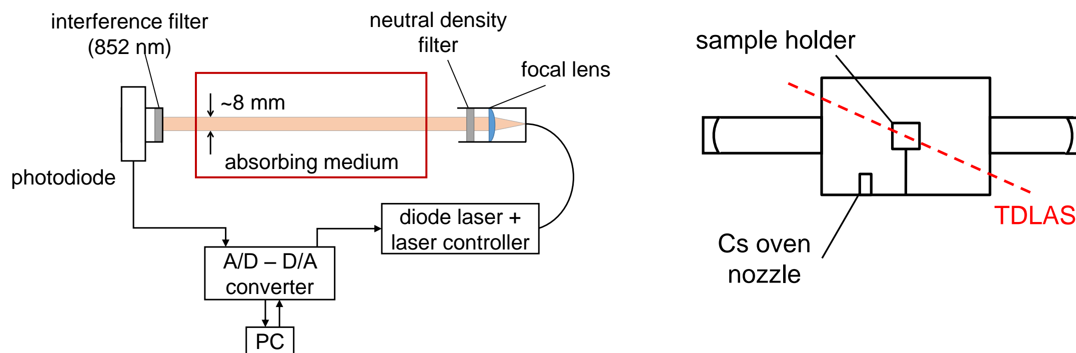


**Figure 6.6:** *On the left: schematic of the tunable diode laser absorption spectroscopy (TDLAS) installed at ACCesS. On the right: front view sketch of ACCesS, with the TDLAS line of sight highlighted.*

Figure 6.7 shows a typical absorption signal (black line): the two Cs absorption peaks are clearly visible (see for a comparison figure 5.1). The increasing baseline $I(\lambda, 0)$ is due to the variation of the diode laser current, which influences not only the wavelength but also the intensity of the laser beam (red line). The initial intensity variation of the laser $I(\lambda, 0)$ is obtained for every single spectrum by a 9th degree polynomial fit of the baseline without considering the two regions where the absorption peaks appear. The detection limit for the Cs density measurement at the current setup is $n_{\mathrm{Cs}} \geq 2 \times 10^{13}$ m$^{-3}$, and the measured Cs density has an error of typically $\pm 10\,\%$ (for densities close to the detection limit the error increases up to $50\,\%$ due to the low signal-to-noise ratio).

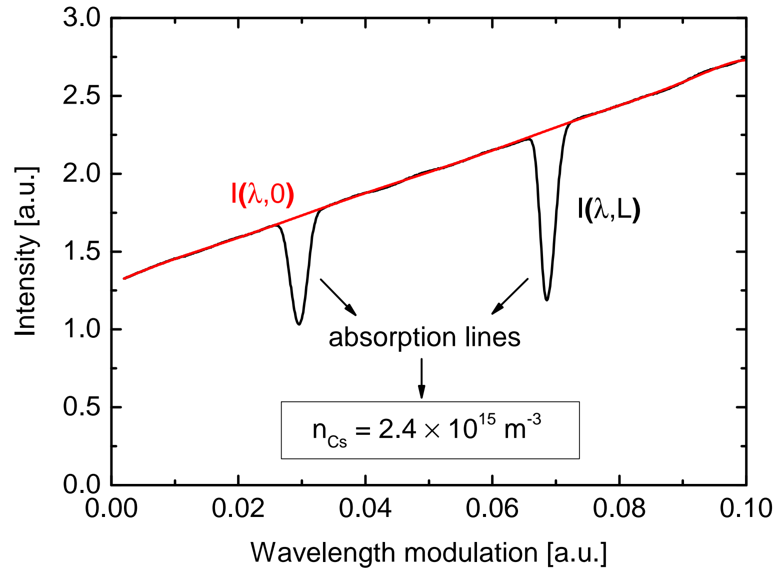


**Figure 6.7:** *Typical TDLAS absorption signal. The baseline used for the evaluation of the Cs density is shown in red, and the resulting measured Cs density is indicated by $n_{Cs}$.*

### 6.4.2 Optical emission spectroscopy (OES) for hydrogen species

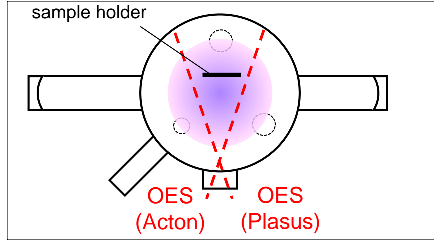


A multitude of parameters can be obtained by means of optical emission spectroscopy (OES) applied at the Fulcher system of the hydrogen molecule and at the Balmer series of the hydrogen atom. By OES it is possible to determine the gas temperature, the vibrational temperature of the $H_2$ molecule, the atomic hydrogen density, the electron density, and the electron temperature, averaged along the line of sight [FFF+06]. The emissivities of the Fulcher system and the Balmer series are measured at the same line of sight and by means of the same high-resolution spectrometer (Acton) applied for the Cs emission.

Additionally, a survey spectrometer (Plasus Emicon MC, with an apparatus profile between 1.5 nm at the wavelength of 400 nm and 1.2 nm at 850 nm) is applied to monitor the stability of the plasma. It records the emission of the Balmer lines, of the Fulcher system and of the Cs $D_2$ line every 500 ms. This spectrometer is only used to monitor the relative behavior of the different emissions, and it is not absolutely calibrated.

#### Spectroscopy at $H_2$ molecule

The emission of part of the Fulcher system $(\mathrm{d}^3\Pi_\mathrm{u}, \nu', N' \rightarrow \mathrm{a}^3\Sigma_\mathrm{g}^+, \nu'', N'')$ diagnostically accessible by OES is used to obtain the gas temperature, the vibrational temperature of the ground state of the hydrogen molecule, and the integrated emission of the entire Fulcher system [Fan04]. The optical transitions which are experimentally accessible are the first 12 rotational Q-lines $(N' = 1, ..., 12 \rightarrow N'' = N')$ of the first four diagonal vibrational bands $(\nu' = 0, ..., 3 \rightarrow \nu'' = \nu')$. The emissivity $\epsilon_{\mathrm{d}\rightarrow\mathrm{a}}^{\nu',\nu'',N',N''}$ of the ro-vibronic transitions is given by [Her50]

$$\epsilon_{\mathrm{d}\rightarrow\mathrm{a}}^{\nu',\nu'',N',N''} \propto n_{\mathrm{d},\nu',N'} S_{N',N''} \quad , \tag{6.6}$$

where $n_{\mathrm{d},\nu',N'}$ is the absolute density in the upper ro-vibronic state and $S_{N',N''}$ is the Hönl-London factor [Kov69].

The rotational levels of the ground state are usually mainly populated due to heavy particle collisions. However, in low temperature low pressure plasmas

other mechanisms can occur, such as electron impact excitation or surface recombination of H atoms to $H_2$, which may lead to deviations from the thermal equilibrium [GD41, LST80, VSE04]. For this reason, the ground state may deviate from a Boltzmann distribution. To determine the gas temperature $T_{\mathrm{gas}}$, a Bi-Maxwellian distribution of the rotational levels of the ground state with two characteristic rotational temperatures is assumed [VSE04], with $T_{\mathrm{gas}}$ corresponding to the rotational temperature of the coldest ensemble [BRF17].

The rotational population in the ground state is correlated to the ones in the electronic excited states according to the Franck-Condon principle for electron impact excitation [Her50], and for Fulcher the relative rotational distribution is the same in the excited levels as in the ground state [BRF17]. The excited states have accordingly a Bi-Maxwellian distribution, with rotational temperatures specific for each vibrational level $\nu$. It is possible to obtain these temperatures from the relative rotational density distribution $n_{\mathrm{d},\nu',N'}/n_{\mathrm{d},\nu',N'=1}$ of the upper Fulcher level for the four considered vibrational levels from the measured emissivities by equation (6.6). A simulation of the ground state population distribution considers the rotational temperatures of the ground state as fitting parameters and projects the ground state into the upper Fulcher level. The gas temperature of the ground state results from a comparison between the simulation and the relative rotational density distribution obtained via the measured emissivities.

The vibrational levels of the ground state are populated due to collisions not only with heavy particles but also with energetic electrons [BW15], leading to deviations from the thermal equilibrium [Mos05]. Thus, the vibrational density distribution is assumed to be a superposition of two Boltzmann distributions, characterized by two different vibrational temperatures [Wün05, RKF15, Kur16]. The vibrational density distribution of the low lying vibrational levels ($\nu \leq 3$) is characterized by the vibrational temperature $T_{\mathrm{vib}}^{\mathrm{low}}$, diagnostically accessible by OES [FH98]. It is possible to obtain this temperature from the relative vibrational density distribution $n_{\mathrm{d},\nu'}/n_{\mathrm{d},\nu'=0}$ of the upper Fulcher level for the first four vibrational levels. The densities $n_{\mathrm{d},\nu'}$ for each vibrational level are derived from equation (3.14) considering the corresponding Einstein coefficients and the measured emissivities of each diagonal vibrational transition, considering a Bi-Maxwellian distribution of the rotational states. A simulation of the population distribution is calculated by using a vibrational temperature in the ground state projected into the upper Fulcher level, depending on the electron temperature,

the Frank-Condon factors, and the vibrationally resolved relative rate coefficient for electron impact collision [FH98, WF16]. Thus, $T_{\mathrm{vib}}^{\mathrm{low}}$ results from a comparison between the simulation and the relative vibrational density distribution obtained with the measured emissivities.

The vibrational density distribution for $\nu > 3$ is characterized by the vibrational temperature $T_{\mathrm{vib}}^{\mathrm{high}}$, which instead is not diagnostically accessible.

The entire Fulcher emission $\epsilon_{\mathrm{Ful}}$ can be finally deduced from the emission of the first four diagonal transitions by

$$\epsilon_{\mathrm{Ful}} = f(T_{\mathrm{vib}}^{\mathrm{low}}, T_{\mathrm{e}}) \sum_{\nu'=0,\ldots,3} \epsilon_{\mathrm{d}\to\mathrm{a}}^{\nu'\to\nu''=\nu'} \quad , \tag{6.7}$$

where $f(T_{\mathrm{vib}}^{\mathrm{low}}, T_{\mathrm{e}})$ is a scaling factor calculated as the ratio of the first four diagonal vibrational bands to the entire Fulcher transition for a spectrum simulated with a vibrationally resolved corona-model [FH98, WF16]. The model considers the population distribution at the ground state and derives the population of the upper Fulcher level by balancing the electron impact excitation from the ground state (considering the Franck-Condon factors, the electron temperature, and the vibrationally resolved relative rate coefficients) as population mechanism and the spontaneous emission as depopulation channel. The highest vibrational temperature $T_{\mathrm{vib}}^{\mathrm{high}}$ has only a slight impact on the scaling factor, hence its influence can be neglected [FH98].

The errors associated with the different evaluated plasma parameters are given in the following table:

| Parameter | Typical error |
|---|---|
| $T_{\mathrm{gas}}$ | $\pm 25$ K |
| $T_{\mathrm{vib}}^{\mathrm{low}}$ | $\pm 500$ K |
| $\epsilon_{\mathrm{Ful}}$ | $\pm 15\,\%$ |

**Spectroscopy at H atom**

The emission of the first four Balmer lines (listed in table 3.1) is used to determine the temperature of the hydrogen atoms, the atomic hydrogen density and line of sight integrated plasma parameters such as the electron density and temperature.

The line profile of the Balmer lines is mainly affected by the Doppler broadening,

introduced already for the case of the Cs atom in section 5.1. From equation (5.1) applied to the hydrogen Balmer lines, the temperature $T_{\mathrm{H}}$ of the hydrogen atoms can be calculated. However, the calculations must take into account the fine splitting of the Balmer lines together with the apparatus profile of the spectrometer applied to detect the light. The temperature is then deduced by a comparison between the measured FWHM and a simulated emission line FWHM with $T_{\mathrm{H}}$ as input parameter.

The emission of the Balmer lines can be used to determine plasma parameters such as the electron temperature and electron density, and the densities of several hydrogen species, in particular the atomic hydrogen density in the ground state, by means of a collisional radiative (CR) model called *YACORA H*. The model is widely described in [WDF09] and [WF16], and a brief description is presented in the following: several excitation and de-excitation channels which populate the different electronic states of the hydrogen atom are considered, like direct electron impact excitation, dissociative excitation (see equation (3.25)), dissociative recombination (see equation (3.26)), or mutual neutralization (see equation (4.8)). The probability for these reactions to occur strongly depends on the electron temperature and the densities of the involved particles (neutral atoms and molecules, positive and negative ions, and electrons). Thus, the absolute Balmer emissions and the ratios between the line emissivities are used to compare simulations and measurements, in order to deduce in particular the electron temperature and the electron density, with the densities of the hydrogen species as free parameters as well. To this purpose, also the measured total Fulcher emission is compared to the simulations obtained by the model *YACORA* $H_2$ [WF16], for determining the electron temperature and density.

Furthermore, the ratio of the $\mathrm{H}_\gamma$ emissivity to the total Fulcher emission is correlated to the ratio of the atomic hydrogen density to the molecular hydrogen density [Fan04], and the model YACORA H can be used for an estimation of the atomic hydrogen density.

For the current investigations, typical errors for the different evaluated plasma parameters are listed in the following table:

| Plasma parameter | Typical error |
|---|---|
| $T_{\mathrm{e}}$ | $\pm\,0.5$ eV |
| $n_{\mathrm{e}}$ | $\pm\,35\,\%$ |
| $n_{\mathrm{H}}$ | $\pm\,35\,\%$ |

YACORA H and $H_2$ are specific models for the hydrogen species. In case of deuterium, the coupling to other species (as molecules) might differ and there is a lack of available data about the corresponding processes in deuterium plasmas. Some cross sections are available in literature for the deuterium case (see section 3.26), while no information about the mutual neutralization is available. As a consequence, the YACORA H and $H_2$ models are not applied for the deuterium case for the current investigations.

### 6.4.3 Langmuir probe

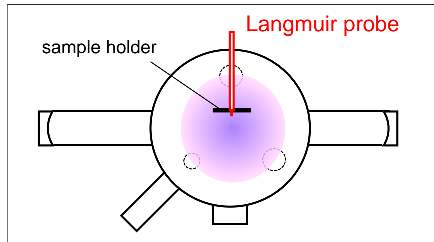


A Langmuir probe is a useful diagnostic system to locally determine plasma parameters such as the electron density, the electron temperature, and the electrostatic potentials. It is an electrostatic probe to which a varying voltage is applied against the grounded walls and the corresponding current flowing through the probe is measured [ML26]. At ACCesS, the Langmuir probe consists of a stainless steel rod inside a quartz tube in order to insulate the probe from the plasma and the walls. At the end of the rod, a narrow nozzle hosts the actual probe tip (a tungsten wire of 100 µm diameter and 1 cm length), which is the only part in contact with the plasma. The narrow nozzle allows inserting the probe in the sample holder hole, in order to measure the plasma parameters close to the surface (the end of the tip is located around 8 mm away from the surface for the current investigations). The Langmuir probe can be easily moved and removed when the experiment needs to be opened, e.g. to exchange the sample.

In the following, a brief description of the evaluation method is given for the different plasma parameters obtained by a probe measurement. More detailed information can be found in [LL05, CB11, Che03].

Figure 6.8 shows a typical current-voltage characteristic ($I$–$V$ curve) for a plasma where electrons are the dominant negatively charged species and negative ions can be neglected. The measured current is the sum of the electron current (by definition a positive current) and the positive ion current (by definition a negative current).

When a high negative voltage is applied to the probe, electrons are repelled from the tip and positive ions are attracted and collected on the probe. The measured current is thus dominated by positive ions, resulting in a negative probe

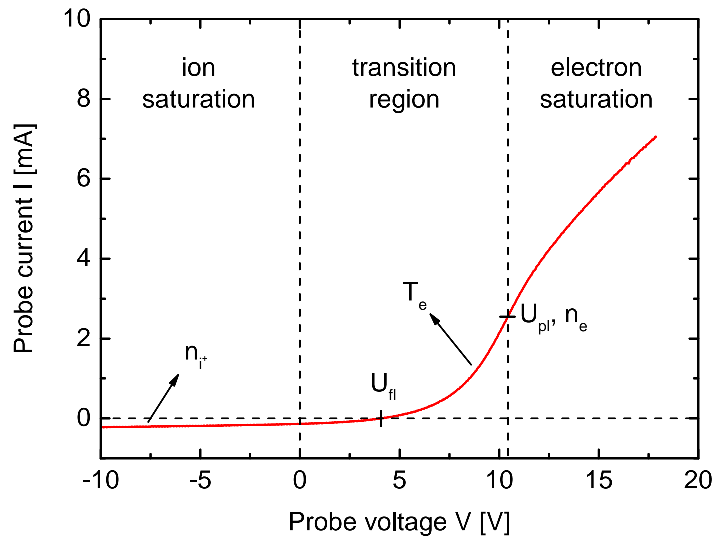


**Figure 6.8:** *Typical current signal by varying the voltage of a cylindrical Langmuir probe. The plasma parameters that can be determined in the different current regimes are indicated.*

current. This region is called *ion saturation* region.

By increasing the probe voltage electrons start to be collected on the tip, and the probe current consists of both positive ion current and electron current. In case of a Maxwellian velocity distribution of the electrons, the electron current increases exponentially. This region is called *transition region*. When the electron and positive ion currents balance each other, the total probe current is zero and the floating potential $U_{\mathrm{fl}}$ is reached (i.e. electron and positive ion fluxes towards the probe are equal).

For applied voltages higher than the plasma potential only electrons reach the probe, and this region is called *electron saturation* region. Here the resulting net current is much higher with respect to the ion saturation region due to the fact that electrons have a lighter mass and a higher temperature (the electron and positive ion densities are instead equal due to quasi-neutrality). As it can be seen in figure 6.8, the current does not reach a real saturation, but it increases with increasing applied voltage due to the cylindrical geometry of the probe [ML26, CB11].

The plasma potential $U_{\mathrm{pl}}$ corresponds to the voltage applied when the slope of the $I$–$V$ curve reaches its maximum. Thus, the root of the second derivative of the probe current determines the plasma potential, as also shown in figure 6.9 on

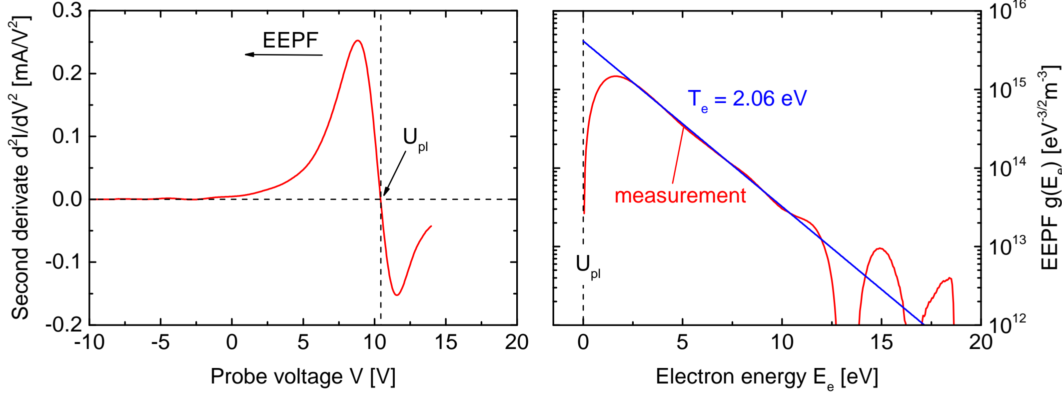


**Figure 6.9:** *On the left: second derivative of the probe current used to determine the plasma potential and the region considered for evaluating the EEPF. On the right: the EEPF plotted against the electron energy measured with the Langmuir probe and the linear fit to determine the electron temperature $T_e$.*

the left:

$$V = U_{\mathrm{pl}} \quad \leftrightarrow \quad \left.\frac{\mathrm{d}^2 I}{\mathrm{d}V^2}\right|_{U_{\mathrm{pl}}} = 0 \quad . \tag{6.8}$$

The electron energy distribution function (EEDF) can be derived from the second derivative of the probe current, after having subtracted the positive ion current. Considering the electron energy $E_{\mathrm{e}} = e(U_{\mathrm{pl}} - V)$ in [eV] for applied voltages $V \leq U_{\mathrm{pl}}$, the EEDF $f(E_{\mathrm{e}})$ in $[\mathrm{eV}^{-1}\mathrm{m}^{-3}]$ is given by [Dru30]

$$f(E_{\mathrm{e}}) = \frac{\sqrt{8 m_{\mathrm{e}} E_{\mathrm{e}}}}{e^{3/2} A} \, \frac{\mathrm{d}^2 I}{\mathrm{d}V^2} \quad . \tag{6.9}$$

The corresponding electron energy probability function (EEPF) $g(E_{\mathrm{e}})$ is plotted on a logarithmic scale in figure 6.9 on the right and is given by

$$g(E_{\mathrm{e}}) = \frac{\sqrt{8 m_{\mathrm{e}}}}{e^{3/2} A} \, \frac{\mathrm{d}^2 I}{\mathrm{d}V^2} \quad . \tag{6.10}$$

For a Maxwellian distribution the logarithm of the EEPF is directly proportional to the inverse of the electron temperature (see section 3.2), hence the electron temperature $T_{\mathrm{e}}$ can be obtained from a linear fit of the logarithm of $g_{\mathrm{M}}(E_{\mathrm{e}})$:

$$k_{\mathrm{B}} T_{\mathrm{e}} = -\left(\frac{\mathrm{d}}{\mathrm{d}E_{\mathrm{e}}} \ln g_{\mathrm{M}}(E_{\mathrm{e}})\right)^{-1} \quad . \tag{6.11}$$

This evaluation is valid only for a certain range of electron energies, as it can be seen on the right of figure 6.9: only the low energy region of the EEPF is accessible

with the Langmuir probe, since for energies higher than 10 eV a low signal-to-noise ratio occurs (due to the low electron currents for $V \leq U_{\mathrm{fl}}$). However, for energies lower than 2.5 eV the measured EEPF is no more reliable, due to a variety of factors such as inappropriate probe dimensions, RF noise or possible contaminations of the probe [GMS95]. Moreover, deviations from a linear regression can be due to a non-Maxwellian distribution, e.g. in case of a Bi-Maxwellian distribution. In this case, a Bi-Maxwellian fit of the measured EEPF would be appropriate.

In case of a Maxwellian EEDF, the electron current $I_{\mathrm{e}}$ in the transition region ($V \leq U_{\mathrm{pl}}$) is given by

$$I_{\mathrm{e}}(V) = \frac{1}{4}\, e\, n_{\mathrm{e}}\, \langle v_{\mathrm{e}} \rangle\, A\, \mathrm{e}^{\frac{e(V-U_{\mathrm{pl}})}{k_{\mathrm{B}} T_{\mathrm{e}}}} \quad , \tag{6.12}$$

with $\langle v_{\mathrm{e}} \rangle$ the mean thermal velocity of the electrons $\left( \langle v_{\mathrm{e}} \rangle = \sqrt{\frac{8 k_{\mathrm{B}} T_{\mathrm{e}}}{\pi m_{\mathrm{e}}}} \right)$ and $A$ the surface area of the probe tip. Hence, when the electron temperature is known, the electron density $n_{\mathrm{e}}$ can be deduced from equation (6.12) from the current $I(U_{\mathrm{pl}})$ at the plasma potential.

Since quasi-neutrality has to be fulfilled, the positive ion density is equal to the electron density ($n_{\mathrm{ion}} = n_{\mathrm{e}}$). It is also possible to deduce the ion density from the $I$–$V$ curve in the ion saturation region, however different theories exist in the literature in order to correctly calculate the ion density [Che03], and the evaluation strongly depends on the ion mass. In the current work, the positive ion density is directly considered for convenience as equal to the electron density (if the negative ion density is not negligible, the positive ion density is given by the sum of the electron density and the negative ion density).

The additional presence of negative ions can have a significant impact on the $I$–$V$ curve, depending on the density ratio of negative ions to electrons $n_{\mathrm{H^-}}/n_{\mathrm{e}}$ and the corresponding temperatures $T_{\mathrm{H^-}}$ and $T_{\mathrm{e}}$. When the applied voltage is equal to the plasma potential, the resulting net current is given both by electrons and by negative ions:

$$I_{\mathrm{e}}(U_{\mathrm{pl}}) = I_{\mathrm{e}} + I_{\mathrm{H^-}} \propto n_{\mathrm{e}} \sqrt{\frac{k_{\mathrm{B}} T_{\mathrm{e}}}{m_{\mathrm{e}}}} + n_{\mathrm{H^-}} \sqrt{\frac{k_{\mathrm{B}} T_{\mathrm{H^-}}}{m_{\mathrm{H^-}}}} \quad . \tag{6.13}$$

Due to the high mass difference between negative hydrogen ions and electrons, the influence of negative ions on the evaluation procedure becomes significant only when the negative ions are by far the dominant negatively charged particles,

hence for density ratios $n_{\mathrm{H}^-}/n_{\mathrm{e}} \gg 10$. This is not the case at ACCesS, however in negative ion sources a positive ion/negative ion plasma [WPL73] might occur in the region close to the caesiated plasma grid, and the $I$–$V$ curve becomes symmetric [MS10, TNK+12].

The control unit and data acquisition system of the Langmuir probe applied at ACCesS is described in details in [MDC+09]. The errors associated with the evaluated quantities depend mainly on the RF noise since the probe is not compensated at ACCesS: the RF in fact affects the plasma potential, which oscillates of ±1.5 V with the RF frequency, and the frequency of the data acquisition system is slower than the RF frequency (each $I$–$V$ curve is taken in circa ten seconds). As a consequence, the $I$–$V$ curve is smoothed as described in [LL05, CB11, Che03]. The statistical errors on $T_{\mathrm{e}}$ and $n_{\mathrm{e}}$ obtained by the Langmuir probe are summarized in the table below, together with the error on the measured potentials:

| Plasma parameter | Typical error |
|---|---|
| $U_{\mathrm{fl}}$, $U_{\mathrm{pl}}$ | ± 1.5 V |
| $T_{\mathrm{e}}$ | ± 0.2 eV |
| $n_{\mathrm{e}} = n_{\mathrm{i}}$ | ± 20 % |

### 6.4.4 Residual gas analyzer (RGA)

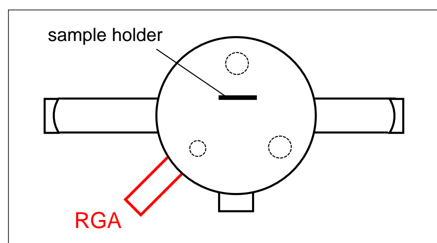


To monitor the impurities and the behavior of the background gases during vacuum and plasma operation, a residual gas analyzer (RGA) is applied. An aperture of 300 µm diameter is located between the RGA (Pfeiffer Vacuum PrismaPlus QMG 220) and the vacuum vessel, and the RGA is differentially pumped via a turbomolecular and a rotary vane pump. It detects masses from 1 to 200 amu with a secondary electron multiplier for high sensitivity measurements.

The RGA is heated up to 80 °C in order to prevent the accumulation of Cs in the system and at the aperture. However, the RGA cannot be used to detect caesium, since Cs quickly sticks to the walls due to its high reactivity and the probability that it passes through the aperture is thus negligible.

The residual gas analyzer is not absolutely calibrated, but it is applied to monitor the relative behavior of the background gases.

# 7 Determination of work function and $H^-$ density & experimental procedure

In the following, the two main diagnostic systems applied in the current work are described: the setup for the work function measurements and the cavity ring-down spectroscopy for the $H^-$ detection. The typical plasma scenarios for the different investigations carried out in the present work are explained in section 7.3.

## 7.1 Work function diagnostic

### 7.1.1 Fowler method

The work function $\chi$ of a surface is diagnostically accessible by using a non-invasive method which relies on the photo-emission of electrons from the solid when it is irradiated with light with photon energy $h\nu > \chi$ ($\nu$ is the photons' electromagnetic frequency). The photoelectrons released by the surface have thus a maximal kinetic energy $E_{\mathrm{kin,e}}^{\mathrm{max}} = h\nu - \chi$. After the so-called *Fowler method* [Fow31], an increasing photon energy does not only increase the maximal kinetic energy of the released electrons, but it also increases the number of the emitted photoelectrons by considering the electron energy distribution within the solid.

The Fowler method is described in detail in [Fow31, Fri13, Fri16], and in the following a brief description of the working principle is given. Figure 7.1 shows a schematic of the photoemission of an electron from the valence band of a solid state. The electrons in the valence band follow the Fermi-Dirac distribution, hence the probability $N_i$ of an electron to occupy the energy state $i$ with energy $E_i$ is

$$N_i = \frac{1}{1 + \exp\left(\frac{E_i - \mu}{k_{\mathrm{B}} T}\right)} \quad , \tag{7.1}$$

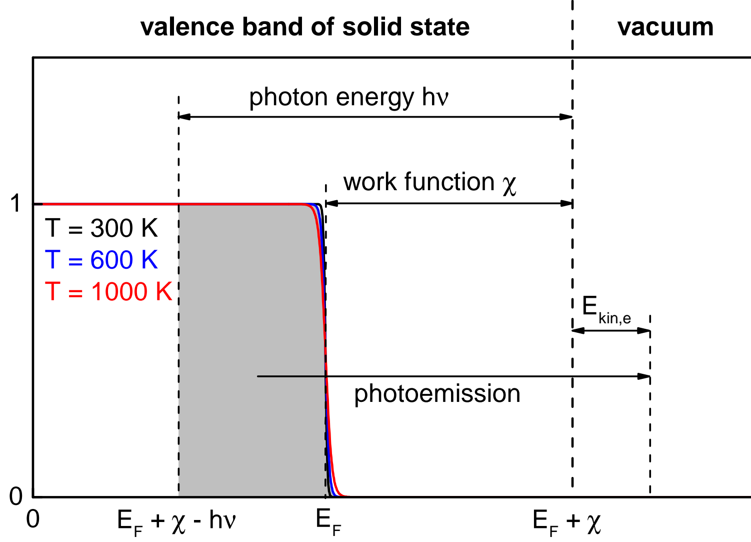


**Figure 7.1:** *Schematic of the photoemission of electrons within the solid state characterized by the Fermi energy $E_F$ and the work function $\chi$ at different temperatures due to absorption of a photon of energy $h\nu$.*

where $\mu$ is the chemical potential and $T$ is the temperature of the solid. Temperatures of metals are usually far below the Fermi temperature, which is of the order of $10^4$–$10^5$ K. In this case, the chemical potential can be approximated by the Fermi energy $E_\mathrm{F}$, which is usually in the range between 2 and 10 eV. In figure 7.1, the Fermi-Dirac distributions for three different temperatures are shown. When light with photon energy $h\nu$ irradiates the surface, electrons with energies $E_\mathrm{e}$ higher than $E_\mathrm{F} + \chi - h\nu$ (the gray shaded area in the figure) can leave the valence band and be transferred to the vacuum by absorbing the photon energy. The exceeding energy is converted into the kinetic energy $E_\mathrm{kin,e}$.

By biasing the surface against the walls the electrons released beyond the vacuum level can be collected, and the corresponding photocurrent $I_\mathrm{ph}(h\nu)$ can be measured for different photon energies. After [Fow31], the photocurrent depends on the sample surface temperature $T_\mathrm{spl}$, the work function $\chi$, and the photon energy $h\nu$, assuming that the photon energies are greater than but close to the work function ($h\nu \gtrapprox \chi$):

$$\frac{I_\mathrm{ph}(h\nu)}{F(h\nu)} = A\,T_\mathrm{spl}^2\, f\left(\frac{h\nu - \chi}{k_\mathrm{B} T_\mathrm{spl}}\right) \quad , \tag{7.2}$$

where $F(h\nu)$ is a correction factor accounting for the relative intensity of the

applied light source at the frequency $h\nu$, $A$ is a constant, and $f(\kappa)$ with $\kappa = \frac{h\nu-\chi}{k_B T_{\rm spl}}$ is the following function valid for $h\nu \gtrapprox \chi$ [Fow31]:

$$f(\kappa) = \frac{\pi^2}{6} + \frac{1}{2}\kappa^2 - \left[ e^{-\kappa} - \frac{e^{-2\kappa}}{2^2} + \frac{e^{-3\kappa}}{3^2} - ... \right] \quad . \tag{7.3}$$

The work function is experimentally obtained by dividing the measured photocurrents by the correction factor $F(h\nu)$ and $T_{\rm spl}^2$, and plotting its logarithm against $h\nu/k_B T_{\rm spl}$ producing the so-called *Fowler plot*. The Fowler plot can be then fitted with the following function:

$$\ln\left[\frac{I_{\rm ph}(h\nu)/F(h\nu)}{T_{\rm spl}^2}\right] = B + \ln\left[f\left(\frac{h\nu}{k_B T_{\rm spl}} - \frac{\chi}{k_B T_{\rm spl}}\right)\right] \quad , \tag{7.4}$$

where the fitting parameters are the constant $B$ and the work function $\chi$.

Figure 7.2 shows a simulation of the photocurrent plotted as function of $h\nu - \chi$ via equation (7.2) for a trivial case ($F = A = 1$) and for a sample temperature $T_{\rm spl} = 300$ K. The axes at the right and at the top of the figure correspond to the Fowler plot from equation (7.4). As it can be clearly seen from the plot, the photocurrent strongly increases with increasing photon energy $h\nu$ or decreasing work function $\chi$, and it approaches asymptotically zero at the threshold $h\nu = \chi$.

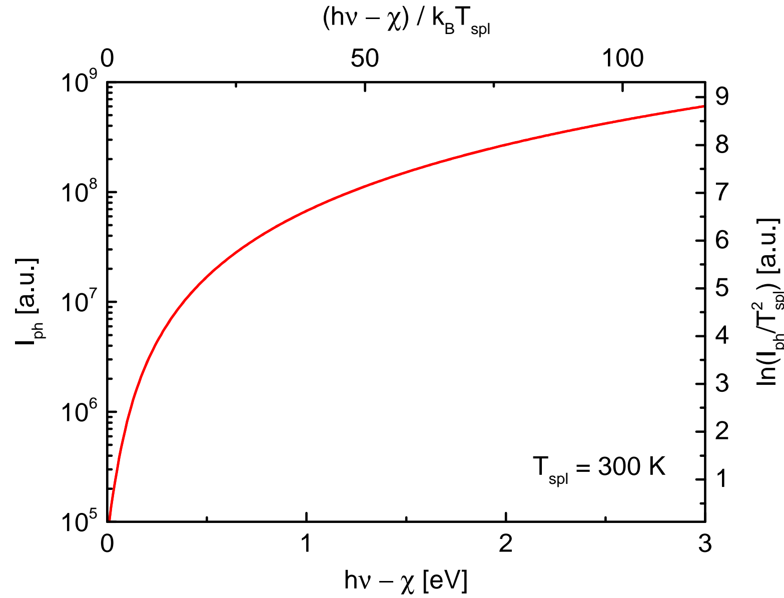


**Figure 7.2:** *Photocurrent as function of the difference between the photon energy and the work function after equation (7.2) with F=A=1 and a surface temperature of 300 K. The right and top axes refer to the corresponding Fowler plot.*

As already mentioned, the Fowler method can be applied only if $h\nu \gtrapprox \chi$. If this condition is not fulfilled, some corrections must be applied in order to obtain the actual work function, following the method described in [Fri13, Fri16]. Alternatively, the photon energies need to be adapted to fulfill the required condition.

### 7.1.2 Setup for work function measurements at ACCesS

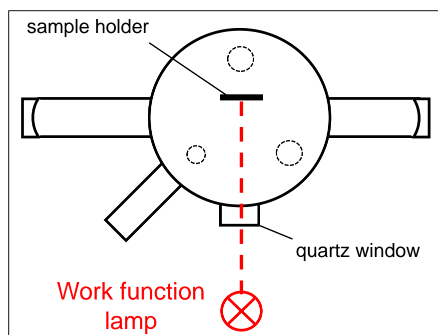


By applying interference filters in front of a broadband light source it is possible to select the photon energy impinging on the surface of unknown work function, and by measuring the corresponding photocurrents the work function is deduced via the Fowler plot. The setup installed at ACCesS is shown in detail in figure 7.3: a high pressure mercury lamp (100 W) is applied as a broadband light source since it has a high emission from UV throughout the visible range. The light passes through an interference filter and is focused on the sample holder by means of two focal quartz lenses. The resulting light spot on the sample holder is determined by the position of the second lens: the position is adjusted in order to obtain the maximal photocurrent (compromise between the power density on the sample and

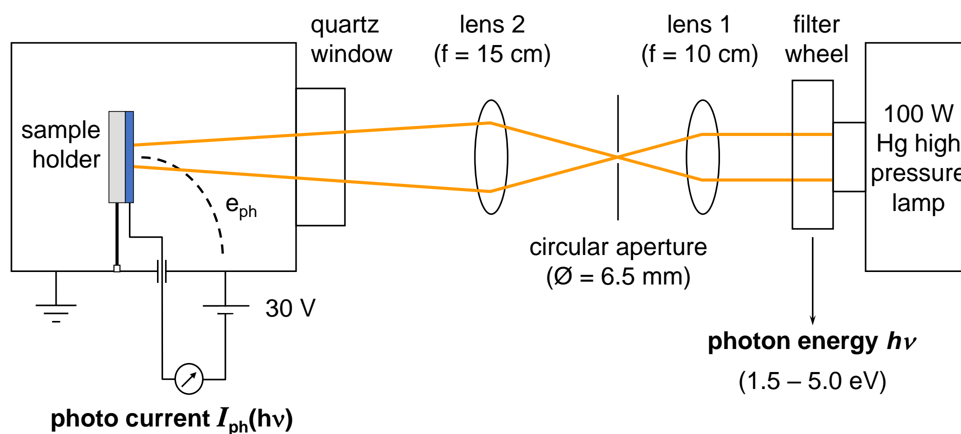


**Figure 7.3:** *Side view schematic of the setup for the work function measurements applied at ACCesS after the Fowler method.*

the absolute absorbed power), resulting in a spot diameter of about 1.5 cm. To avoid additional halos around the spot, an aperture is applied in between the two lenses, with a diameter of 6.5 mm. The photoemitted electrons are collected at the vessel walls by applying a negative bias voltage of −30 V to the sample against the grounded walls. The photocurrents are measured by a Keithley 602 Electrometer, capable of measuring currents down to the pA range. The bias and thus the measurement of the photocurrents cannot be applied during plasma operation since the plasma would lead to extremely high currents and the contribution of the photocurrents to the total current would be hardly detectable.

A filter wheel hosting 6 filters is directly mounted at the Hg lamp, in order to change the interference filter (i.e. the photon energy). The filters available for the current investigations are listed in table 7.1.

To characterize every single filter, the work function setup (including quartz lenses, the aperture, and the quartz window) was separated from the vessel,

**Table 7.1:** *Interference filters available for the current investigations, with the corresponding wavelength and energy range and the mean photon energy used for the evaluation of the work function in the Fowler plots.*

| Filter label | Wavelength range [nm] | Energy range [eV] | Mean photon energy [eV] |
|---|---|---|---|
| 239 nm | 236 – 253 | 4.9 – 5.3 | 5.04 |
| 254 nm | 244 – 253 | 4.9 – 5.1 | 4.96 |
| 280 nm | 274 – 305 | 4.1 – 4.5 | 4.31 |
| 289 nm | 280 – 316 | 3.9 – 4.4 | 4.19 |
| 300 nm | 288 – 322 | 3.9 – 4.3 | 4.06 |
| 313 nm | 296 – 336 | 3.7 – 4.2 | 3.94 |
| 334 nm | 330 – 344 | 3.6 – 3.8 | 3.69 |
| 365 nm | 359 – 374 | 3.3 – 3.5 | 3.39 |
| 405 nm | 399 – 414 | 3.0 – 3.1 | 3.06 |
| 430 nm | 421 – 442 | 2.8 – 2.9 | 2.87 |
| 480 nm | 470 – 493 | 2.5 – 2.6 | 2.58 |
| 505 nm | 495 – 517 | 2.4 – 2.5 | 2.45 |
| 589 nm | 576 – 602 | 2.1 – 2.2 | 2.1 |
| 610 nm | 600 – 622 | 2.0 – 2.1 | 2.02 |
| 656 nm | 647 – 671 | 1.8 – 1.9 | 1.88 |
| 671 nm | 660 – 685 | 1.8 – 1.9 | 1.85 |
| 694 nm | 678 – 716 | 1.7 – 1.8 | 1.78 |
| 730 nm | 715 – 752 | 1.6 – 1.7 | 1.69 |
| 852 nm | 836 – 874 | 1.4 – 1.5 | 1.45 |

and a lens tube connected to an absolutely calibrated spectrometer was placed at the position where the sample surface would have been. The transmission spectrum from each filter was measured and the corresponding wavelength ranges are summarized in table 7.1 (with a cutoff at 1 %). Converting the x-axis of the different spectra from the wavelength to the corresponding photon energy $E_{\mathrm{ph}}$, the resulting spectra $S(E_{\mathrm{ph}})$ give information on the energy ranges and on the mean photon energies $\langle E_{\mathrm{ph}} \rangle$ for each filter by the following equation:

$$\langle E_{\mathrm{ph}} \rangle = \frac{\int E_{\mathrm{ph}}\, S(E_{\mathrm{ph}})\, \mathrm{d}E_{\mathrm{ph}}}{\int S(E_{\mathrm{ph}})\, \mathrm{d}E_{\mathrm{ph}}} \quad . \tag{7.5}$$

The resulting ranges and mean photon energies are listed in table 7.1 as well.

To determine $F(h\nu)$ of equation (7.2) for each interference filter, the lens tube was replaced by a radiant power meter (ThermoOriel, Model 70260) in order to measure the irradiated power. By dividing the power by the mean photon energy, the absolute number of photons per second $\#ph(h\nu)$ reaching the sample surface is determined for each interference filter. The correction factor $F(h\nu)$ is then defined by the ratio of $\#ph(h\nu)$ to the number of photons per second for the "280 nm" filter $\left(F(h\nu) = \frac{\#ph(h\nu)}{\#ph("280nm")}\right)$, and it is shown in figure 7.4 for each filter.

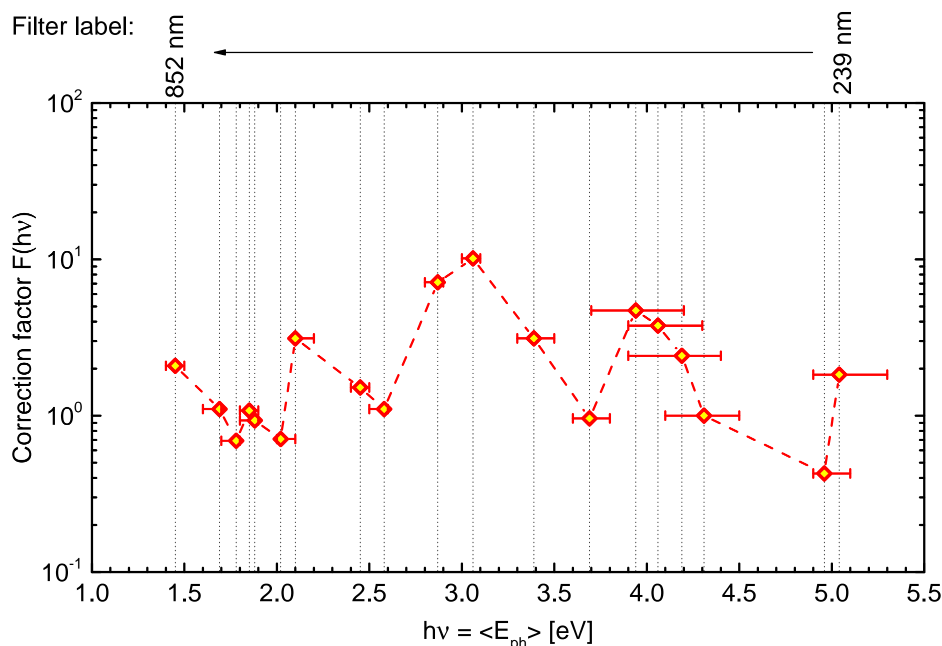


**Figure 7.4:** *Correction factor $F(h\nu)$ plotted against the corresponding mean photon energy for each interference filter. The x-errors correspond to the energy range of the transmitted spectra.*

The photocurrents of at least 5 filters are measured for a single work function evaluation, and the time needed to record them is usually of about 2 minutes. In order to fulfill the validity condition of the Fowler method ($h\nu \gtrsim \chi$), the interference filters are exchanged appropriately depending on the work function. Typical error for the work function evaluation is ±0.1 eV from the fitting routine. Moreover, an overestimation of 0.1 eV of the work function occurs due to the application of the Fowler method [Fri13, Fri16].

### 7.1.3 Benchmark and typical procedure for the work function measurements

A sample of europium, with a nominal work function of 2.5 eV [Mic77], was applied in order to benchmark the work function measurement. In figure 7.5, the work function evaluated via the Fowler method is shown for increasing sample temperature. At the beginning of the campaign, a high work function (above 4.5 eV) is observed, it means only two photocurrents were measured corresponding to the filters "239 nm" and "254 nm". Such a high work function is due to the

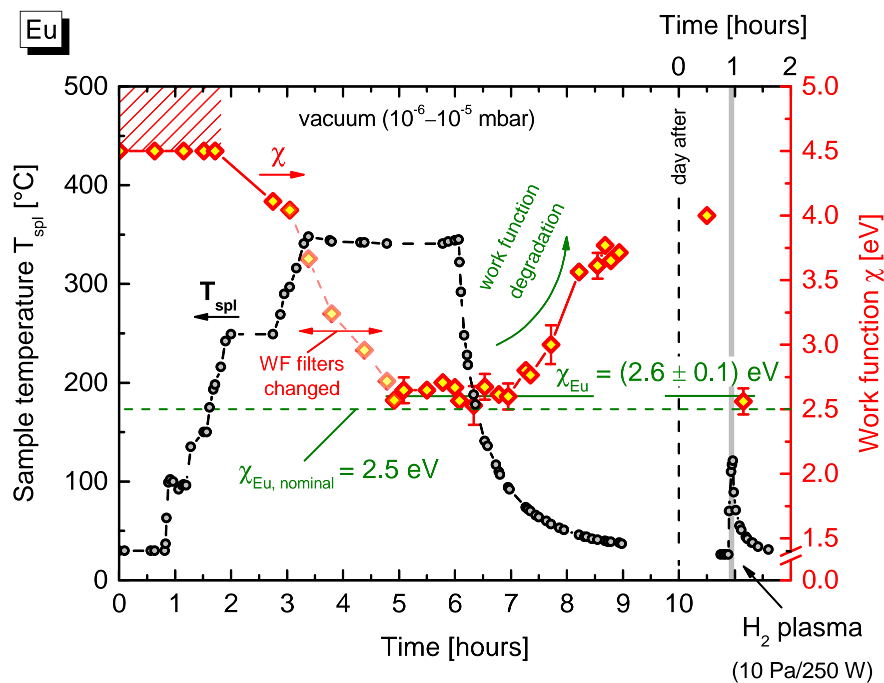


**Figure 7.5:** *Work function of the europium sample during an experimental campaign where the sample temperature increases in vacuum and after a plasma exposure of 5 minutes. The minimal measured work function of (2.6±0.1) eV is in good agreement with the expected value of 2.5 eV [Mic77].*

presence of impurities on the surface coming from air exposure preceding the installation of the sample in ACCesS. These impurities can be removed by heating the sample (the maximum temperature that can be reached at the current setup is 450 °C) or by exposure to hydrogen plasma.

During the subsequent heating procedure small peaks in the RGA signals for $H_2O$, $CO_2$, and $N_2$ are observed, and the work function starts to decrease for temperatures above 250 °C. In this phase the interference filters have to be changed, as also indicated in the figure, in order to assure the conditions of validity of the Fowler method (photon energy close to the work function) and to correctly evaluate the work function. Figure 7.6 shows two Fowler plots obtained with two different sets of filters and acquired in sequence: the photocurrent measurements with higher energy filters overestimate the work function as described by [Fri13, Fri16]. In the current work, the validity of the work function evaluation ($h\nu \gtrapprox \chi$) has always been checked by using appropriate interference filters, i.e. during a typical campaign the filters are changed until the photocurrent is no more measurable in order to identify the correct set of filters to be used. Once the correct set of filters is chosen, the work function measurement is performed.

In figure 7.5, for a temperature of 350 °C the measured work function of the Eu

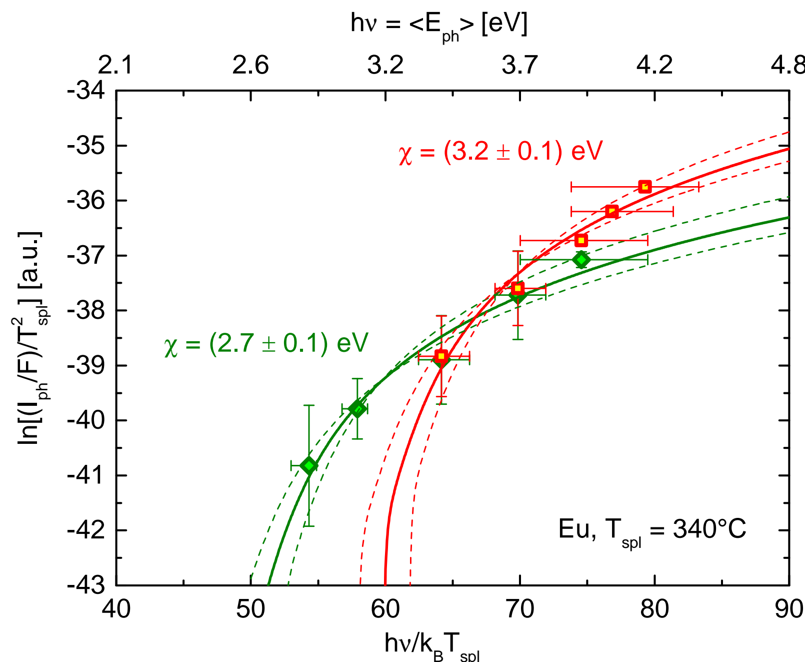


**Figure 7.6:** *Two Fowler plots before (in red) and after (in green) the filter change in the example given in figure 7.5.*

sample decreases down to the stable value of $(2.6 \pm 0.1)$ eV, while the nominal value for Eu is of 2.5 eV [Mic77]. This constitutes the benchmark of the work function diagnostic at ACCesS and shows that the Eu sample can be activated at a temperature of 350 °C.

In the following, the typical procedure to investigate a low work function material is described. This procedure has been followed for all the materials tested in chapter 8. When a new sample is installed in the setup, its measured work function is typically high (usually above 4.5 eV) due to the impurities from air exposure. To remove such impurities, the sample can be heated or exposed to a plasma. However, during the plasma exposure the temperature of the sample increases with the time due to the particles' fluxes onto the surface. For a pulse of 5 minutes, the temperature increases up to $\sim$ 120 °C, while for long pulses it can reach stable values around 200–250 °C (depending on the size of the sample, which has a slight influence on the plasma parameters) after half an hour in the plasma. In order to decouple the temperature effect from the plasma effect, the sample is first heated in vacuum in order to observe only the temperature effect.

As shown exemplary for europium in figure 7.5, during the *temperature campaign* in vacuum the surface is cleaned from the impurities, and the work function decreases. However, when the heating system is turned off and the sample is let to cool down, an increase of the work function occurs. This *degradation* of the work function can be explained by the presence of residual gases (mainly water vapor) at the background pressure of $10^{-6}$–$10^{-5}$ mbar: with time, more and more impurities adsorb on the surface, leading to the formation of oxides and hydroxides. As a consequence, the work function measured the day after is again back to high values (around 4 eV).

In order to observe the effect of a plasma treatment on the surface, a 5 minutes hydrogen plasma is applied at 10 Pa and 250 W of RF power. The maximal temperature reached by the sample during the 5 min plasma is around 125 °C. The work function is usually measured within 3–4 minutes after the plasma pulse. The plasma is able to clean the surface from impurities, and the resulting work function reaches again the value of 2.6 eV.

Details about the particular campaign performed with the Eu sample will be given in section 8.4, however the described procedure (temperature campaign + plasma campaign) represents the standard approach to study the different materials at ACCesS experiment.

## 7.2 $H^-$ density diagnostic

### 7.2.1 Cavity ring-down spectroscopy (CRDS)

For absolute measurements of the $H^-$ density during plasma operation, cavity ring-down spectroscopy (CRDS) is applied. CRDS is a particular type of absorption spectroscopy, where radiation of wavelength $\lambda$ crosses the absorption medium not only once (like for the case of TDLAS) but several thousands of times by using two high-reflectivity mirrors [OD88]. This technique is applied when the density of the absorbing particles is low or when the absorption transition has a low probability to occur. In the case of negative hydrogen ions, the absorption of light leads to photodetachment via the following process:

$$H^- + h\nu \rightarrow H + e \quad . \tag{7.6}$$

This process can occur if the energy of the incident photon is higher than the binding energy of the $H^-$ additional electron (0.75 eV), hence the wavelength of the incident light must be lower than 1653 nm. The cross section $\sigma_{PD}(\lambda)$ for the $H^-$ photodetachment is shown in figure 7.7 from [BRR+77], and it is quite broad over several 100 nm. The CRDS measurements are performed by using a short pulse

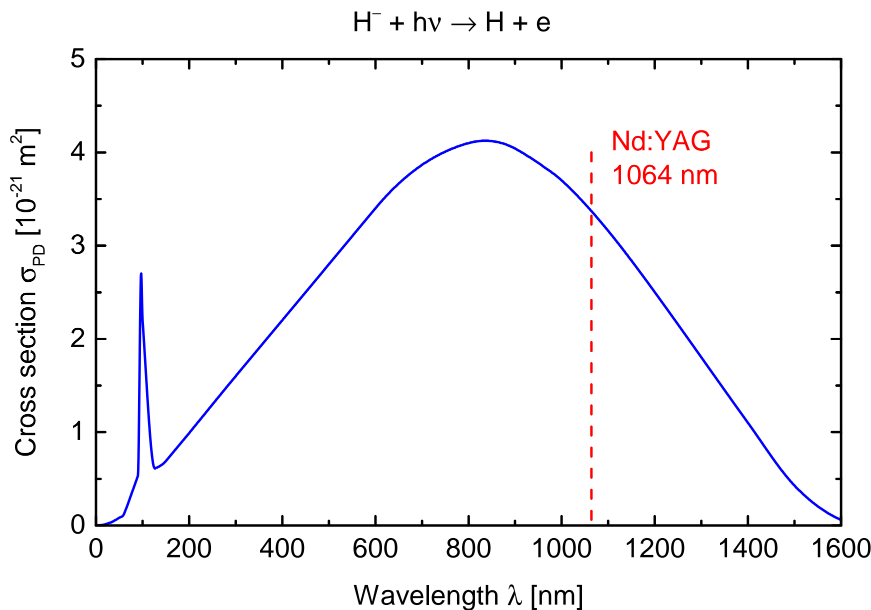


**Figure 7.7:** *Cross section of the $H^-$ photodetachment [BRR+77], with the wavelength chosen for the CRDS at ion sources and ACCesS.*

laser with a narrow wavelength range ($\Delta\lambda \ll 1$ nm), hence a constant cross section can be assumed, and the $H^-$ density $n_{H^-}$ integrated over the absorption length can be measured. A Nd:YAG laser emitting at the wavelength of 1064 nm is used as laser source, resulting in a photodetachment cross section of $3.5 \times 10^{-21}$ m$^2$.

For CRDS, a laser pulse of intensity $I(\lambda, 0)$ at the wavelength $\lambda$ is driven through an optical cavity, consisting of two identical high-reflectivity mirrors (typical reflectivity $R > 99.99\,\%$) distant $d$ from each other as shown in the schematic in figure 7.8. The optical cavity must fulfill the following condition to be stable [HW97]:

$$0 < \left(1 - \frac{d}{r}\right)^2 < 1 \quad , \tag{7.7}$$

where $r$ is the radius of curvature of the two concave mirrors which constitute the optical cavity.

Once in the cavity, the laser light is reflected back and forth between the two mirrors. The temporal length $t_{\text{pulse}}$ of the laser pulse must be shorter than $2d/c$ in order to assure that each laser pulse does not interfere with itself inside the cavity ($t_{\text{pulse}}$ is typically of the order of ns). After each round trip, the transmitted light through the second mirror is detected by a photodiode. The measured intensity of the laser $I(\lambda, t)$ after the cavity decreases exponentially with the time $t$:

$$I(\lambda, t) = I(\lambda, 0) \exp\left(-\frac{t}{\tau(\lambda)}\right) \quad , \tag{7.8}$$

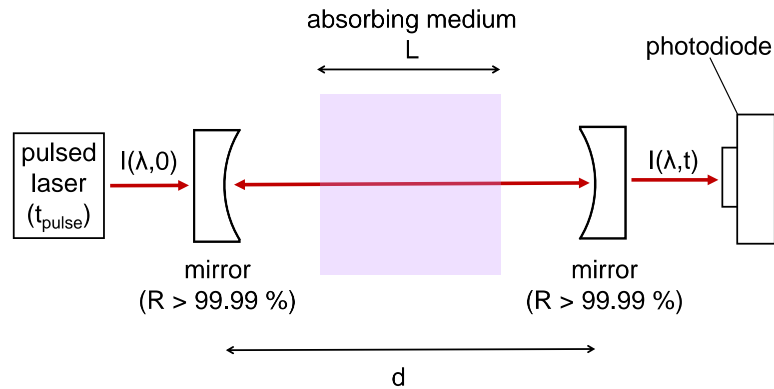


**Figure 7.8:** *Schematic of the cavity ring-down spectroscopy (CRDS) setup.*

with $\tau(\lambda)$ the exponential decay time equal to [RL93]

$$\tau(\lambda) = \frac{d}{c\,[1 - R(\lambda) + k(\lambda)\,L]} \quad , \tag{7.9}$$

where $k(\lambda)$ is the absorption coefficient corresponding to $k(\lambda) = n_{\mathrm{H}^-}\sigma_{\mathrm{PD}}(\lambda)$ and L is the length of the absorption medium.

At $\lambda = 1064$ nm, the absolute $\mathrm{H}^-$ density is finally obtained by a comparison of the decay time $\tau_0$ measured without the absorption medium ($k = 0$) and the decay time $\tau'$ measured with the absorption medium ($k \neq 0$), resulting in

$$n_{\mathrm{H}^-} = \frac{d}{c\,L\,\sigma_{\mathrm{PD}}}\left(\frac{1}{\tau'} - \frac{1}{\tau_0}\right) \quad . \tag{7.10}$$

### 7.2.2 CRDS setup at ACCesS

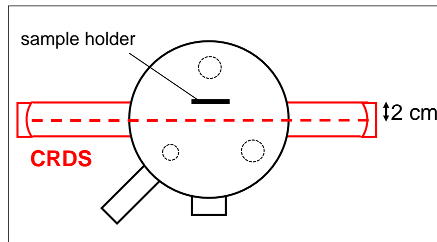


A top view schematic of the CRDS setup installed at ACCesS is shown in figure 7.9. A Nd:YAG laser (Continuum Minilite I) emitting at the wavelength of 1064 nm is used as laser source, with a beam diameter at the exit of the laser of 3 mm and a beam divergence lower than 3 mrad. The pulse length is 7 ns, with a maximal pulse energy of 43 mJ. In the current work, a pulse energy below 10 mJ is applied in order to not deplete the population of the negative hydrogen ions. The repetition rate applied in the current work is 3 Hz. An optical isolator is placed in front of the laser in order to avoid back reflections into the laser. The laser beam is guided into the optical cavity by means of three adjustment mirrors. The line of sight of the CRDS is parallel to the sample holder at 2 cm distance and at half height of the vessel. The two high-reflectivity mirrors (CVI Melles Griot, $r = 1$ m, $R = 99.999\,\%$ at 1064 nm), each installed in a mirror holder, are located at a distance $d = 1.2$ m from each other, fulfilling the stability requirement (7.7). The mirrors can be finely adjusted for a proper alignment by means of three micrometer screws on each mirror holder. The length of the absorbing medium, i.e. the plasma, is assumed to correspond to the vessel diameter, hence $L = 0.15$ m. Additionally, two circular apertures of 8 mm inner diameter are installed between the plasma and the mirrors, as close as possible to the plasma vessel (few cm), in order to protect the mirrors from the degrading effect caused by the plasma [Rau14, RKF15]. During plasma operation, in fact, the reflectivity of

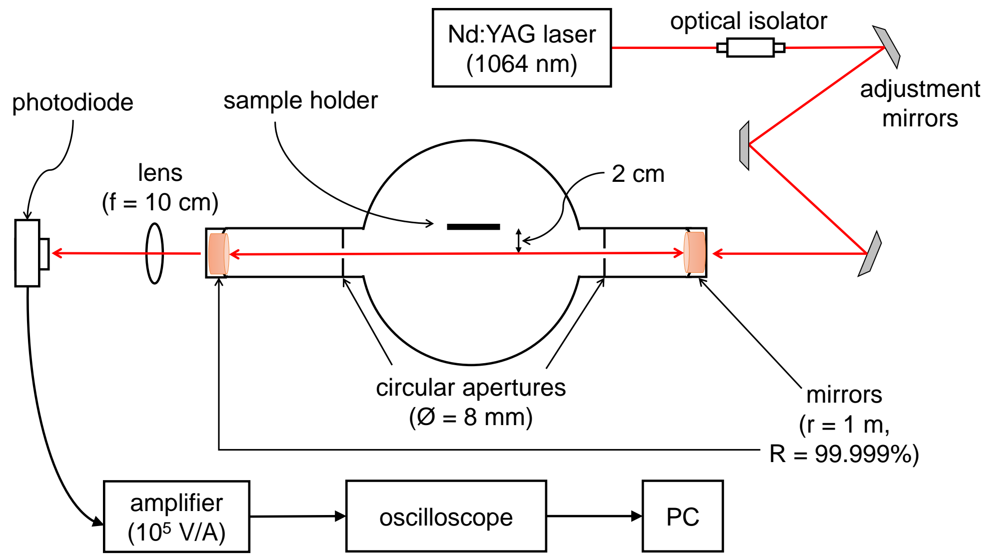


**Figure 7.9:** *Top view schematic of the CRDS setup at ACCesS.*

the mirrors (and consequently the decay time) continuously decreases, while after the plasma the reflectivity slowly recovers. The signal after the cavity is focused by a focal lens onto a photodiode connected to a fast transimpedance amplifier, with an amplification of $10^5$ V/A. The obtained signal is then transmitted to a computer by using an oscilloscope. A more detailed description of the CRDS setup can be found in [Rau14, RKF15], where the same setup was first tested and benchmarked in a comparable experiment.

Figure 7.10(a) shows two typical CRDS signals with and without absorbing medium. The decay time measured in vacuum (hence without absorbing medium) is typically around 350 µs, as shown by the fit performed to the blue line in the figure. The measured decay time decreases when a hydrogen plasma is present, as shown by the red line.

For the current investigations the exponential decay signals are recorded automatically every 1.3 s, and a fitting routine is automatically applied to each signal in order to calculate the decay time. Figure 7.10(b) shows the decay time before, during and after plasma exposure: during plasma phase the decay time strongly decreases in the first 5 minutes of plasma exposure, due to the degradation of the mirrors. The decay time after 7 minutes of plasma exposure starts to stabilize, however during long plasma exposures the decay time slightly decreases continuously. Hence, for reliable $H^-$ density measurements, the decay time at the end of the plasma pulse is considered (while at the beginning of the pulse the plasma is not yet stable, leading to not reproducible negative ion densities at comparable

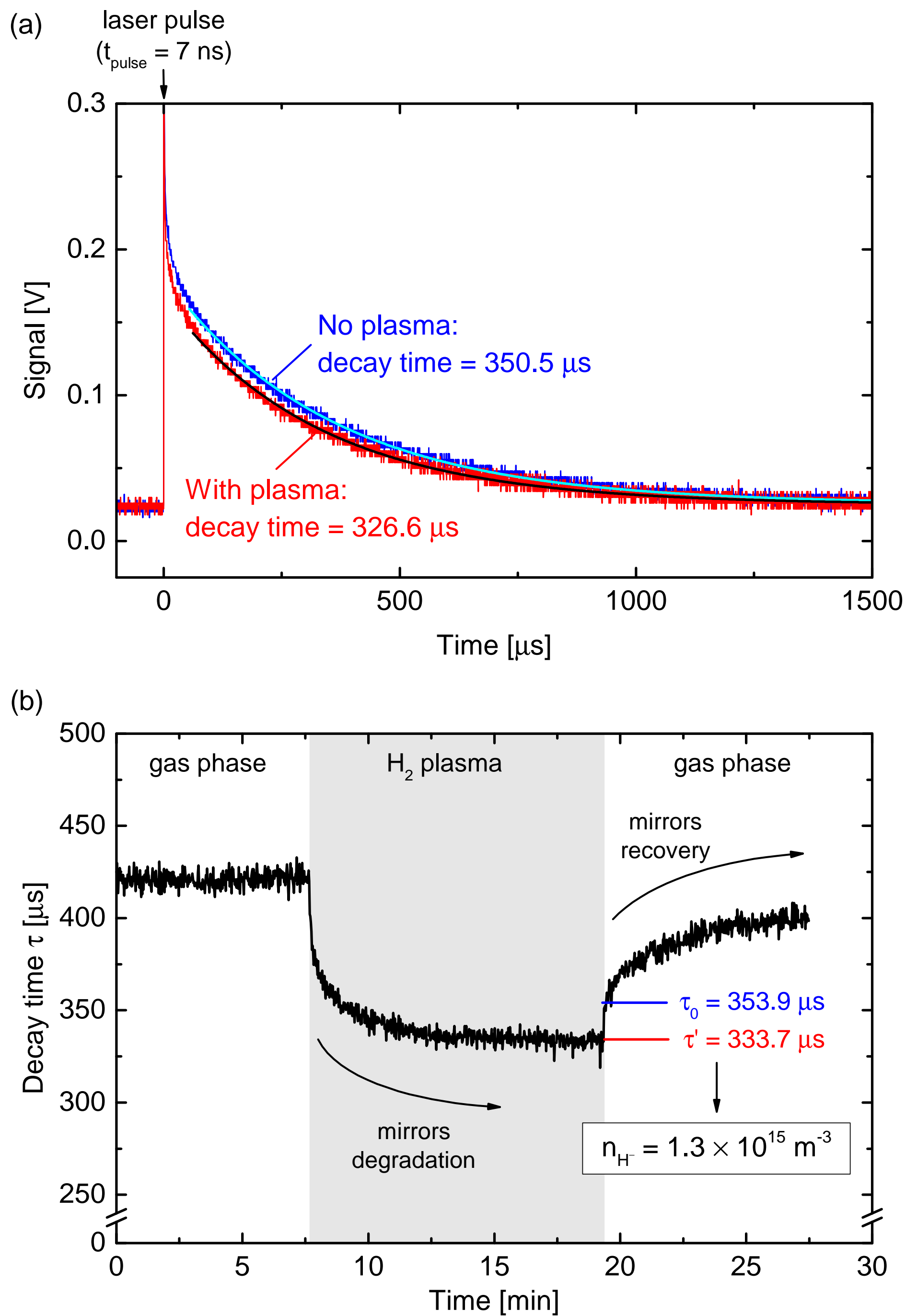


**Figure 7.10:** *(a) Two exemplary CRDS signals: in blue the measurement performed in vacuum (without absorbing medium) and in red the measurement in a plasma containing $H^-$ (with absorption medium). In both cases, the exponential decay fit is plotted. (b) Decay time before, during and after exposure to a plasma. The resulting $H^-$ density obtained at the end of the plasma pulse is indicated by $n_{H^-}$.*

plasma conditions). Hence, for the evaluation of $n_{\mathrm{H}^-}$ the last $\sim 50$ samples at the end of a plasma pulse are taken for the evaluation of $\tau'$ during plasma, and the first 20–30 samples immediately after the plasma pulse are considered for the evaluation of $\tau_0$ in vacuum (since the decay time is not stable after plasma due to the mirrors recovery, a lower number of samples are considered for $\tau_0$ with respect to $\tau'$). The resulting $\mathrm{H}^-$ density in the example shown in figure 7.10(b) is $1.3 \times 10^{15}$ m$^{-3}$.

The standard deviation of the averaged decay time is around $\pm(1\text{–}2)\,\%$, and this determines the detection limit of the evaluated negative hydrogen ion density for the current setup corresponding to $n_{\mathrm{H}^-} \geq 5 \times 10^{14}$ m$^{-3}$. The error associated with the measured $n_{\mathrm{H}^-}$ is around $\pm 30\,\%$ for high densities ($\geq 10^{15}$ m$^{-3}$), while the error can increase up to $100\,\%$ for densities close to the detection limit.

## 7.3 Typical plasma operation

The schematic in figure 7.11 explains the experimental procedure and timing for the different measurement acquisitions, considering all the different diagnostics. For vacuum operation (e.g. for temperature campaigns or for Cs evaporation during vacuum) the only diagnostic systems running are the work function diagnostic and the RGA for monitoring the background gases, and in case of caesium campaigns also the two SIDs for monitoring the Cs fluxes and the TDLAS system for absolute

**Vacuum operation:**

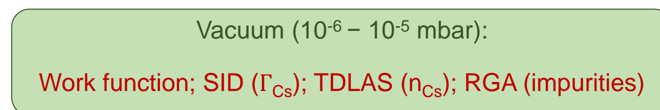


**Plasma operation (2 – 10 Pa in $H_2$ or $D_2$):**

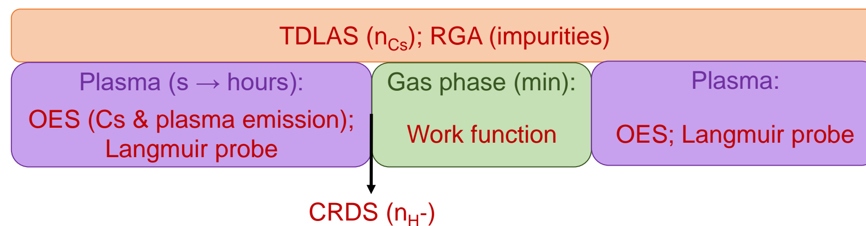


**Figure 7.11:** *Schematic of the diagnostics applied for the different experimental conditions, with the corresponding timing.*

measurements of Cs density are applied.

During plasma operation in hydrogen or deuterium, plasma pulses of different lengths are applied, from few seconds up to several hours. When the plasma is switched off, the gas (hydrogen or deuterium) is maintaned at the operating pressure, and this phase is denoted as *gas phase*. During the plasma phase, OES is applied for monitoring the Balmer and Fulcher emission, together with the Cs emission when caesium is involved. If the sample under investigation is punched in the middle, the Langmuir probe can be applied for measuring the plasma parameters close to the surface during plasma operation. The negative ion density is obtained at the end of the pulse (as described in the last section), while the work function of the surface can be measured only in the gas phase.

Typically, the gas phase lasts some minutes before starting a new plasma pulse, allowing to measure the work function a few times to check its reproducibility. The RGA and the TDLAS system are instead running both in plasma and in gas phase for the whole campaign.

In the current work, two plasma conditions are investigated: for the low work function materials in chapter 8 and for investigating the plasma effect on caesiated surfaces in chapter 9 a pressure of 10 Pa and an RF power of 250 W are applied. The resulting plasma parameters are shown in table 7.2 for a hydrogen plasma. $U_{\mathrm{spl}}$ is the potential of the floating sample, which can be easily measured with respect to the ground during plasma operation thanks to the bias connection, and the difference between the plasma potential and the sample potential determines the energy of the impinging positive ions onto the sample surface. The plasma parameters at 10 Pa/250 W are similar to those in front of the plasma grid at

**Table 7.2:** *Comparison between the plasma parameters obtained for hydrogen at 10 Pa/250 W and at 2 Pa/450 W.*

| | 10 Pa, 250 W | 2 Pa, 450 W |
|---|---|---|
| $n_{\mathrm{H}}$ [m$^{-3}$] | $2 \times 10^{19}$ | $4 \times 10^{18}$ |
| $n_{\mathrm{e}} = n_{\mathrm{i+}}$ [m$^{-3}$] | $1.4 \times 10^{16}$ | $1.1 \times 10^{16}$ |
| $n_{\mathrm{H^-}}$ (in volume) [m$^{-3}$] | $1.7 \times 10^{15}$ | $\leq 5 \times 10^{14}$ |
| $T_{\mathrm{gas}} = T_{\mathrm{H}}$ [K] | 550 | 500 |
| $T_{\mathrm{e}}$ [eV] | 2.1 | 4.6 |
| $U_{\mathrm{pl}}$ [V] | 9 | 22 |
| $U_{\mathrm{pl}} - U_{\mathrm{spl}}$ [V] | 8 | 21 |
| $\Gamma_{\mathrm{H}}$ [m$^{-2}$s$^{-1}$] | $1.3 \times 10^{22}$ | $1.6 \times 10^{20}$ |
| $\Gamma_{\mathrm{H_x^+}}$ [m$^{-2}$s$^{-1}$] | $1.3 \times 10^{20} (x = 3)$ | $1.6 \times 10^{20} (x = 2)$ |

negative ion sources. Hence, comparable influence of the plasma on the surface work function and on the caesiation process is expected at ACCesS.

However, at 10 Pa/250 W the surface production of negative ions is barely detectable. Since the aim of the investigations in chapter 10 is the comparison between hydrogen and deuterium in producing negative ions for varying work function, a pressure of 2 Pa and an RF power of 450 W are chosen. At these conditions, the plasma parameters (shown in table 7.2 for a hydrogen plasma) are more favorable for the negative ion surface formation at ACCesS experiment, since the volume production is lower, and the surface production is enhanced by the higher energy of the positive ions (accelerated towards the sample in the sheath region), as explained in the following sections.

### 7.3.1 $H^-$ volume production at ACCesS

The volume production of negative hydrogen ions represents a detection limit for investigation of surface formation, hence suitable plasma parameters must be chosen in order to have a low production rate of negative hydrogen ions produced by volume processes. In order to determine the amount of volume produced $H^-$, CRDS is applied in the two different plasma scenarios with a non-caesiated stainless steel surface, having a work function around 4.5 eV (the surface formation is negligible at such high work function).

The measured $H^-$ density, electron density, atomic hydrogen density, and electron temperature for the two different plasmas in hydrogen are shown on the left of figure 7.12. At 10 Pa and 250 W, the measured negative hydrogen ion density is $1.7 \times 10^{15}$ m$^{-3}$, much higher with respect to the case at 2 Pa and 450 W, where the $H^-$ density is below the detection limit ($n_{\mathrm{H}^-} \leq 5 \times 10^{14}$ m$^{-3}$).

The volume production of negative hydrogen ions can be modeled by balancing the different production and destruction rates (the processes are described in sections 4.1 and 4.3, respectively) via equation (3.9) for steady state conditions. This model is called *YACORA H⁻* and is described in detail in [Kur16, KFF17]. For the destruction rates, the input parameters are all diagnostically accessible, i.e. the molecular and atomic hydrogen density, the electron and positive ion density, and the electron temperature are obtained by means of the different diagnostics described in chapter 6, while the $H^-$ temperature is assumed equal to 0.2 eV, as explained in section 4.3. The rate coefficients are also known, and they are shown in chapter 4. Instead, for the production rates the electron density and temperature are diagnostically accessible as already mentioned, while the

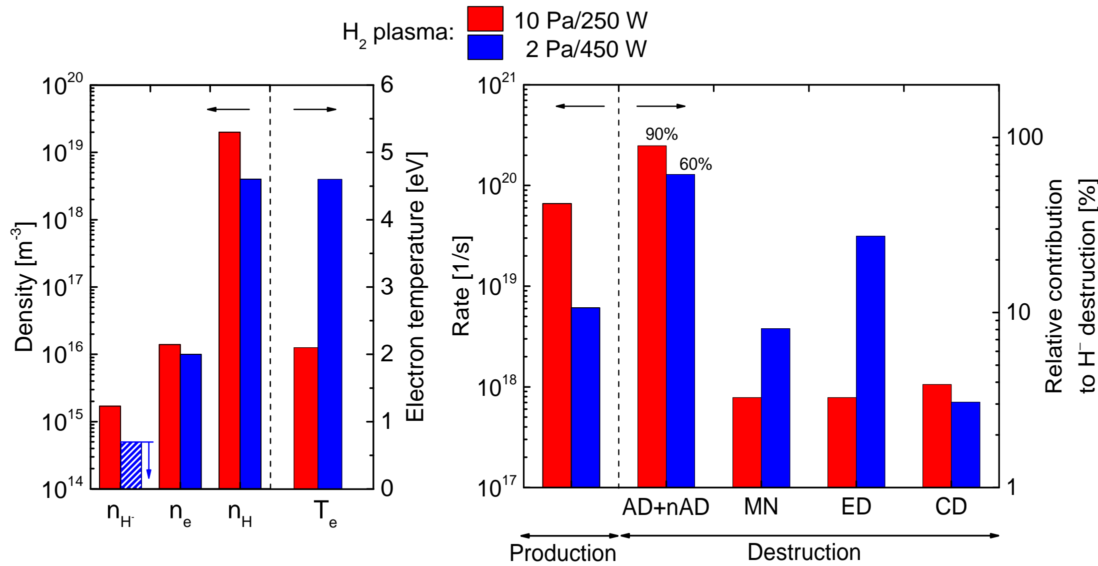


**Figure 7.12:** *Comparison between the two hydrogen plasma conditions with a stainless steel sample: the red bars refer to 10 Pa and 250 W, while the blue bars refer to 2 Pa and 450 W. On the left the $H^-$ density, the electron density, and the atomic hydrogen density, together with the electron temperature, are plotted. The $H^-$ density at 2 Pa is below the detection limit of the CRDS ($\leq 5 \times 10^{14}$ $m^{-3}$). On the right, the production rate for the volume formation of $H^-$ and the corresponding relative contributions of the different destruction processes listed in section 4.3 and obtained via YACORA $H^-$ are shown.*

vibrational population of the hydrogen molecules is considered as a superposition of two Boltzmann distributions, as described in section 6.4.2: the lower vibrational temperature $T_{\text{vib}}^{\text{low}}$ is experimentally obtained by means of OES, while the higher vibrational temperature $T_{\text{vib}}^{\text{high}}$ is a free parameter applied to adapt the modeled $H^-$ density to the one measured by CRDS.

On the right of figure 7.12, the production rates and the contribution of the different destruction processes are given. The production rate is much smaller at 2 Pa with respect to 10 Pa, since the molecular hydrogen density is a factor of 5 lower at 2 Pa and the electron temperature is higher (leading to lower rate coefficients, as shown in section 4.1). For both plasmas at 10 Pa/250 W and 2 Pa/450 W, the main destruction process of volume created $H^-$ is the associative detachment (discussed in section 4.3) due to collisions with neutral atomic hydrogen. However, its contribution to the total destruction rate is lower in the case of 2 Pa, and the electron detachment contribution is significantly enhanced due to the higher electron temperature and the lower atomic hydrogen density at lower pressures.

### 7.3.2 $H^-$ surface production at ACCesS

Negative hydrogen ions created at a low work function surface by conversion of atomic hydrogen and/or positive hydrogen ions may contribute to the total $H^-$ density in addition to the volume produced $H^-$. As explained in section 4.2, the flux of negative hydrogen ions leaving the surface depends on the incoming particles' fluxes and the conversion yields, which in turn depend on the energy of the impinging particles, as shown in figure 4.3 for a partially caesiated Mo surface of work function of 1.4–1.5 eV (no data are instead available for bulk Cs). For the fluxes and energies at 10 Pa/250 W and at 2 Pa/450 W (see table 7.2), the conversion yields extrapolated from figure 4.3 are shown in table 7.3.

The temperature of hydrogen atoms is assumed equal to the gas temperature (around 500 K), hence the atoms are in thermal equilibrium with the hydrogen molecules. However at ion sources, which operate at a lower pressure (0.3 Pa), the atomic hydrogen has a temperature around $10^4$ K (0.8 eV), hence one order of magnitude higher than the gas temperature [FFK+09, WMF+14]. This is due to the fact that the hydrogen atoms gain energy during the dissociation process by dissociative excitation into the repulsive state as in equation (3.24), and subsequent collisions cool them down to 0.8 eV. For higher pressures (as at ACCesS), the cooling down of the atoms is more efficient due to more frequent collisions, and the atoms thermalize with the hydrogen molecules. Moreover, due to the dissociative recombination in equation (3.26) high energetic H atoms can be formed. This process is particularly relevant at low pressures since the positive ion $H_2^+$ is the dominant ion species. The so created hydrogen atoms form a hot ensemble visible also by OES, forming a Gaussian profile with a broader FWHM as observed in a different experimental setup operating at 0.3 Pa [Kur16]. However at ACCesS, this hot ensemble is not observed in the line profile of the Balmer lines even at 2 Pa, and the atomic hydrogen temperature is always equal to the gas temperature.

**Table 7.3:** *Surface conversion yields in hydrogen at 10 Pa/250 W and at 2 Pa/450 W, extrapolated from figure 4.3 for a partially caesiated Mo surface of work function of 1.4–1.5 eV.*

| | 10 Pa/250 W | 2 Pa/450 W |
|---|---|---|
| $Y_{\mathrm{H}\rightarrow\mathrm{H}^-}$ | $< 10^{-10}$ | $< 10^{-10}$ |
| $Y_{\mathrm{H}_x^+\rightarrow\mathrm{H}^-}$ | 0.14 | 0.32 |

Hence, regarding the conversion process of atomic hydrogen, the low atom temperature in both plasma conditions leads to very low conversion yields (below $10^{-10}$, as extrapolated from figure 4.3 for a partially caesiated Mo surface). The main conversion process is thus involving positive ions. At 10 Pa the dominant positively charged species is $H_3^+$, while it is $H_2^+$ at 2 Pa, and the flux of positive ions is obtained from equation 3.21. The maximal energy of the impinging ions is determined by the difference between plasma potential and sample potential, which is about a factor of 2.5 higher at 2 Pa, as shown in table 7.2. At 10 Pa/250 W the resulting conversion yield extrapolated from figure 4.3 is around 14 %, while at 2 Pa/450 W it is 32 % due to the higher ion energy per nucleus.

In figure 7.13 the determined incoming fluxes for atomic and positive ion conversion are plotted together with the simulated outgoing $H^-$ fluxes, considering the conversion yields in table 7.3. Thus, a more efficient surface conversion is expected at 2 Pa with respect to the higher pressure case.

Consequently, the investigations about negative ion surface formation for varying work function and about the isotopic differences in hydrogen and deuterium are performed at 2 Pa and 450 W, because of the lower volume produced $H^-$ density on the one hand and the higher conversion efficiency for the surface conversion on the other hand.

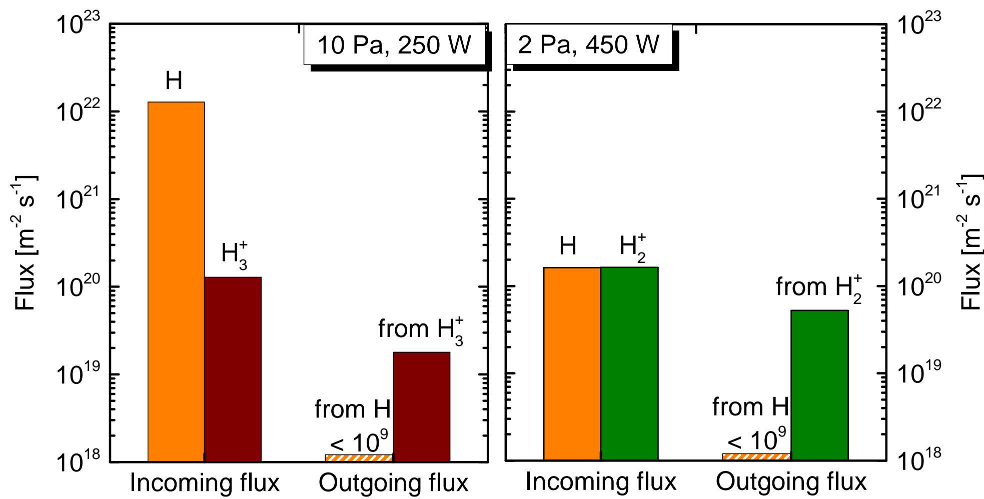


**Figure 7.13:** *Comparison of the fluxes for two hydrogen plasma conditions: on the left 10 Pa/250 W and on the right 2 Pa/450 W. The measured incoming fluxes are plotted for the specified species. The outgoing $H^-$ fluxes are calculated from the conversion yields in table 7.3 for a partially caesiated Mo surface of work function of 1.4–1.5 eV.*

# 8 Low work function materials

In the following chapter, the different low work function materials listed in section 4.4 are tested in order to measure their work function at ion source relevant vacuum and plasma conditions. The results must be compared with the Cs case, which has shown an optimal work function of 2.1 eV measured in the same setup by [Fri13, FF17]. Since some of the considered materials might release heavy metallic impurities, each time before installing a new sample the experiment is cleaned with 5 % hydrochloric acid, distilled water, acetone, and isopropyl alcohol. The release of metallic impurities from the sample is checked by a small stainless steel sample ($10 \times 10$ mm$^2$) laying on the bottom plate in front of the sample: Rutherford backscattering spectroscopy (RBS) measurements are performed[1] on the stainless steel sample after having been applied in ACCesS. For all the following samples, no release of impurities occurred after the application of high temperatures or after plasma treatment [Rei17], unless explicitly stated. Some of the materials investigated here were also tested at a different setup with similar plasma conditions as in ACCesS for local $H^-$ density measurements above the sample surface. Details can be found in [Kur16, KFF17, FHF$^+$18].

## 8.1 Lanthanum hexaboride

The nominal work function for a pure lanthanum hexaboride ($LaB_6$) surface is 2.7 eV [Laf51] after an activation procedure consisting in heating the sample up to 1500 °C for few minutes in order to clean the surface from impurities.

The sample of $LaB_6$ was purchased from the commercial distributor Sindlhauser [Sin14] in 2014. The sample has a polycrystalline structure and is manufactured by press sintering. The sample size is $30 \times 30$ mm$^2$, with a thickness of 5 mm. The sample was stored in air for several years, and an oxidation of the

[1]Department of Experimental Physics IV, University of Augsburg.

first layers at the sample surface was expected. Thus, the sample was scratched with a diamond rotary blade in order to expose the bulk material. The resulting scratched surface is shown in the picture in the previous page.

Figure 8.1(a) shows the work function achieved by increasing the sample temperature and after hydrogen plasma exposure. Before any treatment, the surface work function is around 4.3 eV due to the presence of adsorbed impurities at the surface from exposure to atmospheric air. During the heating procedure in vacuum, the sample temperature is increased up to 400 °C. Small peaks in the RGA signals for $H_2O$, $N_2$, $CO_2$, and $O_2$ are observed in this phase, indicating a partial desorption of impurities from the surface. As a consequence, the work function starts to decrease at a surface temperature of 200 °C, reaching $(3.7 \pm 0.1)$ eV at 350 °C. The work function shows then a slight increase to 3.8 eV at a surface temperature of 400 °C, which is anyway comparable within the error bars to the work function measured at lower temperature. However, when the heating is switched off, the work function increases with a degradation rate of $\sim$ 0.2 eV/h due to the re-adsorption of contaminants from the background gases. When a hydrogen plasma at 10 Pa/250 W is applied for 5 minutes, a work function of $(3.6 \pm 0.1)$ eV is achieved despite a maximum temperature of 120 °C, lower than during the heating procedure. Longer plasma exposure times do not change the final work function, which results to be stable even after 1 h and 45 min of plasma. However, such work function is far away from the expected value of an activated sample. Since it is known from the literature that the performance of the $LaB_6$ cathodes are not significantly affected by hydrogen exposure [Gal69], the adsorption of hydrogen at the surface is not causing the high work function. Hence, the hydrogen plasma at 10 Pa/250 W ($\Gamma_{H_3^+} \sim 10^{20}$ m$^{-2}$s$^{-1}$, $U_{pl} - U_{spl} \sim 8$ V) is not sufficient to clean properly the surface (e.g. the binding energies of La-O and B-O are 8.2 eV and 8.4 eV [Lid05], respectively, slightly higher with respect to the energy of impinging ions onto the surface) and to reach the nominal work function of 2.7 eV. After plasma, the work function degradation rate is $\sim$ 0.3 eV/h, slightly higher with respect to the degradation observed after the heating procedure.

An argon plasma at a lower pressure and a higher RF power with respect to hydrogen is applied, as shown in figure 8.1(b). Higher particles energies are thus expected, and a higher surface temperature is reached due to the higher mass of the Ar particles and the higher impinging energy. Hence, a stronger impact of the plasma on the surface composition is expected with respect to hydrogen, and its influence on the sample work function is studied. Unfortunately, no specific

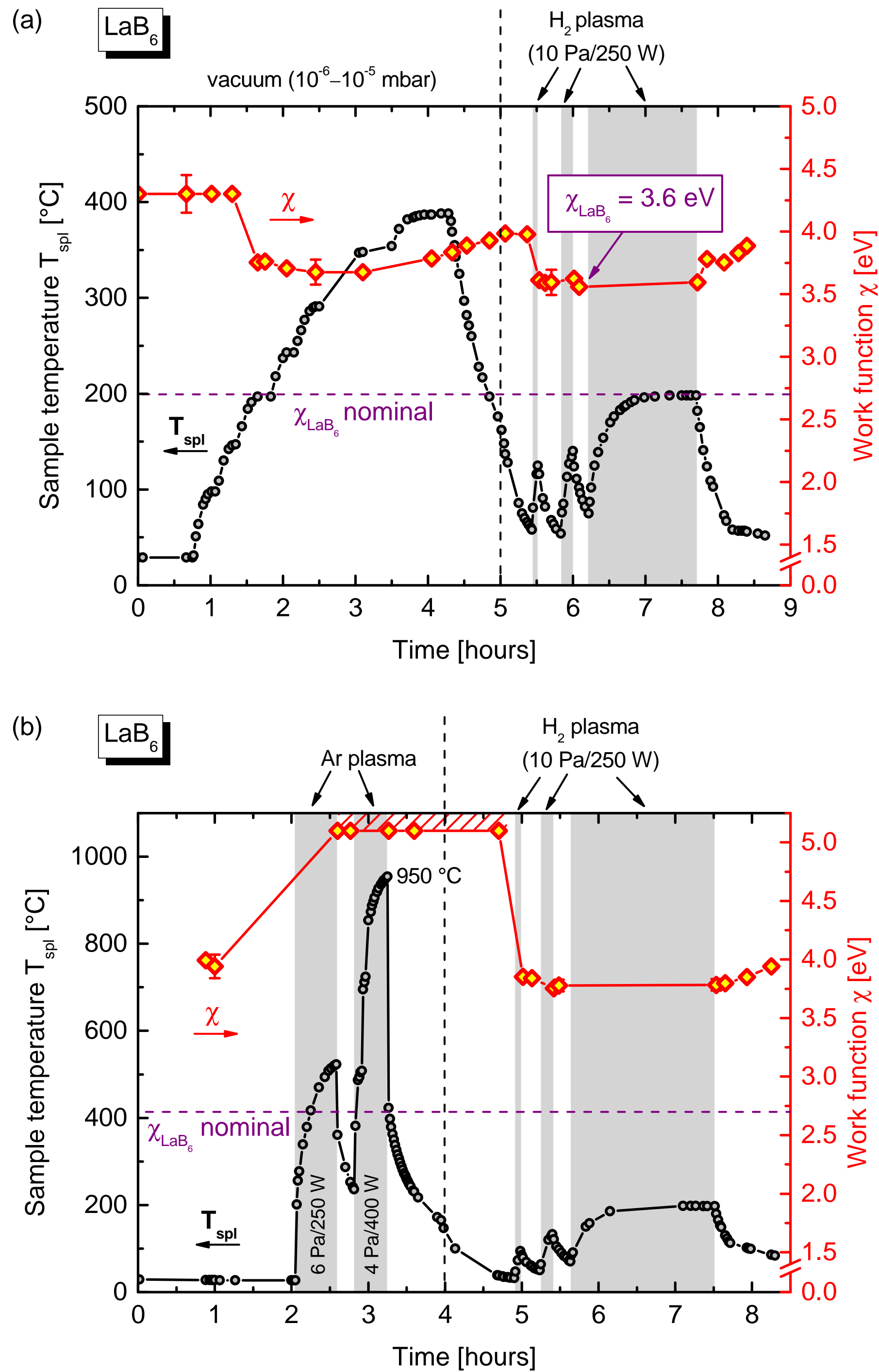


**Figure 8.1:** *(a) Work function of the $LaB_6$ sample during an experimental campaign where the sample temperature is first increased in vacuum and then a hydrogen plasma at 10 Pa and 250 W is applied (total exposure: 1 h 45 min). (b) Work function of $LaB_6$ during and after Ar plasma treatment and hydrogen plasma. The vertical dashed lines separate the different experimental phases (vacuum, hydrogen gas, argon gas).*

diagnostics for investigating the Ar plasma are available at ACCesS, and the Langmuir probe could not be applied with the current sample. For a pressure of 4 Pa and an RF power of 400 W, a surface temperature of 950 °C is achieved. After Ar plasma exposure, the measured work function is very high ($\geq 5.1$ eV). This effect is due to the adsorption of Ar at the surface, which disturbs the determination of the work function as observed in [KLM+00], leading to higher measured values. In order to retrieve the same surface condition as during typical hydrogen plasma operation, hydrogen plasma exposure is again applied, resulting in a stable work function of 3.8 eV independent from the plasma-on time and still far away from the nominal value. As a consequence, neither the Ar ion fluxes nor the high temperature reached during argon operation helps to reach a work function lower than 3.6 eV, but instead the work function increases by 0.2 eV. Hence, the $LaB_6$ cannot be activated at ion source plasma conditions, and a minimum work function of only 3.6 eV is achieved.

## 8.2 Lanthanated materials

Refractory metals containing lanthanum oxide gain a low work function when heated to temperatures above 1300 °C for an annealing time of at least one hour [BBG78, HHB+15], thanks to the diffusion of lanthanum to the surface. Two different materials based on lanthanum diffusion are tested here in order to check whether a plasma-induced diffusion at lower temperatures is possible: lanthanated molybdenum (MoLa), with a nominal work function of 2.6 eV [YNX+04], and lanthanated tungsten (WL), with a nominal work function of 2.8 eV [HHB+15].

The MoLa sample was purchased from the commercial distributor Plansee [Pla01] in 2001 and stored in atmospheric air. It has a size of $30 \times 30$ mm$^2$ and a thickness of 2 mm, with a $La_2O_3$ concentration of 0.7 % in weight. Due to visible oxidation of the surface, the sample is first mechanically polished and then cleaned with distilled water, acetone and isopropyl alcohol before the installation at ACCesS. The same experimental investigations described for $LaB_6$ are applied to the MoLa sample. By heating the sample in vacuum up to temperatures of 450 °C, the work function is around 4.3 eV, far away from the nominal value. After a hydrogen plasma exposure of 2 hours at 10 Pa/250 W (with a maximal surface temperature of 200 °C), the work function is around 4.5 eV, approaching the work function of pure Mo (4.6 eV [Mic77]). As in the case of $LaB_6$, MoLa is further exposed to Ar

plasma, allowing to reach higher surface temperatures (up to 950 °C), however after a subsequent hydrogen exposure of 2 hours the work function results to be still around 4.5 eV. Hence, an activation in a low temperature plasma is not possible for this material.

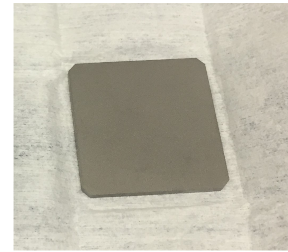

Two lanthanated tungsten samples with two different La concentrations are tested: WL10 with 1.0 % in weight of $La_2O_3$ and WL2 with $\sim$ 2 % in weight of $La_2O_3$. The first sample (see picture on the right) was purchased from Plansee [Pla16] in 2016 as a cylindrical rod with a diameter of 40 mm and a length of 15 mm. This rod was cut at IPP in order to create a sample suitable for ACCesS, with a size of $30 \times 30$ mm$^2$ and a thickness of 2 mm. The sample was then mechanically polished in order to remove possible impurities deposited on the sample during the cutting procedure, and the surface composition was checked via energy-dispersive X-ray spectroscopy (EDX) at IPP before the installation at ACCesS. An experimental procedure similar to the one shown in figure 8.1(a) is performed: during the heating of the sample up to 400 °C, the work function is always higher than 4.3 eV, while during hydrogen plasma exposure the work function is stable at 4.1 eV. As for MoLa, also the lanthanated tungsten does not show any evidence of activation.

In order to test if a higher concentration of La in the bulk material can help to ease the activation and to reach lower work functions, a WL2 sample was received in 2016 from the Karlsruher Institut für Technologie (KIT) [Kar16]. However, neither during the heating campaign in vacuum nor after hydrogen or argon plasma exposure (with temperatures up to 950 °C) the work function reaches values below 4.1 eV, showing no difference to the WL10 sample.

Hence, none of the lanthanated materials can be activated at ion source relevant conditions, and a different concentration of La in the bulk material from 1 % to 2 % does not ease the activation procedure.

## 8.3 Tungsten dispenser cathode

This cathode is based on diffusion of Ba to the surface, driven by an activation temperature of 1000 °C. The resulting surface work function for an activated sample is 2.1 eV [Cro81].

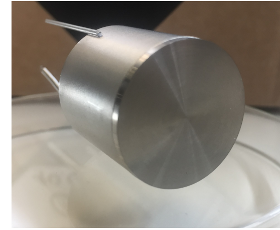

The tungsten dispenser cathode (TDC) consists of a tungsten rod (see picture on the right) with both diameter and length of 25.4 mm. The inner part of the cathode is made of porous tungsten with barium, calcium and alumina oxides dispersed homogeneously throughout. The cathode was purchased from Spectra-Mat [Spe16] in 2016. For this specific cathode, the ratio among the oxides is 3 BaO : CaO : $Al_2O_3$. In order to heat the cathode efficiently and uniformly up to 1000 °C, a coaxial heating wire runs through the sample. A new sample holder was specially manufactured to hold this particular sample (electrically and thermally insulated from the vessel walls as well). The bias connection and the thermocouple are clamped to the front of the sample as shown in figure 8.2, and the work function is measured on the flat side of the rod.

In the case of the TDC, a different experimental procedure with respect to the other materials is followed, in order first to test the reaction of the cathode to the hydrogen plasma before activating it: after around 5 minutes of plasma exposure at 10 Pa/250 W, the work function is $(3.8 \pm 0.1)$ eV and is stable also after a longer exposure (ca. 3 hours, with a maximal surface temperature of 220 °C). Hence, the plasma cannot activate the cathode, and a heating procedure with high temperatures is mandatory for the activation of the sample.

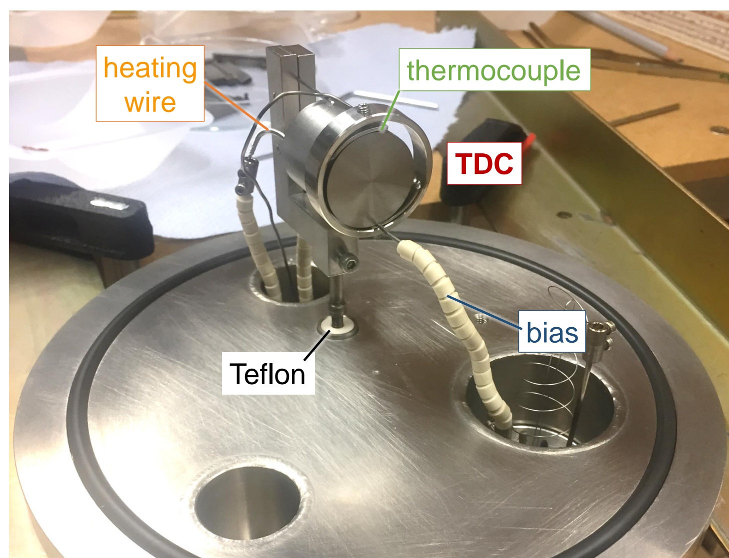


**Figure 8.2:** *Picture of the bottom plate with the tungsten dispenser cathode (TDC) installed on the specially manufactured sample holder. During the investigations, a stainless steel sample is placed on the bottom plate in front of the cathode (not shown in the picture).*

Figure 8.3 shows the heating campaign performed in vacuum: by gradually heating the cathode, the work function decreases. Between 200 °C and 500 °C peaks clearly appear in the RGA concerning the $H_2O$ and $N_2$ signals. At 600 °C, the RGA signals stabilize, and the measured work function is $(3.6 \pm 0.1)$ eV.

However, once the temperature reaches 700 °C the background current from the work function setup (called here *dark current*) increases due to the thermionic emission of electrons from the surface, following the Richardson's law ($I \propto T^2 e^{-\frac{\chi}{k_B T}}$). The dark current, hence, increases with increasing temperature and decreasing work function. Figure 8.4(a) shows the dark current measured at different sample temperatures: the dark current at room temperature is typically in the range of nA, and it increases with increasing temperature. At around 700 °C the dark current is in the µA range, and such a dark current is already too high with respect to the photocurrents (which are usually between nA and µA), precluding the possibility to measure the work function. The dark current is even higher than the µA range when the temperature of the cathode reaches the activation temperature of 1000 °C. Furthermore, at 1000 °C the sample is glowing very brightly, as it can be seen in the pictures of figure 8.4(b), where three different temperatures are compared. The emission of light is uniform over the entire cathode surface,

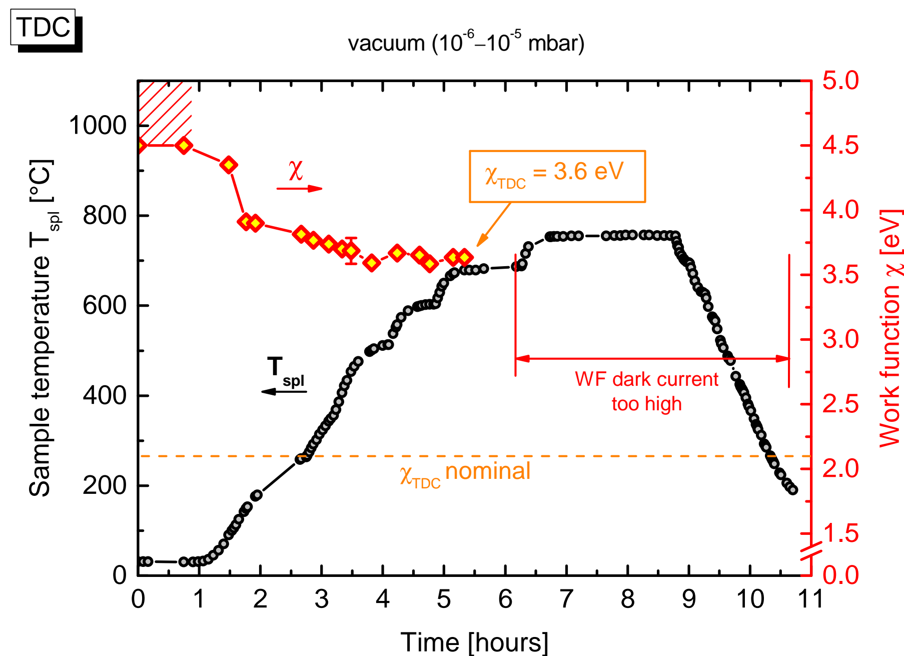


**Figure 8.3:** *Work function of the TDC in vacuum with increasing sample temperature. Once the temperature reaches 700 °C, the work function is no more measurable due to the high dark current at the work function setup.*

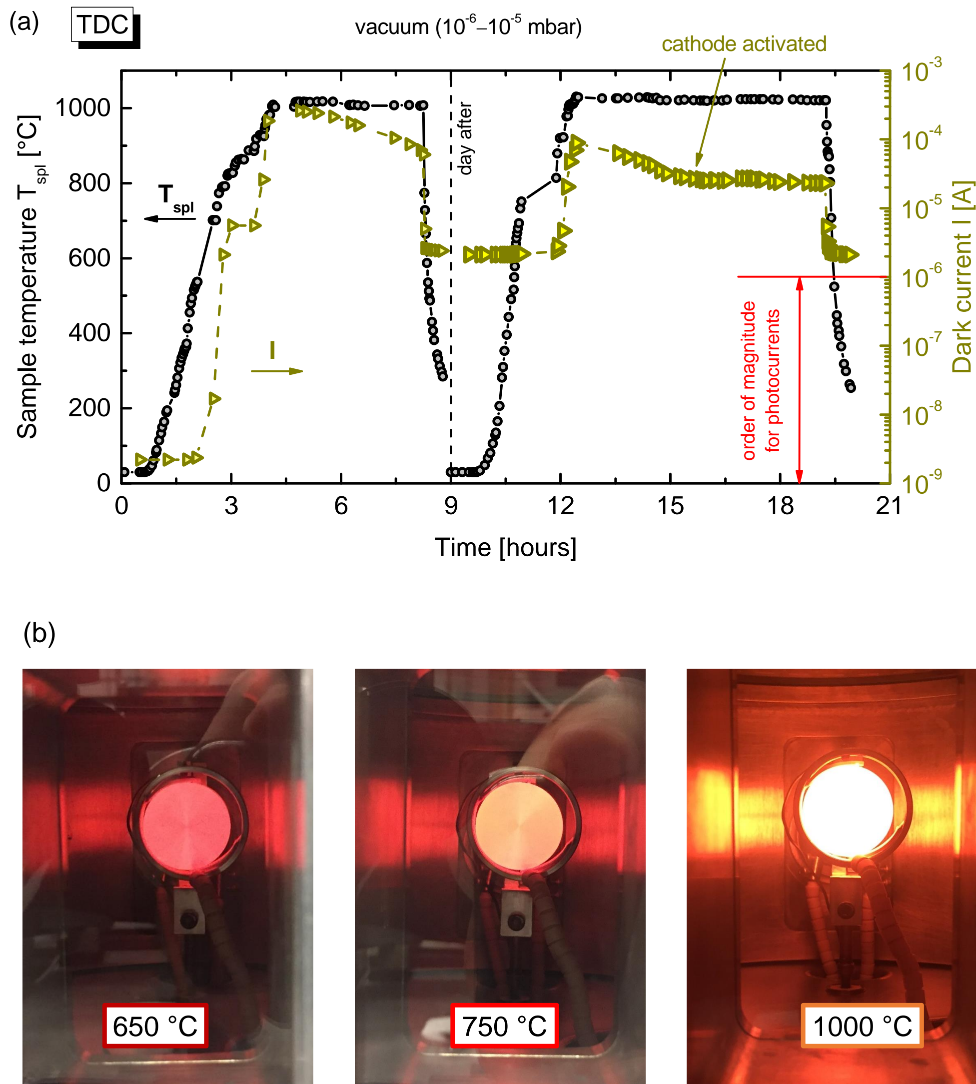


**Figure 8.4:** *(a) Dark current from the WF setup with increasing temperature of the TDC over two days in vacuum (the usual range of the measured photocurrents is also indicated). (b) Pictures of the cathode taken from the front window during the heating campaign.*

suggesting a spatially constant temperature.

After reaching 1000 °C and having maintained this temperature for 4 hours the sample is let to cool down, and the dark current decreases as it can be seen in figure 8.4(a). However, the dark current is still in the µA range also when the sample temperature is below 600 °C, down to room temperature. Hence, the dark current has an offset which does not allow to measure the work function also after the cooling down of the sample. The reason of this offset is the desorption of metallic particles (such as Ba) from the surface at such high temperatures, which

has created a leakage current between the sample and the vessel walls. The release of metallic impurities was afterwards also confirmed by the RBS measurement on the stainless steel piece placed on the bottom plate in front of the sample during the investigations (not shown in figure 8.2): a significant presence of barium and tungsten was observed [Rei17], which contaminated the whole experiment. Due to the leakage current, the work function could not be measured by the Fowler method. An estimation of the work function from the Richardson's law would be in principle possible, however it cannot be applied for the current investigations since the Richardson's law is valid only if the work function or the Richardson constant are constant during the heating process, which is not the case for the TDC sample during the heating campaign.

However, even if it is not possible to estimate the work function, the relative behavior of the dark current at high temperatures during the heating campaign, shown in figure 8.4(a), still provides information about the activation of the TDC in a limited vacuum environment (background pressure of $10^{-6}$–$10^{-5}$ mbar): as soon as the sample reaches 1000 °C, the dark current significantly increases by many orders of magnitude, from $\sim 10^{-9}$ A at room temperature to $\sim 10^{-4}$ A at 1000 °C. When the sample temperature is then set constant at 1000 °C (with the exception of operation during the night, when the heating was stopped), the dark current slowly decreases by one order of magnitude (due to variation of the work function or of the Richardson constant). The dark current reaches finally a stable value of $2.5 \times 10^{-5}$ A after a total of 7 hours at 1000 °C. The sample at this point is considered to be activated [Spe15].

Furthermore, since the emission of light from the cathode, and hence its temperature, is uniform (as observed in figure 8.4(b)), the diffusion and eventual desorption of metallic impurities are uniform in all directions as well. After the opening of the experiment, the bottom plate and the walls were covered by a brownish layer, and the experiment was intensively cleaned with hydrochloric acid and further polished with sandpaper. This desorption of metallic impurities during the activation, leading to leakage currents or even shortcuts in the vessel, demonstrates that this material is not suitable for ion sources, although the work function might actually be low after the activation procedure. Moreover, a plasma grid of such a material would be difficult to be manufactured, due to the need of the internal heating wire for a uniform heating of the grid.

## 8.4 Europium

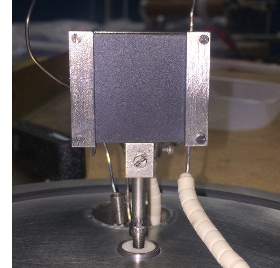

The nominal work function for Eu is 2.5 eV [Mic77], the lowest among the lanthanides. This material is chosen for benchmarking the work function diagnostic, as shown in section 7.1.3. The sample of europium (shown on the right) was purchased from the supplier company abcr [abc16] in 2016, stored in a sealed can in Ar atmosphere to prevent any oxidation. It has a size of 30 × 30 mm$^2$ and thickness of 1 mm. In order to install the sample at ACCesS, the sample was exposed to air for maximum 10 minutes, and during this time it did not show evidence of oxidation.

Figure 8.5 shows the heating campaign performed in vacuum, with the measured work function at varying temperature. This campaign constitutes also the benchmark of the work function measurements. At the beginning of the campaign, the work function is higher than 4.5 eV due to impurities present on the surface after air exposure (e.g. $Eu_2O_3$ and EuO). During the sample heating, the RGA signals corresponding to $H_2O$, $CO_2$ and $N_2$ show small peaks, and when the temperature

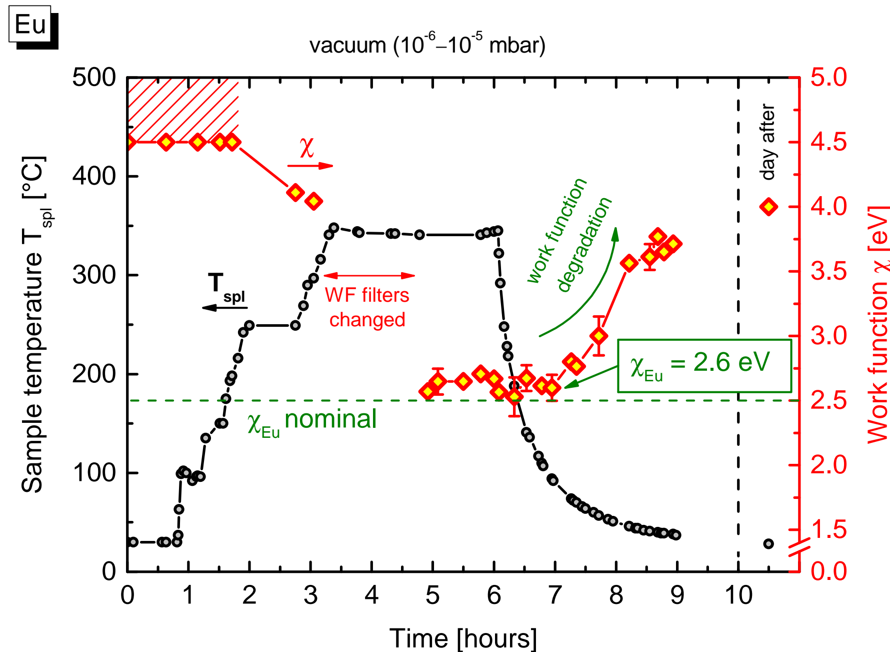


**Figure 8.5:** *Work function of Eu in vacuum with increasing sample temperature. Once the temperature reaches 350° C, the measured work function is (2.6 ± 0.1) eV, close to the nominal value.*

of the sample reaches 250 °C the work function starts to decrease. At 350 °C the work function reaches the stable value of (2.6 ± 0.1) eV. During the cooling down of the sample, the work function shows a degradation at a rate of 0.7 eV/h (much higher with respect to $LaB_6$ due to the high reactivity of Eu) due to the influence of the background gases adsorbing on the low work function surface, reaching a work function of 4.0 eV over a night in vacuum. A similar degradation occurs also if the sample is located in hydrogen gas, but without plasma (campaign not shown here).

The low work function after the degradation in vacuum or in hydrogen gas can be retrieved either by heating the surface again to 350 °C or by a short plasma pulse, as shown in figure 8.6. A pulse of 1 minute is sufficient to clean the surface from background impurities (e.g. the binding energy of Eu-O is 5 eV [Lid05], hence positive ions and energetic photons impinging onto the surface are able to break the bonds), resulting in a work function of (2.6 ± 0.1) eV. However, a longer exposure to hydrogen plasma causes a gradual increase of the work function: after 30 minutes of overall plasma exposure, the work function increases up to 3.5 eV (with a maximal sample temperature of 200 °C), hence with a degradation rate in plasma of 1.8 eV/h (much higher than in the case of vacuum), until the work

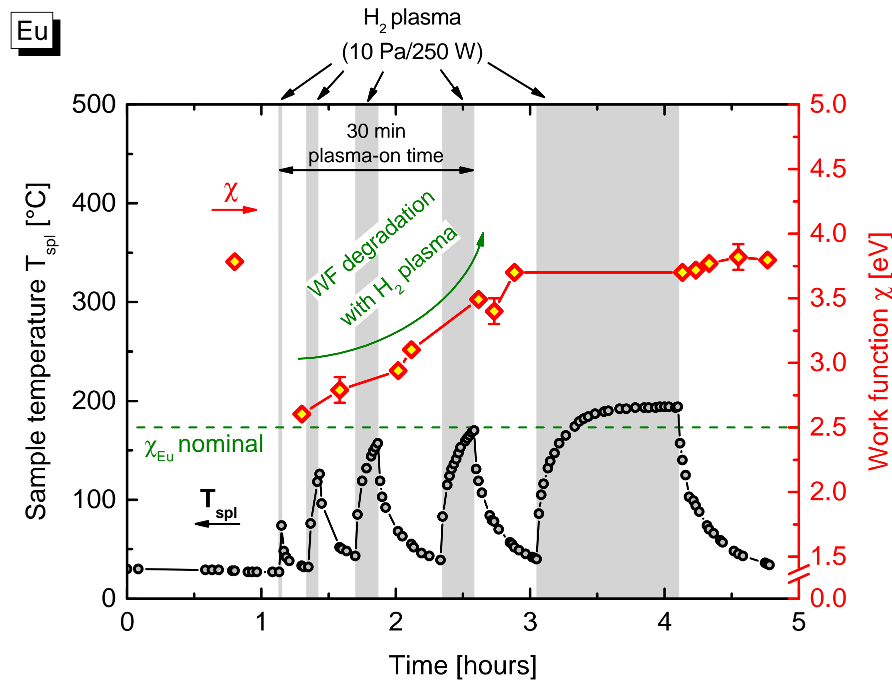


**Figure 8.6:** *Sample temperature and work function of Eu due to exposure to $H_2$ plasma pulses. The sample is located in hydrogen gas at 10 Pa for the entire campaign.*

function saturates for longer plasma exposure. A work function of 3.7–3.8 eV is measured after 1 hour of total plasma exposure. This particular degradation of the work function occurs only during hydrogen plasma phases, and it might be due to the adsorption, or even absorption, of atomic hydrogen at the surface. In fact, rare-earth metals can be applied for hydrogen storage and the surface molecular structure can be strongly affected by the hydrogen ad- and absorption [Sim12]. This effect is not observed with the other investigated materials.

Hence, in the case of europium the hydrogen plasma has a double effect: the plasma is able to retrieve a low work function (2.6 eV) on a short time scale, but then the work function is not temporally stable for long plasma exposures. In order to release the possible ad- and absorbed hydrogen particles, the sample must be heated again to a temperature of 350 °C (campaign not shown here). During the heating of the sample after being exposed to hydrogen plasma, the RGA shows a higher signal of the atomic hydrogen content (mass 1 amu), suggesting a release of hydrogen from the surface. Consequently, after heating the sample and desorbing hydrogen particles from the surface, the low work function of 2.6 eV is retrieved.

In order to maintain a low work function also during plasma, it is thus mandatory to keep the sample at high temperatures. This is shown in figure 8.7: before the shown campaign, the surface was exposed to plasma for a long time, hence the surface work function is saturated at high values, as proved by the high work function measured after the first short plasma pulse ($\sim$ 4.2 eV). The temperature of the sample is then increased during a long plasma exposure ($\sim$ 5 hours) up to 400 °C. In this way, the hydrogen adsorbed at the surface is in turn released due to thermal desorption, resulting in a work function of $(2.7 \pm 0.1)$ eV, close to the lowest value previously measured. A sample temperature higher than 400 °C might be even more beneficial to counteract the adsorption of atomic hydrogen at the current plasma conditions ($\Gamma_{\mathrm{H}} \sim 10^{22}$ m$^{-2}$s$^{1}$), while a lower temperature seems to be not sufficient to maintain the low work function during plasma operation (as confirmed by a campaign not shown here). The degradation of the work function after the exposure to plasma and induced by adsorption of background impurities is 1.5 eV/h, higher than the value measured in vacuum after the heating campaign. The reactivity of europium is thus enhanced by the application of a hydrogen plasma in front of the surface.

During the heating and plasma campaigns, the sample did not show any visible deterioration, showing a good resistance and mechanical stability in vacuum

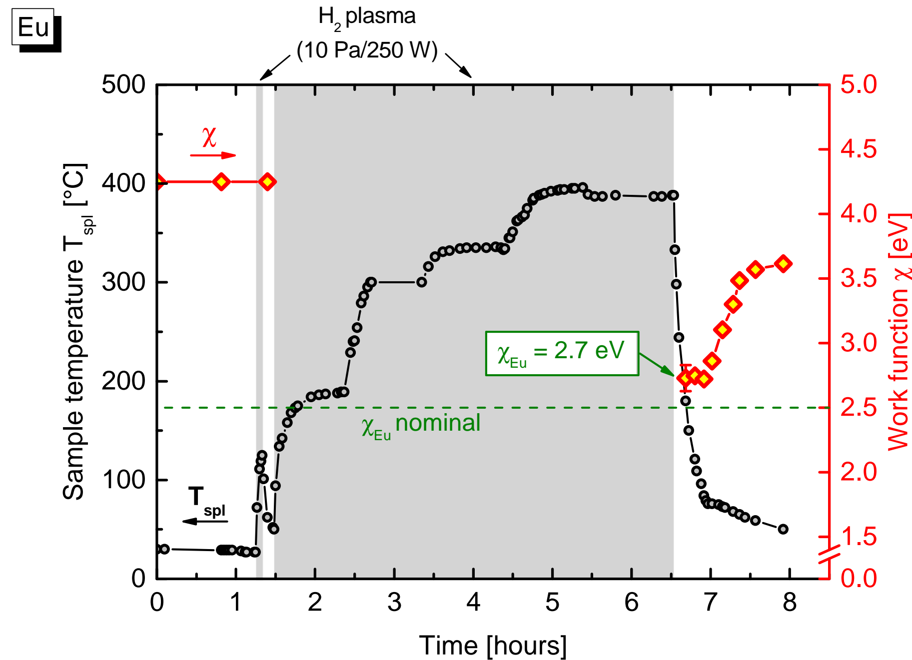


**Figure 8.7:** *Work function of europium due to exposure to a long $H_2$ plasma pulse, heating additionally the sample up to 400 °C.*

with temperatures up to 400 °C and in plasma environment. However, once the experiment was vented and the sample was exposed to air, a fast oxidation of the surface appeared and a white layer covered the surface within 15 minutes, as shown in figure 8.8 (while during the sample installation at the beginning, the sample did not show evidence of oxidation after 10 minutes of air exposure). In particular, the portion of the surface previously exposed to plasma was oxidizing much faster than the sides of the sample, which were covered by the clamps during the investigations. Such a white layer might be produced by hydroxide species, e.g. $Eu(OH)_3$ (formation enthalpy of −13.9 eV [Rar85]). Hence, the exposure of Eu to hydrogen plasma leads to a faster deterioration of the surface once it is exposed to air.

In order to preserve the Eu sample after the current investigations, the sample was stored in a separate vacuum chamber connected to a small pump stand (with a typical background pressure of $10^{-6}$ mbar), with a window in the front to monitor the sample conditions with time. Once back in vacuum the oxidation stopped, and the surface is stable since then (i.e. a year, at present). This fast oxidation and reactivity of Eu are similar to the caesium case, however the measured work function of Eu (2.6 eV) is higher than the one measured for a caesiated surface (2.1 eV, see next chapter).

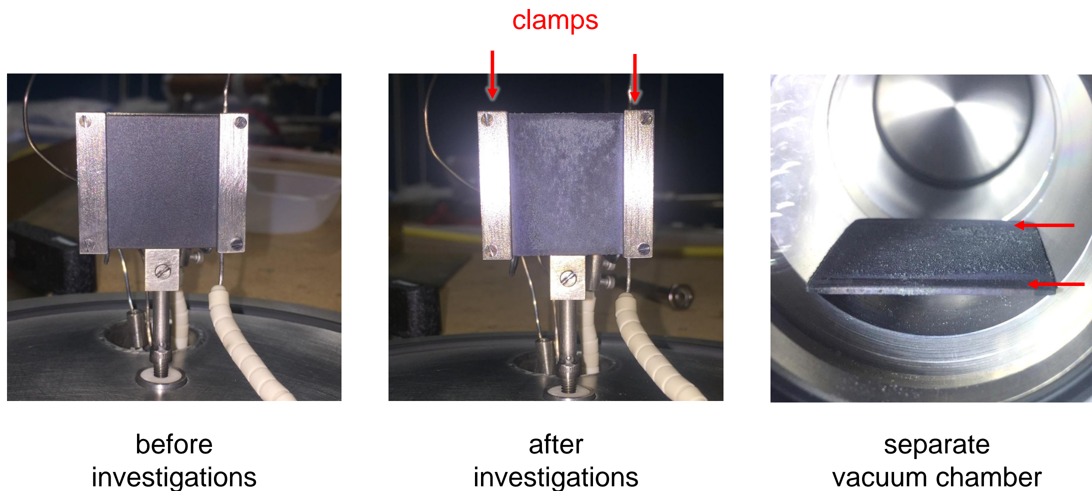


**Figure 8.8:** *Pictures of the Eu sample before and after the investigations with hydrogen plasma and in a separated vacuum chamber. Clear evidence of oxidation of the portion of the sample previously in contact with the plasma is observed, while the region below the clamps is less affected.*

## 8.5 Summary

Table 8.1 summarizes the measured work functions for the several materials investigated under ion source relevant conditions in vacuum and plasma environment.

The $LaB_6$ sample and the lanthanated materials (MoLa and WL) could not be activated by plasma exposure, and a surface temperature of 950 °C in maximum is still too low for the activation. Hence, their resulting work functions are always higher than 3.6 eV, too high for an efficient surface production of negative ions. For $LaB_6$ the degradation rate of the work function after the heating campaign and after the plasma exposure is of 0.2 and 0.3 eV/h, respectively.

For the tungsten dispenser cathode (TDC), it was possible to follow the activation procedure at high temperatures ($\sim$ 1000 °C) in a moderate vacuum, however the massive thermionic emission and the undesired desorption of metallic impurities (Ba and W) do not allow a reliable measurement of the work function and create leakage currents within the experiment. As a consequence of the heavy particle desorption, this material is not suitable for ion source applications for fusion.

The sample of europium has shown the best performance (2.6 eV), though to have a stable work function during plasma exposure it is mandatory to maintain a temperature higher than 400 °C. However, the high degradation rate of the work function ($\geq$ 0.7 eV/h), especially due to hydrogen adsorption in plasma phases

**Table 8.1:** *Composition, nominal work function, and minimal measured work function values of the materials investigated under ion source relevant conditions, during heating in vacuum and after plasma exposure.*

| Material | Bulk composition | Nominal WF [eV] | Measured WF [eV] in: heating campaign | plasma campaign |
|---|---|---|---|---|
| $LaB_6$ | $LaB_6$ | 2.7 @ 1500 °C | 3.7 | 3.6 |
| MoLa | $La_2O_3$ in Mo (0.7 % $La_2O_3$) | 2.6 @ 1300 °C | 4.3 | 4.5 |
| WL10 & WL2 | $La_2O_3$ in W (1.0 % & 2 % $La_2O_3$) | 2.8 @ 1500 °C | 4.3 | 4.1 |
| TDC | 3 BaO : CaO : $Al_2O_3$ in porous W | 2.1 @ 1000 °C | $< 3.6^{*}$ | 3.8 |
| Eu | Eu | 2.5 | 2.6 | $2.7^{**}$ |

* For the TDC sample, a significant desorption of Ba and W is observed, leading to an increase of the dark current which disturbs the work function measurement.
** To maintain a low work function during plasma exposure, it is mandatory to heat simultaneously the sample up to at least 400 °C.

and after plasma exposure, indicates a much higher reactivity with respect to the other materials here investigated. Thus, this material cannot be considered a valid option for negative ion sources for fusion, since it shows similar issues of caesium (e.g. high reactivity and fast oxidation), and it owns a higher work function with respect to Cs, which leads to less performance at ion sources.

In conclusion, none of the investigated low work function materials constitutes a valid alternative to Cs evaporation for negative ion sources in view of DEMO.

# 9 Work function of caesiated surfaces

## 9.1 Cs evaporation at ACCesS

Different Cs sources, described in section 6.3, were applied during the current work. Figure 9.1 shows a comparison between the different configurations and Cs sources in terms of absolute Cs density achieved at ACCesS along the line of sight of the absorption spectroscopy in front of the sample during vacuum and plasma operation. Typical neutral Cs densities achieved at the ion sources in front of the plasma grid are in the range of $10^{14}$–$10^{15}$ m$^{-3}$ [KWF+18].

The Alvatec dispensers [Alv16] were mainly applied during the work of [Fri13], together with the Cs dispenser oven described in [FFF12]. These dispensers

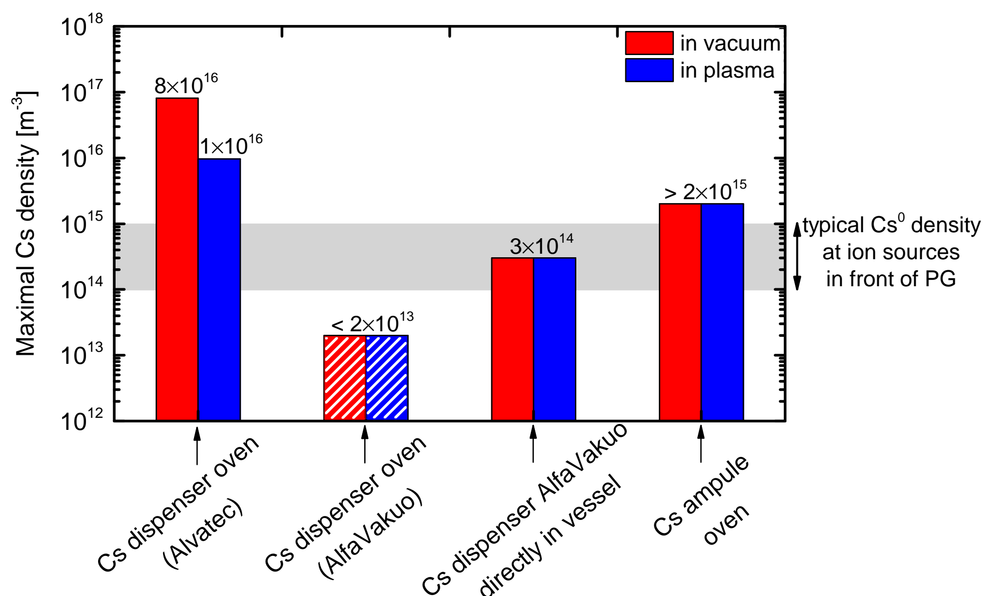


**Figure 9.1:** *Comparison of the different Cs sources applied in the current work, with the maximal Cs density achieved at ACCesS during vacuum and plasma operation.*

allowed to obtain Cs densities higher than $10^{16}$ m$^{-3}$ during vacuum and plasma operation [Fri13]. However, such high densities were obtained with ohmic currents higher than 8 A, leading to the release of Bi and In in addition to Cs, as confirmed in a later stage by RBS [Sch15, Rei15]. In the current work, the experiment was first cleaned with 5 % hydrochloric acid, distilled water, acetone, and isopropyl alcohol to completely remove the contaminants. One remaining Alvatec dispenser of 2010 was used during the current investigations, and ohmic currents of 8 A in maximum were applied in order to avoid contamination with Bi and In. The resulting Cs density was however lower than $10^{15}$ m$^{-3}$.

Due to termination of operation at the Alvatec company, new dispensers were ordered from AlfaVakuo in 2016 [Alf16]. The evaporation rate of these dispensers is much lower with respect to the Alvatec dispensers: when an AlfaVakuo dispenser was applied in the Cs dispenser oven and heated by a current of 8 A in vacuum operation, no Cs was detected by means of TDLAS. Therefore, the Cs density was below the TDLAS detection limit ($< 2 \times 10^{13}$ m$^{-3}$), not enough to have Cs deposition on the stainless steel sample installed for the investigations.

The AlfaVakuo dispensers were thus positioned directly in the vacuum vessel, in order to have direct evaporation from the dispenser towards the sample. In this configuration, Cs densities up to $3 \times 10^{14}$ m$^{-3}$ could be achieved during vacuum and plasma operation. However, these densities are lower than the typical values at ion sources in front of the plasma grid, and the direct application of the dispenser in plasma leads to instabilities of the evaporation, with the eventual release of Bi and In. The release of impurities was confirmed by RBS [Rei17] and EDX [Har17] measurements, and it was observed to occur when the gas temperature was around 500 K and the dispenser current was 7 A. The low evaporation rate of these dispensers, together with their possibly violent reaction to high temperatures (see for example the picture in figure 9.2), makes these dispenser not suitable for the current investigations (and neither for applications at ion sources).

In order to have a pure and reliable Cs source able to reach Cs densities higher than $10^{15}$ m$^{-3}$ Cs ampules are applied instead of the Cs dispensers, and a specific Cs ampule oven had to be designed and manufactured for the application at ACCesS. The oven is described in section 6.3, and the reservoir temperature allows to easily control the evaporation of Cs into the experiment. In the current investigations, a maximal Cs density of $2 \times 10^{15}$ m$^{-3}$ is reached at a reservoir temperature of 150 °C. However, higher Cs densities are in principle allowed by increasing further the reservoir temperature. Furthermore, the application of a

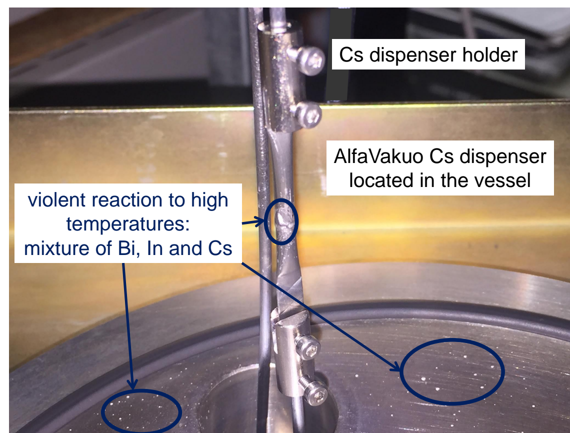


**Figure 9.2:** *Picture of the AlfaVakuo dispenser located directly in the vessel after a violent reaction to high temperatures ($T_{gas}$=500 K, dispenser current = 7 A) in plasma operation. Metallic droplets are clearly visible by eye.*

pure Cs source, like the ampule, avoids the possibility of contamination by heavy metallic impurities.

### 9.1.1 Evaporation under vacuum conditions

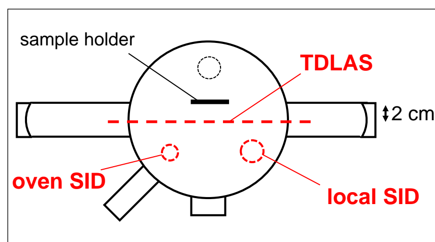


Prior to systematic investigations with Cs evaporation, the Cs ampule oven is tested in vacuum conditions in order to monitor its stability, controllability and reliability. It is to mention that once the ampule is cracked, not all the Cs drops from the ampule in the reservoir, but some Cs remains in the ampule. Hence, for the first days of operation with caesium it is not the temperature of the reservoir to control the Cs evaporation, but the temperature of the ampule, called $T_2$ (see figure 6.4). Once the residual caesium in the ampule is evaporated, $T_2$ can be kept at 280 °C without effects on the evaporation rate (as the rest of the oven body), and the evaporation of Cs is driven by the temperature in the reservoir ($T_1$).

Figure 9.3 shows the first day of evaporation of Cs in vacuum with the Cs ampule oven. On the top, the temperatures measured by the 5 thermocouples placed at the Cs oven are plotted, while on the bottom the signals from the oven SID, the local SID and the TDLAS system are shown. During the campaign, the sample temperature is 85 °C in maximum (the sample is heated due to irradiation from the hot SID filaments and due to the oven heating), while the walls' temperature

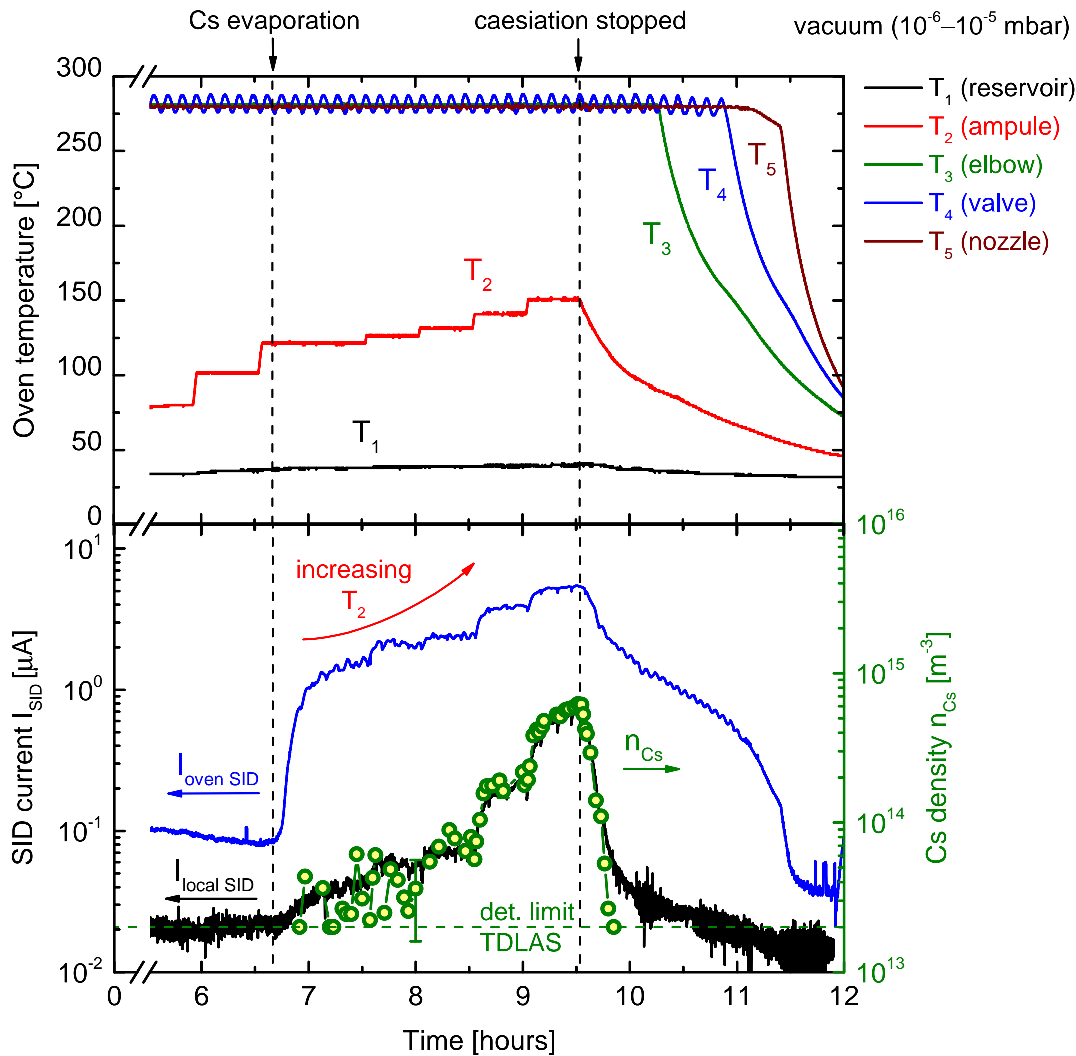


**Figure 9.3:** *Temperature of the different components of the oven: in particular, by increasing $T_2$ Cs is evaporated into the experiment. The Cs signals from the oven SID, local SID and TDLAS are monitored simultaneously.*

is below 30 °C. The control on the temperature of the walls allows avoiding cold spots (which would already lead to a Cs redistribution within the chamber) and to assure reproducible conditions at each campaign. The temperatures of the oven body are first increased to 280 °C, except for the part of the oven where the ampule is located and for the reservoir. The temperature of the valve ($T_4$) shows an oscillating signal probably due to the feedback control parameters of the oven, which might be not perfectly adjusted for $T_4$. However, this oscillation does not affect the Cs evaporation from the oven, hence it is not necessary to change the control parameters.

In order to evaporate Cs from the ampule, the temperature $T_2$ is gradually increased, while $T_1$ is kept at room temperature: consequently, the Cs redistribution inside the oven is driven towards the reservoir. In the first days of operation, $T_2$ is gradually increased up to 280 °C until it does not have anymore any influence on the Cs evaporation. Around 15 hours of operation are needed until the evaporation is controlled by $T_1$.

The evaporation of Cs into the chamber occurs at $T_2 = 120$ °C, as it can be seen in the bottom part of figure 9.3: the oven SID is the first diagnostic to clearly detect Cs, since it is located directly at the nozzle. Its current signal increases by one order of magnitude as soon as Cs starts to evaporate. A small increase is also visible at the local SID, while the TDLAS system detects Cs with a density close to the detection limit and shows small oscillations probably due to the big measurement uncertainty in this range of densities.

By increasing further the temperature of the ampule ($T_2$), all the Cs signals increase accordingly: for each temperature step, the signals react immediately and are stable after 5–10 minutes. The Cs density can thus be easily controlled just by the temperature of the oven. At $T_2 = 150$ °C, a Cs density of $6 \times 10^{14}$ m$^{-3}$ is reached. As soon as the heating of the ampule is stopped, the temperature gradually decreases, as well as all the Cs signals. It takes around 20 minutes to have a Cs density below the TDLAS detection limit. Hence, for an immediate termination of the Cs evaporation into the experiment, during usual vacuum operation the Cs oven valve should be closed when the caesiation is required to stop. This assures that the Cs content inside the experiment significantly decreases within few seconds.

As it can be seen in the bottom part of figure 9.3, the signals from the local SID and TDLAS follow the same relative behavior, thus the Cs evaporated from the edge cut nozzle is equally distributed towards the sample holder and towards the bottom plate where the local SID is located (the walls' temperature is constant at 28 °C).

During typical Cs operation in vacuum, the Cs evaporation is controlled by $T_1$. In this case Cs evaporation starts at 90 °C, and the typical temperature range for Cs operation is usually 90–110 °C during the current work, leading to measured Cs densities up to $2 \times 10^{14}$ m$^{-3}$.

### 9.1.2 Evaporation during plasma operation

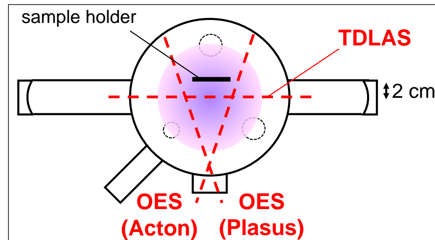


During plasma operation, the bias of the two SIDs is switched off, however the filaments are heated in order to avoid deposition of Cs on them. The Cs density is monitored by TDLAS, while the Cs emission of the $D_2$ resonance line is monitored by means of the two spectrometers (high resolution spectrometer: Acton; survey spectrometer: Plasus) along two different lines of sight.

Figure 9.4 shows typical plasma operation, in which Cs is evaporated into the experiment during the plasma pulse. The Cs signals from TDLAS and OES are plotted, together with the ampule temperature $T_2$. The oven body is heated to the working temperature of 280 °C, and the part where the ampule is located is gradually heated. The walls' temperature is always below 40 °C during plasma exposure. In this case, evaporation of Cs starts at 160–170 °C, i.e. at higher temperatures with respect to the vacuum case. For this specific campaign, the

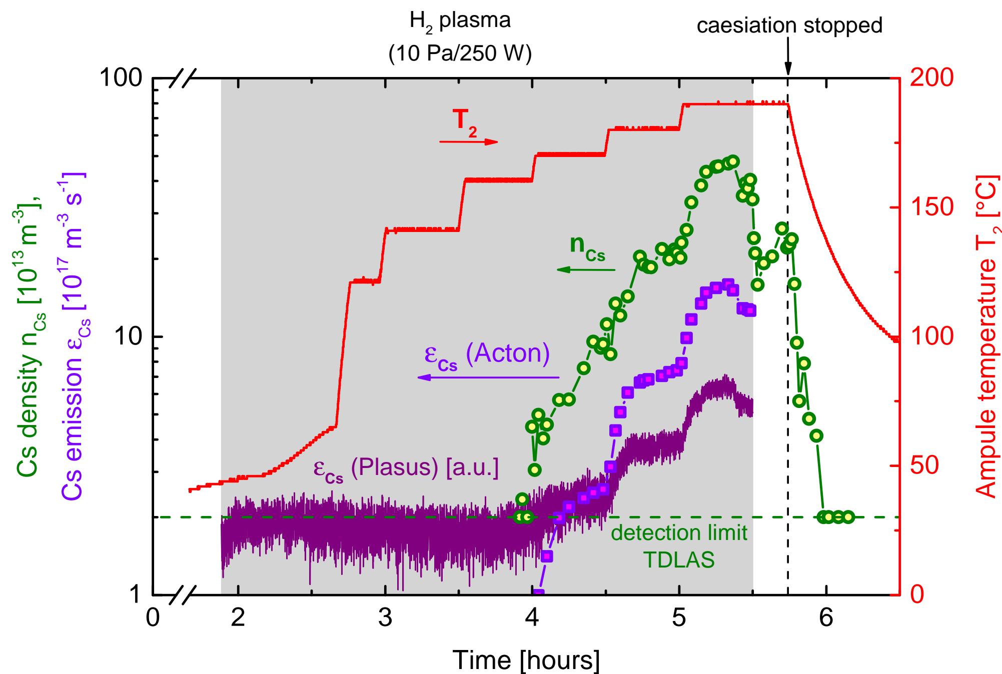


**Figure 9.4:** *Cs evaporation during plasma operation: the temperature of the ampule is gradually increased, while the Cs signals from TDLAS and OES (Acton and Plasus) are measured.*

Cs evaporation is still driven by $T_2$ since some Cs is still located in the ampule. However, the high temperature required to evaporate Cs suggests that Cs in the ampule is gradually depleted.

During typical plasma operation, Cs evaporation starts when $T_1$ is set to 90 °C, and the Cs densities obtained at varying $T_1$ are comparable to the vacuum case. The typical range of temperatures applied during the current work is 90–150 °C, leading to measured Cs densities up to $2 \times 10^{15}$ m$^{-3}$.

In figure 9.4 the increase of $T_2$ above 160 °C leads to an immediate response of the Cs signals monitored by TDLAS and OES. The Cs signals are not stable for ampule temperatures below 180 °C, while they are stable after around 20 minutes for constant ampule temperature above 180 °C. A Cs density of $5 \times 10^{14}$ m$^{-3}$ is reached at an ampule temperature of $T_2 = 190$ °C. However, in the last ten minutes of the plasma pulse, a small decrease of the Cs signals is observed.

The instabilities here observed are due to the depletion of the Cs in the ampule part of the oven. In fact, during typical Cs operation driven by $T_1$, the Cs signals are stable after around 20 minutes for constant temperature between 90 and 150 °C. Moreover, the RF noise during plasma operation does not affect the operation of the oven, whose temperatures are reliable and stable also during plasma.

Figure 9.5 shows the relative Cs signals from TDLAS and OES normalized to their maximum value. About the OES signal from the Plasus spectrometer, the background signal measured in the first hour of plasma is subtracted from the signal before the normalization. The three Cs signals measured along three different lines of sight, exhibit similar relative behaviors. Thus, the distribution of Cs during plasma operation is uniform inside the vessel.

After the plasma pulse, the Cs density immediately decreases as shown in figure 9.4. On the one hand, this decrease might be due to a decrease of the oven nozzle temperature by 5 °C when the plasma is switched off. On the other hand, during plasma operation the caesium particles deposited on the surfaces are redistributed in the vessel by the plasma (see section 9.3), hence when the plasma is switched off the Cs redistribution from the surfaces does not occur, leading to lower Cs densities in the volume. However, the Cs density starts to increase again after 2–3 minutes, reaching an equilibrium after around 10 minutes. When the heating of the ampule is switched off the Cs density decreases, assuming values below the TDLAS detection limit after around 20 minutes.

Such behavior after plasma suggests a strong redistribution dynamics every time the plasma is switched off. Hence, for the plasma investigations in the current

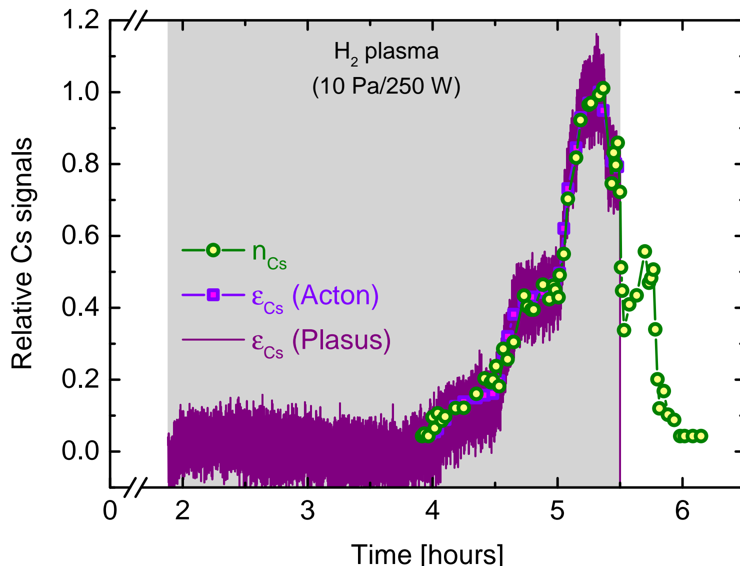


**Figure 9.5:** *Relative behavior of the different Cs signals from TDLAS ($n_{Cs}$) and OES (Acton and Plasus) during caesiation in plasma.*

work, when the plasma is stopped the heating of the oven is simultaneously switched off and the oven valve is closed, in order to avoid further Cs evaporation into the chamber during gas phases which would lead to undesired modification of the Cs layer on the sample surface after the plasma exposure.

## 9.2 Surface caesiation in vacuum

The purpose of the current investigations is to study the influence of plasma exposure on a caesiated layer. In order to achieve a caesiated layer, Cs is evaporated in vacuum ($10^{-6}$–$10^{-5}$ mbar) until the work function of 2.7 eV is achieved (from [Fri13, FF17] it is know that this value corresponds to a thick non-pure Cs layer). For the investigations shown in the present chapter, a stainless steel sample of size of $30 \times 30$ mm$^2$ and thickness of 2 mm is applied. Stainless steel was chosen as testing material due to its machinability and since it was the reference material in [Fri13], where it was shown that the impact of the substrate material on the work function of a caesiated surface is irrelevant for thick Cs layers ($>$ 1 ML). Before the caesiation, the sample surface is first exposed to hydrogen plasma (not shown here) in order to clean the surface from impurities coming from the air exposure and obtaining a work function around 4.5 eV. The work function of the

stainless steel sample the day after the plasma exposure results to be higher than 4.5 eV. For the present campaign in vacuum, the temperature of the sample is 85 °C in maximum. The walls' temperature during the caesiation in vacuum is below 30 °C.

Figure 9.6 shows the caesiation process of the sample. The Cs density is monitored with TDLAS, while the work function is measured at increasing Cs density. At the beginning of the campaign the work function is higher than 4.5 eV, and it decreases to 3.3 eV when Cs starts to be evaporated into the chamber with a Cs density of $4 \times 10^{13}$ m$^{-3}$.

The measured work function further decreases with increasing Cs density, until reaching the value of $\chi_{\mathrm{vac}} = (2.7 \pm 0.1)$ eV for a Cs density around $2 \times 10^{14}$ m$^{-3}$, with a corresponding Cs flux towards the surface of about $1.5 \times 10^{16}$ m$^{-2}$s$^{-1}$.

From [Fri13, FF17] it is known already that $\chi_{\mathrm{vac}} = 2.7$ eV is a saturation value for surfaces that are caesiated at moderate vacuum conditions: higher Cs fluxes do not allow to reach the expected work function for pure Cs, and $\chi_{\mathrm{vac}}$ does not depend on the substrate material used for the investigations, hence the resulting layer is a thick layer. For the campaign shown in figure 9.6, if only pure Cs is involved, a Cs flux of $1.5 \times 10^{16}$ m$^{-2}$s$^{-1}$ would lead to an equilibrium coverage of 0.84 monolayer (determined from figure 5.3 by balancing adsorption

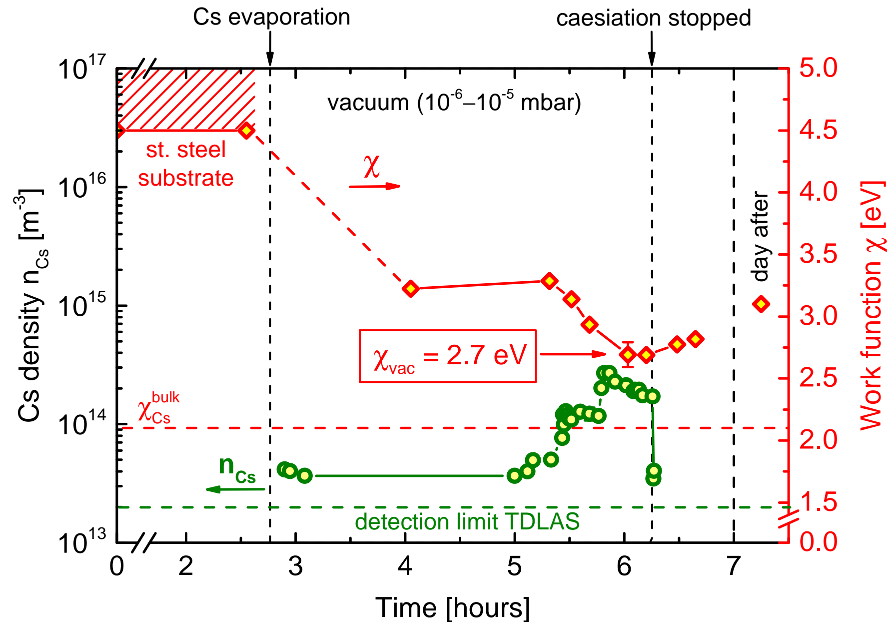


**Figure 9.6:** *Work function of a stainless steel sample in vacuum with increasing Cs density.*

and desorption fluxes for a sample temperature of 80 °C). This Cs coverage would in turn lead to a surface work function below 2.1 eV (as shown in figure 5.2), at least 0.6 eV lower than $\chi_{\mathrm{vac}} = 2.7$ eV. Moreover, the flux of impurities (mainly water vapor) towards the surface at $10^{-6}$ mbar is around two orders of magnitude higher than the Cs flux. Hence, such a high measured work function is due to the formation at the surface of a thick layer of non-metallic Cs compounds with the background gases. Unfortunately, the surface composition of the caesiated sample cannot be analyzed ex-situ, e.g. by means of EDX, since the air exposure of the sample would lead to a fast oxidation of the Cs layer.

When caesium evaporation is stopped the work function starts to increase, showing the degradation effect due to the influx of background gases. The measured degradation rate is of 0.1 eV/h, lower than the degradation rates found with the materials studied in the previous chapter. Moreover, the degradation rate at the caesiated surface decreases with time, and a work function of 3.1 eV is measured the day after the caesiation campaign in vacuum.

## 9.3 Plasma exposure on caesiated surfaces

When a caesiated surface (work function in vacuum of 2.7 eV) is in contact with plasma, several effects take place: the plasma particles, as well as UV and VUV light, impinge on the surface and modify the Cs layer (including residuals from the background gases), and additionally Cs is removed from the surface and redistributed all over the experiment. As a consequence, the work function is not temporally stable.

In order to study the effect of plasma exposure on the work function of a caesiated surface at ion source relevant parameters, a stainless steel sample is caesiated in vacuum until the work function decreases to 2.7 eV. At this point the Cs evaporation is stopped, and a pulsed hydrogen plasma at 10 Pa/250 W is applied ($\Gamma_{\mathrm{H}} \sim 1 \times 10^{22}$ m$^{-2}$s$^{-1}$, $\Gamma_{\mathrm{H}_x^+} \sim 1 \times 10^{20}$ m$^{-2}$s$^{-1}$, $U_{\mathrm{pl}} - U_{\mathrm{spl}} \sim 8$ V). The length of the pulses can be varied between seconds and hours, and the work function is measured directly after each pulse. The walls' temperature is always below 40 °C during plasma exposure.

Figure 9.7 shows the work function of a caesiated surface due to plasma exposure: already after 5 seconds of plasma the work function drops from 2.7 eV to 2.2 eV, reaching the value for pure Cs within the error bar, showing a cleaning effect of the plasma on the Cs layer by removing impurities present at the surface, as

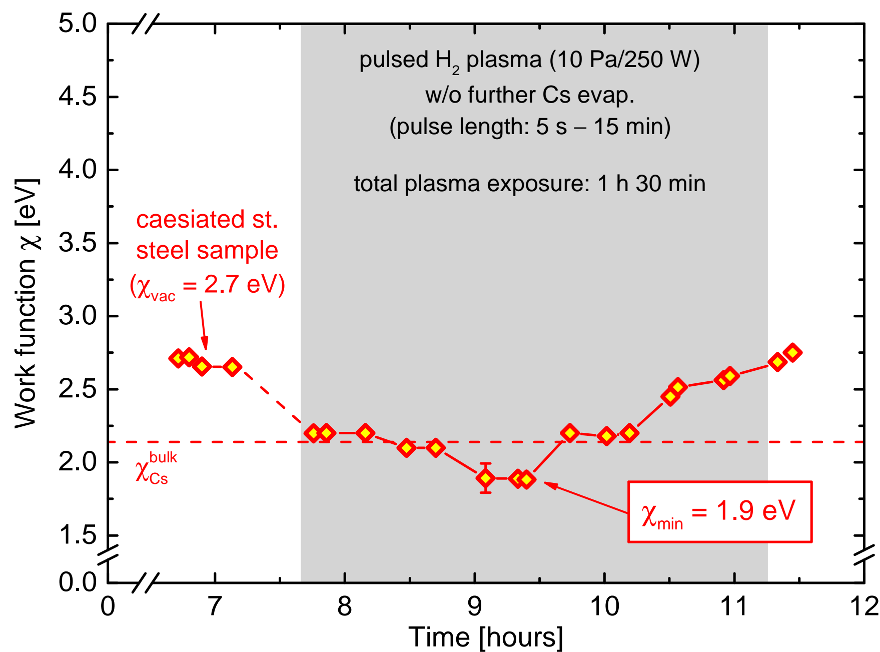


**Figure 9.7:** *Work function of an already caesiated stainless steel sample during pulsed hydrogen plasma exposure (length of the pulses between 5 s and 15 min).*

explained in section 5.4. The plasma-on time is then increased stepwise from 5 seconds to 15 minutes, interrupted only to measure the work function. The time interval between one plasma pulse and the following one is usually of 5–10 minutes. Due to the additional plasma exposure and the interaction of the plasma particles with the surface, the Cs is gradually removed from the surface since no fresh Cs is evaporated into the volume. The removal of the Cs layer leads to a change of the work function.

The work function reaches a minimum of $\chi_{\mathrm{min}} = (1.9 \pm 0.1)$ eV after an overall plasma-on time of 15 minutes. Such value is below the work function of bulk caesium, and this is due either to a Cs coverage below one monolayer on the sample surface and to the adsorption of hydrogen on a clean Cs monolayer. Regarding the former effect, the minimum value that is usually reached in ultra-high vacuum systems for some sub-monolayer of Cs coverage is between 1.4 and 1.8 eV (see section 5.2), depending on the substrate material. These values are slightly lower with respect to the one here measured, however none of the literature values refers to a stainless steel substrate and a moderate vacuum. Moreover, the presence of hydrogen particles adsorbed in the Cs layer have an influence on the resulting work function: as observed in [EKP87], the effect of hydrogen adsorption on a clean Cs

monolayer decreases the work function by few 0.1 eV, which is comparable with the measurements obtained at ACCesS. The resulting outcome observed on the work function is thus a combination of the two influences: both the adsorption of H in the Cs layer and the presence of a sub-monolayer of Cs on the surface lead to a lower work function with respect to the bulk Cs value.

After reaching $\chi_{\rm min}$ the work function starts to increase due to the removal of the Cs layer during plasma operation, and after an overall plasma-on time of 1.5 hours the surface work function is 2.7 eV at the end of the campaign, reaching the vacuum minimum value.

In order to confirm the Cs removal performed by plasma and to study the Cs redistribution during the plasma pulses, the campaign is repeated but with a longer plasma exposure: an already caesiated stainless steel sample is exposed to hydrogen plasma at 10 Pa/250 W with pulse lengths varying between 5 minutes and 2 hours. The surface work function and the Cs emissivity measured with the Acton spectrometer during the pulses are shown in figure 9.8. The Cs emissivity increases during one single pulse. This behavior of the Cs emissivity is due to the interaction of the plasma with the caesiated surface inside the experiment, breaking the bonds and releasing Cs from the surfaces. However, this is valid for

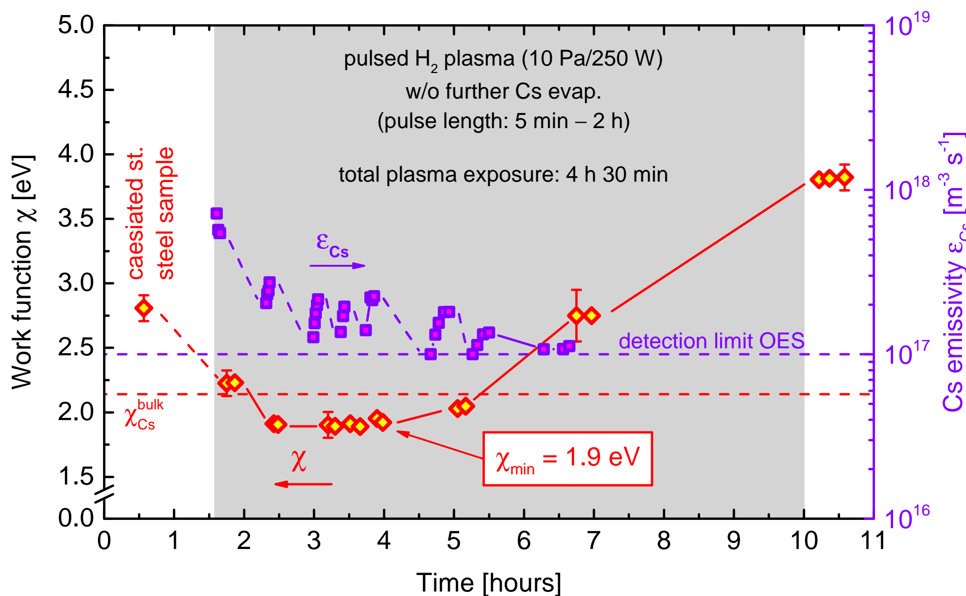


**Figure 9.8:** *Work function of a caesiated stainless steel sample during long pulsed hydrogen plasma exposure (length of the pulses between 5 min and 2 h). The Cs emissivity measured with the Acton spectrometer during the plasma pulses is also plotted.*

pulses up to 20 minutes long, while for longer pulses the Cs emissivity shows a maximum at 20 minutes and then it decreases, due to a depletion of the Cs layer at the surfaces. In the first plasma pulse of 5 minutes, the Cs emissivity reaches in maximum $7\times10^{17}$ m$^{-3}$s$^{-1}$, which corresponds to a Cs density around $2\times10^{14}$ m$^{-3}$ as determined from figure 9.4 (unfortunately the TDLAS system was not available for the present experimental campaign). Then, the Cs emissivity generally decreases from pulse to pulse, showing a strong dynamics between plasma and gas phases, until the signal reaches the detection limit for Cs detection, corresponding to Cs densities lower than $10^{13}$ m$^{-3}$.

The work function of the surface follows the same behavior observed in the previous campaign (shown in figure 9.7), but the longer plasma exposure in the current campaign leads to an increase of the work function up to 3.8 eV after an overall plasma-on time of 4.5 hours. A further plasma exposure (not shown here) leads to even higher values ($\chi \geq 4.2$ eV), approaching the work function of the bare stainless steel substrate (4.5 eV), confirming that the plasma is able to completely remove the Cs layer from the sample surface, resulting in a temporally unstable work function, if no fresh Cs is evaporated into the volume to counteract the Cs removal.

The behavior of the work function of a caesiated surface against the plasma-on time is plotted in figure 9.9 for several reproducible campaigns performed at similar conditions, together with the maximal temperature of the sample during each plasma pulse. The work function behavior proves to be reproducible and insensitive to slight variations of the plasma parameters among the different campaigns (caused by different geometries of the samples under investigation). 5–10 seconds of plasma exposure are sufficient to clean the Cs layer and to reach the value for bulk Cs (2.14 eV), while $\chi_{\text{min}}$ is achieved after around 10 minutes of plasma exposure. Longer plasma exposure times lead then to the increase of the work function, reaching a value of 3.8 V after 3–4 hours of plasma operation and approaching the work function of a clean stainless steel surface after more than 4 hours of plasma application. The sample temperature is always below 250 °C, hence in the case of caesiated surfaces the low work function is not determined by the temperature (which was the most relevant parameter for all the other materials investigated in chapter 8), but it is controlled by the interactions between the surface and the plasma facing the surface. Hence, the plasma exposure results to have the most crucial role for determining the status of the Cs layer, and consequently its surface work function.

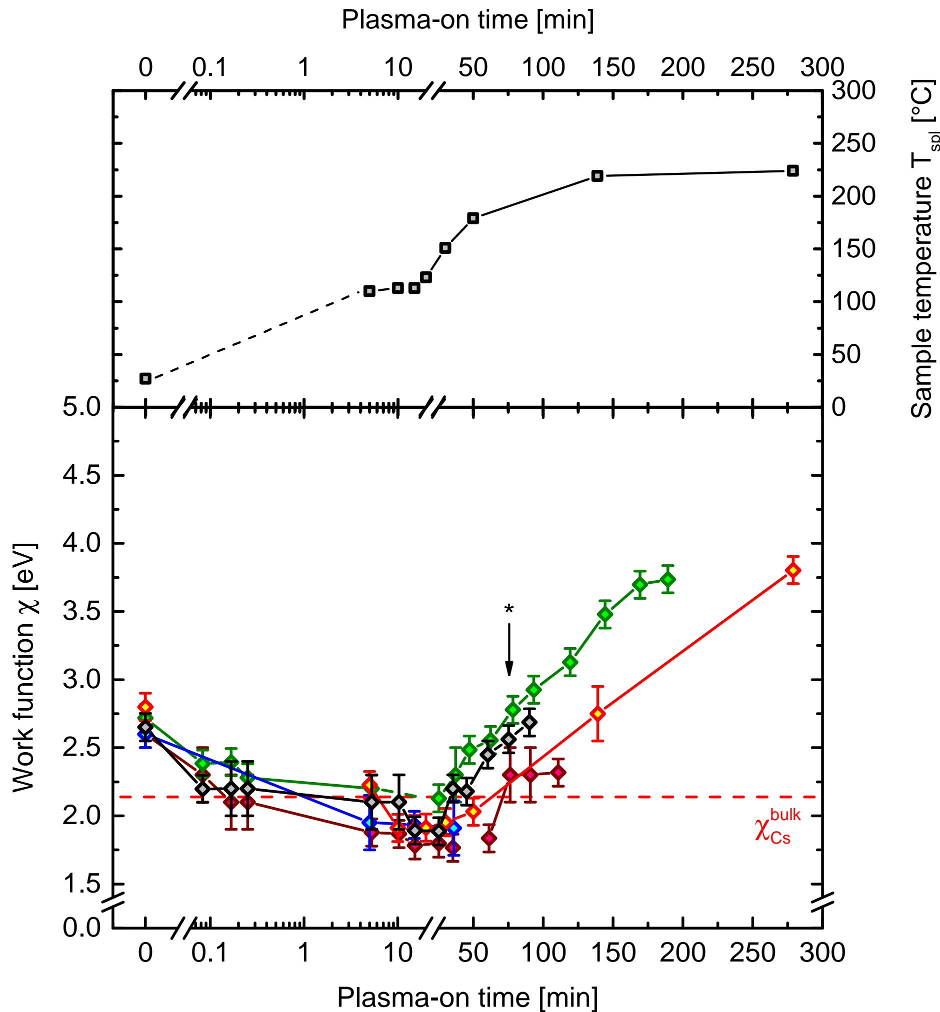


**Figure 9.9:** *Work function of a caesiated stainless steel sample plotted against plasma-on time during pulsed plasma operation at 10 Pa/250 W for different reproducible campaigns. The sample temperature is plotted on the top of the figure. * indicates the value for the work function after 1 hour and 15 minutes (useful for a comparison with the results obtained with Cs evaporation during plasma, shown in section 9.4).*

### Influence of a $D_2$ plasma on a caesiated surface

Since ion sources must operate also and especially in deuterium, the same investigation is performed with a deuterium plasma in order to determine whether the isotopic difference in the mass of the impinging particles is resulting in a faster removal of the Cs layer. The plasma parameters for hydrogen and deuterium at 10 Pa/250 W are summarized in table 9.1. In deuterium, the fluxes of impinging atoms and positive ions are slightly higher than in hydrogen, while the potential difference $U_{\mathrm{pl}} - U_{\mathrm{spl}}$ is similar for the two cases (8 V for hydrogen and 11 V for

**Table 9.1:** *Comparison between the plasma parameters obtained at 10 Pa/250 W for a hydrogen and a deuterium plasma.*

| | $H_2$ plasma | $D_2$ plasma |
|---|---|---|
| $n_\mathrm{e}$ [m$^{-3}$] | $1.4 \times 10^{16}$ | $2.0 \times 10^{16}$ |
| $T_\mathrm{e}$ [eV] | $1.5 - 2.1$ | $1.9 - 2.5$ |
| $T_\mathrm{gas} = T_\mathrm{H,D}$ [K] | 550 | 530 |
| $T_\mathrm{spl,max}$ [°C] | 225 | 275 |
| $\Gamma_\mathrm{H,D}$ [m$^{-2}$s$^{-1}$] | $1.3 \times 10^{22}$ | $1.8 \times 10^{22}$ |
| $\Gamma_{\mathrm{H}_3^+,\mathrm{D}_3^+}$ [m$^{-2}$s$^{-1}$] | $1.3 \times 10^{20}$ | $1.8 \times 10^{20}$ |
| $U_\mathrm{pl} - U_\mathrm{spl}$ [V] | 8 | 11 |

deuterium). Due to the higher mass of the impinging particles, the maximal temperature reached by the sample is 50 °C higher in deuterium, which would lead to higher Cs desorption fluxes with respect to the hydrogen case.

However, a comparable temporal behavior of the work function is observed, as shown in figure 9.10 in comparison with two of the hydrogen campaigns. Since the energies of the impinging positive ions are higher than the binding energy of the Cs compounds both for hydrogen and deuterium, both plasmas can clean the Cs layer within a short time scale: in deuterium the work function of a pure Cs layer is reached after 10 seconds of plasma exposure, comparable to the hydrogen case.

The plasma then gradually removes the Cs layer, and a minimum work function is reached at $(1.8 \pm 0.1)$ eV for deuterium. This value is slightly lower with respect to the one measured in hydrogen, i.e. $(1.9 \pm 0.1)$ eV, however the two values are in good agreement within the error bars, hence no difference can be deduced.

The rate of removal of the Cs layer is then really similar for the two plasmas as it can be seen in the figure until 250 minutes of plasma-on time. After 250 minutes, the results for deuterium show a different behavior: this is due to the fact that the campaign in deuterium was performed in two subsequent days, and the different behavior is caused by the stop overnight of the operation in deuterium, and the measurement at a work function of 3.8 eV should not be considered for the comparison between the two isotopes.

Hence, the behavior of the work function during plasma exposure is similar for hydrogen and deuterium plasmas, without any significant isotopic effect despite the slightly higher fluxes and the higher sample temperature achieved in deuterium.

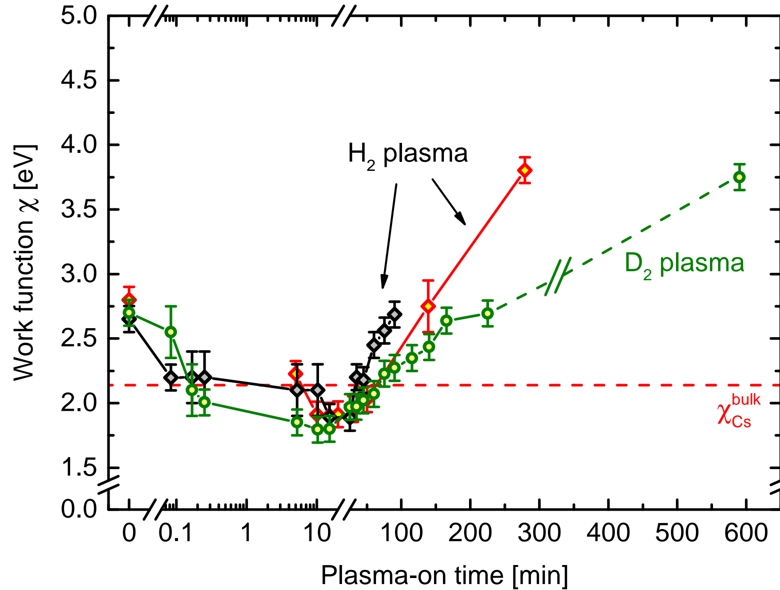


**Figure 9.10:** *Work function of a caesiated stainless steel sample plotted against plasma-on time during pulsed plasma operation at 10 Pa/250 W in hydrogen and in deuterium.*

## 9.4 Caesiation during plasma

To counteract the Cs removal during plasma operation, it is mandatory to continuously evaporate fresh Cs into the experiment. In this way, it is possible to maintain a stable Cs layer on the sample surface and hence a temporally stable work function. Ion source must operate with bulk Cs, hence a sufficient Cs flux must be assured to maintain a work function of 2.1 eV. Investigations are thus performed at ACCesS in order to study the evolution of the work function when a stable Cs flux is evaporated towards the surface in plasma operation. In [FF17] only the case of high Cs fluxes was studied, corresponding to $10^{17}$ $m^{-2}s^{-1}$. Such flux assures a thick layer of Cs also during plasma, with a work function of 2.1 eV. However, for the current investigations the low range of Cs fluxes is studied, in order to determine the minimum sufficient Cs flux to assure the work function of bulk Cs (after the request of minimizing the Cs consumption).

In order to avoid strong dynamics of Cs redistribution occurring when the plasma is switched on and off (as observed in section 9.1.2), Cs evaporation is performed during continuous plasma operation. When the plasma is switched off, the heating of the reservoir is stopped and the oven valve is simultaneously closed,

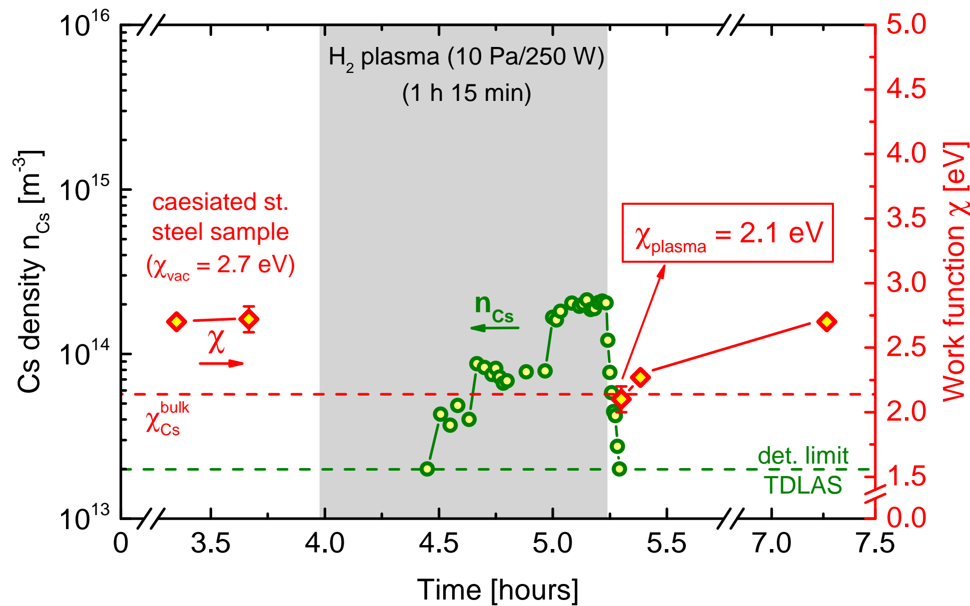


**Figure 9.11:** *Work function of a caesiated stainless steel sample due to hydrogen plasma exposure at 10 Pa/250 W with fresh Cs evaporated during plasma.*

in order to avoid Cs evaporation after plasma.

Figure 9.11 shows the work function of a caesiated stainless steel sample (work function of 2.7 eV) after 1 hour and 15 minutes of continuous exposure to hydrogen plasma at 10 Pa/250 W, with fresh Cs evaporated into the vessel during plasma. The sample reaches temperatures up to 225 °C, while the walls' temperature is always below 40 °C. In order to maintain a bulk Cs work function at the caesiated surface also during plasma, a Cs density of $2 \times 10^{14}$ m$^{-3}$ (corresponding to a Cs flux towards the surface of $1.5 \times 10^{16}$ m$^{-2}$s$^{-1}$) is sufficient to achieve a work function of $\chi_{\text{plasma}} = (2.1 \pm 0.1)$ eV. In fact, if no fresh Cs is evaporated into ACCesS, the work function of the surface would reach values higher than 2.3 eV after 75 minutes of plasma exposure, as marked by * in figure 9.9, instead of 2.1 eV.

After plasma exposure the typical work function degradation occurs due to the presence of background impurities, reaching a work function of 2.7 eV after 2 hours at a degradation rate of 0.3 eV/h. Such value measured after plasma exposure is higher by a factor of 3 than the degradation rate measured after caesiation in vacuum, and it is similar to the degradation rate observed with the $LaB_6$ sample after plasma treatment suggesting a higher reactivity of these surfaces after plasma treatment. However, the degradation rate is still much lower

respect to the Eu sample in section 8.4, showing thus a lower reactivity of Cs with respect to Eu especially after plasma exposure.

In order to determine if this Cs flux towards the surface is the minimum flux required to maintain a bulk Cs layer and a temporally stable work function at 2.1 eV, the same caesiation procedure is repeated with different Cs fluxes at reproducible conditions. The work function measured for different Cs fluxes during long pulse plasma operation is shown in figure 9.12. For Cs fluxes lower than $2 \times 10^{15}$ m$^{-2}$s$^{-1}$ the fresh caesium coming to the surface is not enough to balance the removal of Cs performed by the interaction with the plasma, hence the work function increases up to 3.8 eV during long plasma exposures, as confirmed in figure 9.8 after a plasma exposure of 4 hours and 30 minutes. At a continuous Cs flux of $4.5 \times 10^{15}$ m$^{-2}$s$^{-1}$ ($n_{\mathrm{Cs}} = 6 \times 10^{13}$ m$^{-3}$), the incoming Cs flux is not sufficient to maintain a bulk Cs layer, leading to a work function of 2.3 eV, hence the Cs coverage is below one monolayer. Instead, a Cs flux of $1.5 \times 10^{16}$ m$^{-2}$s$^{-1}$ is sufficient to maintain a work function of 2.1 eV also during plasma.

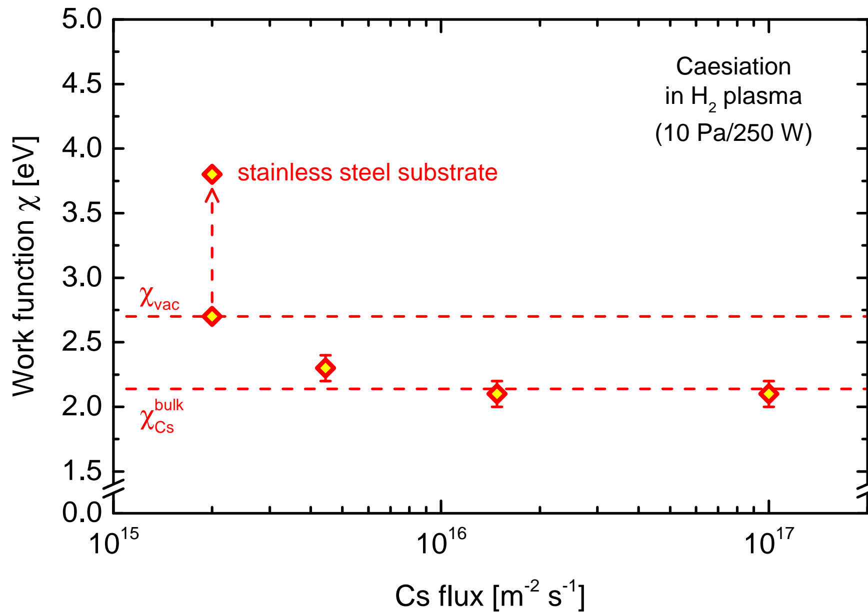


**Figure 9.12:** *Work function of a caesiated stainless steel sample due to hydrogen plasma exposure at 10 Pa/250 W with fresh Cs evaporated during plasma. The value corresponding to a Cs flux of* $10^{17}$ *m*$^{-2}$*s*$^{-1}$ *refers to measurements of [FF17] in the same setup.*

# 10 Correlation between $H^-/D^-$ density and work function

To investigate the correlation between the work function and the resulting $H^-$ density measured in front of a surface, an appropriate choice of plasma parameters is performed as introduced in section 7.3: a pressure of 2 Pa and an RF power of 450 W are applied, in order to have a low volume produced $H^-$ density (constituting the detection limit for the surface production) and to increase the energy of the positive ions impinging on the surface (which increases the surface production probability).

Since the CRDS system provides a line of sight averaged measurement of the $H^-$ density, the total number of negative ions created along the line of sight is decisive for the sensitivity of the CRDS and the detection of negative hydrogen ions created by surface processes. Hence, for the investigations presented in this chapter a clean stainless sample (work function of around 4.5 eV) with a size of $140 \times 24$ mm$^2$ and thickness of 1 mm is applied, elongated along the vessel diagonal. The $H^-$ density is thus measured first with the clean sample to measure the volume produced $H^-$, then the caesiation of the sample is performed during continuous plasma operation, and all the diagnostics run simultaneously in order to monitor all the plasma parameters. Caesiation in plasma is performed in order to assure a surface work function of 2.1 eV at the end of the plasma pulse, and the $H^-$ density is measured. Caesiation and plasma are stopped simultaneously. Finally, a pulsed plasma is applied without any further caesiation in order to change the work function of the surface by reducing the Cs layer, as observed in section 9.3. For each work function obtained thereby the negative hydrogen ion density is measured.

The whole procedure is then repeated with a deuterium plasma at 2 Pa/450 W for a comparison between $H^-$ and $D^-$ surface formation at similar plasma parameters.

## 10.1 Caesiation in $H_2$ plasma at 2 Pa/450 W

Caesiation of the stainless steel sample is performed in continuous plasma operation, since during caesiation in pulsed operation the Cs redistribution and evaporation from the oven are strongly affected by the recurring switching between gas and plasma phases, as observed in section 9.1.2. Moreover, the plasma does not ignite at such low pressures (2 Pa) since it would require an RF power higher than the currently available (> 600 W). Thus, the pressure must be first increased to 10 Pa at the beginning of the pulse to ignite the plasma and then decreased to the operating pressure of 2 Pa to allow the investigations. Hence, pulsed operation would lead to very complex Cs dynamics, and the caesiation is therefore performed during continuous plasma operation.

During the caesiation procedure, the Cs density is stepwise increased up to $1.8 \times 10^{15}$ m$^{-3}$, necessary to obtain a work function of 2.1 eV at such plasma conditions (2 Pa/450 W). Such a Cs flux is one order of magnitude higher than the Cs flux required to obtain the same work function of 2.1 eV during plasma operation at 10 Pa/250 W (see section 9.4). The higher required Cs flux is due the higher impinging positive ion energy (which is higher by a factor of 2.5 at 2 Pa), while the ion flux is similar (see table 7.3). Furthermore, the sample temperature reached during the present investigations at 2 Pa is 320 °C, almost 100 °C higher than in the case at 10 Pa. Hence, higher desorption fluxes are expected at 2 Pa, confirmed in the need of a higher Cs flux towards the surface to counteract the Cs removal.

Every time the Cs density is increased, the plasma is let to stabilize for half an hour before measuring the plasma parameters via OES and Langmuir probe. During this time the Cs density is very stable, and it reaches the maximum density of $1.8 \times 10^{15}$ m$^{-3}$ (for the current investigations) after around 5 hours of continuous plasma exposure. In order to avoid Cs deposition on the Langmuir probe, the tip is shortly heated until it is glowing before each measurement acquisition. In the present campaign, the walls' temperature is always below 45 °C.

The behavior of the several plasma parameters during Cs evaporation is already shown in [Fri13, FF14] for the case of 10 Pa/250 W. A similar behavior occurs for plasmas at 2 Pa/450 W, hence the current investigations are not focusing on the effect of Cs on the bulk plasma, but on the new results of negative ion density in correlation with the relevant plasma parameters and the surface work function.

Figure 10.1 shows the electron density and temperature during the caesiation

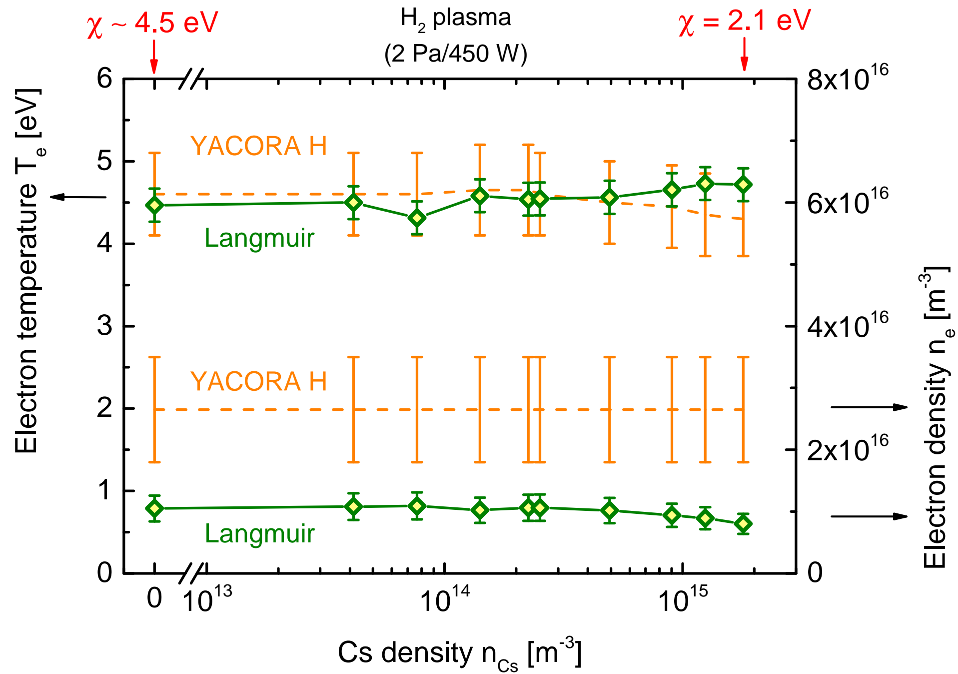


**Figure 10.1:** *Electron density and electron temperature obtained with the Langmuir probe (in green) and with the CR model YACORA H (in orange) for different Cs densities during hydrogen plasma at 2 Pa/450 W. The total plasma exposure time is around 5 hours.*

process, hence for increasing Cs density. The measurements obtained by means of the Langmuir probe are plotted in green, while the ones obtained from the CR models YACORA H (together with YACORA $H_2$) by means of the OES measurements (with the Acton spectrometer) are shown as a range of possible values in orange. For brevity, in the following section only YACORA H will be named, also if YACORA $H_2$ is applied in combination. It must be considered that the Langmuir probe measures locally the plasma parameters in the vicinity of the surface (at around 8 mm distance), while the spectroscopic measurements are averaged along the line of sight which crosses the experiment above the sample (see the top view schematic in section 6.4.2).

The electron temperature is stable around 4.6 eV both from the Langmuir probe and the YACORA H model, showing also no dependency on the Cs density. The electron density evaluated with YACORA H is instead higher with respect to the one measured by the Langmuir probe. This discrepancy can be traced back to the different position of the diagnostics and distance from the sample, and the electron density is expected to be lower in the vicinity of the sample, as also observed in [SFA+01] and [Fri13, FF14]. During the caesiation of the sample the electron

density from YACORA H seems stable, however the range of possible values given by the YACORA H model is quite large to effectively deduce a general behavior. Instead, the electron density measured via the Langmuir probe in the vicinity of the surface decreases for Cs densities higher than $2 \times 10^{14}$ m$^{-3}$: in absence of Cs and with a high surface work function ($\chi \sim 4.5$ eV) the electron density is around $1.1 \times 10^{16}$ m$^{-3}$, and it decreases until reaching $8 \times 10^{15}$ m$^{-3}$ for a caesiated surface ($\chi = 2.1$ eV and $n_{\mathrm{Cs}} = 1.8 \times 10^{15}$ m$^{-3}$), showing a decrease of $-26\,\%$, comparable to the value found in [Fri13] (i.e. $-25\,\%$ at 5 mm distance of the Langmuir probe tip from the sample surface).

Concerning the atomic hydrogen density, the emissivity ratio of the $\gamma$-Balmer line to the Fulcher emission is considered: it decreases with increasing Cs density, and when the Cs density is at $1.8 \times 10^{15}$ m$^{-3}$ the ratio is decreased by $50\,\%$ as shown in figure 10.2. The related atomic density obtained by means of the model YACORA H shows the same decreasing behavior, though the absolute value is not exactly determined and a range of possible values is given as output from the model: $n_{\mathrm{H}}$ is of the order of $10^{18}$ m$^{-3}$ at the beginning of the campaign, when no Cs is involved, and it decreases by one order of magnitude for Cs densities up to nearly $2 \times 10^{15}$ m$^{-3}$. The strong decrease of the atomic hydrogen density arises

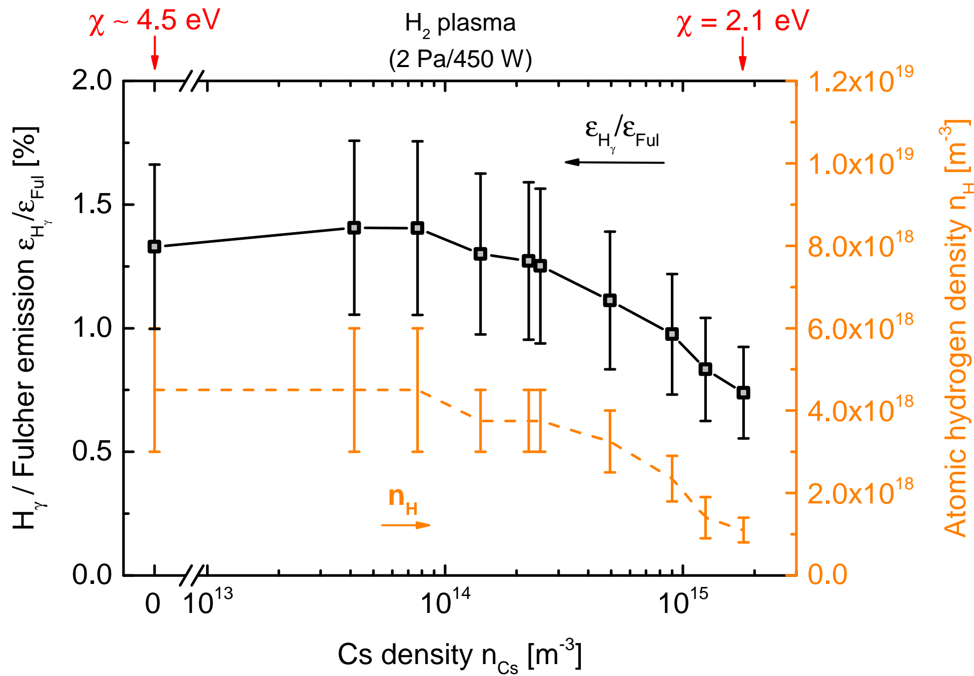


**Figure 10.2:** *The measured $H_\gamma$ to Fulcher emissivity ratio and the atomic hydrogen density obtained via the CR model YACORA H are plotted for different Cs densities during hydrogen plasma at 2 Pa/450 W.*

from the getter effect of Cs at the experiment surfaces, comparable to the case at 10 Pa/250 W observed in [Fri13, FF14].

The negative hydrogen ion density measured by means of CRDS is plotted in figure 10.3, together with the electron density from the Langmuir probe (i.e. close to the surface) and the difference between plasma potential (measured via the Langmuir probe) and sample potential, which determines the energy of the positive ions impinging on the surface. When the surface work function is $\sim 4.5$ eV and the Cs density is zero (hence with the bare stainless steel sample), the $H^-$ are created by volume processes and the $H^-$ density is below the detection limit of the CRDS system, i.e. $\leq 5 \times 10^{14}$ m$^{-3}$. During the caesiation process, the negative hydrogen ion density is difficult to be tracked, since reliable measurements can only be performed at the end of the plasma pulse, as explained in section 7.2.2. Hence, the $H^-$ density is measured only at the last phase, for a Cs density of $1.8 \times 10^{15}$ m$^{-3}$ and a surface work function of 2.1 eV. The resulting $n_{H^-}$ is of $1.4 \times 10^{15}$ m$^{-3}$, hence the $H^-$ density is increased by at least a factor of 2.8 due to the enhanced surface production at a low work function surface. The decrease of the electron density is thus connected to the simultaneous enhancement of

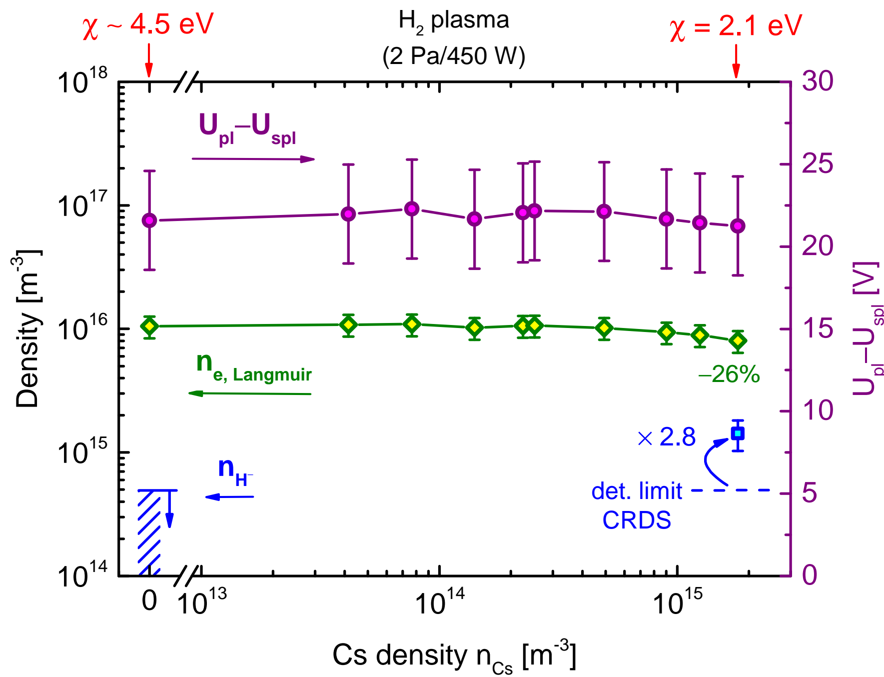


**Figure 10.3:** *Negative hydrogen ion density and electron density, measured via CRDS and Langmuir probe respectively, for different Cs densities in hydrogen plasma at 2 Pa/450 W. The potential difference between plasma and sample is also shown.*

the negative hydrogen ion density: in order to fulfill quasi-neutrality, the sum of the negative ion density and the electron density must be constant to balance the positive ions density which corresponds to $\sim 1.1 \times 10^{16}$ m$^{-3}$. Furthermore, figure 10.3 shows the difference between plasma potential and sample potential, which is constant and stable around 21 V over the whole campaign, resulting in a constant energy of the positive ions impinging on the surface for increasing Cs density. As a consequence, the flux of surface produced negative ions increases during the caesiation campaign only due to a decrease of the work function, since both the positive ion flux and the energy of the impinging positive ions are constant.

## 10.2 Correlation between $H^-$ density and work function

After the sample was caesiated during the long plasma operation at 2 Pa/450 W, reaching the final work function of 2.1 eV, the caesiation was stopped. From section 9.3 it is known that the plasma exposure can remove gradually caesium from the surface, and consequently change the work function if no fresh Cs is evaporated into the vessel. Hence, after caesiation of the sample plasma pulses are applied to vary the work function of the surface. For each work function, the corresponding $H^-$ density at 2 Pa/450 W is measured for a correlation between negative ion density in front of the surface and the corresponding work function.

Figure 10.4 shows the $H^-$ density measured at 2 Pa/450 W for different surface work functions, as well as the electron density measured in the vicinity of the surface by the Langmuir probe, and the potential difference between plasma and sample. The performed experimental procedure is the following: the very first measurement is the one corresponding to the bare stainless steel, at a work function of around 4.5 eV and before any caesiation of the sample. Then, measurements at 2.1 eV (at the end of the sample caesiation shown in section 10.1) are performed. The subsequent plasma exposures, with no further caesiation of the sample, allow to investigate the case of intermediate work functions (for the present campaign: 2.3 eV, 2.6 eV, and finally 3.7 eV).

For a surface work function of 4.5 eV and 3.7 eV, the negative hydrogen ion density is below the detection limit of the CRDS ($< 5 \times 10^{14}$ m$^{-3}$). At $\chi = 2.6$ eV the $H^-$ density is slightly above the detection limit ($n_{H^-} \sim 6 \times 10^{15}$ m$^{-3}$), and for lower work functions the negative ion density increases gradually up to

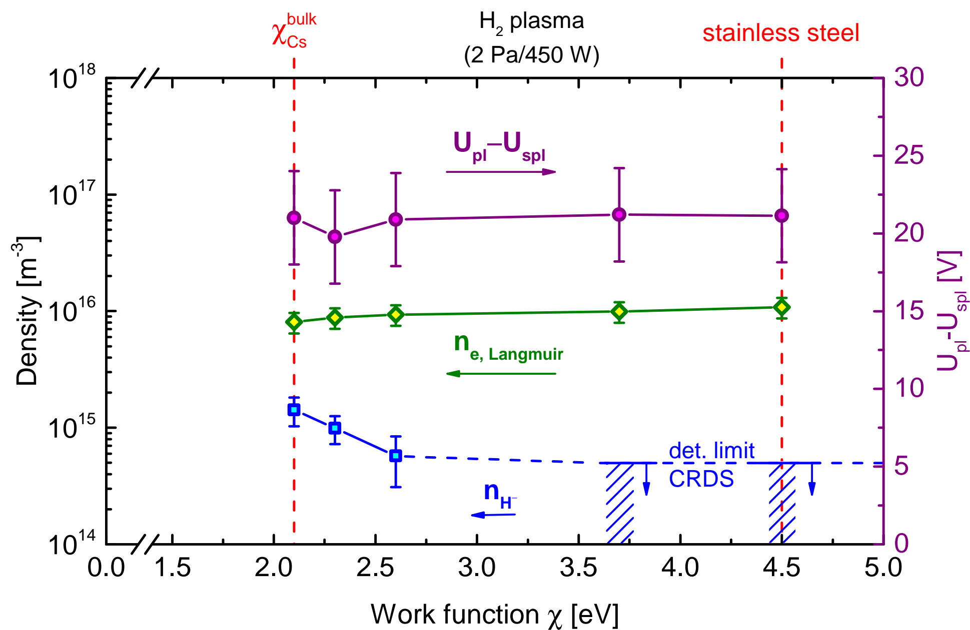


**Figure 10.4:** *Negative hydrogen ion and electron densities for different surface work functions for hydrogen plasma at 2 Pa/450 W. The difference between plasma potential and sample potential is also plotted.*

$1.4 \times 10^{14}$ m$^{-3}$ at $\chi = 2.1$ eV. Simultaneously, the electron density decreases from $1.1 \times 10^{16}$ m$^{-3}$ (measured at 4.5 eV) until a reduction of 26 % is obtained at 2.1 eV, as described in the last section. The decrease of the electron density is thus correlated to the simultaneous increase of the $H^-$ density at low work functions, while the sum of the densities (corresponding to the positive ion density due to the quasi-neutrality principle) is constant within the error bars ($\sim 1.1 \times 10^{16}$ m$^{-3}$). The energy of the positive ions impinging on the sample, determined by $U_{pl} - U_{spl}$ plotted in figure 10.4, is also constant for the different surface work functions. The main surface conversion mechanism at ACCesS is the one associated to the positive ions, as explained in section 7.3.2. Since the amount of positive ions and their energy are constant for varying work function, the decrease of the work function leads to an enhancement of the surface production of the negative ions.

In order to determine if the increase of the $H^-$ density occurring at low work function values is effectively due to an enhanced surface production, the volume production of negative ions is investigated for the different cases. Given the plasma parameters in hydrogen, the density of volume produced negative hydrogen ions is predicted by the YACORA $H^-$ model, introduced in section 7.3.1. For the present investigations, $T_{vib}^{low}$ (obtained by means of OES) varies between 2500 K at $\chi = 2.1$ eV and 3500 K at $\chi = 4.5$ eV. $T_{vib}^{high}$ is deduced from the $H^-$ density

measured at a work function of 4.5 eV, since the surface production mechanisms are negligible and the total $H^-$ density originates from volume processes only. Unfortunately, the negative ion density at $\chi = 4.5$ eV is below the CRDS detection limit, hence it is below $5 \times 10^{14}$ m$^{-3}$. As a consequence, the resulting $T_{\mathrm{vib}}^{\mathrm{high}}$ cannot be precisely deduced. However, in order to obtain an $H^-$ density of $5 \times 10^{14}$ m$^{-3}$, a high vibrational temperature of 6850 K is required. Thus, $T_{\mathrm{vib}}^{\mathrm{high}}$ is assumed to lay in the range between $T_{\mathrm{vib}}^{\mathrm{low}}$ (in this case a Boltzmann distribution of the vibrational population of $H_2$ molecules occurs) and 6850 K. This range of $T_{\mathrm{vib}}^{\mathrm{high}}$ is then applied to all the different cases with work function lower than 4.5 eV in order to calculate the volume produced $H^-$ density, which in turn will be given as a range shown in figure 10.5 as a gray shaded area. The negative hydrogen ion density expected from volume production might slightly increase for low work functions due to a decrease of the destruction rate of the associative detachment in equation (4.9), since the atomic hydrogen density decreases when Cs is applied (as observed in figure 10.2). However, the range of values corresponding to the volume production is lower than the actual $H^-$ density measured by CRDS at work functions of 2.1 eV and 2.3 eV, assuring that the increase of the $H^-$ density is due to the contribution of surface produced negative ions at low work functions.

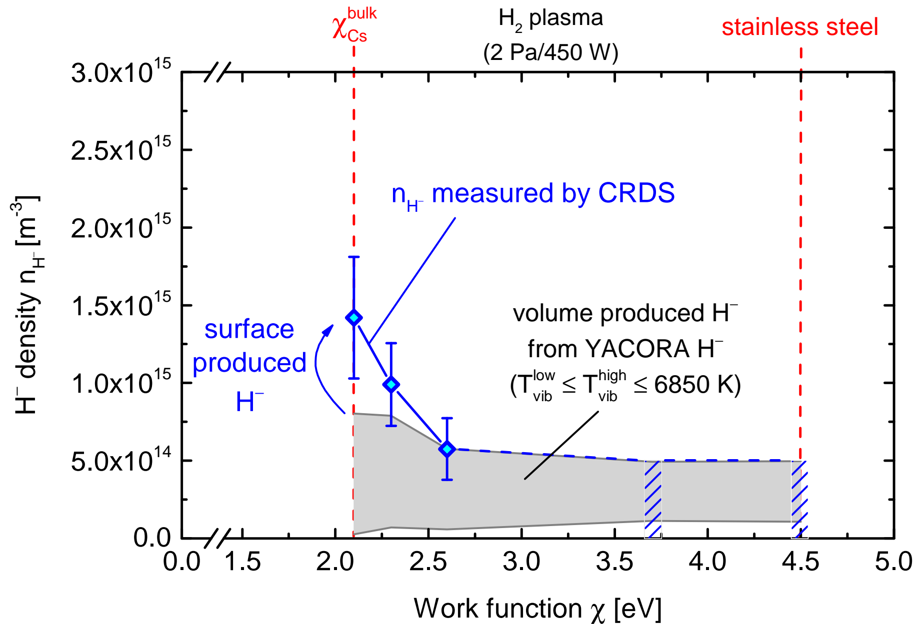


**Figure 10.5:** *The negative hydrogen ion density measured by CRDS is shown for different work functions at 2 Pa/450 W. The gray shaded area shows possible values for the $H^-$ density created by volume processes and obtained from the YACORA $H^-$ model.*

## 10.3 Comparison between $H_2$ and $D_2$ plasmas regarding surface production of negative ions

Since at ion sources deuterium operation is more relevant, and only barely information is available on the isotopic difference, similar caesiation procedure and investigations described in the previous sections are repeated in deuterium at 2 Pa/450 W. Figure 10.6 shows the negative ion density $n_{\mathrm{i}^-}$, measured by the CRDS, and the electron density $n_{\mathrm{e}}$, measured by means of the Langmuir probe close to the sample surface, for the hydrogen case in blue and for the deuterium case in red.

On the one hand, the electron density is higher in deuterium ($1.6 \times 10^{16}$ m$^{-3}$) with respect to the hydrogen plasma. The 45 % higher electron density leads to a higher volume production rate of negative ions in deuterium operation with respect to hydrogen. On the other hand, the main destruction mechanism is the associative detachment with atoms (as observed in section 7.3.1) and the emissivity ratio of the $\gamma$-Balmer line to the Fulcher emission, which is connected to the atom density, is 17 % higher in deuterium with respect to hydrogen, increasing

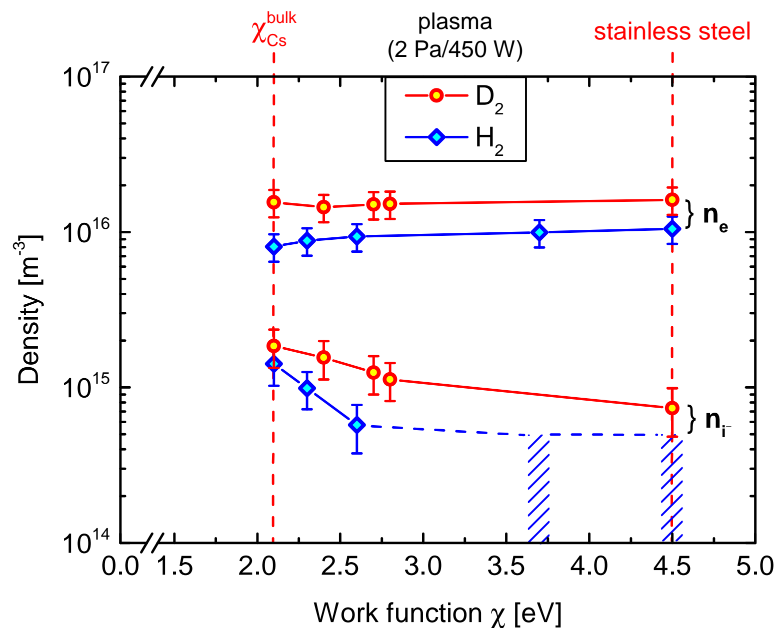


**Figure 10.6:** *Comparison between hydrogen (in blue) and deuterium (in red) for the negative ion density and the electron density (from the Langmuir probe) for different work functions.*

slightly the destruction rate. However, a lower increase is observed in deuterium for the atom density (+17 %) with respect to the electron density (+45 %). As a consequence, the resulting volume produced negative ion density is higher in deuterium: for a work function of 4.5 eV, corresponding to a clean stainless steel surface, the negative ions are mainly produced by volume mechanisms, and while for hydrogen the H$^-$ density is below the detection limit of the CRDS ($\leq 5 \times 10^{14}$ m$^{-3}$), in case of deuterium operation the measured D$^-$ density is $n_{\mathrm{D^-}} = 7 \times 10^{14}$ m$^{-3}$.

For decreasing work function down to 2.1 eV, the negative ion density increases for both isotopes, reaching $1.4 \times 10^{15}$ m$^{-3}$ for hydrogen and $1.8 \times 10^{15}$ m$^{-3}$ for deuterium at $\chi = 2.1$ eV. The D$^-$ density shows an increase by a factor of 2.5 from the value measured at $\chi = 4.5$ eV, comparable with the hydrogen case where at least a factor of 2.8 is observed.

However, while in the hydrogen case the electron density decreases for increasing negative ion density, during deuterium plasma operation the electron density is stable over the whole range of work functions. Figure 10.7 shows on the bottom the ratio of the negative ion density to the electron density for the two different isotopes. For hydrogen it strongly increases for low work functions, from values below 5 % at $\chi = 4.5$ eV to 18 % at $\chi = 2.1$ eV. In deuterium, the ratio increases from 5 % at $\chi = 4.5$ eV to 12 % at $\chi = 2.1$ eV, lower value with respect to the ratio measured in hydrogen. Hence, the density ratio is less affected by the change of the work function in deuterium operation. The reason for a reduced influence of the negative ions on the electrons during deuterium operation might be attributed to a less surface production of negative ions, hence the surface mechanism is investigated in the following for deuterium and hydrogen.

In order to determine if the difference between the measured H$^-$ and D$^-$ density is due to isotopic differences in the surface production of negative ions, the positive ion flux and the positive ion energy are considered since they determine the resulting surface produced negative ion density. The positive ion density is given by the sum of electron density and negative ion density: the positive ion density does not significantly change over the work function range for both the isotopes, and it is around $1.1 \times 10^{16}$ m$^{-3}$ for hydrogen and $1.7 \times 10^{16}$ m$^{-3}$ for deuterium. However, though the deuterium plasma shows a higher density with respect to the hydrogen plasma, the flux of positive ions towards the surface is comparable for the two isotopes due to the difference in mass, resulting in a flux of $1.6 \times 10^{20}$ m$^{-2}$s$^{-2}$ for hydrogen and $1.7 \times 10^{20}$ m$^{-2}$s$^{-2}$ for deuterium.

The difference between plasma potential and sample potential, shown on the top of figure 10.7, is around 18 V for deuterium, slightly below the potential difference measured in hydrogen (21 V), and it is constant over the work function range. The potential difference determines the energy of the positive ions impinging on the surface, and thus the conversion yield for the process involving the positive ions: for hydrogen, a conversion yield of 32 % is extrapolated from the 3rd degree polynomial fit in figure 4.3, while for deuterium a slightly lower conversion yield is found (29 %). Such conversion yields refer to a partially caesiated surface, but they give an indication of the dependence of the conversion yield on the impinging particle energy. However, considering the large error bars on $U_{\text{pl}} - U_{\text{spl}}$ and the large scattering of the measured conversion yields in figure 4.3, a comparable

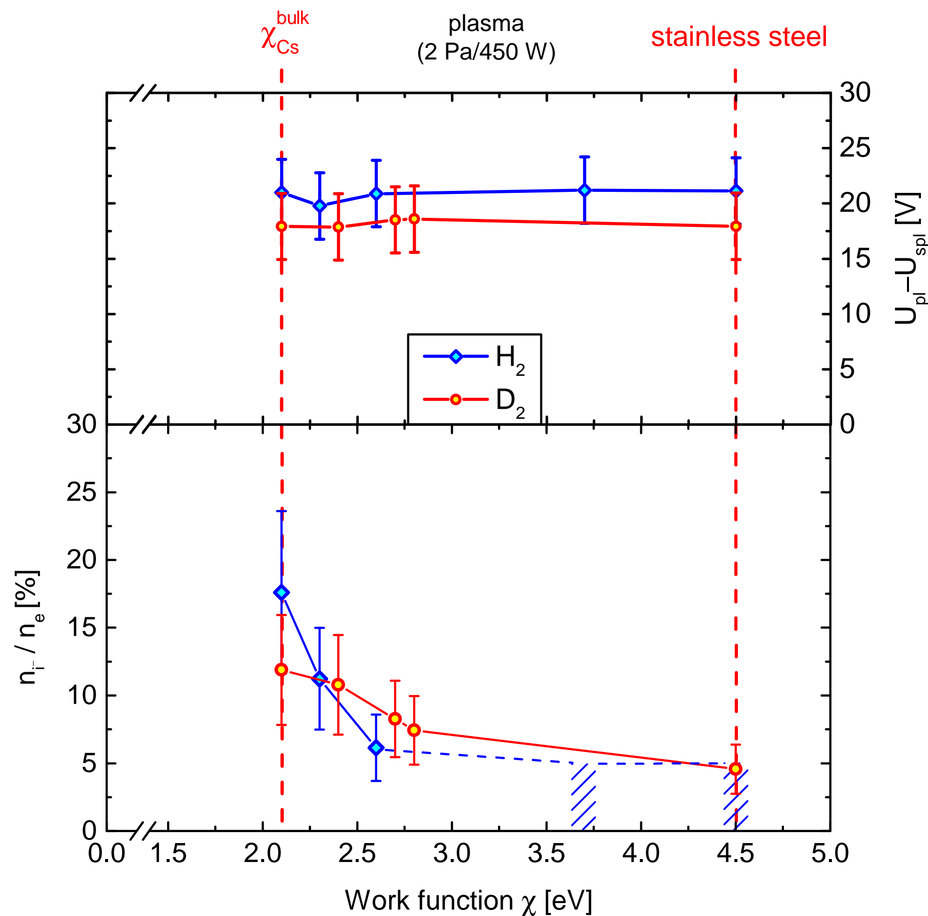


**Figure 10.7:** *Comparison between hydrogen (in blue) and deuterium (in red): on the top, the difference between plasma potential and sample potential is plotted for different surface work functions. In the lower part of the graph, the negative ion density to the electron density ratio is shown.*

conversion yield is expected for hydrogen and deuterium. The resulting outgoing $H^-$ flux is predicted to be around $5 \times 10^{19}$ m$^{-2}$s$^{-1}$ after equation (4.6). Considering the velocity that the negative ions acquire after the acceleration in the sheath region towards the bulk plasma, a density of $8 \times 10^{14}$ m$^{-3}$ is expected for surface produced negative ions.

Figure 10.8(a) shows again the negative ion density measured by CRDS for the hydrogen and deuterium cases, however including the contribution from the volume production of negative ions (see figure 10.5 for hydrogen). For deuterium, the model YACORA $H^-$ cannot be applied due to a lack of information on the rate coefficients for the different processes. Hence, the reference value for the volume produced $D^-$ density is the density measured at $\chi = 4.5$ eV (where the surface processes are assumed to be negligible), and eventual variations of the volume production level at different work functions are considered to occur within the range defined by the error bar at $\chi = 4.5$ eV. Such a range is shown in figure 10.8(a) as a red shaded area.

The surface produced negative ion density in figure 10.8(b) is obtained as the difference between the values measured by the CRDS system and the range for the volume production as depicted in figure 10.8(a) for hydrogen and deuterium. As a consequence, the values for the surface produced $H^-$ and $D^-$ densities are given by a range depicted in the figure in blue for hydrogen and in red for deuterium. In both cases, the density is in maximum around $1 \times 10^{15}$ m$^{-3}$ at $\chi = 2.1$ eV, comparable to the density previously foreseen.

Moreover, the enhancement of the negative ion density relating to the surface production is similar for the two isotopes. Hence, the slightly higher absolute negative ion density measured for the deuterium case with respect to the hydrogen plasma observed in figure 10.6 is due to the higher starting volume production observed in deuterium.

Finally, the different reaction of the electrons to the increasing negative ion density observed in hydrogen and deuterium is not due to a different negative ion surface production for the two isotopes, and it is not yet clearly explained. The reduced impact of the $D^-$ surface production on the electron density close to the surface might be due to the bigger mass of the involved ions, a lower velocity of the outgoing negative ions which determines the fluxes in the vicinity of the surface, and/or a differing space charge close to the sample in deuterium with respect to hydrogen.

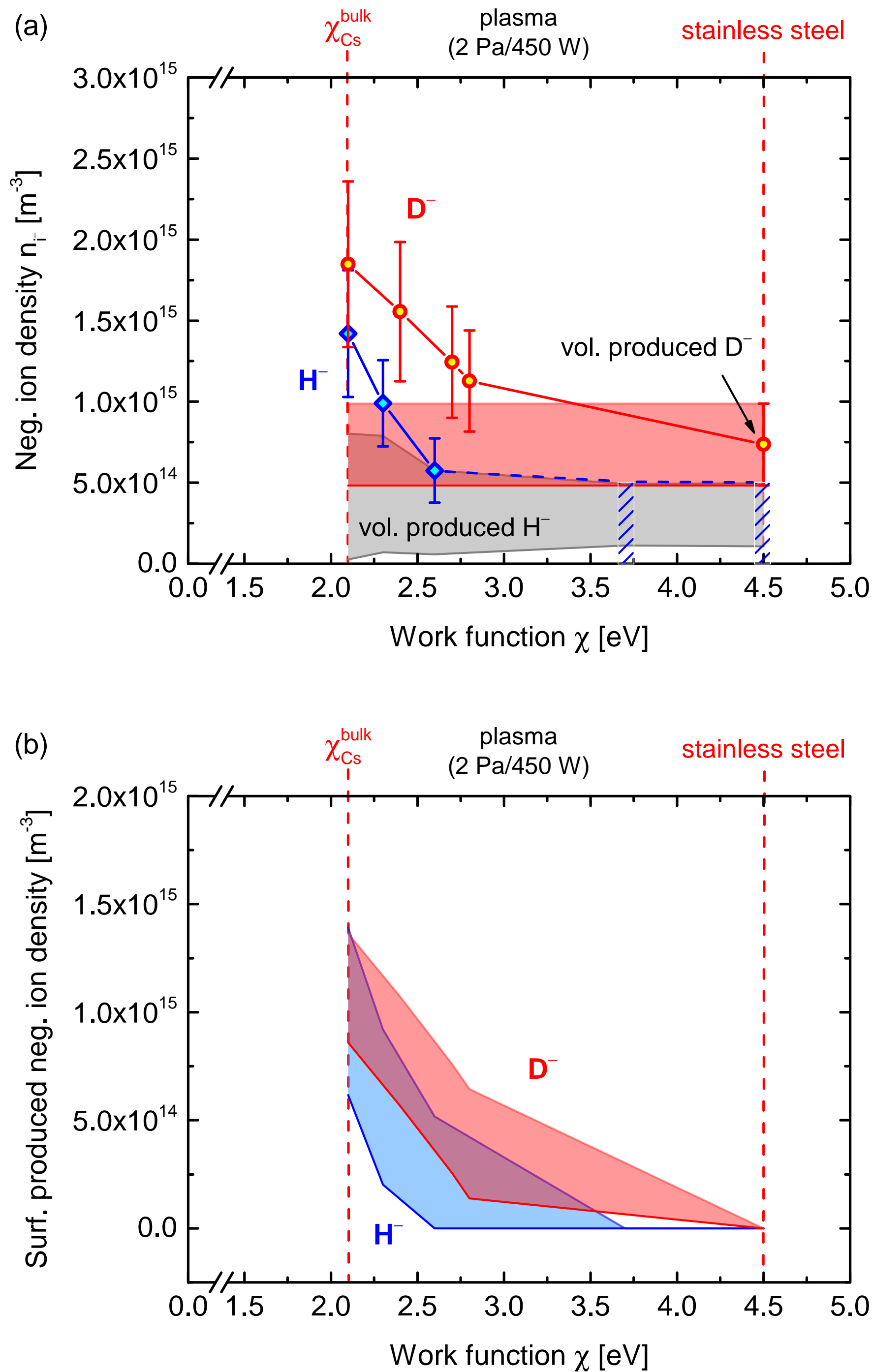


**Figure 10.8:** *Comparison between hydrogen (in blue) and deuterium (in red). In (a), the negative ion density measured by CRDS is shown for different work functions. The volume produced negative ion density is illustrated as well. In (b), the enhancement of the negative ion density only due to surface conversion is shown.*

# 11 Application to negative ion sources for fusion

As described in chapter 2, the experiment ACCesS can reproduce similar vacuum and plasma conditions as at the negative ion sources for fusion in front of the plasma grid. Thus, the implications of the investigations carried out at ACCesS during the current work on the NNBI ion source are compiled in the following.

### Caesium source

Different Cs reservoirs in the caesium oven were applied at ACCesS: the Cs dispensers and a pure Cs ampule. The Cs dispensers are not a reliable Cs source, due to limitations on the evaporation rate and to the not reproducible manufacturing process. Moreover, the undesired and uncontrolled release of heavy metallic impurities, like Bi and In, observed when the dispenser is overheated represents a limit and a risk for operation. The release of such impurities affects the caesiation of the converter surface: the Cs layer is thus constituted by a mixture of different particles, possibly affecting the Cs conditioning procedure and the source performance. Instead, the Cs ampule assures evaporation of pure Cs achieving the required Cs densities.

### Cs consumption

At the ion sources for the NNBI system, the Cs consumption must always be monitored: the evaporation of Cs into the source should be maintained as low as possible, both to avoid possible breakdowns within the multi-grid system [FHW+17] and to fulfill the RAMI requirements of reliability, availability, and maintainability [FAA+17], especially in view of the reactor DEMO. Hence, during the current work investigations are carried out trying to minimize the evaporation of Cs into the experiment: the Cs evaporation from the oven is managed in order to find and apply the minimal Cs density required to achieve and maintain a low surface

work function corresponding to bulk Cs (2.1 eV).

In a moderate vacuum environment as at the ion sources and at ACCesS ($\sim 10^{-6}$ mbar), a Cs flux of around $1.5 \times 10^{16}$ m$^{-2}$s$^{-1}$, corresponding to a Cs density of $2 \times 10^{14}$ m$^{-3}$ at the temperature of 550 K, is required to reach and sufficient to maintain a surface work function of 2.7 eV. Such work function is the minimal work function achievable at such a limited vacuum, far from a pure Cs layer (2.1 eV) due to the presence of impurities from background gases, which leads also to a degradation of the work function if no fresh Cs is evaporated. A work function of 2.1 eV can only be achieved during plasma operation.

**Plasma operation: cleaning and removal of the Cs layer**

A hydrogen plasma at 10 Pa/250 W is applied at ACCesS in order to reproduce similar plasma parameters as in front of the plasma grid at the ion sources. Comparable fluxes are achieved ($\Gamma_{\mathrm{H}} \sim 10^{22}$ m$^{-2}$s$^{-1}$, $\Gamma_{\mathrm{H}_x^+} \sim 10^{20}$ m$^{-2}$s$^{-1}$), though the flux of atomic hydrogen is the most relevant one at the ion sources, while at ACCesS the flux of positive ions plays a major role due to the different energies of the particles. The plasma has several effects on the caesiated surface. On the one hand, the plasma cleans the Cs layer allowing to reach a work function of 2.1 eV already after 5–10 seconds of plasma exposure, which is a short time scale for ion sources for fusion. On the other hand, the plasma removes easily the Cs layer: if no fresh Cs is further evaporated towards the already caesiated surface and not enough Cs is deposited on the surface, the work function shows a temporal instability during long plasma exposure (a possible solution would be to create a really thick Cs layer, but this would increase the Cs consumption, not complying with the requests for DEMO).

After figure 2.4, the first extraction beam blip of 10 s in the test stand ELISE shows the best performance with a low co-extracted electron current and a high extracted $\mathrm{H}^-$ current, correlated thus to a low work function. The increasing co-extracted electron current observed during subsequent beam blips is then related to an increase of the work function: as observed at ACCesS, the plasma particles (namely the energetic positive ions) and/or the UV and VUV plasma radiation remove the deposited caesium, affecting the resulting work function. ACCesS has shown that the Cs layer can eventually be even totally removed: the work function of a bare stainless steel surface can be retrieved by long plasma exposure (more than 4 hours) if no fresh Cs is evaporated towards the surface.

### Cs flux required for a stable work function

To counteract the Cs removal and to maintain a temporally stable surface work function, a minimum flux of fresh Cs towards the surface must be maintained. At ACCesS a Cs flux of $1.5 \times 10^{16}$ m$^{-2}$s$^{-1}$, corresponding to a Cs density of $2 \times 10^{14}$ m$^{-3}$ (with a Cs temperature of around 550 K), is required to maintain a work function of 2.1 eV also during long plasma exposure.

At ion sources a different Cs redistribution is present, due to the complexity of the system and the additional (and relevant) presence of positive Cs ions. However, the investigations at ACCesS clearly demonstrated that the work function will change during long plasma pulses if the flux of Cs towards the surface is not sufficient to maintain a stable bulk Cs layer.

Moreover, within each extraction phase at the ion source, the co-extracted electron current slightly decreases as shown in figure 2.4, and this decrease is caused by the release of Cs from the backplate due to the back-streaming ions [Mim18, FHF$^+$18]. As a consequence, the flux of fresh Cs reaching the plasma grid during the beam blip is higher than the Cs flux in between the beam blips, and the higher Cs flux counteracts the Cs removal and decreases the surface work function. However, such Cs flux is still not sufficient to retrieve the optimal work function of 2.1 eV and the low co-extracted electron current as achieved at the beginning of the plasma pulse. Hence, higher Cs fluxes or a continuous extraction with enough Cs on the backplate to be able to counteract the Cs removal on the plasma grid for the entire plasma pulse [Mim18, FHF$^+$18] are needed.

Hence, the key parameter for good performance of ion sources during long plasma pulses is to maintain a sufficient Cs flux towards the plasma grid (determined not only by the evaporation rate from the Cs ovens but also by Cs redistribution) which assures the temporal stability of the surface work function at 2.1 eV, and consequently stabilizes and improves the ion source performance for long pulse operation.

### $H^-$ density at low work function surfaces

A low work function enhances the probability of surface conversion of atomic hydrogen and positive hydrogen ions into negative ions. In particular, a strong enhancement of the negative ion density occurs for work functions lower than 2.6–2.8 eV, as observed in figure 10.8(a), due to the surface production of negative

ions at the converter surface. Instead, for higher work functions the negative ion density is mainly constituted by volume produced negative ions.

The $H^-$ density for a caesiated surface of work function $\chi = 2.1$ eV is at least by a factor of 2.8 higher than the value observed for a clean stainless steel sample at $\chi = 4.5$ eV. This enhancement of the $H^-$ density for a caesiated surface in plasma is comparable to the one observed at a different setup in [Kur16, KFF17], where the $H^-$ density was locally measured in front of a caesiated surface, but no work function measurements were available. With the current investigations it is confirmed that the increase of the $H^-$ density observed in [Kur16] and at ACCesS is correlated with the low work function of the surface. Moreover, in the two experiments the enhancement of the negative ion density is due to two different conversion processes. At ACCesS, in fact, the main conversion process involves the positive ions, while in [Kur16, KFF17] the conversion from hydrogen atoms is the main surface process due to the higher atomic hydrogen temperature. Thus, at the ion sources where a combination of the two processes takes place (with the conversion of atoms as the most significant process), a relevant enhancement of surface created negative ion is expected. The negative ion density measured for short pulses at the BATMAN test facility, in fact, has shown an enhancement by a factor of 10 from volume to surface $H^-$ formation, leading to negative ion densities of up to $10^{17}$ m$^{-3}$ [HFK+17].

### Comparison between hydrogen and deuterium

Deuterium operation is relevant for negative ion sources for fusion, in particular in view of DEMO. However, more data is available for the hydrogen processes. Hence, it is important to investigate the isotopic difference between hydrogen and deuterium operation at experiments assuring a high reproducibility, as at ACCesS.

The cleaning and removal effects of a plasma on the Cs layer (with no fresh Cs evaporated into the vessel) are similar in hydrogen and deuterium plasmas, as indicated by the temporal behavior of the work function in figure 9.10: the rate of Cs removal by plasma exposure is comparable for both plasmas at similar plasma particles fluxes and energies ($\Gamma_{\mathrm{H,D}} \sim 10^{22}$ m$^{-2}$s$^{-1}$, $\Gamma_{\mathrm{H}_x^+,\mathrm{D}_x^+} \sim 10^{20}$ m$^{-2}$s$^{-1}$, $U_{\mathrm{pl}} - U_{\mathrm{spl}} \sim 10$ V).

Also regarding the surface formation of negative ions at a low work function surface, the enhancement observed at ACCesS of the negative ion density is comparable for hydrogen and deuterium, as shown in figure 10.8(b). However, a difference between hydrogen and deuterium operation is observed regarding the

electron density measured in vicinity of the surface by the Langmuir probe. In hydrogen, the increase of the $H^-$ density at low work functions occurs together with a decrease of the measured electron density by 26 %. Instead, in deuterium the electron density is not influenced by the increase of the $D^-$ density. Hence, while the negative ion density in front of the surface at low work functions is comparable for the two isotopes at similar plasma parameters, an isotopic difference occurs regarding the behavior of the electron density for decreasing work function. At the ion sources, the higher co-extracted electron current observed during deuterium operation [WFN16, KWF+18] can thus be due to a lower impact of the increasing negative ion density at the converter surface. However, the presence of an extraction system at the ion sources leads to different potential curves at the converter surface with respect to ACCesS, and a direct correlation between the electron density measured in front of the surface at ACCesS and the co-extracted electron current at ion sources is not currently possible.

### Alternatives to caesium

As observed in figure 10.8(a), the negative ion density shows a steep increase for work functions below 2.7 eV. Hence, only materials with a work function lower than 2.7 eV can be considered as possible alternatives to Cs evaporation and adsorption. Some of those materials were already considered in the work of [Kur16, KFF17].

$LaB_6$ (nominal work function of 2.7 eV) and the lanthanated materials MoLa, WL10 and WL2 (with nominal work functions between 2.6 and 2.8 eV) cannot be activated by the low temperature plasma or by applying temperatures up to 950 °C by means of an Ar plasma, leading to measured work functions much higher than the nominal values ($\geq$ 3.6 eV).

In order to measure the work function of an activated material, a tungsten dispenser cathode is considered. It was particularly manufactured to reach the required activation temperature (1000 °C) for the Ba diffusion onto the surface to occur. Once the sample is activated, the nominal work function of 2.1 eV should be achieved. However, reaching such high temperatures leads to the release of heavy metallic impurities such as Ba and W, which create leakage currents or even –more severe– shortcuts within the vessel. Despite the possible low work function of this material, the undesired emission of heavy particles precludes the application at ion sources for fusion.

A material that showed a low work function is europium (nominal work function:

2.5 eV, measured work function: 2.6 eV), however its reaction to the hydrogen plasma must be considered in view of long plasma operation at DEMO: the fast oxidation reaction of the sample to air exposure, especially in the region previously in contact with the plasma, suggests that its chemical stability is not better than Cs (on the contrary, the work function degradation rate of Eu is much higher than the one for Cs, showing even a higher reactivity). Furthermore, the measured work function is higher with respect to the work function measured for caesiated surfaces. Hence, Eu does not represent a suitable option to replace Cs at the ion sources.

In conclusion, up to now none of the considered materials constitutes a valid alternative to Cs evaporation, which showed the best performance in terms of work function and reliability.

**Outlook**

ACCesS has already proved to be an extremely useful and unique experiment for fundamental investigations of the caesiation process and of the negative ion formation processes as well as for studies on isotopic differences, due to its reliability and to the feasibility to operate at reproducible and controlled conditions. Possible further investigations are shortly described in the following.

The model of Cs distribution *CsFlow3D*, typically applied by IPP to negative ion sources for fusion [Gut10, Mim18], requires several input data not available in literature such as the Cs sticking coefficient and the Cs thermal desorption flux from a heated surface at ion source relevant vacuum and plasma conditions. To improve the input parameters for the CsFlow3D model, fundamental investigations can be performed at ACCesS since it assures reproducible conditions and stable Cs evaporation.

The influence of impurities (such as oxygen) on the work function and on the caesiation process should be investigated, since ion sources operate in a limited vacuum environment and the presence of oxygen leads to the formation of Cs compounds at the Cs layer. Such compounds strongly affect the work function and the Cs consumption. In ACCesS, it would be possible to introduce different admixtures of oxygen and hydrogen and to observe the impact of the oxygen content on the Cs density and on the surface work function in vacuum and during plasma exposure.

The cleaning and removal of the Cs layer during plasma operation is determined by the interaction of the surface with the plasma particles and/or with the UV and

VUV plasma emission. In order to distinguish the impact of the hydrogen atoms, the positive hydrogen ions and the UV/VUV emission on the work function of a caesiated surface, a second plasma source could be added to ACCesS in order to decouple the three different plasma components in separate investigations.

Moreover, a substrate material similar to the one used as plasma grid at ion sources (Mo-coated copper) should be applied and caesiated at ACCesS, in order to investigate the impact of the substrate on the work function for sub-monolayers of Cs coverage, e.g. on the minimum work function that could be achieved during plasma operation with no further evaporation. The different substrate will not have any effect instead on the work function of thick Cs layers.

Since ACCesS is a reliable setup for work function measurements, several other materials as alternative to Cs for DEMO should be investigated, e.g. lanthanated materials with a much higher concentration of La or the electride C12A7:$e^-$ (nominal work function of 2.4 eV [TYI+07]).

Furthermore, in order to investigate the dynamics of the extracted negative ion current and the co-extracted electron current, it is important to have an extraction system also at a flexible laboratory experiment where reproducible and controlled conditions are assured. The extraction system modifies heavily the potential profiles at the surface, and a correlation among the plasma parameters, the surface work function and the extracted currents is thus the next step for a more complete comprehension of fundamental mechanisms occurring at the ion sources.

Finally, the work function diagnostic should be implemented directly at the ion sources, in order to measure the work function of the plasma grid, which is the relevant parameter for high source performance. The possibility to measure the work function will give a direct access to the conditions of the Cs layer on the plasma grid.

# 12 Conclusions

One of the main components of future fusion machines like ITER and DEMO is the neutral beam injection based on negative hydrogen ions (NNBI). The ITER NNBI system must deliver a high energy and homogeneous beam for pulses of up to one hour, with an accelerated $D^-$ current density of 200 $A/m^2$ and a co-extracted electron to extracted negative ion current density ratio below unity. At the NNBI ion sources, the extracted negative ions are mainly created by surface conversion of atomic hydrogen and positive hydrogen ions at a low work function surface. Cs is evaporated into the source to achieve the bulk Cs work function (2.1 eV). However, the Cs layer on the converter surface is strongly influenced by the presence of background impurities and by the plasma interaction with the surface, affecting the resulting work function which is the key parameter for good performance.

Test facilities equipped with the prototype source has shown a temporal instability of the co-extracted electron current, especially in deuterium operation. Such instability is connected to a degradation or vanishing of the Cs layer at the converter surface, causing a variation of the work function during long pulse operation. Investigations of the mechanisms of negative ion formation and characterization of the Cs surfaces are thus needed in a controlled experiment. Fundamental investigations are performed at the flexible laboratory ICP experiment ACCesS, operating at ion source relevant vacuum and plasma conditions. In order to study the caesiation process on a stainless steel sample, ACCesS is equipped with a Cs oven similar to the one used at the ion source. The Cs density is monitored by tunable diode laser absorption spectroscopy in vacuum and in plasma operation, while the Cs evaporation and redistribution within the vessel are monitored by two surface ionization detectors. The work function of the surface is evaluated by means of the Fowler method considering the photoelectric effect, while the $H^-$ density is measured by cavity ring-down spectroscopy at 2 cm distance from the sample for investigations of the negative ion formation. The plasma parameters (such as electron temperature and density) and the residual gases are constantly monitored in order to guarantee controlled and reproducible investigations.

When Cs is evaporated towards the surface in vacuum creating a thick Cs layer, the work function does not reach values below 2.7 eV due to the influence of the background impurities in the moderate vacuum level ($10^{-6}$ mbar, as at the ion sources) and to the consequent formation of Cs compounds at the surface. However, the exposure of the surface to a hydrogen plasma clearly shows that the impinging positive ions and/or the UV/VUV plasma emission clean the Cs layer, allowing to achieve the bulk Cs work function of 2.1 eV already after 5–10 s of plasma exposure (a short time scale in comparison to 1 hour pulses). However, the interactions between plasma and the surface lead to a removal of the Cs layer when no fresh Cs is evaporated into the volume, resulting in a temporal variation of the work function: the work function shows a minimum of 1.8–1.9 eV after around 10 minutes of plasma exposure, and then it gradually increases up to values close to a clean stainless steel surface (4.5 eV after 4 hours of plasma exposure).

Hence, if not enough fresh Cs flux is reaching the surface, the Cs is gradually removed and the work function of bulk Cs is lost, leading to not stable performance of the ion source. The removal of the Cs layer must be thus counteracted by a sufficient fresh Cs flux towards the surface, in order to assure a work function constant in time during the plasma pulse and corresponding to the value for bulk Cs. For plasmas at ACCesS, a minimum flux of $1.5 \times 10^{16}$ $m^{-2}s^{-1}$ (corresponding to a Cs density of $2 \times 10^{14}$ $m^{-3}$ at a temperature of 550 K) is required to have a stable surface work function of 2.1 eV during plasma exposure.

The possibility of controlled and reproducible investigations allows to study the transition from negative ion volume formation to surface formation at low work function surfaces, comparing in particular the hydrogen and deuterium cases for an analysis of the isotopic effect. The main conversion mechanism at ACCesS involves the positive ions, while at the ion sources the atomic hydrogen is the most relevant species for the conversion, hence plasma conditions different from ion sources must be considered for such investigations at ACCesS. However, the work function of the surface is easily controlled and quantified at ACCeS, allowing to outline the correlation between the negative ion density $n_{\mathrm{i}^-}$ in front of the surface and the work function at controlled plasma conditions. In particular, $n_{\mathrm{i}^-}$ shows a steep increase for work functions below 2.7 eV, while above this value the main contribution to the negative ion density is due to volume formation. For a work function of 2.1 eV (bulk Cs), the $H^-$ density increases by at least a factor of 2.8 with respect to a non-caesiated surface, reaching densities of around

$1 \times 10^{15}$ m$^{-3}$ of surface produced negative ions. By applying a deuterium plasma, no isotopic effect occurs regarding the surface negative ion formation: the $D^-$ density measured for a work function of 2.1 eV increases by a factor of 2.5 with respect to a non-caesiated surface, reaching densities of surface produced negative ions comparable to the hydrogen case.

However, an isotopic difference affects the electron reaction to the lowering of the surface work function at ACCesS: while in a hydrogen plasma the electron density decreases with low work functions due to the increasing amount of $H^-$ (because of the quasi-neutrality principle), in deuterium the electron density is constant. Hence, in deuterium operation the electrons are less affected by the lowering of the work function.

In order to find possible alternatives to Cs in view of DEMO, several materials under discussion are tested at ACCesS. Among these materials, the Eu sample has the lowest work function (nominal value: 2.5 eV, measured value at ACCesS: 2.6 eV). However, Eu strongly reacts with hydrogen plasma: the work function is not temporally stable, clearly showing a degradation effect during plasma. To counteract this effect, it is necessary to heat the sample to 400 °C simultaneously. The work function degradation rate after the plasma treatment due to the residual gases is also much higher than any other material tested at ACCesS (including Cs). Such a strong dynamics and chemical reactivity, together with the higher work function with respect to bulk Cs, makes this material not a suitable alternative.

The other materials did not show a low work function (always higher than 3.6 eV) since they require an activation procedure at high temperatures, and the plasma at ACCesS cannot activate them. Moreover, the application of high temperatures lead to the release of metallic impurities from the bulk material, contaminating the whole experiment. Hence, $LaB_6$, MoLa, lanthanated tungsten and bariated tungsten are not valid options for ion sources.

In conclusion, at present there is no valid alternative to Cs evaporation, thus continuous effort should be spent in investigations of the Cs dynamics and optimization of the Cs management in view of DEMO. Moreover, the correlation of the extracted negative ion current and the co-extracted electron current with the work function of a caesiated surface in controlled conditions as in a laboratory experiment should be the next step for new investigations, in order to understand the underlying mechanisms of negative ion extraction at ion sources.

# Bibliography

[abc16] abcr GmbH, Germany, 2016, https://www.abcr.de/.

[Alf16] AlfaVakuo e.U., Austria, 2016, http://alfavakuo.eu/.

[Alv16] Alvatec GmbH, Austria, 2010 (operations ceased in 2016).

[ATG85] P. W. van Amersfoort, Y. C. Tong, and E. H. A. Granneman, *A model for the stationary cesium coverage on a converter surface in a cesium seeded hydrogen discharge*, J. Appl. Phys. **58** (1985), 2317.

[BBB+91] M. Bacal, P. Berlemont, A. M. Bruneteau, et al., *Measurement of the $H^-$ thermal energy in a volume ion source plasma*, J. Appl. Phys. **70** (1991), 1212.

[BBG78] R. Bachmann, C. Buxbaum, and G. Gessinger, *Lanthanated thermionic cathodes*, U.S. Patent 4 083 811, April 11, 1978.

[BDD74] Y. I. Belchenko, G. I. Dimov, and V. G. Dudnikov, *A powerful injector of neutrals with a surface-plasma source of negative ions*, Nucl. Fusion **14** (1974), 113.

[Beh91] K. Behringer, *Diagnostics and modelling of ECRH microwave discharges*, Plasma Phys. Control. Fusion **33** (1991), 997.

[BF94] K. Behringer and U. Fantz, *Spectroscopic diagnostics of glow discharge plasmas with non-Maxwellian electron energy distributions*, J. Phys. D: Appl. Phys. **27** (1994), 2128.

[BPS75] K. H. Berkner, R. V. Pyle, and J. W. Stearns, *Intense, mixed-energy hydrogen beams for CTR injection*, Nucl. Fusion **15** (1975), 249.

[BRF17] S. Briefi, R. Rauner, and U. Fantz, *Determination of the rotational population of $H_2$ and $D_2$ including high-$N$ states in low temperature plasmas via the Fulcher-$\alpha$ transition*, J. Quant. Spectrosc. Radiat. Transfer **187** (2017), 135.

[Bri17] S. Briefi, *Private communication*, Max-Planck-Institut für Plasmaphysik, Garching, 2017.

[BRR+77] C. F. Barnett, J. A. Ray, E. Ricci, et al., *Atomic data for controlled fusion research*, Tech. Report ORNL-5206 (Vol.1), Oak Ridge National Lab., TN (USA), 1977.

[BW79] J. N. Bardsley and J. M. Wadehra, *Dissociative attachment and vibrational excitation in low-energy collisions of electrons with $H_2$ and $D_2$*, Phys. Rev. A **20** (1979), 1398.

[BW15] M. Bacal and M. Wada, *Negative hydrogen ion production mechanisms*, Appl. Phys. Rev. **2** (2015), 021305.

[CB11] P. Chabert and N. Braithwaite, *Physics of Radio-Frequency Plasma*, Cambridge University Press, Cambridge, 2011.

[CBB95] C. Courteille, A. M. Bruneteau, and M. Bacal, *Investigation of a large volume negative hydrogen ion source*, Rev. Sci. Instrum. **66** (1995), 2533.

[CCD+11] D. Ćirić, B. C. Crowley, I. E. Day, et al., *Performance of Upgraded JET Neutral Beam Injectors*, Fusion Eng. Des. **86** (2011), 509.

[CF72] R. P. Clow and J. H. Futrell, *Ion-molecule reactions in isotopic hydrogen by ion cyclotron resonance*, Int. J. Mass Spectrom. Ion Phys. **8** (1972), 119.

[Cha98] M. W. Chase, *NIST-JANAF Thermochemical Tables*, 4th ed., J. Phys. Chem. Ref. Data, Monograph 9, National Institute of Standards and Technology, Gaithersburg, MD, 1998, available online at `https://webbook.nist.gov/`.

[Che03] F. F. Chen, *Lecture Notes on Langmuir Probe Diagnostics*, Mini-Course on Plasma Diagnostics, IEEE-ICOPS meeting (Jeju, South Korea), 2003.

[CJ69] D. H. Cotton and D. R. Jenkins, *Bond dissociation energies of gaseous alkali metal hydroxides*, Trans. Faraday Soc. **65** (1969), 1537.

[CJL+01] R. Celiberto, R. K. Janev, A. Laricchiuta, et al., *Cross section data for electron-impact inelastic processes of vibrationally excited molecules of hydrogen and its isotopes*, At. Data Nucl. Data Tables **77** (2001), 161.

[Cro81] J. L. Cronin, *Modern dispenser cathodes*, IEE Proc. I **128** (1981), 19.

[Cui91] H. L. Cui, *Resonant charge transfer in the scattering of hydrogen atoms from a metal surface*, J. Vac. Sci. Technol. A **9** (1991), 1823.

[DAB+89] P. Devynck, J. Auvray, M. Bacal, et al., *Photodetachment technique for measuring $H^-$ velocities in a hydrogen plasma*, Rev. Sci. Instrum. **60** (1989), 2873.

[DP40] M. J. Druyvesteyn and F. M. Penning, *The Mechanism of Electrical Discharges in Gases of Low Pressure*, Rev. Mod. Phys. **12** (1940), 87.

[Dru30] M. J. Druyvesteyn, *Der Niedervoltbogen*, Z. Phys. **64** (1930), 781.

[EKP87] M. L. Ernst-Vidalis, M. Kamaratos, and C. Papageorgopoulos, *The effects of Cs on the adsorption of $H_2$ on Mo(110)*, Surf. Sci. **189-190** (1987), 276.

[Ert10] D. Ertle, *Teilchendichten in HF-angeregten Wasserstoff- und Deuteriumplasmen*, Diploma thesis, Ulm University in cooperation with University of Augsburg, 2010.

[FAA+17] T. Franke, P. Agostinetti, K. Avramidis, et al., *Heating & current drive efficiencies, TBR and RAMI considerations for DEMO*, Fusion Eng. Des. **123** (2017), 495.

[Fan04] U. Fantz, *Emission Spectroscopy of Molecular Low Pressure Plasmas*, Contrib. Plasma Phys. **44** (2004), 508.

[FBB+16] G. Federici, C. Bachmann, W. Biel, et al., *Overview of the design approach and prioritization of R&D activities towards an EU DEMO*, Fusion Eng. Des. **109–111** (2016), 1464.

[FBG+17] G. Federici, W. Biel, M. R. Gilbert, et al., *European DEMO design strategy and consequences for materials*, Nucl. Fusion **57** (2017), 092002.

[FBR+16] U. Fantz, S. Briefi, D. Rauner, et al., *Quantification of the VUV radiation in low pressure hydrogen and nitrogen plasmas*, Plasma Sources Sci. Technol. **25** (2016), 045006.

[FF14] R. Friedl and U. Fantz, *Fundamental studies on the Cs dynamics under ion source conditions*, Rev. Sci. Instrum. **85** (2014), 02B109.

[FF17] ———, *Influence of $H_2$ and $D_2$ plasmas on the work function of caesiated materials*, J. Appl. Phys. **122** (2017), 083304.

[FFF+06] U. Fantz, H. Falter, P. Franzen, et al., *Spectroscopy–a powerful diagnostic tool in source development*, Nucl. Fusion **46** (2006), S297.

[FFF12] U. Fantz, R. Friedl, and M. Fröschle, *Controllable evaporation of cesium from a dispenser oven*, Rev. Sci. Instrum. **83** (2012), 123305.

[FFK+07] U. Fantz, P. Franzen, W. Kraus, et al., *Negative ion RF sources for ITER NBI: status of the development and recent achievements*, Plasma Phys. Control. Fusion **49** (2007), B563.

[FFK+09] ———, *Physical performance analysis and progress of the development of the negative ion RF source for the ITER NBI system*, Nucl. Fusion **49** (2009), 125007.

[FFW12] U. Fantz, P. Franzen, and D. Wünderlich, *Development of negative hydrogen ion sources for fusion: Experiments and modelling*, Chem. Phys. **398** (2012), 7.

[FH98] U. Fantz and B. Heger, *Spectroscopic diagnostics of the vibrational population in the ground state of $H_2$ and $D_2$ molecules*, Plasma Phys. Control. Fusion **40** (1998), 2023.

[FHF+13] P. Franzen, B. Heinemann, U. Fantz, et al., *Commissioning and first results of the ITER-relevant negative ion beam test facility ELISE*, Fusion Eng. Des. **88** (2013), 3132.

[FHF+18] U. Fantz, C. Hopf, R. Friedl, et al., *Technology Developments for a Beam Source of an NNBI system for DEMO*, Fusion Eng. Des. **136** (2018), 340.

[FHW+17] U. Fantz, C. Hopf, D. Wünderlich, et al., *Towards powerful negative ion beams at the test facility ELISE for the ITER and DEMO NBI systems*, Nucl. Fusion **57** (2017), 116007.

[Fow31] R. H. Fowler, *The Analysis of Photoelectric Sensitivity Curves for Clean Metals at Various Temperatures*, Phys. Rev. **38** (1931), 45.

[Fri13] R. Friedl, *Experimental investigations on the caesium dynamics in $H_2/D_2$ low temperature plasmas*, Ph.D. thesis, University of Augsburg, 2013.

[Fri16] ______, *Enhancing the accuracy of the Fowler method for monitoring non-constant work functions*, Rev. Sci. Instrum. **87** (2016), 043901.

[Frö18] M. Fröschle, *Private communication*, Max-Planck-Institut für Plasmaphysik, Garching, 2018.

[FW11] U. Fantz and C. Wimmer, *Optimizing the laser absorption technique for quantification of caesium densities in negative hydrogen ion sources*, J. Phys. D: Appl. Phys. **44** (2011), 335202.

[GAB+15] G. Giruzzi, J. F. Artaud, M. Baruzzo, et al., *Modelling of pulsed and steady-state DEMO scenarios*, Nucl. Fusion **55** (2015), 073002.

[Gal69] H. E. Gallagher, *Poisoning of $LaB_6$ Cathodes*, J. Appl. Phys. **40** (1969), 44.

[GD41] N. Ginsburg and G. H. Dieke, *Intensity Measurements in the Molecular Spectrum of Hydrogen*, Phys. Rev. **59** (1941), 632.

[GMS95] V. A. Godyak, V. P. Meytlis, and H. R. Strauss, *Tonks-Langmuir Problem for a Bi-Maxwellian Plasma*, IEEE Trans. on Plasma Sci. **23** (1995), 728.

[Gut10] R. Gutser, *Experiments and Simulations for the Dynamics of Cesium in Negative Hydrogen Ion Sources for ITER N-NBI*, Ph.D. thesis, University of Augsburg, 2010.

[GWF+11] R. Gutser, D. Wünderlich, U. Fantz, et al., *Dynamics of the transport of ionic and atomic cesium in radio frequency-driven ion sources for ITER neutral beam injection*, Plasma Phys. Control. Fusion **53** (2011), 105014.

[Har17] A. Hartwig, *Private communication*, University of Augsburg, Anwenderzentrum Material- und Umweltforschung, 2017.

[HDC83] M. S. Huq, L. D. Doverspike, and R. L. Champion, *Electron detachment for collisions of $H^-$ and $D^-$ with hydrogen molecules*, Phys. Rev. A **27** (1983), 2831.

[HDG+09] R. Hemsworth, H. Decamps, J. Graceffa, et al., *Status of the ITER heating neutral beam system*, Nucl. Fusion **49** (2009), 045006.

[Her50] G. Herzberg, *Molecular Spectra and Molecular Structure, I. Spectra of Diatomic Molecules*, 2nd ed., D. Van Nostrand Company, Toronto New York London, 1950.

[HFK+17] B. Heinemann, U. Fantz, W. Kraus, et al., *Towards large and powerful radio frequency driven negative ion sources for fusion*, New J. Phys. **19** (2017), 015001.

[HHB+15] T. Hoebing, P. Hermanns, A. Bergner, et al., *Investigation of the flickering of $La_2O_3$ and $ThO_2$ doped tungsten cathodes*, J. Appl. Phys. **118** (2015), 023306.

[Hot75] E. Hotston, *Threshold energies for sputtering*, Nucl. Fusion **15** (1975), 544.

[HW97] N. Hodgson and H. Weber, *Optical Resonators: Fundamentals, Advanced Concepts and Applications*, Springer, London, 1997.

[IAE02] IAEA, *ITER Technical Basis*, ITER EDA documentation series 24, International Atomic Energy Agency, Vienna, 2002.

[IKS92] J. D. Isenberg, H. J. Kwon, and M. Seidl, *Surface production of $H^-$ ions by backscattering of $H^+$ and $H_2^+$ ions in the 3–50 eV ion energy range*, AIP Conf. Proc. **287** (1992), 38.

[ITE17] ITER Organization, *2016 Annual Report*, St. Paul-lez-Durance, July 2017.

[JRS03] R. K. Janev, D. Reiter, and U. Samm, *Collision Processes in Low-Temperature Hydrogen Plasmas*, Berichte des Forschungszentrums Jülich, vol. 4105, Forschungszentrum Jülich, 2003.

[Kar16] Karlsruher Institut für Technologie, Germany, 2016, http://www.kit.edu/.

[KFF+12] W. Kraus, U. Fantz, P. Franzen, et al., *The development of the radio frequency driven negative ion source for neutral beam injectors (invited)*, Rev. Sci. Instrum. **83** (2012), 02B104.

[KFF17] U. Kurutz, R. Friedl, and U. Fantz, *Investigations on Cs-free alternatives for negative ion formation in a low pressure hydrogen discharge at ion source relevant parameters*, Plasma Phys. Control. Fusion **59** (2017), 075008.

[KH06] A. Krylov and R. S. Hemsworth, *Gas flow and related beam losses in the ITER neutral beam injector*, Fusion Eng. Des. **81** (2006), 2239.

[KHT+10] A. Kojima, M. Hanada, Y. Tanaka, et al., *Achievement and improvement of the JT-60U negative ion source for JT-60 Super Advanced*, Rev. Sci. Instrum. **81** (2010), 02B112.

[KLM+00] J. S. Kim, B. Lägel, E. Moons, et al., *Kelvin probe and ultraviolet photoemission measurements of indium tin oxide work function: a comparison*, Synth. Met. **111-112** (2000), 311.

[KLT12] M. Kikuchi, K. Lackner, and M. Q. Tran, *Fusion Physics*, International Atomic Energy Agency, Vienna, 2012.

[Kov69] I. Kovács, *Rotational structure in the spectra of diatomic molecules*, Adam Hingler, London, 1969.

[Kur16] U. Kurutz, *Investigations on Cs-free alternative materials for negative hydrogen ion formation*, Ph.D. thesis, University of Augsburg, 2016.

[KVG+05] Y. Kudriavtsev, A. Villegas, A. Godines, et al., *Calculation of the surface binding energy for ion sputtered particles*, Appl. Surf. Sci. **239** (2005), 273.

[KWF+18] W. Kraus, D. Wünderlich, U. Fantz, et al., *Deuterium results at the negative ion source test facility ELISE*, Rev. Sci. Instrum. **89** (2018), 052102.

[Laf51] J. M. Lafferty, *Boride Cathodes*, J. Appl. Phys. **22** (1951), 299.

[Lid05] D. R. Lide, *CRC Handbook of Chemistry and Physics*, CRC Press, Boca Raton, FL, 2005.

[Lin17] M. Lindauer, *Laserabsorptionsspektroskopie zur Quantifizierung der Caesiumdichte in Gasphase und im Plasma*, Fachpraktikumarbeit, University of Augsburg, 2017.

[LL05] M. A. Lieberman and A. J. Lichtenberg, *Principles of Plasma Discharges and Materials Processing*, 2nd ed., John Wiley & Sons, Hoboken, NJ, 2005.

[LN83] N. D. Lang and J. K. Nørskov, *The Theory of Ionization Probability in Sputtering*, Phys. Scr. **T6** (1983), 15.

[LS92] B. S. Lee and M. Seidl, *Surface production of $H^-$ ions by hyperthermal hydrogen atoms*, Appl. Phys. Lett. **61** (1992), 2857.

[LST80] B. P. Lavrov, A. A. Solov'ev, and M. V. Tyutchev, *Populations of the rotational levels of the $d^3\Pi_u^-$ levels of $H_2$, HD, and $D_2$ in an RF discharge*, J. Appl. Spectrosc. **32** (1980), 316.

[MBC+12] K. A. Miller, H. Bruhns, M. Čížek, et al., *Isotope effect for associative detachment: $H(D)^- + H(D) \rightarrow H_2(D_2) + e^-$*, Phys. Rev. A **86** (2012), 032714.

[McA14] R. McAdams, *Beyond ITER: Neutral beams for a demonstration fusion reactor (DEMO) (invited)*, Rev. Sci. Instrum. **85** (2014), 02B319.

[MDC+09] P. McNeely, S. V. Dudin, S. Christ-Koch, et al., *A Langmuir probe system for high power RF-driven negative ion sources on high potential*, Plasma Sources Sci. Technol. **18** (2009), 014011.

[MDL77] G. R. Möhlmann, F. J. De Heer, and J. Los, *Emission cross sections of balmer-$\alpha, \beta, \gamma$ radiation for electrons (0–2000 eV) on $H_2$ and $D_2$*, Chem. Phys. **25** (1977), 103.

[Mic77] H. B. Michaelson, *The work function of the elements and its periodicity*, J. Appl. Phys. **48** (1977), 4729.

[Mim18] A. Mimo, *Optimization of Caesium Dynamics in Large and Powerful RF Sources for Negative Hydrogen Ions*, Ph.D. thesis, University of Augsburg, 2018.

[ML26] H. M. Mott-Smith and I. Langmuir, *The Theory of Collectors in Gaseous Discharges*, Phys. Rev. **28** (1926), 727.

[Möl93] W. Möller, *Plasma and Surface Modeling of the Deposition of Hydrogenated Carbon Films from Low-Pressure Methane Plasmas*, Appl. Phys. A **56** (1993), 527.

[Mos05] T. Mosbach, *Population dynamics of molecular hydrogen and formation of negative hydrogen ions in a magnetically confined low temperature plasma*, Plasma Sources Sci. Technol. **14** (2005), 610.

[MS91] S. T. Melnychuk and M. Seidl, *Reflection of hydrogen atoms from alkali and alkaline earth oxide surfaces*, J. Vac. Sci. Technol. A **9** (1991), 1650.

[MS10] P. McNeely and L. Schiesko, *Investigation of fringe plasma parameters on a high power RF driven ion source*, Rev. Sci. Instrum. **81** (2010), 02B111.

[NGH+11] R. Nocentini, R. Gutser, B. Heinemann, et al., *Optimization of the cooling circuit and thermo-mechanical analysis for the extraction grid of ELISE*, Fusion Eng. Des. **86** (2011), 916.

[NK07] S. Nunomura and M. Kondo, *Characterization of high-pressure capacitively coupled hydrogen plasmas*, J. Appl. Phys. **102** (2007), 093306.

[NL79] J. K. Nørskov and B. I. Lundqvist, *Secondary-ion emission probability in sputtering*, Phys. Rev. B **19** (1979), 5661.

[Noc16] R. Nocentini, *Private communication*, Max-Planck-Institut für Plasmaphysik, Garching, 2016.

[NSB98] M. Nishiura, M. Sasao, and B. Bacal, *$H^-$ laser photodetachment at 1064, 532, and 355 nm in plasma*, J. Appl. Phys. **83** (1998), 2944.

[NTN87] K. Nakashima, H. Takagi, and H. Nakamura, *Dissociative recombination of $H_2^+$, $HD^+$, and $D_2^+$ by collisions with slow electrons*, J. Chem. Phys. **86** (1987), 726.

[OD88] A. O'Keefe and D. A. G. Deacon, *Cavity ring-down optical spectrometer for absorption measurements using pulsed laser sources*, Rev. Sci. Instrum. **59** (1988), 2544.

[PC73] C. A. Papageorgopoulos and J. M. Chen, *Coadsorption of electropositive and electronegative elements: I. Cs and $H_2$ on W(100)*, Surf. Sci. **39** (1973), 283.

[Pla01] Plansee Composite Materials GmbH, Germany, 2001, `https://www.plansee.com`.

[Pla16] ———, 2016, `https://www.plansee.com`.

[Rar85] J. A. Rard, *Chemistry and thermodynamics of europium and some of its simpler inorganic compounds and aqueous species*, Chem. Rev. **85** (1985), 555.

[Rau14] D. Rauner, *Cavity-Ring-Down-Spektroscopie zur Quantifizierung negativer Wasserstoffionen in einem ECR-Plasma*, Master thesis, University of Augsburg, 2014.

[RBB+12] F. Romanelli, P. Barabaschi, D. Borba, et al., *Fusion Electricity - A roadmap to the realization of fusion energy*, Tech. report, European Fusion Development Agreement (EFDA), 2012.

[Rei15] W. Reiber, *Private communication*, University of Augsburg, Experimental Physics IV, 2015.

[Rei17] ———, *Private communication*, University of Augsburg, Experimental Physics IV, 2017.

[RKF15] D. Rauner, U. Kurutz, and U. Fantz, *Comparison of measured and modelled negative hydrogen ion densities at the ECR-discharge HOMER*, AIP Conf. Proc. **1655** (2015), 020017.

[RL93] D. Romanini and K. K. Lehmann, *Ring-down cavity absorption spectroscopy of the very weak HCN overtone bands with six, seven, and eight stretching quanta*, J. Chem. Phys. **99** (1993), 6287.

[RWL82] B. Rasser, J. N. M. van Wunnik, and J. Los, *Theoretical models of the negative ionization of hydrogen on clean tungsten, cesiated tungsten and cesium surfaces at low energies*, Surf. Sci. **118** (1982), 697.

[SAB+17] P. Sonato, P. Agostinetti, T. Bolzonella, et al., *Conceptual design of the DEMO neutral beam injectors: main developments and R&D achievements*, Nucl. Fusion **57** (2017), 056026.

[Sch15] L. Schiesko, *Private communication*, Max-Planck-Institut für Plasmaphysik, Garching, 2015.

[SCI+96] M. Seidl, H. L. Cui, J. D. Isenberg, et al., *Negative surface ionization of hydrogen atoms and molecules*, J. Appl. Phys. **79** (1996), 2896.

[SCM+07] M. Shimada, D. J. Campbell, V. Mukhovatov, et al., *Progress in the ITER Physics Basis, Chapter 1: Overview and summary*, Nucl. Fusion **47** (2007), S1.

[SFA+01] P. Scheubert, U. Fantz, P. Awakowicz, et al., *Experimental and theoretical characterization of an inductively coupled plasma source*, J. Appl. Phys. **90** (2001), 587.

[SFF+06] E. Speth, H. D. Falter, P. Franzen, et al., *Overview of the RF source development programme at IPP Garching*, Nucl. Fusion **46** (2006), S220.

[Sha70] T. E. Sharp, *Potential-energy curves for molecular hydrogen and its ions*, At. Data Nucl. Data Tables **2** (1970), 119.

[Sha71] ———, *Erratum: Potential-energy curves for molecular hydrogen and its ions*, At. Data Nucl. Data Tables **3** (1971), 299.

[Sim12] A. Simon, *Oxidation by Hydrogen in the Chemistry and Physics of the Rare-Earth Metals*, Angew. Chem. Int. Ed. **51** (2012), 4280.

[Sin14] Sindlhauser Materials GmbH, Germany, 2014, `http://www.sindlhauser.de`.

[SOA+96] K. Shinto, Y. Okumura, T. Ando, et al., *Correlation between Negative Hydrogen Ion Production and Work Function of Plasma Grid Surface in a Cesium-Introduced Volume-Production-Type Negative Hydrogen Ion Source*, Jpn. J. App. Phys. **35** (1996), 1894.

[Spe15] Spectra-Mat, Inc., USA, *Private communication*, 2015.

[Spe16] ———, 2016, `http://www.spectramat.com/`.

[SS68] L. W. Swanson and R. W. Strayer, *Field-Electron-Microscopy Studies of Cesium Layers on Various Refractory Metals: Work Function Change*, J. Chem. Phys. **48** (1968), 2421.

[SS74] W. Stiller and R. Schmidt, *Two-temperature model for ion-molecule reactions*, Int. J. Mass Spectrom. Ion Phys. **14** (1974), 237.

[Ste10] D. A. Steck, *Cesium D Line Data*, available online at `http://steck.us/alkalidata/` (revision 2.1.4, accessed September 10, 2018), 2010.

[SVY81] I. I. Sobelman, L. A. Vainshtein, and E. A. Yukov, *Excitation of Atoms and Broadening of Spectral Lines*, Springer Series in Chemical Physics, vol. 7, Springer, Berlin Heidelberg New York, 1981.

[Tak02] T. Takagi, *Dissociative Recombination and Excitation of $H_2^+$, $HD^+$, and $D_2^+$ with Electrons for Various Vibrational States*, Phys. Scr. **T96** (2002), 52.

[TKT+06] Y. Takeiri, O. Kaneko, K. Tsumori, et al., *High-power and long-pulse injection with negative-ion-based neutral beam injectors in the Large Helical Device*, Nucl. Fusion **46** (2006), S199.

[TL33] J. B. Taylor and I. Langmuir, *The Evaporation of Atoms, Ions and Electrons from Caesium Films on Tungsten*, Phys. Rev. **44** (1933), 423.

[TL37] ———, *Vapor Pressure of Caesium by the Positive Ion Method*, Phys. Rev. **51** (1937), 753.

[TLJ99] A. Thorne, U. Litzén, and S. Johansson, *Spectrophysics: Principles and Applications*, Springer, Berlin Heidelberg New York, 1999.

[TM87] P. A. Thiel and T. E. Madey, *The interaction of water with solid surfaces: Fundamental aspects*, Surf. Sci. Rep. **7** (1987), 211.

[TNK+12] K. Tsumori, H. Nakano, M. Kisaki, et al., *Spatial distribution of the charged particles and potentials during beam extraction in a negative-ion source*, Rev. Sci. Instrum. **83** (2012), 02B116.

[TPB+17] V. Toigo, R. Piovan, S. Dal Bello, et al., *The PRIMA Test Facility: SPIDER and MITICA test-beds for ITER neutral beam injectors*, New J. Phys. **19** (2017), 085004.

[Tre12] M. Trenary, *Surface science studies of metal hexaborides*, Sci. Technol. Adv. Mater. **13** (2012), 023002.

[TS79] I. Toyoshima and G. A. Somorjai , *Heats of Chemisorption of $O_2$, $H_2$, CO, $CO_2$, and $N_2$ on Polycrystalline and Single Crystal Transition Metal Surfaces*, Catal. Rev. **19** (1979), 105.

[TYI+07] Y. Toda, H. Yanagi, E. Ikenaga, et al., *Work Function of a Room-Temperature, Stable Electride $[Ca_{24}Al_{28}O_{64}]^{4+}(e^-)_4$*, Adv. Mater. **19** (2007), 3564.

[UHK+17] N. Umeda, J. Hiratsuka, A. Kojima, et al., *Long pulse and high power density $H^-$ ion beam acceleration for ITER*, AIP Conf. Proc. **1869** (2017), 030008.

[VSE04] P. Vankan, D. C. Schram, and R. Engeln, *High rotational excitation of molecular hydrogen in plasmas*, Chem. Phys. Lett. **400** (2004), 196.

[Wad18] M. Wada, *Plasma-surface interaction in negative hydrogen ion sources*, Rev. Sci. Instrum. **89** (2018), 052103.

[WDF09] D. Wünderlich, S. Dietrich, and U. Fantz, *Application of a collisional radiative model to atomic hydrogen for diagnostic purposes*, J. Quant. Spectrosc. Radiat. Transfer **110** (2009), 62.

[WF16] D. Wünderlich and U. Fantz, *Evaluation of State-Resolved Reaction Probabilities and Their Application in Population Models for He, H, and $H_2$*, Atoms **4** (2016), 26.

[WFN16] C. Wimmer, U. Fantz, and NNBI-Team, *Extraction of negative charges from an ion source: Transition from an electron repelling to an electron attracting plasma close to the extraction surface*, J. Appl. Phys. **120** (2016), 073301.

[WGF09] D. Wünderlich, R. Gutser, and U. Fantz, *PIC code for the plasma sheath in large caesiated RF sources for negative hydrogen ions*, Plasma Sources Sci. Technol. **18** (2009), 045031.

[Wil66a] R. G. Wilson, *Electron and Ion Emission from Polycrystalline Surfaces of Be, Ti, Cr, Ni, Cu, Pt, and Type-304 Stainless Steel in Cesium Vapor*, J. Appl. Phys. **37** (1966), 3161.

[Wil66b] ———, *Electron and Ion Emission from Polycrystalline Surfaces of Nb, Mo, Ta, W, Re, Os, and Ir in Cesium Vapor*, J. Appl. Phys. **37** (1966), 4125.

[Wim14] C. Wimmer, *Characteristics and Dynamics of the Boundary Layer in RF-driven Sources for Negative Hydrogen Ions*, Ph.D. thesis, University of Augsburg, 2014.

[WMF+14] D. Wünderlich, S. Mochalskyy, U. Fantz, et al., *Modelling the ion source for ITER NBI: from the generation of negative hydrogen ions to their extraction*, Plasma Sources Sci. Technol. **23** (2014), 015008.

[WPL73] G. A. Woolsey, I. C. Plumb, and D. B. Lewis, *Langmuir probe characteristics in a positive-ion/negative-ion plasma*, J. Phys. D: Appl. Phys. **6** (1973), 1883.

[Wün05] D. Wünderlich, *Berechnung von Teilchendichten für die Diagnostik an Niedertemperaturplasmen*, Ph.D. thesis, University of Augsburg, 2005.

[Wün17] ———, *Private communication*, Max-Planck-Institut für Plasmaphysik, Garching, 2017.

[YNX+04] J. Yang, Z. Nie, X. Xi, et al., *Emission ability of La-Sc-Mo cathode*, Appl. Surf. Sci. **229** (2004), 51.

# Acknowledgements

This is the end of my Ph.D. thesis, a journey started almost four years ago, with its ups and downs (as most of the events occurring in everyday life), but which has seen my personal and professional growth. This Ph.D. gave me a great opportunity to collect new and exciting experiences, to meet amazing people, to learn in a challenging environment a lot of new things, to become the person I am now. And this journey would have not been possible without the support, the help and the friendship of many people, that here I would like to thank.

First of all, I would like to thank **Prof. Dr.-Ing. Ursel Fantz**, for giving me the opportunity to work as a Ph.D. student and to be part of her group of scientists at the Experimental Plasma Physics (EPP) department at the University of Augsburg and at the ITED division of the Max-Planck-Institut für Plasmaphysik in Garching. Her constant supervision, her suggestions and her constructive comments helped me during the entire Ph.D. period.

I would like to thank **Prof. Dr. Henning Höppe** for having accepted to be the second reviewer of my Ph.D. thesis.

Any word would sound inadequate to explain my gratitude to **Dr. Roland Friedl**: when I arrived, I was a scared girl in a place and in a laboratory completely new for me, and he welcomed me and "introduced" me to ACCesS. He taught me how to control and drive any single component of ACCesS, with patience and care, until I was able to stand on my own feet. I thank him for the many and fruitful discussions about Cs, for the always present support and for carrying the heaviest components of the setup when I needed. Thank you, I have learned a lot.

I would like to thank the entire EPP group (and some "old" members): **Dr. Stefan Briefi**, **Dr. Uwe Kurutz** (always encouraging me, and teaching me that a smile can change the day), **David Rauner**, **Caecilia Fröhler**, **David Ertle**, **Adrian Heiler** (good luck!), **Maria Lindauer** and **Frederik Merk** (thank you for taking care of the tomato plant, a green spot in our dark cellar). I thank all of them for the nice time in the laboratories and in the office, their support was very important for me. In particular, a special thank to Caecilia Fröhler: her spontaneity and honesty are rare qualities (and I love our after work dinners!).

I would like to thank also the entire ITED group at IPP Garching, in particular

**Markus Fröschle** for his help with the Cs ampule oven: when I had no hope, he saved me and my Ph.D as well. I would also like to thank **Dr. Loïc Schiesko** for his time spent performing RBS measurements, searching for the presence of heavy metallic impurities on my samples, and **Dr. Christian Wimmer** for his support in the installation of some of the diagnostics at ACCesS. I want to thank **Dr. Riccardo Nocentini** for helping me in the engineering aspects of the construction of some components for ACCesS and for the nice discussions about all the possible materials that could be investigated (I admit it was very funny and stimulating to deal with so many different materials, always searching for more performing ones).

I thank very much **Wolfgang Reiber** (EP IV at Uni Augsburg) for all the time he spent for further RBS measurements on any kind of sample I had, always available for helping me as soon as he could. I thank him for having introduced me to the world of surface analysis and for his support. I thank also **Dr. Alexander Hartwig** (AMU at Uni Augsburg) for his kindness and availability to perform EDX measurements.

It is time now to thank **Dr. Alessandro Mimo** and **Antonio Pimazzoni**: we know each other since so many years and we have shared so many moments together (during bad days and in the happiest ones, from the university years until now that we are in three different cities), that it is almost not necessary to explicitly say that I thank them. But I do: in the worst period as in the best period during these four years, they were always there to support me, I will never forget that. Thank you (and I thank "l'indiano bello col chiodo nel cervello", too). Vi voglio bene.

I could have never started and finished this Ph.D. experience without the constant support of my family in Italy: I want to thank really a lot my **parents** and my **brother** for the daily calls and their frequent visits (and their refurbishments of food and wine). Your presence was very important for me even if I did not show it. I want to thank also my **grandparents**, who always encouraged me to pursue my dreams. I miss you.

And finally, I want to thank all my friends. The friends in Italy, in particular **Chiara Adele Cavarretta** (noi siamo la fortuna!), **Elena Ponzio** and **Elisa Gennaro** for the long Skype and phone calls: your support was decisive in these four years. The friends that I met here in Germany, in particular **Daryan Parab**, **Filippo Bizzirri** and **Raluca Chişbora**: sometimes a good friend and a good meal is all what we need. The friends that now are spread around the world: I will not forget them.

**To all of you: thank you!**

P.S. And my thanks also to ACCesS: it was a great mate in these four years. Mi mancherai!